Light-Matter Interactions in High-Efficiency Photovoltaics, Light-Emitting Devices, and Strongly Coupled Microcavities

by

MADELEINE REYNOLDS LAITZ

B.S. Chemical Engineering, University of Rochester, 2016
MRes Green Chemistry, Imperial College London, Fulbright Scholar, 2017

Submitted to the Department of Electrical Engineering and Computer Science
in partial fulfillment of the requirements for the degree of

Doctor of Philosophy
in Electrical Engineering and Computer Science

at the

MASSACHUSETTS INSTITUTE OF TECHNOLOGY

May 2022

Author: _____

Department of Electrical Engineering and Computer Science
May 2, 2022

Certified by: _____

Vladimir Bulović
Department of Electrical Engineering and Computer Science
Thesis Supervisor

Accepted by: _____

Leslie A. Kolodziejski
Department of Electrical Engineering and Computer Science
Chair, Department Committee on Graduate Students

Light-Matter Interactions in High-Efficiency Photovoltaics, Light-Emitting Devices, and Strongly Coupled Microcavities

by

Madeleine Reynolds Laitz

Submitted to the Department of Electrical Engineering and Computer Science
on May 2, 2022, in partial fulfillment of the requirements for the degree of
Doctor of Philosophy in Electrical Engineering and Computer Science

ABSTRACT

The interactions of light and matter drive many of today's devices, from electricity generation and consumption to manipulation. Within electricity generation, emerging thin film photovoltaics now rival traditional silicon-based solar cells in terms of power conversion efficiency (PCE) due to dramatic improvements to optoelectronic material properties and device architectures. Within electricity consumption, quantum dot light emitting diodes (QD-LEDs) are a high-efficiency, high color purity, versatile material candidate. Recent efforts to develop heavy metal-free QD-LEDs have led to high external quantum efficiencies in InP- and ZnSe-based QDs rivaling the performance of the colloidal archetype of Cd-based QD-LEDs. Within energy manipulation, the emergence of photonics from electronics presents opportunities to engineer low-loss, low-threshold information transmission and computation by all-optical means and matter-mediated hybrid electronic/photonic processes.

In this work, we investigate light-matter interactions in emerging thin film perovskite photovoltaics, heavy metal-free QD-LEDs and microcavities, and two-dimensional perovskite microcavity exciton-polaritons.

First, we quantify the PCE enhancements due to photon recycling in high-efficiency $Cs_{0.05}(MA_{0.17}FA_{0.83})_{0.95}Pb(I_{0.83}Br_{0.17})_3$ (triple-cation) perovskite thin film photovoltaics as a function of material properties such as non-radiative recombination and the probability of photon escape. We determine that a perovskite active layer material with non-radiative rates k_1

< $1x10^4$ s^{-1} can result in practical PCE improvements of up to 1.8% due to photon recycling alone, and present material and device design principles to harness photon recycling effects in next-generation perovskite solar cells.

Next, we investigate energy and charge transfer in InP/ZnSe/ZnS QD thin films and QD-LEDs as a function of increasing electric field strength. We probe the voltage-controlled photoluminescence (PL) modulation of a QD-LED in reverse bias and achieve 87% PL quenching, which is, to our awareness, the highest reported quenching efficiency in InP-based QDs. We also demonstrate amplified spontaneous emission processes in QD metallic microcavities by spectral coincidence of a three-dimensional confined photon mode and photon recycling-enhanced gain region.

Finally, we form exciton-polaritons (polaritons) at room-temperature in 2D perovskite microcavities resulting in, to the best of our knowledge, a record exciton-photon coupling strength for planar $(C_6H_5(CH_2)_2NH_3)_2PbI_4$ microcavities of $\hbar\Omega_{Rabi} = 260 \pm 5$ meV. By utilizing wedged microcavities in which the cavity detuning is changed as a function of excitation position, we probe the temperature-dependent polariton photophysics for varying polariton exciton/photon character. In this way, we reveal material-specific polariton relaxation mechanisms and intra-cavity pumping schemes from the interplay of 2D perovskite excitonic states.

Thesis Supervisor: Vladimir Bulović

Title: Professor of Electrical Engineering and Computer Science

ACKNOWLEDGEMENTS

It has been a tremendous five years at MIT, and I've been so fortunate to work with dedicated, passionate, and creative researchers within and beyond the ONE Lab. Taking a moment now to reflect on the many directions this research has taken me, I feel profoundly lucky to have had the opportunity to study fundamental photophysics in many device settings – learning not just about a specific function, but rather the interconnectedness between materials, technologies, and techniques.

I'd like to thank my research advisor, Vladimir Bulović, who has allowed me to pursue my varied interests with tremendous freedom. He has challenged me to become a better scientist, to ask the right questions, to internalize the fundamental microscopic picture beyond equations, and to communicate not just the technical details, but the joy of scientific revelation.

I am thankful to Prof. Farnaz Niroui and Prof. Keith Nelson for serving on my thesis committee. Prof. Niroui has an ability with nanoscale devices like no other, and I am grateful for her insights into fabrication and function. Prof. Nelson's boundless enthusiasm and curiosity for light-matter interactions has been a sustaining force in my graduate career. Even in my first year, Prof. Nelson met me with sincerity and respect, and I felt from the first exchange that we were partners in elucidating the photophysical processes of a given system.

Resounding thanks to my mentor, Dr. Dane deQuilettes. I am tremendously grateful for Dr. deQuilettes' support, for long discussions about mechanisms and experimental design, for encouraging words throughout the challenging doctoral program, and for aiding the professional development of all ONE Lab members. I was fortunate to be assigned Prof. Karl Berggren as an academic advisor, and he was an advocate and earnest supporter over the last five years. His clear, actionable advice empowered me to move forward at pivotal moments, and I always left conversations feeling hopeful, determined, and equipped with a plan. Prof. Giulia Grancini, though time-zones away, was available for long scientific conversations about low-dimensional materials, synthesis, and characterization. Her enthusiasm and optimism for our collaborative work was a tremendous buoy. To Prof. Jennifer Jay, there's too much to say – I first donned a

lab coat in Prof. Jay's lab at UCLA, and have ever since been enthralled by the rhythm of research. From the quiet moments of an experiment's design to the rare, and still quiet, moment of its success, Prof. Jay shared with me the delight of identifying and striving to answer the questions *you* find most captivating.

I have been fortunate to work with many wonderful colleagues. Dr. Tom Mahony is the most thoughtful scientist I have ever met, and the care he took in designing and building optical setups extended beyond the inanimate, as, during his time at MIT, he also strove to better the culture and community in the department by supporting his peers at every turn. I aspire to be half the researcher and member of the community as Dr. Mahony. I'd like to thank Ella Wassweiler, a powerful researcher and advocate for diversity, equity, and inclusion. I was lucky to spend countless hours with Ella both in the lab and brainstorming new initiatives for graduate students in EECS. I will treasure Ella's support and friendship throughout this journey. I'd like to thank the entirety of the ONE Lab, from whom I have learned so much, especially Benjia Dak Dou, Mayuran Saravanapavanantham, Melany Sponseller, Richard Swartwout, Anurag Panda, Jonas Xie, Tony Zhu, and Joel Jean. Beyond the ONE Lab, I found a home in Prof. Keith Nelson and Prof. Moungi Bawendi's labs, and feel profoundly fortunate to have had the opportunity to work with and learn from Jude Deschamps, Alex Kaplan, and Dr. Andrew Proppe.

Outside of the lab, I am thankful to THRIVE, EECS REFS, and EECS GAAP. This community of students, passionate about representation in STEM at the graduate level, is unparalleled. To all of the graduate students who spend time beyond their doctoral research thinking about and working on ways to enhance the student experience at MIT, push for equitable structures, and advocate for diversity and inclusion: thank you.

To friends within and beyond the walls of MIT, I'm grateful for the laughs, support, and adventures. Special thanks to Julia, my dear friend and sister; Diana and Jackson, the best friends anyone could ask for; Adrian, who I aspire to be more like in every way; Sam, who makes me laugh and encourages me to dream; and my wildly wonderful cohort of Fulbrighters.

1—6

A big thanks to the Reynolds family, whose warmth, boundless enthusiasm, unconditional support, laughter, creativity, and musicality has been the greatest source of joy throughout my life. I am defined by the times spent together at 741 Spruce St singing rounds, playing music, surviving wrapping paper wars, and losing ping-pong tournaments. I'm so thankful for my parents, Anne-Marie and Steve. I would have fallen down and stayed down long ago if it weren't for their unwavering love and support, encouragement, and unparalleled sense of humor – not a day goes by that I'm not grateful. Finally, to my partner, Martha, I dedicate this thesis. I quite literally could not have done this without her. I'm immeasurably thankful for her patience, belief, validation, love, and unfailing ability to light up my days during the PhD program.

Madeleine Laitz

May 2022

Boston, MA

Contents

List of Figures

Figure 3.1: Exciton-polariton photoluminescence (PL) (left) and reflectivity (right) dispersions with increasing cavity length from (a) higher cavity mode energy to (c) lower cavity mode energy as shown schematically in (d). As the cavity shifts to lower energies and the polariton dispersion becomes increasingly photonic (c), the bottleneck effect emerges with the greatest emission intensity at high $k_{//}$ values. The upper and lower polariton branches are extracted from reflectivity minima (white dotted line) and fitted (white solid line) using Eq. 3.1 (fitted cavity and exciton energies shown, white dashed line) with a Rabi splitting of $\hbar\Omega_{Rabi}$ = 260 meV. (a-c, lower figures) Hopfield coefficients for cavity detunings (photonic fraction C_k^2, black trace; excitonic fraction X_k^2, red trace) ranging from (a) excitonic to (c) photonic depicting the light-matter characteristics of the generated polaritons as a function of $k_{//}$ (Eq. 3.2). (e) Experimental (red dots) and theoretical (black traces) upper and lower polariton branch energies at $k_{//}$ = 0 with $\Omega Rabi$ = 260 meV. Dashed black traces correspond to the exciton energy and cavity energy changing with cavity length. (f) As the cavity energy decreases and the dispersion becomes more negatively detuned, the photoluminescence (PL) distribution shifts to higher $k_{//}$, resulting in a decrease in the fraction of PL within $k_{//}$ = 0 ± 0.2 um^{-1} (red trace). Integrated PL intensity as a function of increasingly negative detuning exhibits inhibited emission (black trace). (g) The energy-integrated PL spectra reveal the re-distribution of the maximum PL intensity to higher $k_{//}$ with increasingly photonic detunings (raw data, solid trace; smoothed data, dashed trace).

Figure 3.2: (a-c) Lower polariton branch (LPB) photoluminescence (PL) for Δ = +28 meV cavity detuning as a function of temperature revealing (e) the shifting of the maximum PL intensity to higher $k_{//}$ at intermediate temperatures before returning to $k_{//}$ = 0 at 4 K. (d-f) The temperature-dependence of the energy-integrated PL was monitored for two detunings established at room temperature ($\hbar\Omega_{Rabi}$ = 175 meV, Δ = +28 meV and +45 meV), with both detunings showing bottlenecked PL at intermediate temperatures and emission from $k_{//}$ = 0 at sufficiently low temperatures (raw data, dashed trace; smoothed data, solid trace; peak PL trend to guide the eye, symmetric about $k_{//}$ = 0, dotted trace). (g) Cavity detuning and Hopfield

Figure 3.9: (a-d) Lower polariton branch (LPB) photoluminescence (PL) as a function of temperature for $\hbar\Omega_{Rabi}$ = 260 meV revealing e) the migration of the maximum PL intensity to higher $k_{||}$ at intermediate temperatures before returning to $k_{||}$ = 0 at 4K. (e,f) The temperature-dependence of the energy-integrated PL for Δ = +41 meV showing bottlenecked PL at intermediate temperatures and emission from $k_{||}$ = 0 at sufficiently low temperatures. (g,h) PL spectra for two detunings (Δ = +41 meV and +65 meV) at 295K, corresponding to the temperature series in (f). Note: asymmetries in PL distribution arise from imperfectly flat substrate seating due to Ag cryo paste used for thermal contact. Additionally, the thicker perovskite active layer results in increased uncoupled exciton PL at elevated temperatures as compared to the thinner active layer yielding $\hbar\Omega_{Rabi}$ = 175 meV. ..... 3—159

Figure 3.10: Temperature-dependent XRD from 295 K to 11 K showing no phase change as a function of temperature. ..... 3—160

Figure 3.11: (a) PLQE measured at 295 K with integrating sphere and 405 nm laser excitation in cw-mode (~0.7%), and used to calculate a 100-fold PLQE increase as a function of temperature. To ensure the PL increase was not from changes in the absorption of the excitation as a function of temperature, (b) temperature-dependent absorption measurements were performed from 295 K to 80 K. The excitation wavelength was tuned to a region with very little change in absorption (c, dashed black trace indicating laser excitation wavelength), with small fluctuations in absorbance quantified in the (d) Abs Factor extrapolated to 4K. ..... 3—161

Figure 3.12: Lower polariton branch (LPB) photoluminescence (PL) ($\hbar\Omega_{Rabi}$ = 175 meV, Δ = +40 meV) as a function of excitation power spanning five orders of magnitude. The top row shows the *k*-space dispersion, and the bottom row shows the *k*-space-integrated PL with high-$k_{||}$ (high energy) and low- $k_{||}$ (low energy) spectral regions fit to determine whether the increase in power results in an increase in emission from the bottom of the LPB due to increased polariton-polariton scattering. No such trends are observed at 4 K, and only a weak increase in the low- $k_{||}$ region is seen at 100 K, indicating that polariton-polariton scattering is likely not the primary factor for the dramatic redistribution of PL to $k_{||}$ = 0 at low temperature. *Row 1,2*: 4 K power series (demonstrates a more rapid increase in high $k_{||}$ PL (blue Gaussian) than low $k_{||}$ (green Gaussian) indicating greater biexciton emission enhancement with increasing

decreases and the DX emission emerges with an increasingly long lifetime, visible as a short-timescale fast component with delayed emission into a longer tail ((e,f) green trace, 100 K). In the cavity (e), the extent of delayed emission is reduced as compared to the bare 2D film (f), and the fast component contribution increased due to the additional pathway of coupling the X and cavity mode to form the strongly coupled short-lifetime polariton emissive state competing with the spin-flip from X to DX. For the bare 2D film, further reductions in temperature show (i,l) the X emission contribution increasing at early timescales as its emissive lifetime decreases and the spin-flip rate ($k_s(T)$) slows, with the DX demonstrating an increasingly long emissive lifetime and $k_s(T)$ additionally slowed via the Arrhenius factor (Figure 3.18b). Conversely, in the cavity, the IRF-limited strong coupling emission of X and the cavity mode competes with the spin-flip and begins to dominate the TRPL decay dynamics at 60 K (h), with weak emission contribution to the decay from the DX state resulting in a long lifetime tail. (k) At 4 K in the cavity, the delayed emission due to the slow $k_s(4K)$ and long tail from the DX is not observed, showing nearly exclusively IRF-limited strongly-coupled emission between the X and cavity mode. .....3—171

Figure 3.23: (a) The bare 2D perovskite film time-resolved photoluminescence decay (TRPL) traces as a function of temperature show a 295 K lifetime of τ_{295K} = 350 ps, increasing with decreasing temperature. With the emergence of the dark exciton (DX) emission in the PL spectrum, the film lifetime trace develops an initial fast decay component attributed to the bright exciton (X) with a longer lifetime component attributed to the DX. (b) The strongly-coupled microcavity ($\hbar\Omega_{Rabi}$ = 175 meV, Δ = +28 meV) lower polariton branch (LPB) emission demonstrates similar trends to the thin film at high temperatures, but deviates sharply at low temperatures, exhibiting only the fast, IRF-limited (40 ps) lifetime of the bare 2D film initial fast decay component. (c) Temperature-dependent 2D thin film TRPL traces with finer temperature steps, showing that, with decreasing temperature, the film lifetime increases to τ_{295K} = 740 ps, consistent with a reduction in non-radiative pathways which quench the lifetime. For temperatures between 180 K and 100 K, we observe reduced emission at early timescales. Below 100 K, with the prominent emergence of the DX, and subsequently XX, emission in the PL spectrum, the film lifetime trace develops an early fast decay component before the flat, delayed emission leading into a long tail. This multi-component lifetime behavior becomes

List of Tables

OVERVIEW

Light-Matter Interactions and Thesis Organization

The interaction of light with matter and interconversion between charge carriers and photons in semiconducting materials are critical processes in numerous energy conversion systems. For *power generation* by solar energy, the key process is photon absorption and conversion to electrons which are subsequently extracted from the device. For *power utilization* in terms of light emission, the reverse process is true, in which electrically injected carriers recombine in the device active layer, emitting photons. In certain excitonic materials, the interconversion between charge carrier and photon can be harnessed in the strong light-matter coupling regime, in which a photon emitted following radiative recombination is re-absorbed and re-emitted many times. By placing the semiconducting material between two highly reflective mirrors, this interconversion process can be enhanced by further confining photons and increasing the number of photon/exciton recycling events. If the exciton-photon coupling rate is faster than the dissipation rate from the system, a hybrid light-matter state is formed, a quasi-particle with properties of both a photon and an exciton known as an exciton-polariton. Exciton-polaritons present opportunities for realizing room-temperature Bose-Einstein condensation, low-threshold polariton lasing, and next-generation qubits.

In this work, we investigate light-matter interactions in photovoltaics, light-emitting diodes, and strongly coupled microcavities. We first provide a semi-empirical model to predict the power conversion efficiency enhancements from photon recycling in perovskite solar cells based on material properties derived from non-contact, optical measurements (Part I). In this way, we deconvolute active layer theoretical performance from experimental device performance to determine material property and optoelectronics design principles for next-generation photovoltaics.

We then investigate charge carrier dynamics such as Förster resonance energy transfer in Cd-free quantum dot (QD) thin films and quantify the dependence of the energy transfer rate on

spectral overlap between absorption and emission (Part II). We again deconvolute thin film dynamics from device performance by investigating the impact of increasing electric field on diffusive processes in a light-emitting diode (QD-LED) configuration via spectrally resolved lifetime measurements and quantification of photoluminescence quenching efficiency.

Finally, we continue to explore the recycling of absorbed photons in two-dimensional perovskite semiconductor microcavities in the strong light-matter coupling regime, in which the bound exciton couples to the cavity photon to form exciton-polaritons at room temperature (Part III). We study microcavities with varying exciton-photon coupling strengths and detunings as a function of temperature to deconvolute two-dimensional perovskite exciton-polariton relaxation mechanisms, highlighting both material-specific scattering processes that could reduce condensation thresholds and intracavity pumping schemes to inform polaritonic device design.

INTRODUCTION

Photovoltaics

HYBRID ORGANIC-INORGANIC PEROVSKITES

Perovskites are a class of materials possessing an ABX_3 structure, where A represents an organic or inorganic cation (e.g., methylammonium (MA), formamidinium (FA), Cs), B denotes a metal (e.g., Pb, Sn), and X a halide ion (e.g., I, Br, Cl).[1] Initially used in dye-sensitized solar cells, perovskite materials have since emerged as a leading active layer material in high efficiency single junction photovoltaics.[2] The power conversion efficiency (PCE) of perovskite solar cells has increased rapidly, from 3.81% power conversion efficiency in 2009 to 25.8% certified PCE in 2021 (Figure A).[3] Characterized by their solution processibility, strong absorption, defect tolerance, long carrier lifetimes and high carrier mobilities, perovskites have risen to the fore as a light-weight, flexible, cost-effective, and competitively efficient alternative to traditional silicon and organic PV materials.[4]

Such advances in perovskite solar cell efficiency have been enabled in part by the optimization of device architectures, though closing the gap between perovskite experimental performance and the theoretical maximum requires developing an understanding of the fundamental photophysics, analogous to the evolution of high-efficiency inorganic solar cell active layer materials. In highly luminescent GaAs solar cells, multiple absorption and emission events within the absorber layer were observed, a phenomenon called photon recycling.[5–7] By utilizing perfect back reflectors, an increase in GaAs power conversion efficiency from 25.1-28.1% was achieved solely by harnessing photon recycling effects.[7–9] This phenomenon is dictated in part by the high refractive index of the material, which leads to a small escape cone for photons within the active layer. Emitted photons can be reabsorbed in strongly absorbing materials with a low Stokes shift, and photons emitted beyond the escape cone can be waveguided, further increasing the likelihood of reabsorption. These reabsorbed photons generate electron-hole pairs, and the re-emission/reabsorption process can continue for many iterations.[8] Under constant

photoexcitation, photon recycling thus effectively increases the charge carrier density within the active layer at steady-state, increasing the quasi-Fermi level splitting and open-circuit voltage in a device setting.[9,10] In highly luminescent materials with low non-radiative recombination rates, the effect of this process can increase the steady-state charge carrier density substantially, as was seen in GaAs solar cells, in which a single photon was determined to undergo up to 50 recycling events.[8,9] Similarly, in single crystal and polycrystalline lead halide perovskites, photon recycling has also been observed, but to a lesser extent.[11–13]

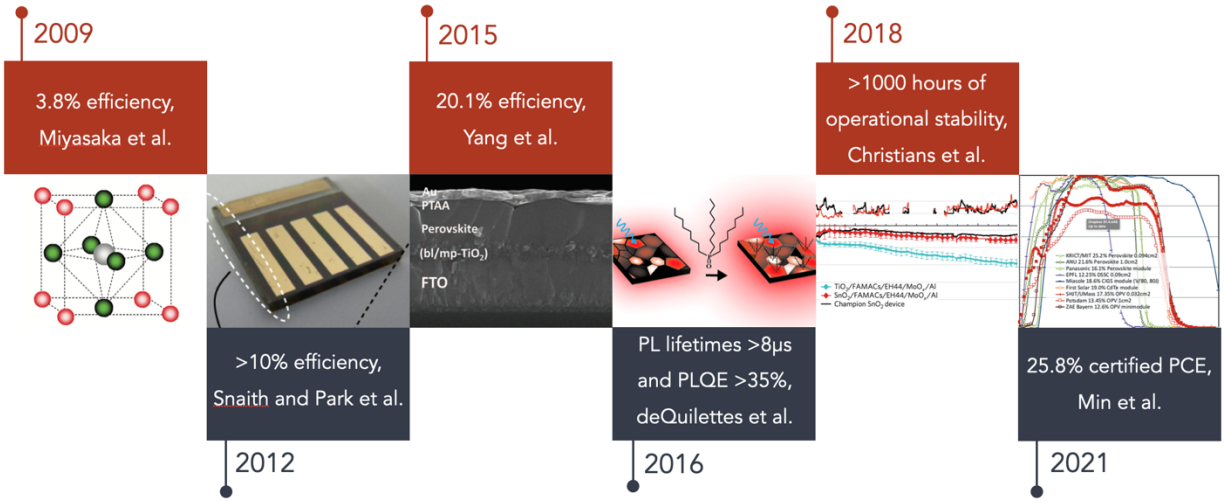

Figure A: Evolution of perovskite solar cell performance, highlighting optimization of both device architectures and material quality yielding rapid advancements from 3.8% power conversion efficiency (PCE) to 25.8% PCE in just twelve years.[3,14–19]

Solution-based perovskite films have traditionally reported high non-radiative recombination rates and low photoluminescence quantum efficiencies (PLQE).[20,21] Recently, passivated perovskite films have demonstrated high internal PLQE, exceeding 90%, high external radiative efficiencies (ERE), and low non-radiative voltage losses ($\Delta V_{OC,nr}$) (Figure B), indicating low non-radiative recombination rates and defect densities.[18,22,23] These emerging optical properties coupled with the small Stokes shift and high absorption coefficient begs the

question: to what extent is photon recycling observed in state-of-the-art perovskite materials, and what are the practical performance gains one can make by harnessing this phenomenon? A rigorous and general quantification of photon recycling as a function of material properties is required to inform future iterations of materials design. It is essential to bridge the effect of photon recycling on the optoelectronic properties and device parameters of mixed organic-inorganic perovskites.

Increases in open-circuit voltage (V_{OC}) due to photon recycling have been explored in the archetypal perovskite formulation, $CH_3NH_3PbI_3$ ($MAPbI_3$) films, but an extension of this analysis to cutting-edge multi-cation perovskites and operationally relevant device parameters such as maximum power point (MPP) has not yet been provided.[5] In this work, the limiting device performance of state-of-the-art triple-cation perovskite films, which demonstrate record efficiencies and high stability,[19,24] is determined theoretically, and current-voltage (JV) curves simulated with and without photon recycling. An extension to $MAPbI_3$ films is provided as a benchmark against which to compare novel compositions. An analysis of the effect of photon recycling on voltage, carrier density, outcoupling, and recombination processes at MPP and as a function of photon escape probability is presented, yielding thresholds for non-radiative recombination above which significant enhancements in device-relevant parameters are observed.

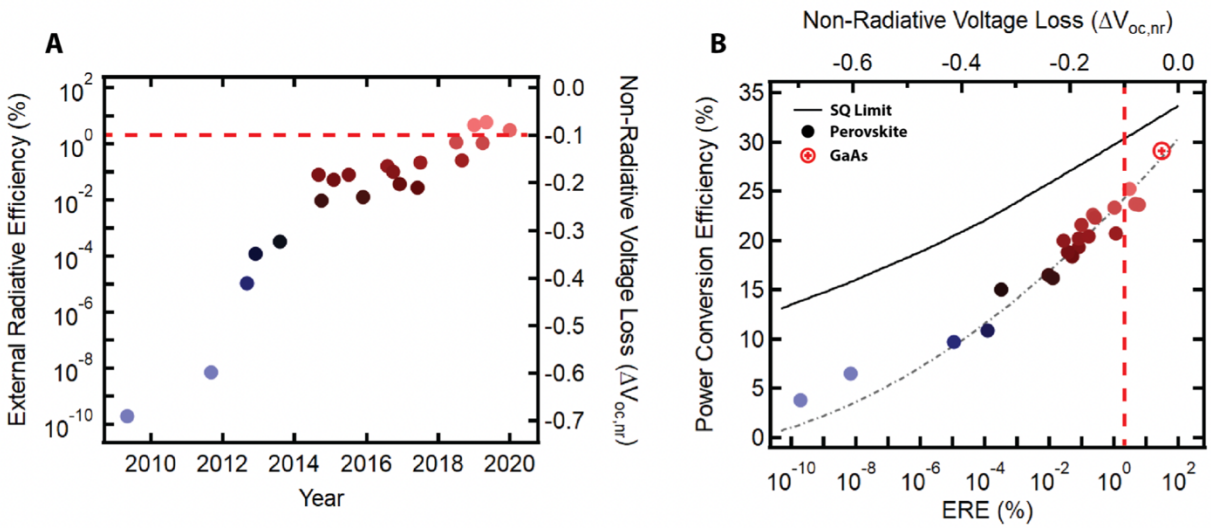

Figure B: For record-holding perovskite solar cells, (a) the external radiative efficiency (ERE, %) over time is presented, showing that the (b) increases in ERE correspond to increases in power conversion efficiency (%) and decreases in voltage deficits from the radiative limit ($\Delta V_{OC,nr}$). The Shockley-Quiesser (SQ) limit (black trace) is shown, with the record GaAs solar cell (red circle) as a benchmark comparison to perovskites. From deQuilettes, D.W., Laitz, M., *et al.*[23]

QUANTUM DOTS FOR LIGHT-EMITTING APPLICATIONS

The ability to deconvolve the photophysics of an active layer from its device setting allows for the evaluation of dynamics unique to the material system and the quantification of the impact of transport layers on fundamental processes. Beyond perovskite photovoltaics, this strategy provides useful insight into the varying properties of semiconducting materials in isolation and in practical device settings. Here, we extend the materials and device exploration to zero-dimensional colloidal quantum dots (QDs) in light-emitting diodes (LEDs).

QDs, or "artificial atoms," generally consist of ~10s to ~10^4s tightly packed atoms, forming highly organized crystals demonstrating unique size-dependent effects due to quantum confinement.[25] These effects arise when the electron and hole wavefunctions within the QD are confined to a region smaller than the corresponding bulk material's Bohr radius.[26] While QDs can be grown epitaxially or in solution via thermally activated nucleation processes (colloidal), we focus exclusively here on solution-formed colloidal QDs. The size of the resulting QD is controlled by various reaction parameters, including reaction time, which, in addition to filtration processes, allows for the careful tuning of QD size and the degree of quantum confinement.[27] The resulting QD emission is thus a function of QD size, with larger diameter crystals resulting in lower energy emission and smaller diameter crystals yielding higher energy emission due to the enhanced degree of confinement resulting in a larger bandgap (Figure C).[28]

The optical quality of QDs can be enhanced by passivating non-radiative surface sites on the nanocrystal (core) with a secondary semiconducting material (shell), such as CdSe-core/ZnS-shell architectures. Core-shell QD structures have exhibited high photoluminescence (PL) quantum efficiencies (PLQE),[29] with subsequent iterations involving a secondary shell material and core/shell gradients yielding ~100% solution PLQE.[30] Further defect passivation is achieved by coating the outermost shell with organic ligands which additionally lend solubility to the QD system in a variety of solvents, as dictated by the ligand chemistry.[25,27]

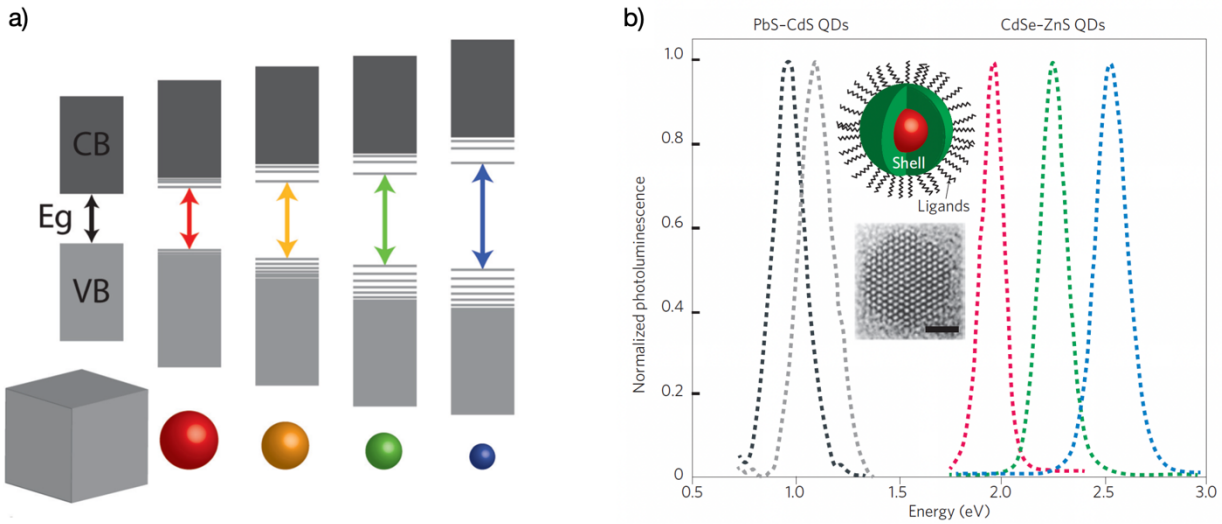

Figure C: (a) Schematic of increasing optical bandgap with increasing quantum confinement, from low energy bulk material (left, cube) to high energy, blue-emitting small-diameter quantum dot (right, blue sphere). (b) Photoluminescence spectra of variable diameter core-shell quantum dots (low energy PbS/CdS; high energy CdSe/ZnS). Upper inset: schematic of core-shell quantum dot architecture with passivating organic ligands. Lower inset: CdSe quantum dot image via high-resolution transmission electron microscope (scale bar = 1.5 nm). (a) From Panfil *et al.*[25] (b) From Shirasaki *et al.*[27]

QDs have since been utilized in a variety of applications, ranging from light-emitting devices, field-effect transistors, photovoltaics, biomarkers, and sensors due to high material PLQE, chemical tunability, narrow spectral linewidths, and flexible deposition schemes.[26,28,31] To date, heavy metal-containing QDs are the most studied and exhibit highly desirable optical properties. As QD-based devices across applications approach commercialization quality rivaling more established materials (e.g., conventional inorganic and organic displays), the need for environmentally benign alternatives is clear.[26,32] Recently, color-tunable InP-based QDs and blue-emitting ZnSe-based QDs have emerged as promising heavy metal-free emitters for light-emitting devices.[30,33,34]

Due to the narrow emission spectra and high efficiency, QDs have become a low-energy and high color purity material candidate for display technologies.[27] QDs have found application as an enhancement film in white light back-lit QD-LCDs, replacing conventional phosphors.[26,28,35,36] In this configuration, the QD thin film absorbs light from LEDs, down-converting the higher energy LED emission. The resulting QD emission yields greatly enhanced color purity, with photoluminescence full-width half-maximum (FWHM) <40 nm, increasing the color gamut figure-of-merit from the National Television System Committee from ~72% of the standard utilizing phosphors to ~110% of the standard using QDs.[26,28] Subsequent work has moved toward direct electrical excitation of QD films without the LED backlight, and some experimental QD-LED devices have demonstrated high external quantum efficiencies (EQE) exceeding 20%.[26,27]

In device settings, it is essential to understand the influence of the electric field on QD photophysics, charge transport, quenching mechanisms, and efficiency, and to mitigate adverse effects during operation. To probe the underlying physics, QD-LED architectures and capacitor structures have been utilized, revealing composition-dependent QD responses.[26] In some QD systems, an electric field induces exciton polarization and decreases electron-hole wavefunction overlap, resulting in reduced radiative recombination via the quantum confined Stark effect.[37] In other systems, photoluminescence quenching studies revealed the detrimental effects of charging, in which the applied electric field can dissociate excitons and ionize QDs, resulting in free carrier generation and trion formation with subsequent increased Auger recombination.[26,38]

Understanding the effect of built-in and applied electric fields in QD-LED architectures employing Cd-free QDs is essential to the commercialization of energy-efficient light emitting technologies and displays. In this work, we explore state-of-the-art InP/ZnSe/ZnS QD thin films and QD-LEDs to quantify diffusive processes in the absence and presence of external fields. We correlate these results to PL quenching efficiency and explore the impact of QDs in various dielectric environments within the thin film resulting in mobile and immobile sites.

COUPLING LIGHT AND MATTER: EXCITON-POLARITONS

The field of optoelectronics arose from the limitations of conventional silicon-based electronics (e.g., modulation speeds[39,40]), and has created the opportunity for engineering fast, low-loss technologies. Photons (optical signals) are difficult to generate, control, and modulate, especially for in-direct band-gap materials like silicon, necessitating the development and optimization of direct band-gap materials beyond silicon.[39] A fundamental challenge in realizing all-optical technologies is that light is weakly interacting. While it is difficult to have one photon influence the behavior of another, it is possible to make interacting quasi-particles, called exciton-polaritons (herein referred to as polaritons), that have characteristics of both photons and excitons – both light and matter. Polaritons are formed in optical microcavities in the strong coupling regime between bound excitons (coulombically-bound electron and hole pairs) and cavity photons, and this quantum superposition results in a half-light, half-matter quasi-particle (Figure D).[41] Strong light-matter coupling was first theorized by J. J. Hopfield in 1958,[42] in which the hybridization of excitons and photons was shown to generate new eigenstates, and realized experimentally by C. Weisbuch *et al.* in 1992.[39,43]

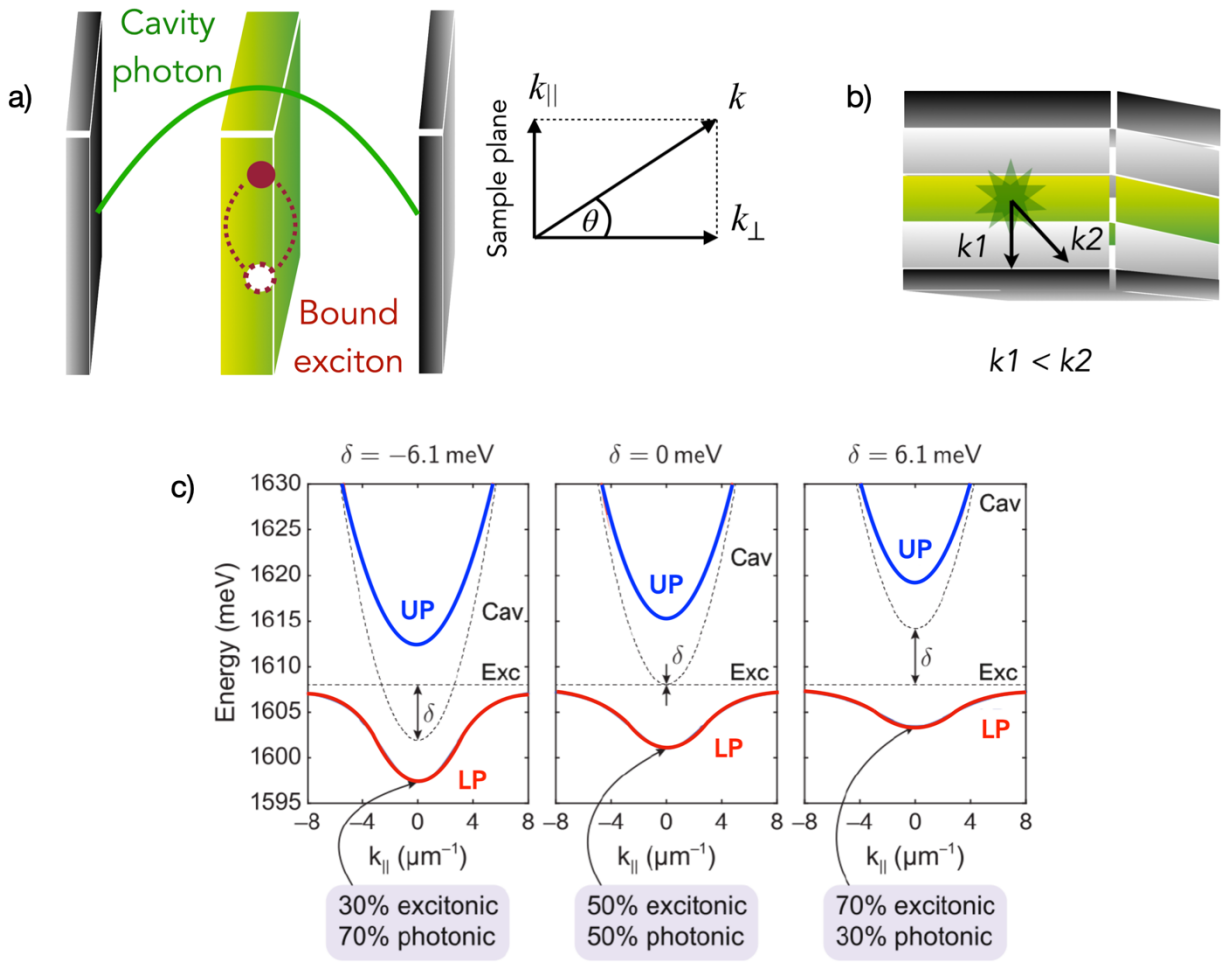

Figure D: (a) Schematic of microcavity structure utilizing two highly reflective surfaces (e.g., Ag mirror or distributed Bragg reflectors (DBRs) comprised of alternating high and low index of refraction materials) separated by $\frac{n\lambda}{2}$ (n = odd integer) with active layer placed at the antinode of the cavity photon electric field. (b) Microcavity cross-section comprised of optically inert spacer layers (gray, e.g., SiO_2, TiO_2, poly(methyl methacrylate)) and active material (green, e.g., GaAs quantum well, organic polymer). Momentum k vectors related to energy by: $E_P = \frac{pc}{n_c} = \frac{\hbar kc}{n_c} = \frac{\hbar c}{n_c}\sqrt{k_\perp^2 + k_{||}^2}$ in which higher energy photons correspond to higher momentum (k_2), generating the parabolic cavity photon dispersion in $k_{||}$-space. (c) Exciton-polariton dispersion in $k_{||}$-space with upper polariton (UP, red) branch, lower polariton (LP, blue) branch, and uncoupled exciton and photon modes (black dashed trace) for three cavity detunings ranging from photonic (left) to excitonic (right), showing the enhanced curvature due to the greater photonic character for positive detunings and flatter dispersion due to the greater excitonic character for negative detunings. (c) From Sun *et al.*[44]

Polaritons exhibit photon-like qualities in that they have small effective masses (10^{-5} the mass of an exciton) and travel at high velocities, but also display strong non-linearities at relatively low excitation densities, which is characteristic of excitons.[40] Polaritons can be tuned to adjust the fraction of photonic or excitonic features, so that, even when mostly photonic, polaritons have a finite interaction strength, resulting in the potential for engineering fast, low-loss, low-power optical devices mediated by matter.[45] The upper and lower polariton branches can be detected via photoluminescence or reflectivity measurements in *k*-space (Figure E), and the photonic/excitonic character quantified. Additionally, these properties establish opportunities for studying out of equilibrium Bose-Einstein condensation (BEC), super-fluidity and quantum vortices for low-threshold polariton lasing.[46–48]

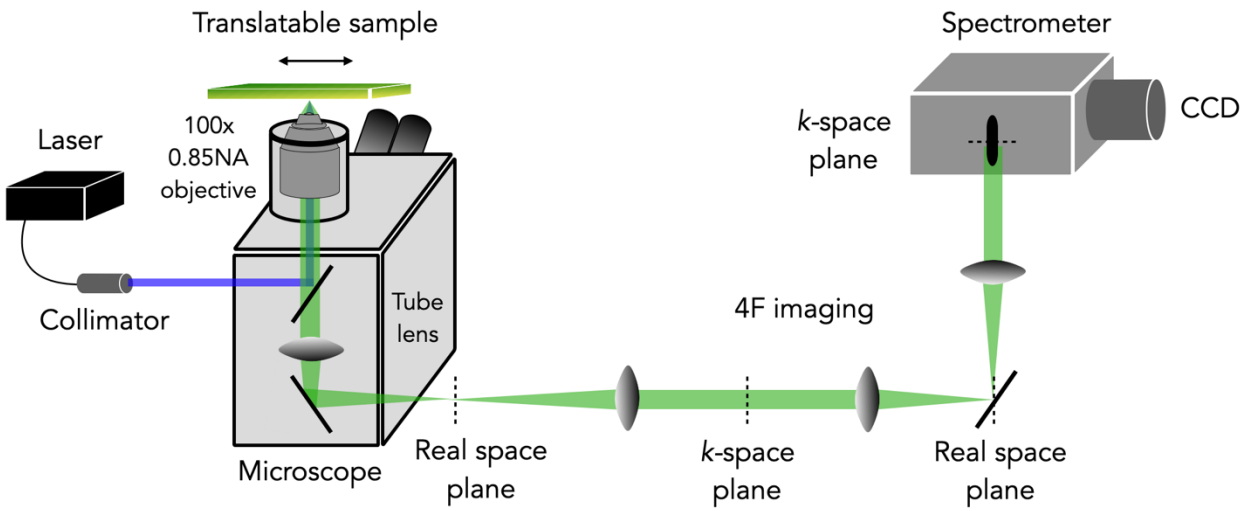

Figure E: Imaging *k*-space emission using a microscope and infinity corrected, high-NA objective. Sample emission from laser excitation is filtered through a dichroic beamsplitter before coupling in free space via a 4F imaging system into a spectrometer and CCD.

BEC is a macroscopic quantum state, which was explored in the mid-1990s in dilute atomic gases at extremely low temperatures (nK regime). Such low temperatures were required to reduce the inter-atomic distances below the thermal de Broglie wavelength, facilitating condensation in

the lowest energy state.[39,49,50] Given that the de Broglie wavelength (λ_{dB}) is inversely related to the mass and system temperature, heavy atomic systems require cryogenic temperatures to reach the condensation threshold:[39]

$$\lambda_{dB} = \sqrt{\frac{2\pi\hbar^2}{mK_BT}}$$

The condensation threshold can thus be tuned by decreasing the system temperature *or* mass. The idea of realizing light-mass BEC at elevated temperatures was explored as early as the 1960s,[39] in which it was hypothesized that excitons and photons could strongly couple and – due to their respective bosonic character – together form a bosonic quasi-particle. The first definitive demonstration of exciton-polariton condensation came in 2006,[51] utilizing inorganic Cd-based II-VI materials at 5 K, much warmer than the nK temperatures required for atomic condensates, and spurred work in GaAs microcavities at low temperature.[39]

Thus, traditionally, polaritons have been formed in high-quality, all-inorganic semiconducting materials (e.g. GaAs heterostructures) which require low operating temperatures (4-70 K) for polariton formation to ensure the strong coupling interaction is faster than the exciton dissipation rate and that the exciton binding energy is above k_BT.[52] The search for highly luminescent, excitonic materials that sustain strong light-matter interactions at room temperature is ongoing. To date, strong light-matter coupling has been successfully realized at room temperature in inorganic materials (e.g., GaN, ZnO) requiring complex growth techniques, and organic semiconducting materials (e.g. J-aggregates), though limited carrier transport and the nature of Frenkel excitons in organics – displaying orders of magnitude lower exciton interactions than inorganic Wannier-Mott excitons – pose design and implementation constraints.[53–58] Transition metal dichalcogenides (TMD) have excitonic interactions an order of magnitude larger than those in organics, and have exhibited room-temperature polariton formation, but the stability of these materials and necessity of a monolayer pose obstacles for larger-area development of robust TMD-based polaritonic systems.[59]

Realizing BEC at room-temperature is a persistent effort, with recent work showing non-equilibrium condensation and polariton lasing in polymer microcavities, organic single-crystal microcavities, and hybrid organic-inorganic microcavities.[60–62] A promising material for scalable room-temperature strong coupling devices and condensation has emerged from its meteoric rise in photovoltaic applications: perovskites.

Perovskites possess an ABX_3 structure, where A represents an organic or inorganic cation, B denotes a heavy metal, and X is a halide ion. Hybrid organic-inorganic perovskites have emerged as a leading active layer material in high efficiency single junction photovoltaics, now surpassing all other thin-film technologies in performance with a certified power conversion efficiency of 25.8%.[3] State-of-the-art perovskite materials demonstrate photoluminescence quantum efficiencies above 90% due to their low non-radiative recombination rates and unparalleled defect tolerance.[18,22,63] The properties that make perovskites work so well in solar cells – high absorption coefficient, small Stokes shift, high photoluminescence quantum efficiency (PLQE), solution processability, chemical tunability – simultaneously situate perovskites to function superbly as a coherent quantum material.[52,59,64–67] The opportunity to explore this traditional PV material in the context of polaritonic devices has generated tremendous recent interest, and the synthetic tunability of perovskites has allowed for the engineering of optimal perovskite formulations for polariton formation, such as high exciton binding energies (E_B ~50-500 meV) with minimal Stokes shift.[65,68]

The dimensionality of perovskites can be reduced by adding bulky cations, which separate the lead octahedra into electrically insulated sheets (Figure F). By varying the stoichiometry of the cationic species, the number of lead layers (n) can be tuned. These materials are called 'Ruddlesden-Popper" low-dimensional perovskites, and possess the general structure of $(C)_2(A)_{n-1}B_nX_{3n+1}$, where A, B, and X are as defined above, and C is an additional, bulky cation.[59,65] The number of single layered sheets can be varied from n = 1 (2D perovskites) to n = ∞ (bulk 3D perovskite). The n = 1 formulation is a quasi-quantum well structure with enhanced confinement in the inorganic layer resulting in an increased exciton binding energy as compared to the n =

∞ bulk perovskite (E_B ~10 meV).[65,68] This results in a blue-shift of the bandgap and increased excitonic feature in the absorption spectrum with decreasing n.

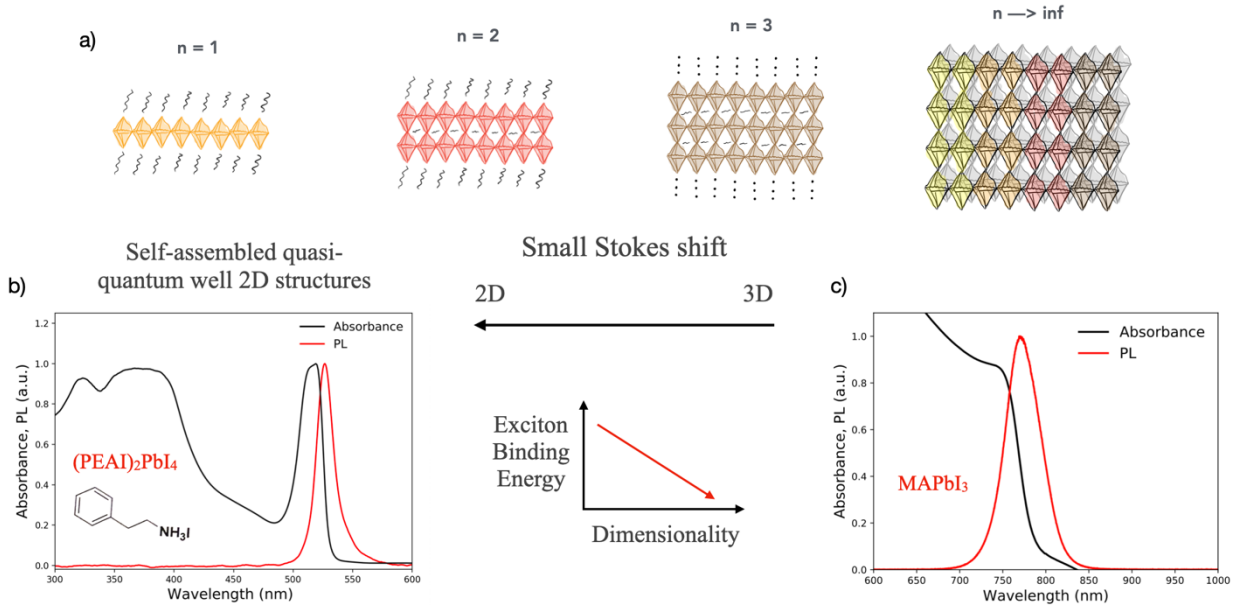

Figure F: (a) Schematic of increasing number of lead layers (n) separated by organic cations representing low-dimensional (n = 1, n = 2, n = 3) and bulk (n = ∞) perovskites. (b) Absorption (black trace) and emission (red trace) of low dimensional (n = 1) $(C_6H_5C_2H_4NH_3)_2PbI_4$ (i.e., $(PEA)_2PbI_4$) showing prominent excitonic feature in the absorption and low Stokes shift in emission. (c) Absorption (black trace) and emission (red trace) for bulk (n = ∞) $CH_3NH_3PbI_3$ (i.e., $MAPbI_3$) showing spectral red-shift due to the decreased quantum confinement and reduced band gap as compared to $(PEA)_2PbI_4$.

In this work, we explore a leading two-dimensional (2D) perovskite formulation, $C_6H_5C_2H_4NH_3)_2PbI_4$ (PEA_2PbI_4), which functions as a highly oriented self-assembled quantum well structure even in solution deposited films. PEA_2PbI_4 was chosen as a test-bed 2D perovskite material due to its exceptionally high exciton binding energy (~370-490 meV; variation between single crystal, ultrathin flake, and thin film has been observed, though the exciton binding energy consistently increases with decreasing halide electronegativity from CL to Br to I)[69], low

Stokes shift, relatively smooth morphology via spin-coating deposition techniques as compared to various other formulations, and strong absorption at the band edge. We fabricate 2D perovskite wedged microcavities and quantify the interplay between intrinsic relaxation mechanisms unique to this material system. We aim to provide microcavity and material design principles towards low-threshold BEC and nonsynthetic electronic structure modification for tunable kinetics.

PART I.
LIGHT-MATTER INTERACTIONS IN STATE-OF-THE-ART PEROVSKITE PHOTOVOLTAICS

CHAPTER 1

1. HIGH-EFFICIENCY SOLAR CELLS: TOWARDS THE RADIATIVE LIMIT

1.1. OVERVIEW

Photon recycling is required for a solar cell to achieve an open-circuit voltage (V_{OC}) and power conversion efficiency (PCE) approaching the Shockley-Queisser theoretical limit. The achievable performance gains from photon recycling in metal halide perovskite solar cells remain uncertain due to high variability in material quality and the non-radiative recombination rate. In this work, we quantify the enhancement due to photon recycling for state-of-the-art perovskite $Cs_{0.05}(MA_{0.17}FA_{0.83})_{0.95}Pb(I_{0.83}Br_{0.17})_3$ (triple-cation) films and corresponding solar cells. We show that, at the maximum power point (MPP), the absolute PCE can increase up to 2.0% in the radiative limit, primarily due to a 77 mV increase in (V_{MPP}). For this photoactive layer, even with finite non-radiative recombination, benefits from photon recycling can be achieved when non-radiative lifetimes and external LED electroluminescence efficiencies measured at open-circuit, $Q_e^{LED}(V_{OC})$, exceed 2 μs and 10%, respectively. This analysis quantifies the significance of photon recycling in boosting the real-world performance of perovskite solar cells toward theoretical limits.

Portions of this chapter are reprinted with permission from:

*Brenes, R., *Laitz, M., Jean, J., deQuilettes, D.W., and Bulović, V., Physical Review Applied **12**, 014017 (2019). Copyright 2019 APS Physics.[70] *These authors contributed equally

1.2. INTRODUCTION

Improving solar cell power conversion efficiency (PCE) requires both optimization of device architectures and an understanding of fundamental photophysics. For example, PCEs of GaAs cells increased from 25.1% to 28.8% through photon management.[6–9] In luminescent optoelectronic materials, such as GaAs, photons can undergo multiple absorption and emission events before escaping, a phenomenon called photon recycling. During steady-state operation, photon recycling increases the charge carrier density within the photoactive cell layers, resulting in a higher quasi-Fermi level energy splitting (μ) and increased open-circuit voltage (V_{OC}) through $\mu = qV_{OC}$.[9,10,71,72] Photon recycling also slows the external photon emission rate, decreasing the radiative saturation current.[73,74] Together, these effects can boost the performance of high-efficiency solar cells toward the Shockley-Queisser theoretical limit. To take advantage of photon recycling, a photovoltaic (PV) absorber material must exhibit a small Stokes shift, strong band-edge absorption, and high photoluminescence quantum efficiency (PLQE).[8,9,71,75–77]

Relatively low PLQEs have thus far limited the extent of photon recycling observed in perovskite thin films and single crystals.[11–13] Low PLQEs of <15% result from high first-order non-radiative recombination rates, (k_1) on the order of 10^6 to 10^9 s^{-1}, which are associated with trap state densities of 10^{15} to 10^{17} cm^{-3}.[18,20,21] For example, Pazos-Outón *et al.* demonstrated that the average photon only undergoes one recycling event in a typical $CH_3NH_3PbI_3$ film, but predicted that up to 25 recycling events could be sustained with a sufficiently high-quality sample.[15] This is in contrast to GaAs films used in state-of-the-art PV devices, where an average photon can participate in up to 50 recycling events.[8] In thick perovskite single crystals, several reports have used time-resolved photoluminescence spectroscopy to show a characteristic red-shift in emission spectra over time due to photon recycling.[11] This phenomenon is expected to be efficient in single crystals, which exhibit low bulk defect densities (~10^{10} cm^{-3}). However, the high surface recombination velocities of 5,800 cm/s lead to rapid quenching of excess carriers, diminishing the probability of photon recycling.[12,78–82]

Passivated perovskite thin films with record-low non-radiative recombination rates and defect densities have achieved internal PLQEs exceeding 90%[18,22,63] — approaching the highest-quality double-heterostructured GaAs films.[83] These recent advances in material quality should enable improved photon recycling and light management in perovskite devices, but thus far it has been unclear how to realize practical efficiency gains. Futhermore, other works have only considered the impact of photon recycling on perovskite solar cells at open-circuit, where the extent of recycling differs significantly from operation at the maximum power point (MPP). Under operation, rapid charge extraction reduces the steady-state carrier density, allowing non-radiative processes to compete with radiative recombination and photon recycling. The practical importance of photon recycling in perovskite solar cells thus remains unclear.

Here we perform a theoretical analysis of photon recycling in state-of-the-art $Cs_{0.05}(MA_{0.17}FA_{0.83})_{0.95}Pb(I_{0.83}Br_{0.17})_3$ (triple-cation) films, which, in photovoltaic devices, have demonstrated record efficiencies and high stability.[19,24] We examine the impact of photon recycling at the MPP with varying first-order non-radiative recombination rates and external emission efficiencies.[5,84] The analysis is extended to $CH_3NH_3PbI_3$ films ($CH_3NH_3PbI_3$ Supplementary Figures), which have been extensively studied previously, serving as a benchmark against which to compare emerging perovskite formulations. Our model reveals the changes in carrier density and luminescence efficiency at MPP attributable to photon recycling and identifies optoelectronic material quality targets— i.e., external luminescence quantum efficiency and non-radiative recombination rates – towards which the community can strive. Quantifying these values is critical, as several reports have shown that devices with low non-radiative recombination can achieve (V_{OC}) deficits below 0.4 V, which is the deficit regime in which GaAs solar cells began to benefit from photon recycling.[7,85–89]

1.3.1. The Radiative Limit

To quantify the effect of photon recycling on device performance, current-voltage (J-V) curves were simulated using a detailed balance model and experimentally determined absorption coefficient and refractive index data for $Cs_{0.05}(MA_{0.17}FA_{0.83})_{0.95}Pb(I_{0.83}Br_{0.17})_3$ (see Figure 1.11).[5,20] In the Supplementary Results and Discussion Section 1.7, we discuss key assumptions used in the model, which are consistent with previous analyses.[5,11,72,90–92]

We first perform a detailed-balance calculation in the radiative limit (i.e., no non-radiative recombination, $k_1 = 0$) by equating the generation current with the recombination and extraction currents. The total current J_{total} as a function of voltage (V) is then defined as:

$$J_{total}(V) = J_{SC} - J_0^{rad,ext}(V) \quad 1.1$$

where J_{SC} is the short-circuit current density

$$J_{SC} = q\int_0^{\infty} a(E)\phi_{sun}(E)dE \quad 1.2$$

and $J_0^{rad,ext}$ is the external radiative saturation current, defined as the photon flux that escapes the film into the surrounding atmosphere multiplied by the fundamental charge, q:

$$J_0^{rad,ext}(V) = q\pi e^{\frac{qV}{kT}}\int_0^{\infty} a(E)\phi_{bb}(E)dE \quad 1.3$$

where k is the Boltzmann constant, T is the cell temperature, $a(E)$ is the absorptivity ($a(E) = 1 - \exp[-2 \cdot \alpha(E) \cdot d]$) as previously defined elsewhere.[93,94] d is the film thickness (d = 500 nm), $\alpha(E)$ is the energy-dependent absorption coefficient, $\phi_{sun}(E)$ is the AM1.5 spectral photon flux, and $\phi_{bb}(E)$ is the blackbody spectral photon flux all as a function of energy, E.

Importantly, and as discussed in depth previously,[91,92] photon recycling is implicit in the Shockley-Queisser detailed balance calculation, where the total photon flux emitted from the

front surface of the device is used to determine the external radiative saturation current: $J_0^{rad,ext}$ (Eq. 1.3). Here, only the emitted photons in the escape cone contribute to $J_0^{rad,ext}$, regardless of the number of photon recycling events before escape.[90,95]

Next, we determine the benefits of photon recycling by considering the radiative saturation current when photon recycling is not included in the calculation.[90,96] The internal radiative saturation current ($J_0^{rad,int}$) is similar to the external radiative saturation current but is enhanced by the photon mode density within the photoactive dielectric medium characterized by the index of refraction, $n_r(E)$, absorption coefficient, and integrated over the sphere of emission.[91] Equation 1.4 describes a microscopic view of recombination within the active region where all photons immediately escape into the surrounding environment:[90,95]

$$J_0^{rad,int}(V) = qe^{\frac{qV}{kT}} \int_0^{\infty} 4\pi n_r^2(E)\alpha(E)\phi_{bb}(E)dE \qquad 1.4$$

We use $J_0^{rad,int}$ to calculate the intrinsic carrier density (van Roosebroeck-Shockley relationship, Eq. 1.5) from standard reported second-order internal radiative recombination rate constants (k_2^{int}) for triple-cation films, $k_2^{int} = 2 \times 10^{-10}$ $\mathrm{cm^{-3}s^{-1}}$.[5,21,97] The radiative recombination rate constant is an intrinsic material property for a given perovskite film composition, and is not varied in this analysis. We find the external radiative recombination rate constant (k_2^{ext}) and intrinsic carrier density to be $k_2^{ext} = 1 \times 10^{-11}$ $\mathrm{cm^{-3}s^{-1}}$ and $k_2^{ext} = n_i = 2.3 \times 10^5$ $\mathrm{cm^{-3}}$ respectively, which agree with experimental reports considering photon recycling effects.[21,63,97–99]

$$\mathrm{k_2^{int} n_i^2} = \int_0^{\infty} 4\pi n_r^2(E)\alpha(E)\Phi_{bb}(E)dE \qquad 1.5$$

In order to make our calculations relevant for real-world perovskite devices exhibiting band-tailing likely due to disorder,[100,101] we experimentally determined the energy-dependent absorption coefficient and refractive index using photothermal deflection spectroscopy and ellipsometry (1.11). Figure 1.1 shows the theoretical current-voltage (J-V) curves for a triple-cation perovskite solar cell (see Section 1.7.5 for $CH_3NH_3PbI_3$) in the radiative limit with and without

photon recycling, calculated using the external and internal radiative saturation currents, respectively. We note that the calculated maximum efficiency with photon recycling of 30.2% corroborates previously reported theoretical limits for a similar bandgap $CH_3NH_3PbI_3$ perovskite solar cell,[5] where the theoretical J_{SC} (25.77 mA cm^{-2}) is only slightly higher than what has been achieved experimentally (25.40 mA cm^{-2}).[102] These results emphasize the need to optimize V_{OC} and fill-factor (FF) through reducing non-radiative recombination and harnessing photon recycling.

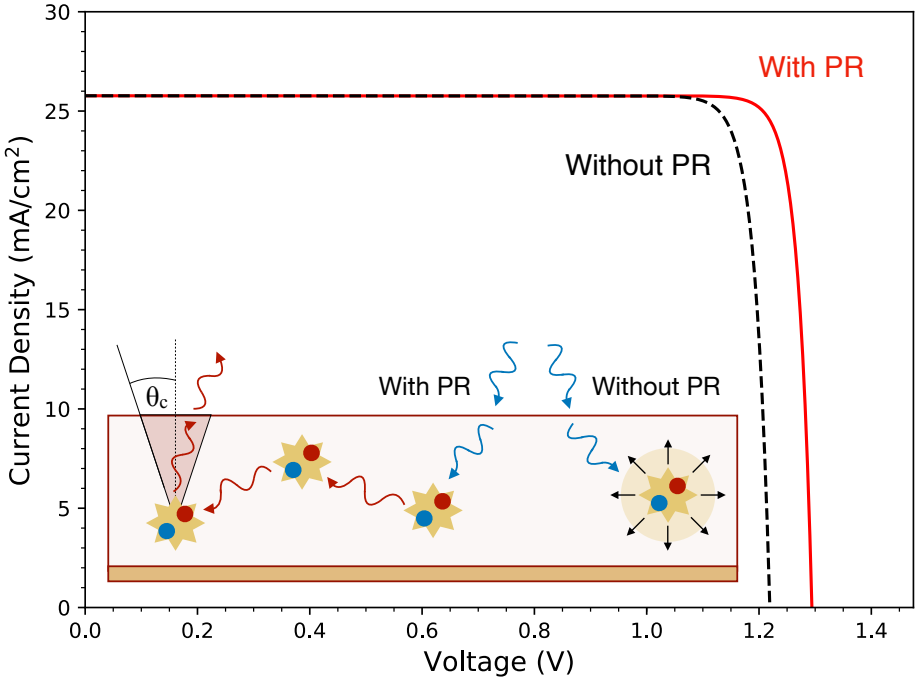

Figure 1.1: Detailed-balance simulation of current-voltage (J-V) curves for an ideal triple-cation $Cs_{0.05}(MA_{0.17}FA_{0.83})_{0.95}Pb(I_{0.83}Br_{0.17})_3$ perovskite photovoltaic device in the radiative limit (no non-radiative recombination) with (red trace) and without (black dashed trace) photon recycling (PR).

	J_{SC} [MA/CM^2]	V_{OC} [V]	FF	J_{MPP} [MA/CM^2]	V_{MPP} [V]	PCE [%]
No PR	25.77	1.22	0.899	25.19	1.12	28.2
With PR	25.77	1.29	0.906	25.23	1.20	30.2

Table 1.1: J-V characteristics and power conversion efficiency (PCE) extracted from the simulated J-V curve in the radiative limit with and without photon recycling (PR). Photon recycling leads primarily to enhancements in the maximum power point (MPP) operating voltage (V_{MPP}).

Table 1.1 shows that photon recycling improves PV device performance at both open-circuit and MPP conditions. The V_{OC} increase of ΔV_{OC}^{PR} = 70 mV calculated in this work is consistent with the 70 mV value predicted by Kirchartz *et al.* for a planar device architecture with Beer-Lambert absorption.45 Extending beyond previous studies, our full J-V simulation also shows that photon recycling improves the MPP voltage V_{MPP} (ΔV_{MPP}^{PR} = 80 mV) and the FF, producing an absolute increase in PCE of 2.0%. We note that the short-circuit current density remains unchanged because, with or without photon recycling, J_{SC} only depends on the absorptivity of the material and the solar irradiance.

One highlight of this analysis is that the maximum V_{OC} achievable without photon recycling is only 1.22 V for both the triple-cation and $CH_3NH_3PbI_3$ films (S22) — a voltage deficit of 0.38 V for each formulation. Our results suggest that perovskite PVs (with bandgap of 1.6 eV) exhibiting V_{OC} > 1.22 V and V_{MPP} > 1.12 V benefit from photon recycling.[85,89] In this regard, Liu *et al.* recently reported a record-setting V_{OC} = 1.26 V in $CH_3NH_3PbI_3$ devices, of which our calculations suggest 40 meV can be attributed to photon recycling effects.

1.3.2. Incorporating Non-Radiative Recombination

Theoretical photovoltaic performance limits are useful for setting efficiency targets, but most absorber layers perform far from the radiative limit due to non-radiative losses. Perovskites are no exception – typical films exhibit PLQEs of <15% at 1-sun equivalent generation, with k_1 ranging from 10^6 s^{-1} to 10^9 s^{-1}, depending on chemical composition and processing methods.[11,20,21] However, with recently developed passivation techniques, k_1 values have been decreasing and will likely continue to decrease as passivation mechanisms are better understood and implemented.[12] For example, a low non-radiative recombination rate of $k_1 = 1.7 \times 10^5$ s^{-1} has been reported for tri-*n*-octylphosphine oxide (TOPO)-treated $CH_3NH_3PbI_3$ films.[18]

To adapt our model to non-idealized scenarios, we modify the saturation current density (Eq. 1.3 and Eq. 1.4) to account for non-radiative Shockley-Read-Hall (SRH) and Auger recombination, as previously reported by Pazos-Outón *et al.* (Eq. 1.6):[5]

$$J_0 = J_0^{rad} + J_0^{nonrad} = J_0^{rad} + J_{SRH} + J_A \quad 1.6$$

where J_0^{rad} is the radiative recombination rate (external or internal) and J_0^{nonrad} is the sum of the non-radiative, first-order SRH (J^{SRH}) and non-radiative, third-order Auger (J_A) recombination currents. The SRH and Auger recombination rates are described for a carrier density (n) in quasi-thermal equilibrium using the law of mass action (Eq. 1.7):

$$n(V) = n_i e^{\frac{qV}{2kT}} \quad 1.7$$

$$J_{SRH}(V) = qk_1 n(V)d \quad 1.8$$

$$J_A(V) = qk_3 n^3(V)d \quad 1.9$$

where n_i is the intrinsic carrier density and k_1 and k_3 are the first-order SRH and third-order Auger recombination rate constants, respectively.

Figure 1.2 shows the impact of different non-radiative recombination values on device performance with and without photon recycling. For these calculations, we used the radiative

rate of $k_2^{int} = 2 \times 10^{-10}\ cm^{-3}s^{-1}$ and the Auger rate of $k_3 = 1 \times 10^{-28}\ cm^6s^{-1}$, which are intrinsic material properties that do not vary significantly with film quality (Table 1.3 and Table 1.4).[21,97] Figure 1.2a shows the simulated J-V curves with $k_1 = 1 \times 10^4\ s^{-1}$, which closely resemble those reported in Figure 1.1 (k_1 = 0), suggesting that radiative recombination outcompetes non-radiative recombination and the benefits of photon recycling are therefore observed at this low k_1. Figure 1.2b shows that, as k_1 increases to $2 \times 10^5\ s^{-1}$, the effect of photon recycling is greatly reduced and eventually becomes negligible when non-radiative rates approach $3 \times 10^6\ s^{-1}$ (Figure 1.2c).

Figure 1.2d shows both the V_{OC} and V_{MPP} with and without photon recycling for varying k_1 values. For k_1 exceeding a threshold value of $2 \times 10^6\ s^{-1}$ (i.e. τ_1 < 500 ns), we observe no increase in V_{OC} and V_{MPP} with photon recycling. For k_1 between $7 \times 10^5\ s^{-1}$ and $2 \times 10^6\ s^{-1}$ (i.e. τ_1 = 500 ns to 1430 ns), photon recycling can improve V_{OC} but the fill-factor decreases and, therefore, PCE enhancements are negligible (Figure 1.12). With the full J-V simulation we can see that V_{MPP} is unaffected at these values. Only when k_1 is reduced below $7 \times 10^5\ s^{-1}$ (τ_1 > 1430 ns) does photon recycling improve the MPP and efficiency (Figure 1.12 and Figure 1.13). For example, at $k_1 = 2 \times 10^5\ s^{-1}$ (Figure 1.2b), photon recycling increases V_{OC} by 50 mV but V_{MPP} by only 20 mV (Table 1.2). We note that for $k_1 = 3 \times 10^6\ s^{-1}$, the PCE is comparable to current record-performing devices.[103]

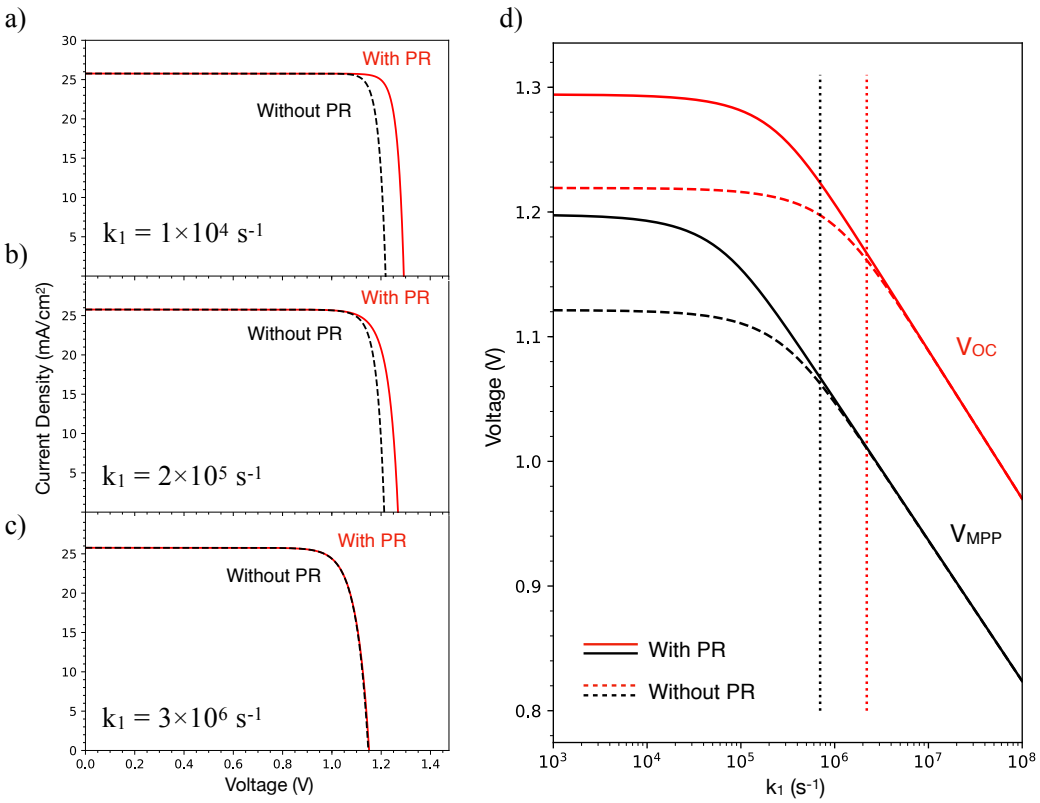

Figure 1.2: Simulated J-V curves (triple-cation, 1.6 eV bandgap) with and without photon recycling (PR) for k_1 values of (a) 1x10^4 s^{-1}, (b) 2x10^5 s^{-1}, and (c) 3x10^6 s^{-1} (k_2^{int} = 2x10^{-10} cm^{-3}s^{-1} and k_3 = 1x10^{-28} cm^{6}s^{-1}). (d) V_{OC} (red lines) and V_{MPP} (black lines) as a function of k_1, revealing differences in the onset of performance improvements due to PR. Dotted vertical red and black lines indicate k_1 thresholds (2x10^6 s^{-1} and 7x10^5 s^{-1}, respectively) below which PR improves performance at open-circuit and the maximum power point (MPP), respectively.

		J_{SC} [mA/cm^2]	V_{OC} [V]	FF	J_{MPP} [mA/cm^2]	V_{MPP} [V]	PCE [%]
$k_1 = 1\times10^4$ s^{-1}	No PR	25.77	1.22	0.897	25.13	1.12	28.2
	With PR	25.77	1.29	0.900	25.17	1.19	30.0
$k_1 = 2\times10^5$ s^{-1}	No PR	25.77	1.21	0.876	24.86	1.10	27.4
	With PR	25.77	1.27	0.850	24.67	1.13	27.8
$k_1 = 3\times10^6$ s^{-1}	No PR	25.77	1.15	0.824	24.50	1.00	24.4
	With PR	25.77	1.15	0.822	24.50	1.00	24.4

Table 1.2: Device parameters extracted from the simulated J-V curves for k_1 = 1x10^4 s^{-1}, 2x10^5 s^{-1}, and 3x10^6 s^{-1} (k_2^{int} = 2x10^{-10} cm^{-3}s^{-1} and k_3 = 1x10^{-28} cm^{6}s^{-1}) with and without photon recycling (PR).

1.3.3. Competition Between Radiative & Non-Radiative Recombination Currents

To better understand the recombination processes governing PV device behavior with and without photon recycling, we break down the J-V curve from Figure 1.2b ($k_1 = 2 \times 10^5$ s^{-1}) into its individual recombination components. The absolute magnitude is calculated using Equations 1.3-1.4 and 1.8-1.9, and the fraction of each recombination mechanism is its magnitude divided by the total recombination current (i.e. $J_{SRH,rad,A}/J_{tot}$).

Figure 1.3a and b show $J_0^{rad,int}$ and $J_0^{rad,ext}$ as a function of voltage, along with J_{SRH} and J_A, which are the SRH and Auger non-radiative pathways, respectively. J_{SRH} and J_A have the same functional form with or without photon recycling, as neither depend on the radiative saturation current (Eqs. 1.8-1.9). Photon recycling requires the reabsorption of emitted photons; if the recombination process is non-radiative (i.e. SRH, Auger), no photons are generated for the reabsorption process. We observe that photon recycling shifts radiative recombination to higher onset voltages and therefore reduces the magnitude of the radiative saturation current at MPP, leading to increases in V_{OC} and V_{MPP} with photon recycling (Table 1.2, $k_1 = 2 \times 10^5$ s^{-1}). Figure 1.3c and d give further insight into these results, where the fractions of each recombination current are compared as a function of voltage. With photon recycling, SRH recombination

becomes the limiting pathway (solid blue and red traces). To harness photon recycling in devices, it is essential to reduce non-radiative recombination pathways through improved processing or passivation techniques. For example, alkali metal salt additives and interfacial passivation layers have yielded low voltage-deficit devices (e.g. <0.35 V) which we predict currently benefit from, but do not fully harness, photon recycling.[89,104]

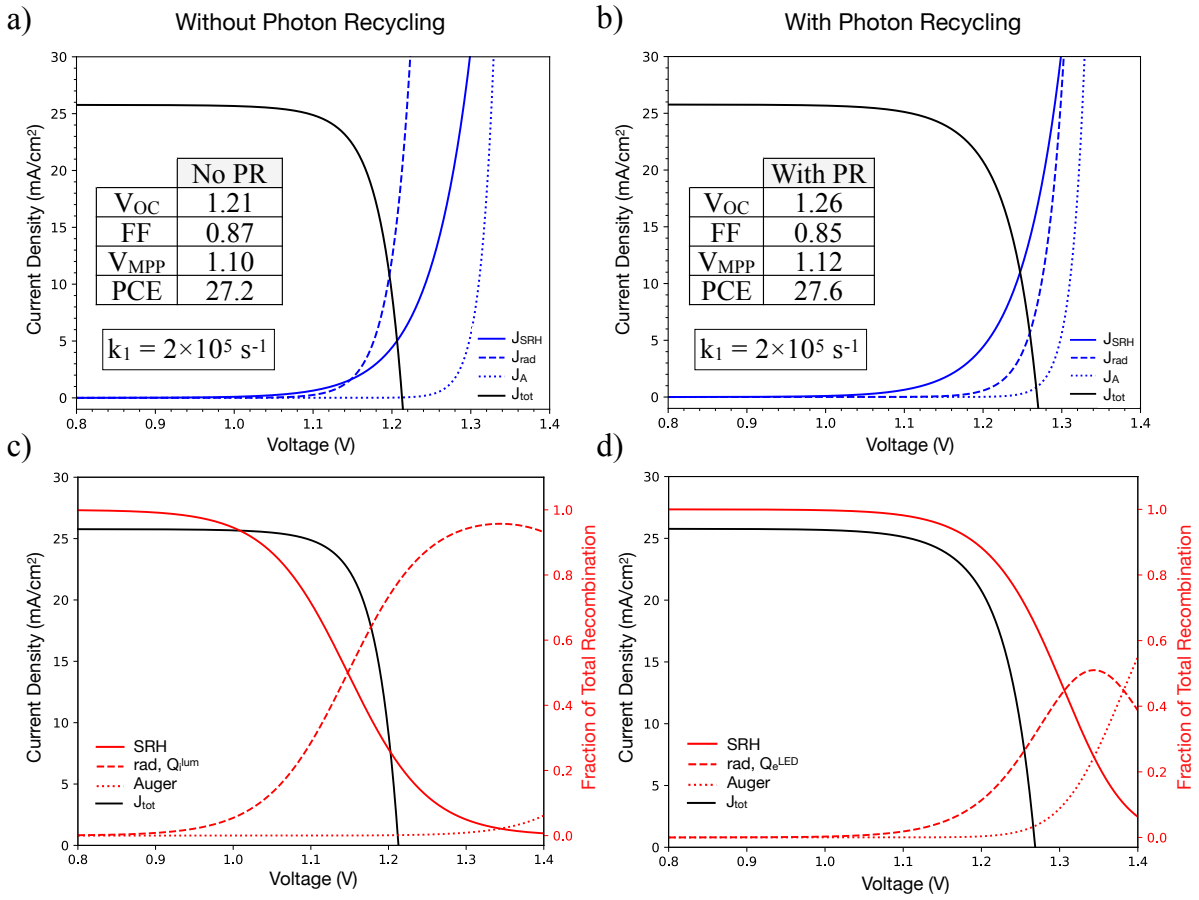

Figure 1.3: Simulated J-V curves (black traces) for k_1 = 2x10^5 s^{-1}, k_2^{int} = 2x10^{-10} cm^{-3}s^{-1}, and k_3 = 1x10^{-28} cm^{6}s^{-1} (a, c) without and (b, d) with photon recycling (PR) are shown with the magnitude of Shockley-Read-Hall (SRH), radiative, and Auger recombination currents as a function of voltage (blue traces). (c, d) The fractions of total recombination current due to SRH, radiative, and Auger recombination are shown at each voltage (red traces) (c) without and (d) with PR. The fraction of radiative recombination as a function of voltage with and without PR is equivalent to Q_e^{LED} and Q_i^{lum}, respectively.

We note that the radiative recombination fraction without photon recycling in Figure 1.3c is equal to the internal luminescence quantum efficiency (Q_i^{lum}), which has similarly been defined elsewhere:[91]

$$Q_{\mathrm{i}}^{\mathrm{lum}}(V) = \frac{J_0^{rad,int}(V)}{J_{SRH}(V)+J_0^{rad,int}(V)+J_A(V)} \quad 1.10$$

The radiative recombination fraction with photon recycling in Figure 1.3d yields the external light-emitting diode (LED) electroluminescence efficiency (Q_e^{LED}), which is connected to the mean probability of photon escape from the film (P_{esc}) through a geometric series:[91]

$$Q_{\mathrm{e}}^{\mathrm{LED}}(V) = \frac{\mathrm{P_{esc}Q_i^{lum}}(V)}{1-\mathrm{Q_i^{lum}}(V)(1-P_{esc})} \quad 1.11$$

Here, the escape probability (P_{esc}) can be defined as the ratio of the external to the internal radiative saturation current:[91]

$$P_{esc} = \frac{J_0^{rad,ext}}{J_0^{rad,int}} \quad 1.12$$

1.4. EXTERNAL ELECTROLUMINESCENCE EFFICIENCY ENHANCEMENTS

Q_e^{LED} is a function of the injection current, and thus it is necessary to denote both the injection current and corresponding voltage at which the current is achieved for a given Q_e^{LED}. Due to the reciprocity relations that link optical output to electrical input, Q_e^{LED} values are often measured at an injection current equivalent to the photocurrent.[105,106] Unless otherwise stated, we report Q_e^{LED} values calculated with an injection current equivalent to J_{SC} – i.e. applied voltage equal to V_{OC}, $Q_e^{LED}(V_{OC})$. Considering Equation 1.11, Figure 1.3d shows that a device with $k_1 = 2 \times 10^5\ s^{-1}$ (i.e. τ_1 = 5 µs) should demonstrate a $Q_e^{LED}(V_{OC})$ of 31.5%. Importantly, the external

emission efficiency of a solar cell is a metric that has been shown to directly correlate with power conversion efficiency and, therefore, serves as a useful optimization parameter.[107,108] Equations 1.9 and 1.10 provide two apparent routes: decreasing J_{SRH} and J_A and/or increasing P_{esc} to increase $Q_e^{LED}(V_{OC})$. To evaluate which method best capitalizes on the benefits of photon recycling, we examine the dependence of $Q_e^{LED}(V_{OC})$ and P_{esc} on V_{OC} and V_{MPP}.

1.4.1. Modification of Non-Radiative Recombination

First, we consider how $Q_e^{LED}(V_{OC})$ and photovoltage are affected by decreasing J_{SRH} (i.e. varying k_1 in Equation 1.8), for a fixed escape probability (P_{esc} = 4.7%). Figure 1.4 shows $Q_e^{LED}(V_{OC})$ increases with decreasing k_1, resulting in voltage enhancements at open-circuit and MPP. We report a photon recycling threshold of $Q_e^{LED}(V_{OC})$ > ~0.3% and significant performance improvements for $Q_e^{LED}(V_{OC})$ = 10%, yielding ΔV_{OC}^{PR} = 36 mV and ΔV_{MPP}^{PR} = 9 mV (Figure 1.4). Recently, Liu *et al.* reported a $Q_e^{LED}(V_{OC})$ of 7.5±2.5% for $CH_3NH_3PbI_3$ devices achieving a V_{OC} of 1.26 V. This experimental V_{OC} is higher than the maximum achievable theoretical V_{OC} in the radiative limit without photon recycling, indicating performance enhancements due to photon recycling.[89]

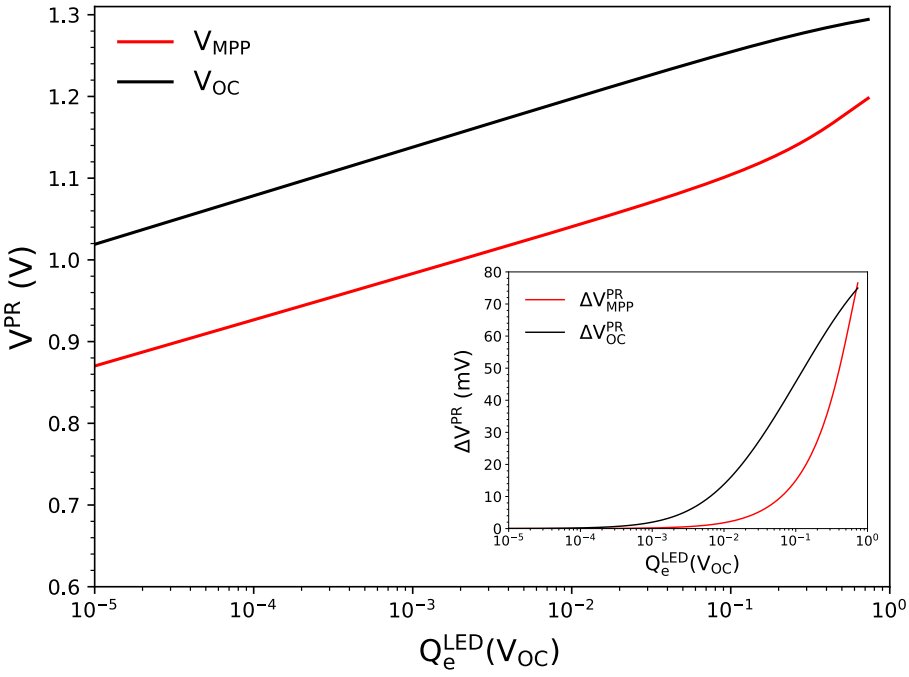

Figure 1.4: The voltage with photon recycling (V^{PR}) for P_{esc} = 4.7% at the maximum power point (MPP) and open-circuit is shown as a function of $Q_e^{LED}(V_{OC})$, which, as non-radiative recombination decreases, approaches unity. Inset: ΔV^{PR} for P_{esc} = 4.7% at MPP and open-circuit as a function of $Q_e^{LED}(V_{OC})$.

1.4.2. Modification of the Probability of Photon Escape

Second, we consider how $Q_e^{LED}(V_{OC})$ and photovoltage (see below) are affected by increasing P_{esc} and decreasing k_1. We note that the photovoltage is proportional to the steady-state carrier density and is, therefore, an intuitive metric to compare across the multiple varying parameters. We calculate the carrier density using the law of mass action (Eq. 1.7) as a function of k_1 and P_{esc}.

Figure 1.5a shows that, at P_{esc} = 4.7% and low k_1 values, photon recycling increases the steady-state carrier density by a factor of four, from 8.5×10^{14} to 3.7×10^{15} cm^{-3} at MPP. This high carrier density results from additional generation associated with the reabsorption of

trapped photons — up to 18-suns equivalent at open-circuit and >1.4 equivalent suns at MPP (see Figure 1.15 for triple-cation and Figure 1.24 for $CH_3NH_3PbI_3$). Figure 1.5 shows that photon recycling allows $Q_e^{LED}(V_{OC})$ to exceed the escape probability, a direct result from the multiple re-absorption events that re-randomize the photon propagation angle. While the emission efficiency can increase beyond P_{esc} as non-radiative recombination decreases, $Q_e^{LED}(V_{OC})$ cannot reach 100% due to the higher fraction of Auger recombination at increased steady-state carrier densities, as shown in Figure 1.3c-d. A similar limiting effect for the efficiency droop at high applied voltages in GaN LEDs has been attributed to Auger recombination processes.[109,110]

Next, we consider scenarios in which P_{esc} is changed without significantly impacting the material absorptivity function (Figure 1.7). Figure 1.5b and c show the carrier density and $Q_e^{LED}(V_{OC})$ for P_{esc} = 9.4% and 14.1%. Here, the steady-state carrier density steadily decreases, while $Q_e^{LED}(V_{OC})$ approaches 90% with photon recycling due to a smaller contribution from Auger recombination at lower carrier densities. These results appear to counteract one another, as both a high steady-state carrier density and high $Q_e^{LED}(V_{OC})$ are desired.

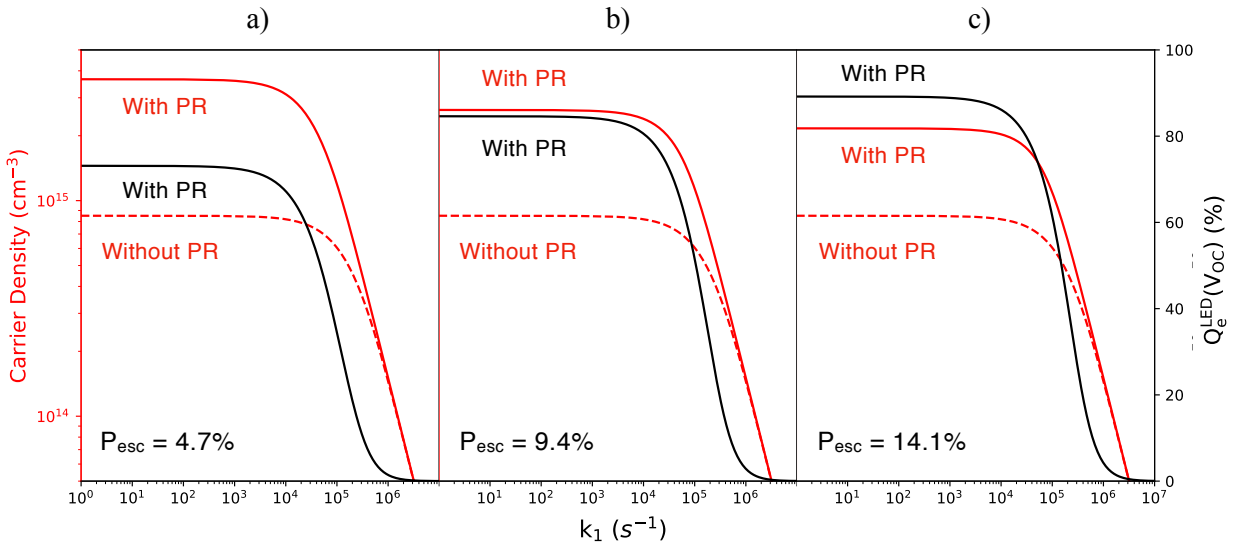

Figure 1.5: The effect of photon recycling (PR) on the maximum power point (MPP) steady-state carrier density and $Q_e^{LED}(V_{OC})$ as a function of k_1 for a) P_{esc} = 4.7%, b) 9.4%, and c) 14.1%.

This observation raises the question as to whether solely increasing the escape probability can enhance device performance and, in particular, open-circuit voltage.[13,20] The traditional definition of the maximum achievable open-circuit voltage (V_{OC}^{max}) is expressed as a function of the external LED electroluminescence efficiency, as described in Equation 1.13.[91,105,111]

$$V_{OC}^{max} = V_{OC}^{rad} + \frac{kT}{q}\ln\left[Q_e^{LED}(V_{OC})\right] \qquad 1.13$$

Here, it appears that increasing $Q_e^{LED}(V_{OC})$ through enhancing the escape probability should allow V_{OC}^{max} to approach V_{OC}^{rad} – however, the implicit dependence of the radiative component (V_{OC}^{rad}) on P_{esc} is often overlooked. This dependence becomes clear if we equate $J_0^{rad,ext}$ with the product of $J_0^{rad,int}$ and P_{esc} (Eq. 1.14), where it can be seen that this term decreases as the escape probability increases.[112]

$$V_{OC}^{rad} = \frac{kT}{q}\ln\left[\frac{J_{SC}}{J_0^{rad,ext}}\right] = \frac{kT}{q}\ln\left[\frac{J_{SC}}{P_{esc}J_0^{rad,int}}\right] \qquad 1.14$$

To better understand the competition between V_{OC}^{rad} and $Q_e^{LED}(V_{OC})$ on V_{OC}^{max}, Figure 1.6a and b show the magnitude of these terms as a function of P_{esc} and k_1. As P_{esc} increases for a given k_1, V_{OC}^{rad} decreases due to the enhanced light outcoupling, which increases the external radiative saturation current. Opposing this negative impact on V_{OC}^{max} from V_{OC}^{rad}, V_{OC}^{nonrad} also decreases with increasing P_{esc}, resulting in a smaller subtractive component from V_{OC}^{max}, as shown in Figure 1.6b. As P_{esc} changes, the radiative and non-radiative terms vary in opposing directions.

Ultimately, V_{OC}^{max} is dominated by the radiative dependence on P_{esc}, so V_{OC}^{max} decreases monotonically with increasing P_{esc} at a constant k_1 value (Figure 1.6c).[20] Thus, it is evident that simply increasing the outcoupling efficiency reduces output voltages due to the reduction in steady-state carrier density (c.f. Figure 1.5). We highlight that we only analyze the voltage in this simulation, and note that overall device performance may not track the changes in voltage if, for example, J_{SC} also changes.

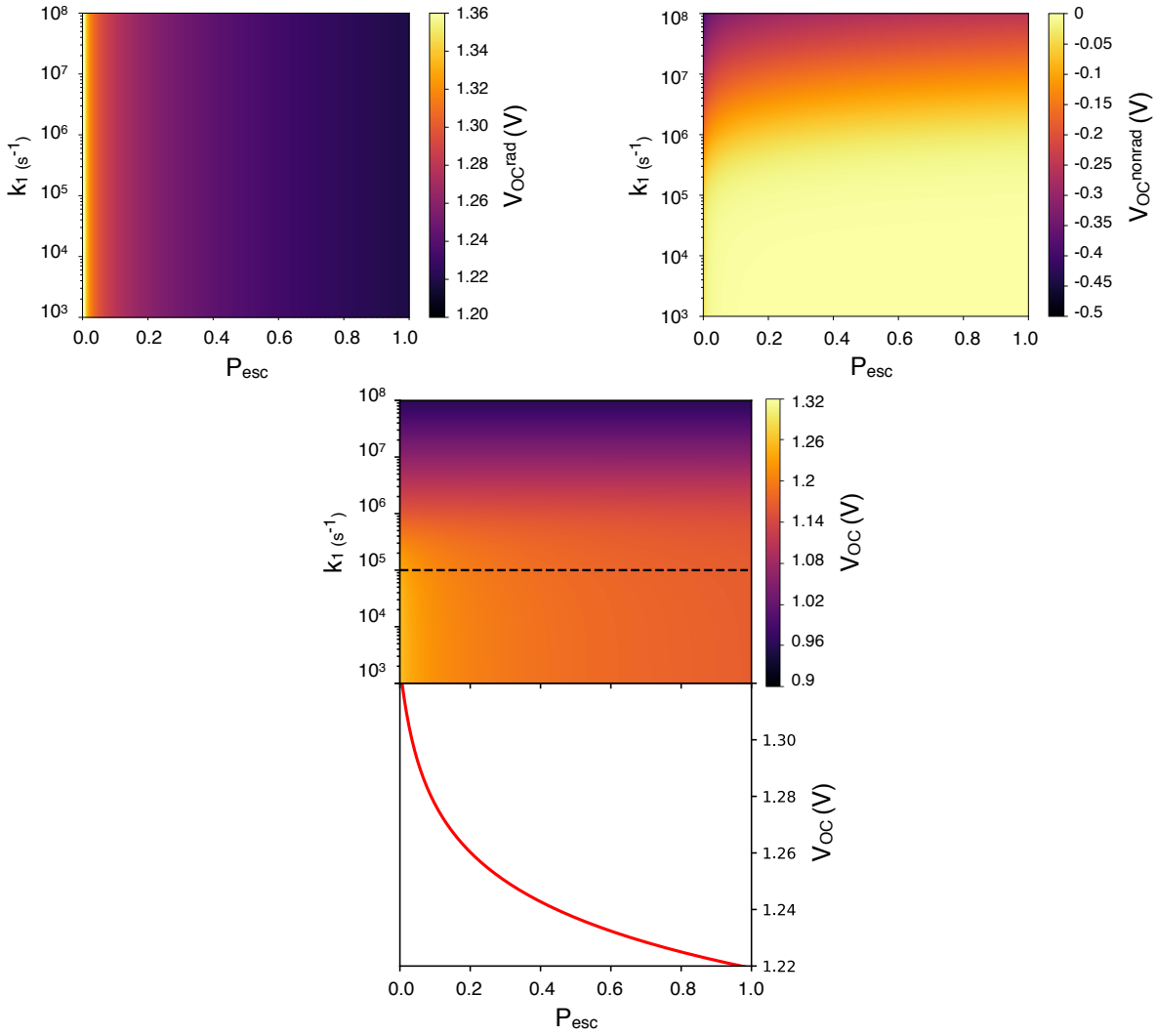

Figure 1.6: a) The V_{OC} with photon recycling (PR) in the radiative limit (V_{OC}^{rad}) is shown along with b) the non-radiative subtractive effect on V_{OC}^{max} (V_{OC}^{nonrad}). Combined, V_{OC}^{rad} + V_{OC}^{nonrad} yield c) the total V_{OC}^{max} as a function of k_1 and P_{esc}, with a dashed line at k_1=1x10^5 s^{-1} showing that increasing P_{esc} for a fixed Q_i^{lum} decreases V_{OC}.

In summary, we present a rigorous method for evaluating the extent of and benefits from photon recycling in emerging perovskite absorbers by exploring device performance limits using experimentally determined optical constants and absorption for triple-cation films. This analysis investigates the effect of photon recycling on both V_{OC} and operationally relevant maximum power point (MPP) parameters, both in the radiative limit and with non-radiative recombination. Our simulations provide a framework for evaluating the improvements attributable to photon recycling in standard current-voltage measurements. This analysis reveals that perovskite devices demonstrating voltage deficits of <0.38 V[85,89] already benefit from photon recycling. This would mean that high-quality devices fabricated today may be further improved by reducing non-radiative recombination and/or modifying the escape probability to harness the benefits of photon recycling.

With recycling, photons waveguided within the film can be re-absorbed and re-emitted in the escape cone, allowing $Q_e^{LED}(V_{OC})$ to approach the intrinsic limit while maintaining a high steady-state carrier density. If $Q_e^{LED}(V_{OC})$ is enhanced only by increasing P_{esc}, the steady-state carrier density will decrease, resulting in a lower V_{OC}. For triple-cation films, enhancements in V_{OC} and V_{MPP} are observed for $k_1 < 2 \times 10^6\ s^{-1}$ ($\tau_1 > 500$ ns) and $k_1 < 7 \times 10^5\ s^{-1}$ ($\tau_1 > 1430$ ns), respectively, while, for $k_1 < 1 \times 10^4\ s^{-1}$ ($\tau_1 > 100$ µs), further performance improvements become negligible. Our analysis, therefore, identifies a target non-radiative recombination rate for perovskite films of $k_1 < 1 \times 10^4\ s^{-1}$. Below this threshold, the steady-state carrier density plateaus at 4x the density without photon recycling. In theory, a perovskite film reaching this lower bound of $k_1 = 1 \times 10^4\ s^{-1}$ (P_{esc} = 4.7%) can achieve a 74 mV increase in V_{OC}, 73 mV improvement in V_{MPP}, 0.3% absolute increase in fill factor, and 1.79% increase in PCE — due solely to photon recycling.

We note that the model used to simulate J-V curves in this study represents an ideal case and sets an upper limit for the target non-radiative recombination rate constants. For example,

perovskite material quality will likely need to be even better than these targets, as charge transport layers in devices introduce new pathways for interfacial recombination. Passivation methods and surface modifiers that reduce the number of defects at the interfaces and lead to favorable band alignment will be critical in minimizing non-radiative loss to fully harness photon recycling.[18,22,63] Toward the development of new perovskite formulations and device architectures, this analysis provides clear material quality targets and device performance limits for evaluating photon recycling in next-generation perovskite solar cells.

1.7. SUPPLEMENTARY RESULTS AND DISCUSSION

1.7.1. Experimental Methods

Materials: Formamidinium iodide (FAI) and methylammonium bromide (MABr) were purchased from GreatCell Solar. Lead iodide (PbI_2) and lead bromide ($PbBr_2$) were obtained from TCI Chemicals. Cesium iodide (CsI), *N*,*N*-dimethylformamide (DMF), dimethyl sulfoxide (DMSO) and all other chemicals were sourced from Sigma Aldrich unless otherwise stated.

Sample Preparation: Glass, fused silica, and p-type silicon substrates were washed sequentially with soap (2% Hellmanex in water), de-ionized water, acetone, and isopropanol, and finally treated under UV-Ozone for 30 min. Thin films of $Cs_{0.05}(MA_{0.17}FA_{0.83})_{0.95}Pb(I_{0.83}Br_{0.17})_3$ (triple cation) were solution processed following the procedure outlined by Saliba *et al.*[24] The precursor solution was prepared in a nitrogen-filled glovebox by dissolving 1 M FAI, 0.2 M MABr, 1.1 M PbI_2, 0.2 M $PbBr_2$, and 0.05 M CsI in a 4:1 volume ratio of DMF to DMSO. The solution was spin coated in a dry-air box with a two-step program, with the first step at 1,000 rpm for 10 s with a 1000 rpm/s ramp followed by a step at 6000 rpm for 20 s with a 6000 rpm/s ramp. 110 µl of chlorobenzene was added 5 s before the spin procedure ended. The films were then annealed at 100°C for 1 hour. Samples were then stored in the dark in a nitrogen-filled

glovebox until use. Thin films deposited on top of fused silica were used for PDS and UV-Vis measurements, while films deposited on top of silicon were used for ellipsometry measurements.

Photothermal Deflection Spectroscopy (PDS): PDS measurements were performed using a custom system optimized for the near-infrared (Fig. 1.10, from Jean, J. *et al.*).[113] The pump beam consists of a 300 W Xe arc lamp chopped at 10 Hz, a dual-grating monochromator (300 lines per mm) with 1 mm slits (15 nm output FWHM), a periscope, and achromatic lenses to collimate and focus the beam. The illuminated spot size at the sample is approximately 3.5 mm wide × 0.4 mm tall, corresponding to a monochromatic intensity of 50–750 mW cm^{-2}. The sample is secured using a custom holder in a standard 10 mm quartz cuvette. Perfluorohexane (Acros Organics Fluorinert FC-72) filtered with 0.02 μm PTFE is used as a deflection medium. The probe beam consists of a 658 nm, 40 mW temperature-controlled laser diode, an anamorphic prism pair, spatial filter, and iris to circularize the beam and isolate the fundamental mode; a bandpass filter to eliminate scattered light; and a quadrant detector with built-in transimpedance amplifier. A DAQ is used to drive the chopper and acquire the quad detector signal. AC lock-in detection is performed using custom LabView software with a low-pass filter cutoff frequency of 0.5 Hz. The entire PDS system is assembled on an optical table to minimize vibrations and enclosed in a box to mitigate stray light and air flow.

Variable Angle Spectroscopic Ellipsometry: Spectroscopic ellipsometry was performed using a variable angle spectroscopic ellipsometer (Woollam) at 65°, 70°, and 75° angles of incidence. Ellipsometry data were fitted to obtain film optical constants and thicknesses used in PDS data analysis.

UV-Vis Reflectivity Measurements: Reflection spectrophotometry was performed with light incident from the film side using an Agilent Cary 5000 dual-beam UV–vis–NIR spectrophotometer. Specular reflectance was collected at an incident angle of 8°. A 3 mm round aperture was used for all measurements.

PDS Data Analysis: Acquired PDS data for the perovskite samples was normalized with respect to the pump power spectrum. The data was then re-normalized to one at a highly absorbing wavelength (400 nm) and divided by the PDS spectrum of a black reference sample to obtain a relative absorptance spectrum. Absolute absorptance was then obtained by scaling the data by (1-R), where R is the reflectivity of the perovskite sample at a highly absorbing wavelength obtained from spectrophotometry measurements. To determine the absorption coefficient from the absolute absorptance spectrum, we followed the procedure developed by Ritter and Weisser utilizing thicknesses and optical constants for fused silica and the perovskite absorber layer determined from ellipsometry.[114]

Corrected Absorption Coefficient Spectrum: The absorption coefficient spectrum determined from ellipsometry was used as the basis data set. Since PDS measurements provide increased sensitivity by multiple orders of magnitude, the absorption coefficient spectrum obtained from PDS measurements was used for the band edge. The PDS data was shifted by 20 meV to match with the absorption coefficient spectrum from ellipsometry. The Urbach expression $\alpha = \alpha_0 \exp\left(\frac{E-E_0}{E_U}\right)$, where α is the absorption coefficient, α_0 is an absorption coefficient scaling factor, E is the photon energy, E_0 is an energy offset and E_U is the Urbach energy was fitted to the band edge to extrapolate the absorption coefficient spectrum beyond the noise floor of the PDS measurements. We obtained a fitted value of $E_U = 15$ meV, consistent with previous reports for other perovskite absorber materials.[115,116]

Determination of $\mathbf{k_2^{int}}$ and $\mathbf{k_2^{ext}}$: Using experimentally determined absorption coefficient $\alpha(E)$ and refractive index $n_r(E)$, we calculated second-order internal and external radiative recombination rate from the internal and external radiative saturation current (Eqs. 1.15-1.19).[5] We assume a perfect back reflector and Beer-Lambert absorptivity $\alpha(E) = 1 - \exp(-2 \cdot \alpha(E) \cdot d)$ where d is the film thickness (500 nm).

$$J_0^{rad,ext}(V) = q\pi e^{\frac{qV}{kT}} \int_0^\infty a(E)\phi_{bb}(E)dE \quad 1.15$$

$$J_0^{rad,int}(V) = q e^{\frac{qV}{kT}} \int_0^\infty 4\pi n_r^2(E)\alpha(E)\phi_{bb}(E)dE \quad 1.16$$

$$\mathrm{k}_2^{\mathrm{int}} = \frac{J_0^{rad,int}(V)}{q n_i^2 d} \quad 1.17$$

$$\mathrm{k}_2^{\mathrm{ext}} = \frac{J_0^{rad,ext}}{J_0^{rad,int}} \mathrm{k}_2^{\mathrm{int}} = P_{esc} \mathrm{k}_2^{\mathrm{int}} \quad 1.18$$

$$P_{esc} = \frac{J_0^{rad,ext}}{J_0^{rad,int}} \quad 1.19$$

1.7.3. Model Assumptions

Critical Mobility: In the radiative Shockley-Queisser (SQ) performance limit, it is assumed that all photogenerated carriers are entirely collected, which would require charge carriers to possess extremely high mobilities. Mattheis *et al.* examined the effect of mobility on idealized photovoltaic devices to determine whether, in relevant materials, there is a PCE ceiling before the SQ limit based on fundamental mobility limitations, even in the radiative limit.[117] A critical mobility was defined based on a reference mobility (μ_{ref}) for each material, with μ_{ref} defined in Eq. 1.20:

$$\mu_{ref} = \frac{q N_A \Phi_{bb}^{E_g}}{kT \alpha_{avg} n_i^2} \quad 1.20$$

where q is the electron charge, N_A the doping density, $\Phi_{\mathrm{bb}}^{E_g} = \int_{E_g}^\infty \phi_{bb}(E)dE$ is the integrated black body spectrum, $\phi_{bb}(E)$ is the black body spectral photon flux, k is the Boltzmann constant, T is the temperature of the material, and α_{avg} is the average absorption coefficient across the AM1.5 spectrum. Mattheis *et al.* showed that the SQ radiative limit can be achieved if the material's mobility was two orders of magnitude larger than μ_{ref} and thus the limiting efficiency was not limited by mobility. Using standard reported doping concentration of $N_A = 1 \times 10^{16}$ cm^{-3} for $MAPbI_3$ films, an intrinsic carrier concentration of $n_i = 2.74 \times 10^5$ cm^{-3}, and

the average absorption coefficient across the AM1.5 spectrum for $MAPbI_3$, $\mu_{ref} = 0.013\ cm^2V^{-1}s^{-1}$.[13,118] Additionally, using reported mobilities for $MAPbI_3$ films, $\mu_{MAPbI_3} = 3\ cm^2V^{-1}s^{-1} = 225 \times \mu_{ref}$.[119] The typical mobility of $MAPbI_3$ is more than two orders of magnitude greater than the reference mobility, and thus we will assume that this analysis is not limited by mobility, and that perfect charge collection can be assumed even when investigating the effect of non-zero non-radiative recombination on JV characteristics. The model can then be extended to determine the impact of photon recycling on device performance when Shockley-Read Hall (SRH) (k_1) and Auger (k_3) recombination rates are non-zero, both at open circuit and at the maximum power point of the device.

Rate Constants and Band Gap of Triple-Cation Thin Films: The band gap for $Cs_{0.05}(MA_{0.17}FA_{0.83})_{0.95}Pb(I_{0.83}Br_{0.17})_3$ used in the simulations is as reported by Soufiani *et al.* for planar $Cs_{0.05}(MA_{0.17}FA_{0.83})_{0.95}Pb(I_{0.83}Br_{0.17})_3$ films at 2K: E_g = 1.593 eV.[120] We prepared triple-cation films using the same method as Kumar *et al.*, where they report a second-order radiative recombination constant which was used for our simulations: $k_2^{int} = 2x10^{-10}\ cm^{-3}s^{-1}$ with a corresponding calculated external radiative recombination constant of $k_2^{ext} = 1x10^{-11}\ cm^{-3}s^{-1}$ and intrinsic carrier density of $2.3x10^5\ cm^{-3}$ (Eqs. 1.17-1.18).[97]

Variation of Photon Probability of Escape from the Film: In this work, we assume that the film escape probability can be changed without significantly altering the material absorptivity function. Although this is a common assumption made in similar simulations to simplify the analysis,[90,112] we explore two different device geometries which are well known to lead to distinct absorptivity functions.[5,8,92] Namely, a textured thin film can be described by previously reported functional forms for *a(E)* as shown in Eq. 1.21.[5,8]

$$a(E) = \frac{4n_r^2(E)\alpha(E)d}{4n_r^2(E)\alpha(E)d+1} \qquad 1.21$$

Whereas a planar device is described using Eq. 1.22:[92]

$$a(E) = 1 - \exp\left(-2 \cdot \alpha(E) \cdot d\right) \qquad 1.22$$

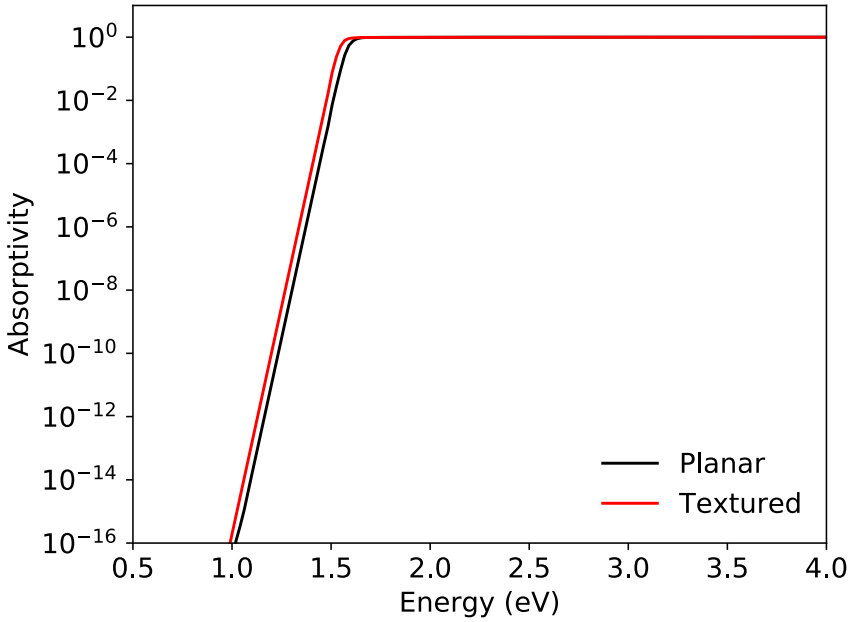

Figure 1.7: Calculated absorptivities for a planar thin film (black) and a randomly textured thin film (red). The textured thin film shows increased absorptivity at lower photon energies.

Figure 1.7 shows the absorptivity as a function of energy in both cases, where the textured device shows an onset at lower photon energies. Next, we consider how the photon escape probability changes for the two different scenarios according to Equations 1.15, 1.16, and 1.19. We calculate P_{esc} to be 4.7% and 22.8% for the planar and textured film, respectively. We can envision scenarios that would allow for intermediate values of 4.7% < P_{esc} < 22.8% as well as geometries in which P_{esc} > 22.8%. Each value of P_{esc} corresponds to a unique absorptivity function either through the modification of the absorptivity *a(E)* via film texturing or by changing the refractive index of the surrounding media.[112]

Model Sensitivity to Variations in k_2^{int} and k_3: Literature reports of k_2^{int} values for triple-cation films prepared in DMF/DMSO range from $1.8x10^{-10}$ – $2.6x10^{-10}$ cm^3s^{-1} and, for $CH_3NH_3PbI_3$ films, reported values span from 0.6 $x10^{-10}$ – 9.2 $x10^{-10}$ cm^3s^{-1}.[21,97] To assess the influence of k_2^{int} on the obtained J-V curves, we simulated J-V characteristics using these upper and lower bounds for both triple-cation and $CH_3NH_3PbI_3$ films (Figure 1.8 and Table 1.3). A constant value of $k_1 = 2x10^5$ s^{-1} was used for the non-radiative rate. In the main text triple-cation photon recycling analysis, a value of $k_2^{int} = 2x10^{-10}$ cm^3s^{-1} was used, which falls within the range reported for triple-cation films. Within this range for triple-cation films, the difference in resulting J-V characteristics is quite small (Figure 1.8a). The second-order recombination rate is significantly less dependent on material quality and processing techniques than the first-order recombination rate, and is largely if not solely a function of active layer perovskite chemical composition.[21] This assumption is consistent with similar studies reported in the literature.[5,91,112] Figure 1.8b shows that the range of k_2^{int} values does lead to differences in the open-circuit voltage and PCE for $CH_3NH_3PbI_3$. In particular, Table 1.3 shows approximately a 30 mV difference in V_{OC} and 0.68 % in PCE.

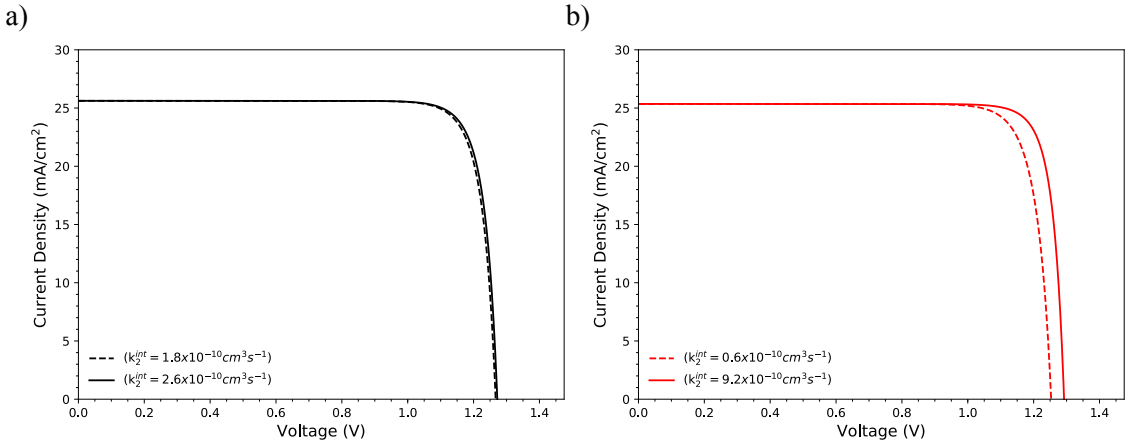

Figure 1.8: Simulated J-V characteristics for a) triple-cation films with $k_2^{int} = 1.8x10^{-10}$ cm^3s^{-1} (dashed line) and $k_2^{int} = 2.6x10^{-10}$ cm^3s^{-1} (solid line). J-V curve for b) $CH_3NH_3PbI_3$ films with $k_2^{int} = 0.6x10^{-10}$ cm^3s^{-1} (dashed line) and $k_2^{int} = 9.2x10^{-10}$ cm^3s^{-1} (solid line). All curves were obtained with: $k_1 = 2x10^5$ s^{-1} and $k_3 = 1x10^{-28}$ cm^6s^{-1}.

Material	k_2^{int} [cm^3s^{-1}]	ΔV_{oc}^{pr} [mv]	ΔPCE^{pr} [%]
Triple-cation	$1.8x10^{-10}$	58.0	0.493
	$2.6x10^{-10}$	54.0	0.401
$CH_3NH_3PbI_3$	$0.6x10^{-10}$	41.0	0.188
	$9.2x10^{-10}$	71.0	0.867

Table 1.3: Difference in V_{OC} and PCE due to photon recycling in triple-cation films[97] and $CH_3NH_3PbI_3$ films[21] for varying k_2^{int} and $k_1 = 2x10^5$ s^{-1}, $k_3 = 1x10^{-28}$ cm^6s^{-1}.

Literature reports of k_3 for $CH_3NH_3PbI_3$ perovskites have a narrow range and are well within the same order of magnitude (Table 1.4).[21] Simulations within this range show no significant variation in simulated J-V characteristics.

Material	k_3 [cm^6s^{-1}]
Triple-cation	$1.3x10^{-28}$
	$1.6x10^{-28}$

Table 1.4: Reported Auger recombination rate constant (k_3) for $CH_3NH_3PbI_3$ show less than an order of magnitude variation.[21]

Calculating Total, Short-Circuit, and Radiative Saturation Currents: J_{total}, J_{SC}, and the radiative saturation current (internal and external) are calculated assuming angle independence of irradiation, optical constants, and absorption. Furthermore, when calculating J_{SC} for these simulations, we assume perfect incoupling due to the low short-circuit current deficit between theoretical and experimental reports ($J_{SC}^{theory} = 25.77$ mA cm^{-2} and $J_{SC}^{exp} = 25.40$ mA cm^{-2}).[102]

V_{OC} Enhancement Due to Photon Recycling: The expression for the enhancement in V_{OC} solely due to photon recycling is as derived by Abebe *et al.* (Eq. 1.23).[112]

$$\Delta V_{OC}^{PR} = \frac{kT}{q} \ln \left[\frac{1}{1 - Q_i^{\text{lum}} (1 - P_{esc})} \right] \quad 1.23$$

Internal Suns: The internal photon population corresponds to the addition of incident photons and the photons generated by radiative recombination that are waveguided within the film. This can be expressed in terms of the short circuit current and saturation currents which, when normalized with respect to the short circuit current, provide an equivalent number of internal suns (Eq. 1.24).

$$\text{Suns} = \frac{J_0^{rad,int}(1 - P_{esc}) + J_{SC} - J_{SRH} - J_A}{J_{SC}} \quad 1.24$$

Definition of Escape Cone: The escape cone for a photon from the bulk film into the atmosphere is a reduced solid angle in 3D, which is determined by the index mismatch between the film and its surroundings. A schematic view in 2D is presented in Figure 1.9, showing the critical angle due to the difference in energy-dependent index of refraction of the medium ($n_r(E)$) and surroundings ($n_a(E)$) as derived from Snell's law. For a perfect rear reflector, emission is only considered from the front surface, so that the critical angle is defined by Eq. 1.25. The solid angle can then be computed by integrating over the projection of the cone defined by the critical angle onto a unit sphere, as seen in Eq. 1.26. The corresponding reduced solid angle Ω_c from θ_c is significantly less than the entire solid angle of the sphere 4π for materials where $\theta_c \ll 1$ radian.[121]

$$2\theta_c = \sin^{-1}\frac{n_a(E)}{n_r(E)} \quad (1.25)$$

$$\Omega_c = \int_{\phi=0}^{2\pi}\int_{\theta=0}^{\theta_c}\sin\theta d\theta d\phi = 4\pi\sin^2\frac{\theta_c}{2} \quad (1.26)$$

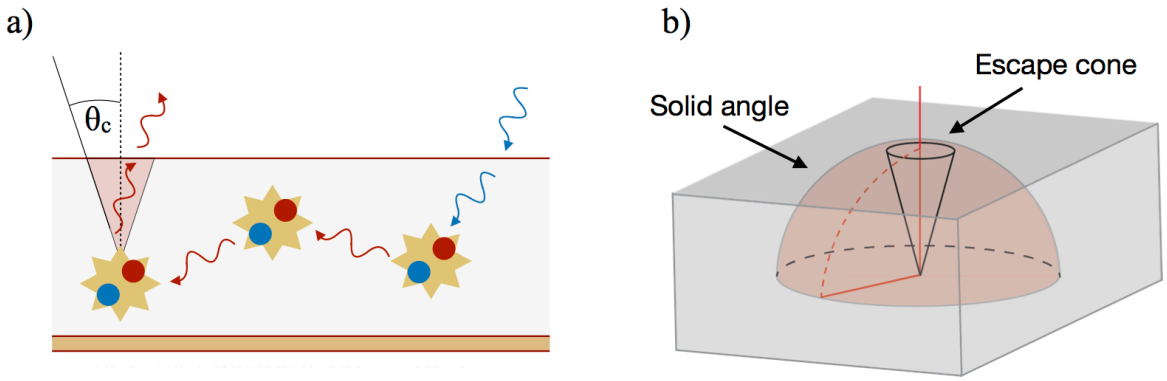

Figure 1.9: With photon recycling, a) a photon escapes the film when its angle of emission falls within the escape cone (critical angle = θ_c). Any photon emitted outside of the solid angle depicted in 2D is waveguided within the film (left). b) The projection of the escape cone onto the unit sphere (adapted from[122]) forms an area smaller than the area of the unit sphere.

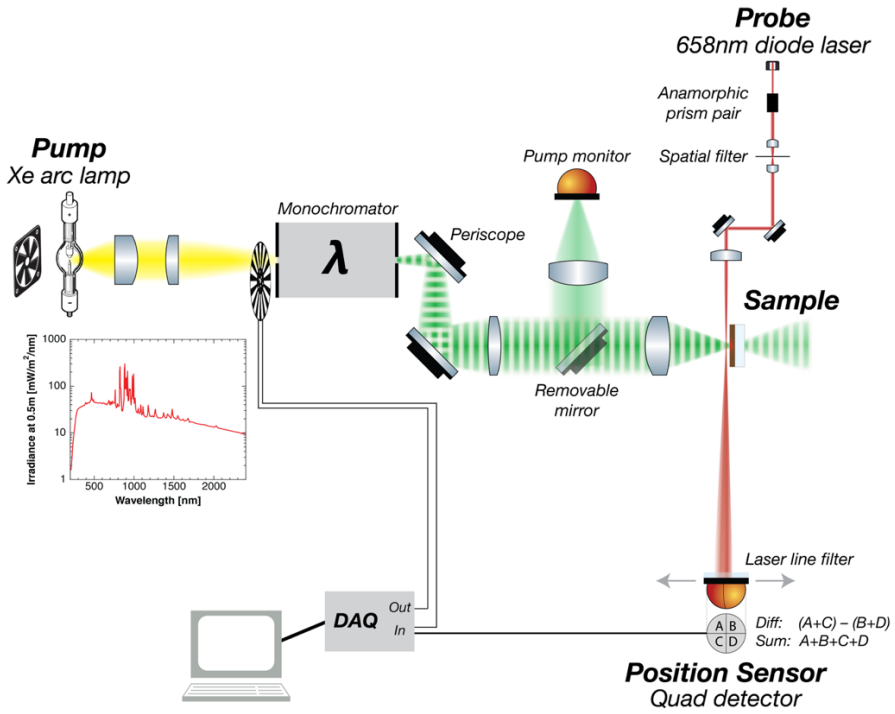

Figure 1.10: Schematic of photothermal deflection spectroscopy with Xe arc lamp pump and 658 nm diode laser probe (from Jean, J. *et al.*).[113]

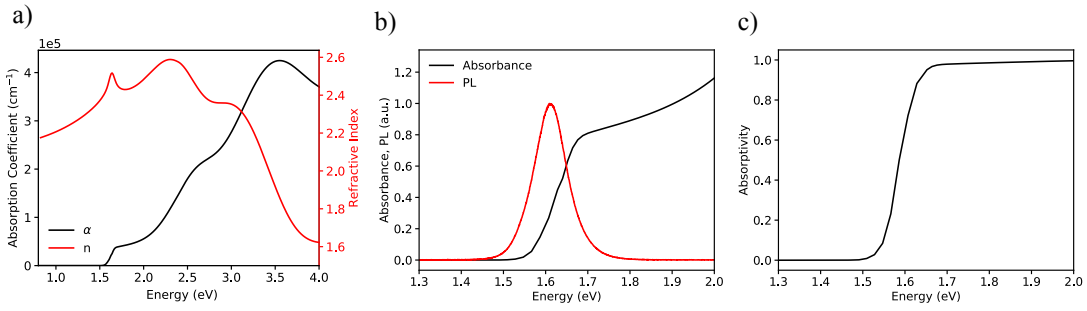

Figure 1.11: a) Absorption coefficient (black trace) and index of refraction (red trace) of triple cation films as a function of photon energy. b) Absorption spectrum (black trace) and photoluminescence (PL) spectrum (red trace) of triple cation films. The overlap between the two spectra is due to the low Stokes shift in the material. c) Beer-Lambert absorptivity of triple-cation films as a function of energy.

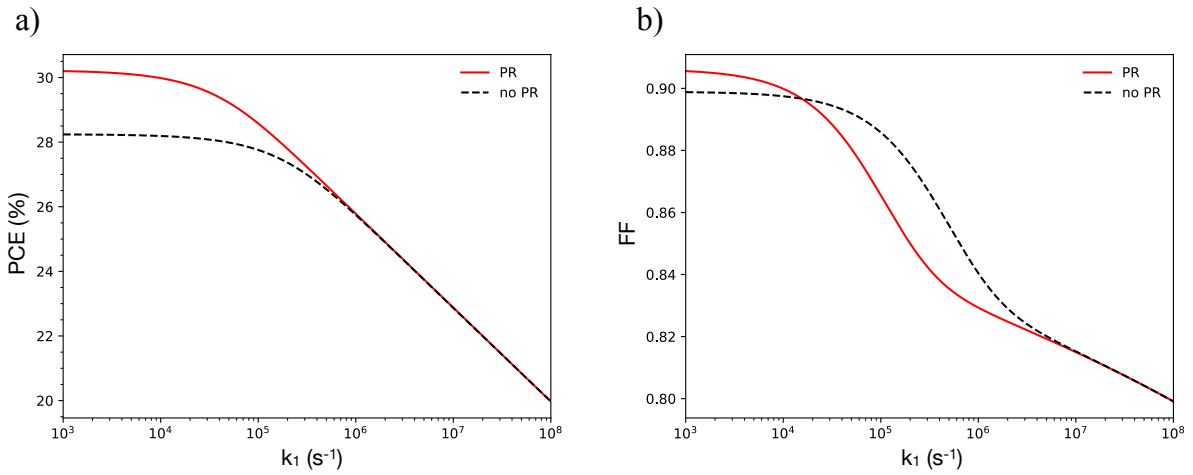

Figure 1.12: a) Power conversion efficiency (PCE) and b) fill-factor (FF) as a function of non-radiative recombination rate (k_1) with and without photon recycling. With photon recycling, the fill-factor initially decreases because of the larger fraction of non-radiative recombination at the maximum-power-point. Ultimately, when k_1 decreases below ~2×10^4 s^{-1}, radiative recombination outcompetes non-radiative recombination and the fill-factor with photon recycling is greater than the fill-factor without photon recycling.

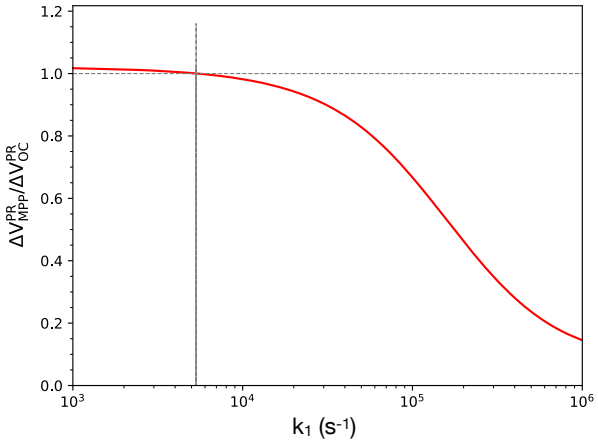

Figure 1.13: The increase in voltage at the maximum-power-point (MPP) due to photon recycling (ΔV_{MPP}^{PR}) divided by the increase in voltage at open-circuit due to photon recycling (ΔV_{OC}^{PR}) is shown as a function of k_1. As k_1 decreases, the fraction exceeds 1, indicating that, at k_1 ~5×10^3 s^{-1}, ΔV_{MPP}^{PR} increases faster than ΔV_{OC}^{PR}.

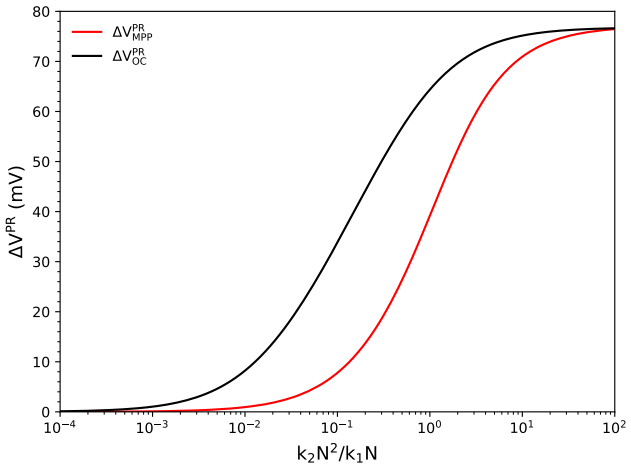

Figure 1.14: The ratio of the second order radiative recombination constant multiplied by the carrier density squared to the first order non-radiative recombination rate constant multiplied by the carrier density. When k_2N^2/k_1N ~ 10, there is a ~70 mV improvement in V_{MPP}.

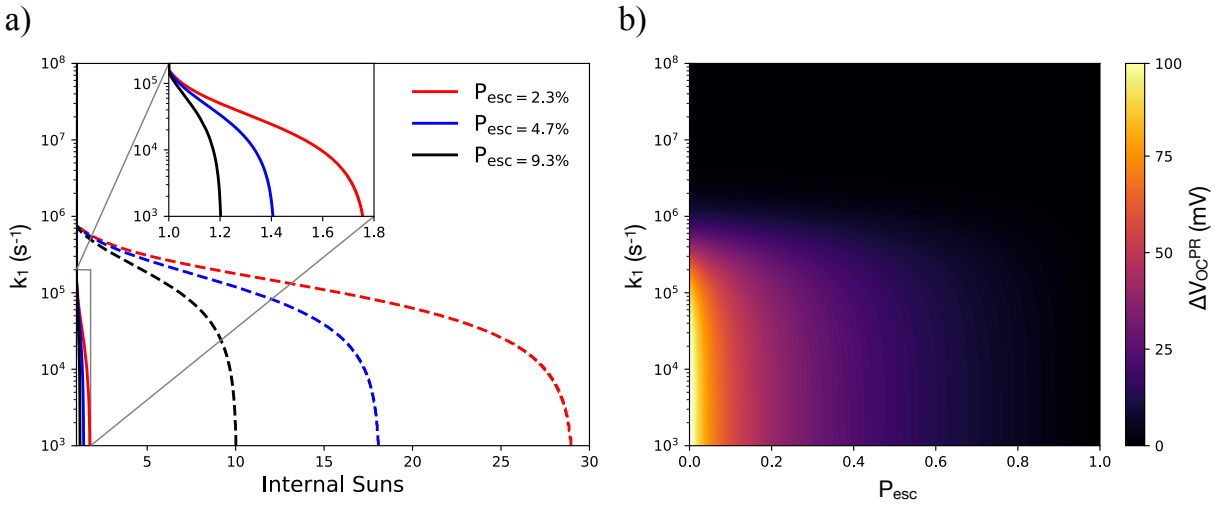

Figure 1.15: a) Internal suns as a function of k_1 at maximum power point (inset, solid lines) and at V_{OC} (dashed lines) for varying probability of escape (P_{esc}). b) Increase in open-circuit voltage due to photon recycling (ΔV_{OC}^{PR}) as a function of k_1 and P_{esc}.

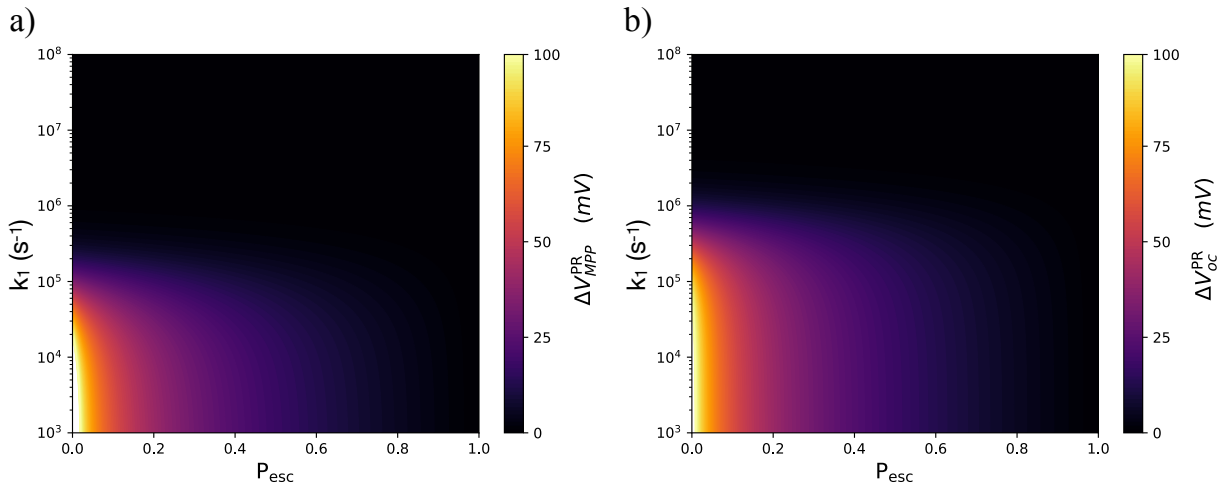

Figure 1.16: Increase in voltage due to photon recycling (ΔV^{PR}) at a) MPP and b) open-circuit as a function of k_1 and P_{esc}.

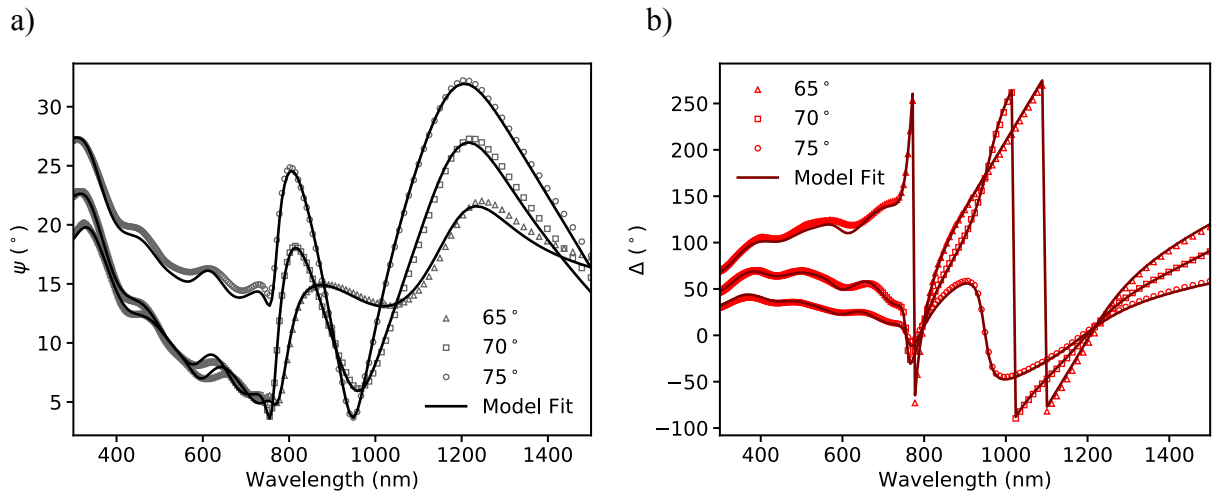

Figure 1.17: a) Ψ and b) Δ variable angle spectroscopic ellipsometry (VASE) data for triple cation perovskite thin films deposited on top of p-type silicon. Data was acquired at incident angles 65° (triangles), 70° (squares) and 75° (circles). An oscillator model was used to fit the experimental data.

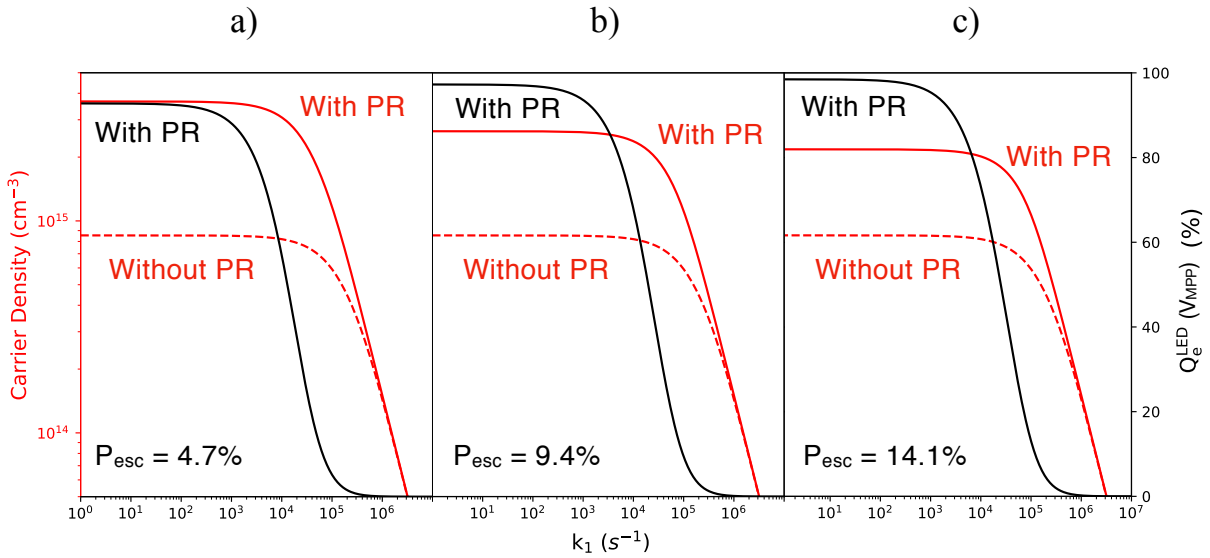

Figure 1.18: The effect of PR on MPP steady-state carrier density and $Q_e^{LED}(V_{MPP})$ (calculated with an injection current achieved at a voltage bias of V_{MPP}) as a function of k_1 for a) P_{esc} = 4.7%, b) 9.4%, and c) 14.1%.

1.7.5. $CH_3NH_3PbI_3$ Supplementary Figures

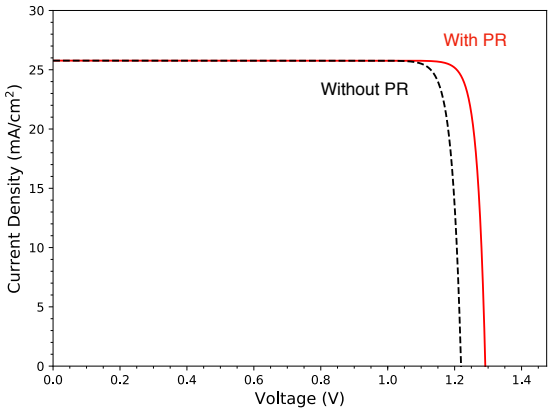

Figure 1.19: J-V characteristics in the radiative limit (no non-radiative recombination) with (red curve) and without (black dashed curve) photon recycling for $CH_3NH_3PbI_3$ ($MAPbI_3$) films.

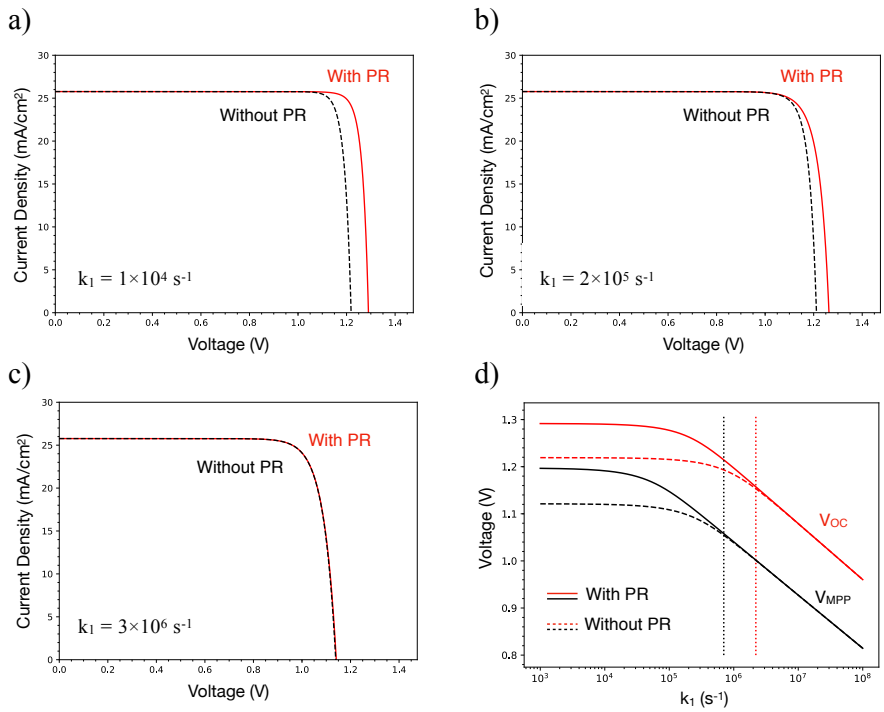

Figure 1.20: Simulated J-V curves ($MAPbI_3$) with and without photon recycling for k_1 values of (a) 1×10^4 s^{-1}, (b) 2×10^5 s^{-1}, and (c) 3×10^6 s^{-1}, all with fixed values for the radiative (k_2 = 1.14×10^{-10} cm^3 s^{-1}) and Auger (k_3 = 1×10^{-28} cm^6 s^{-1}) rate constants. (d) V_{OC} (red lines) and V_{MPP} (black lines) are shown as a function of k_1, revealing differences in the onset of performance improvements due to photon recycling. Dotted vertical red and black lines indicate k_1 thresholds (2.2×10^6 s^{-1} and 7×10^5 s^{-1}, respectively) below which photon recycling improves performance at open-circuit and at MPP, respectively.

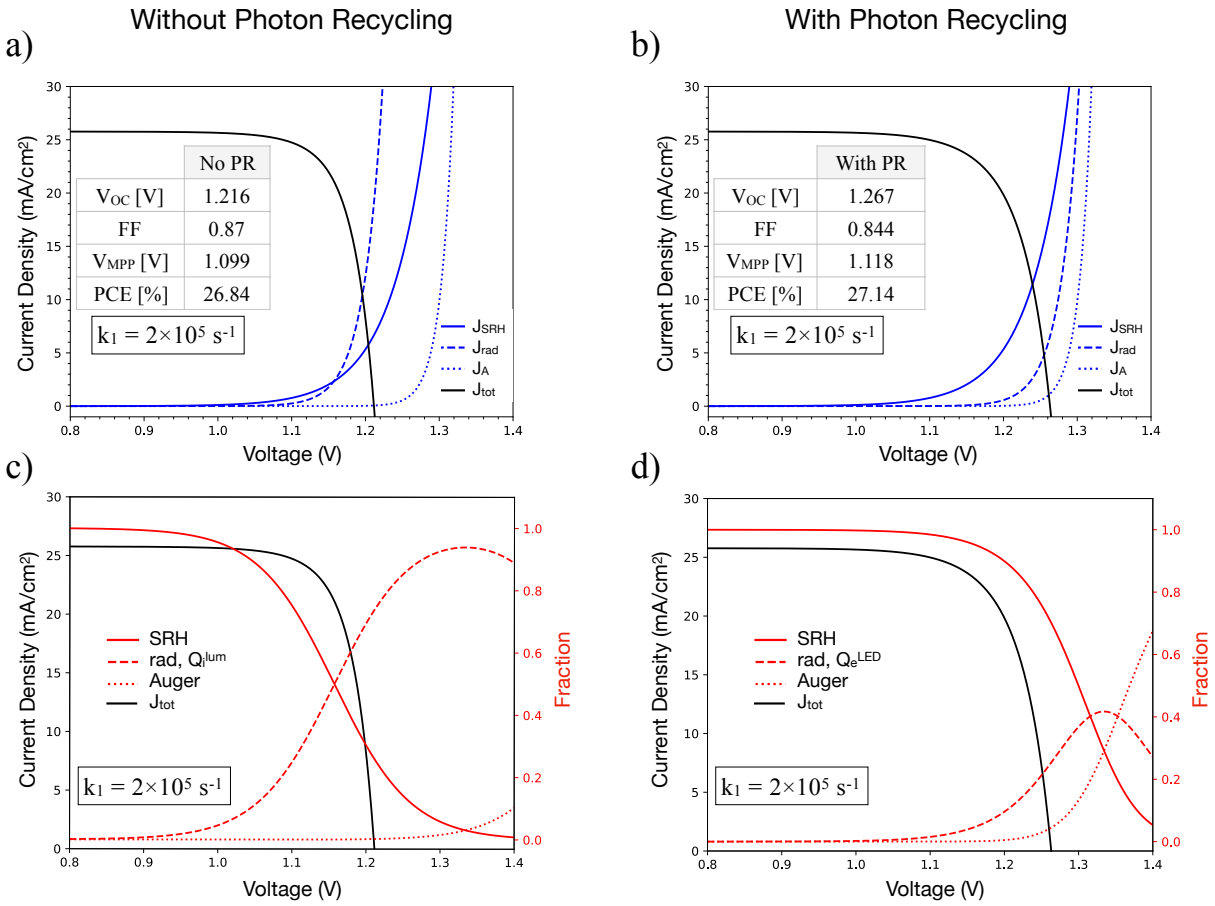

Figure 1.21: The J-V curve for $k_1 = 2\times10^5\ s^{-1}$ (a, c) without and (b, d) with photon recycling (black traces) is depicted along with the magnitude of the three recombination currents (SRH, radiative, and Auger) as a function of voltage (blue traces). (c,d) The fraction of total recombination current due to SRH, radiative, and Auger recombination is shown at each voltage (red traces) (c) without and (d) with photon recycling. The fraction of radiative recombination as a function of voltage with and without photon recycling is equivalent to Q_e^{LED} and Q_i^{lum}, respectively.

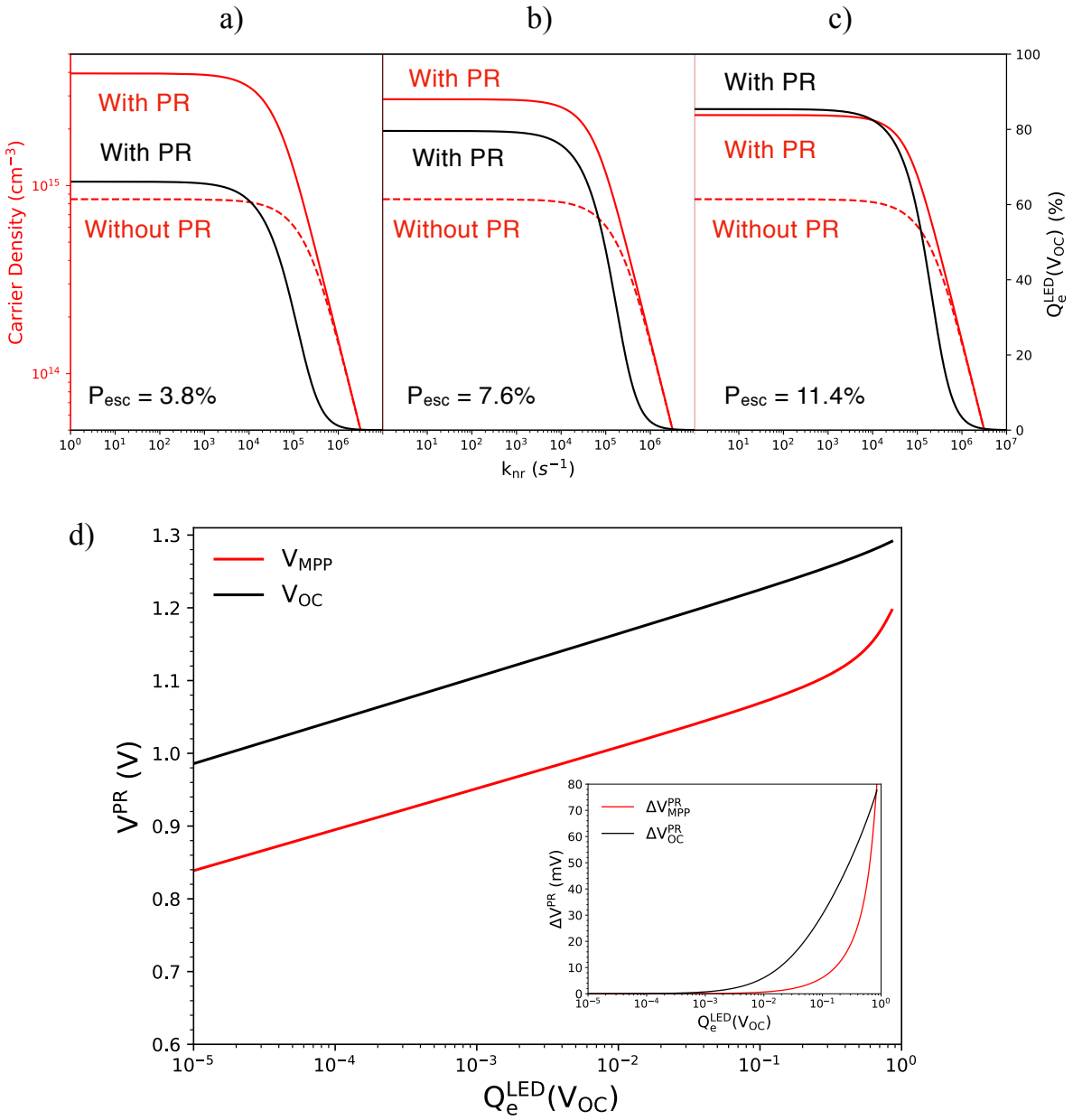

Figure 1.22: The effect of photon recycling on steady-state carrier density and $Q_e^{LED}(V_{OC})$ as a function of non-radiative recombination rate for a) P_{esc} = 3.8% (probability of escape for $MAPbI_3$), b) P_{esc} = 7.8%, and c) P_{esc} = 11.4%. d) ΔV^{PR} for P_{esc} = 3.8% at maximum-power-point and open-circuit is shown as a function of $Q_e^{LED}(V_{OC})$, which, as k_1 decreases, approaches 90%.

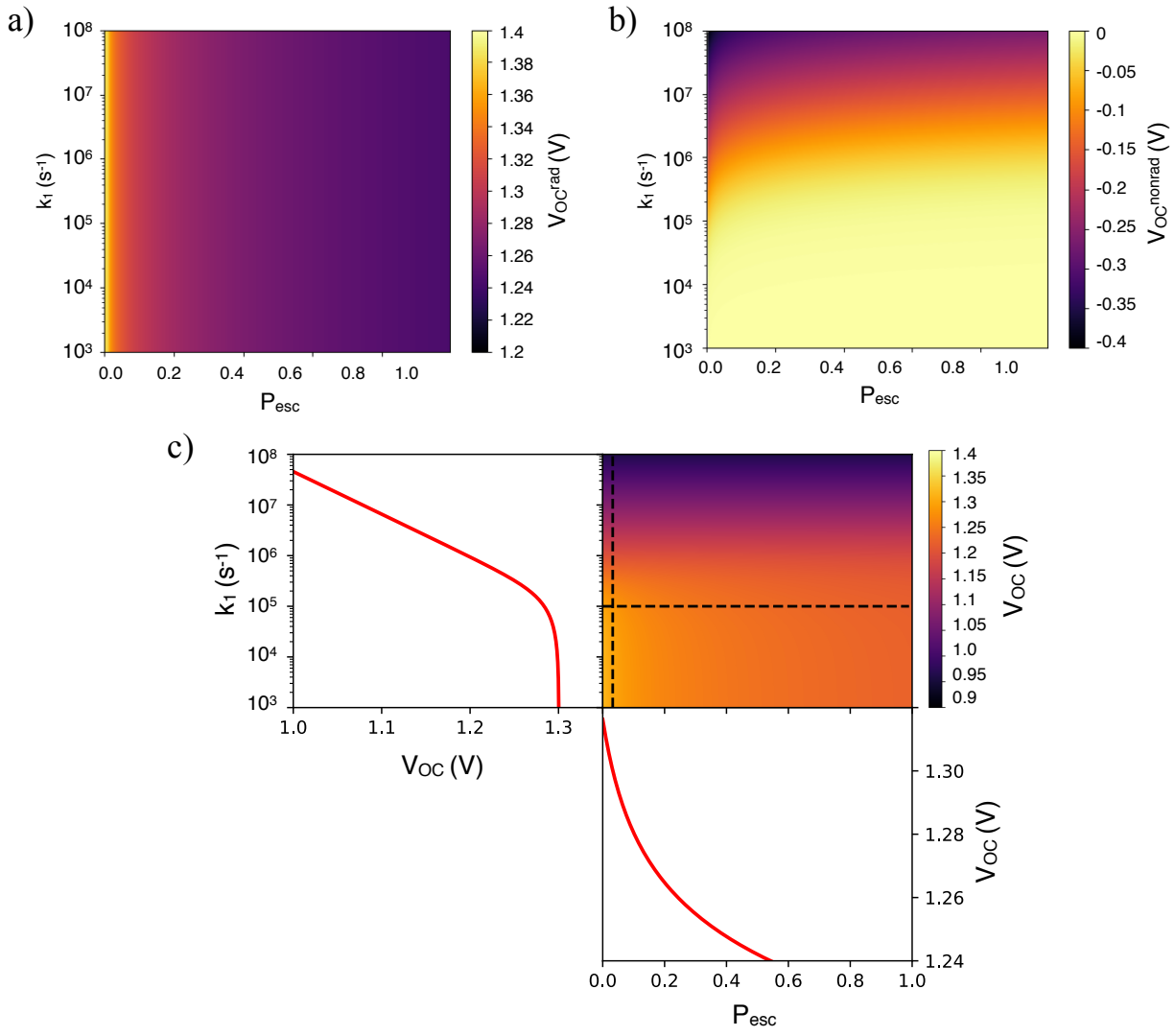

Figure 1.23: The V_{OC} with photon recycling in the radiative limit (V_{OC}^{rad}) is shown along with b) the non-radiative subtractive effect on V_{OC}^{max} (V_{OC}^{nonrad}). Combined, V_{OC}^{rad} + V_{OC}^{nonrad} yield c) the total V_{OC}^{max} as a function of k_1 and P_{esc} with dashed vertical and horizontal lines indicating P_{esc} = 3.8% (for $MAPbI_3$) and $k_1 = 1\times10^5$ s^{-1}, respectively. Increasing P_{esc} for a fixed Q_i^{lum} decreases V_{OC}.

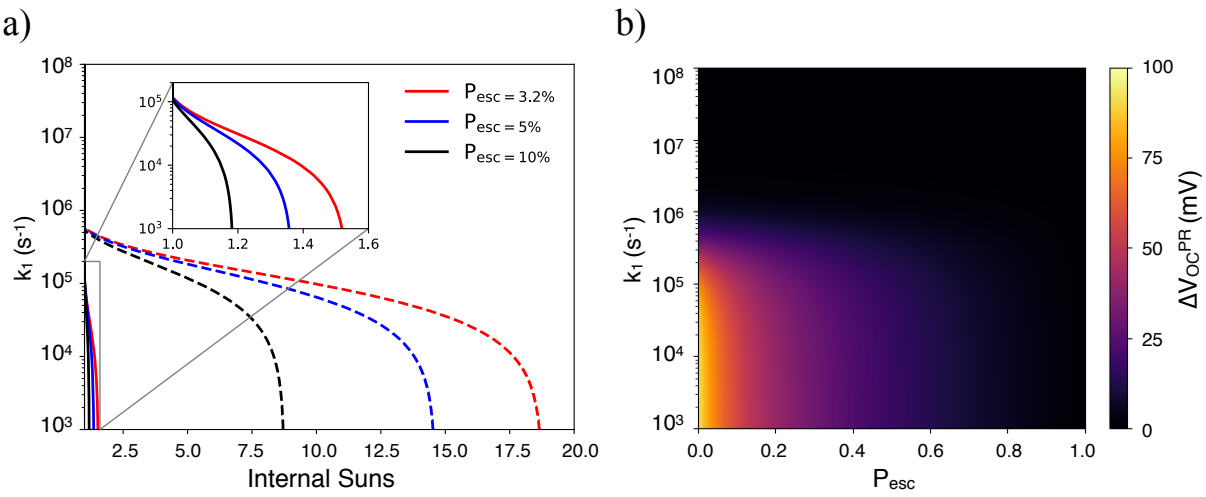

Figure 1.24: a) Internal suns as a function of k_1 at MPP (inset, solid lines) and at V_{OC} (dashed lines) for varying P_{esc}. b) V_{OC}^{PR} as a function of k_1 and P_{esc}.

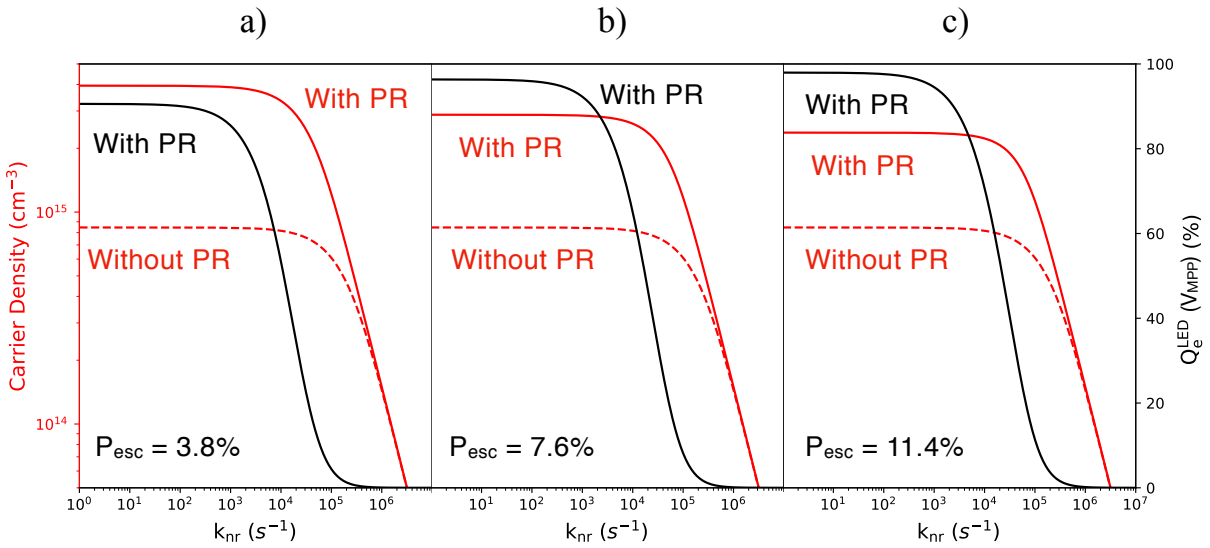

Figure 1.25: The effect of PR on MPP steady-state carrier density and $Q_e^{LED}(V_{MPP})$ (calculated with an injection current achieved at a voltage bias of V_{MPP}) as a function of k_1 for a) P_{esc} = 3.8%, b) 7.6%, and c) 11.4%.

1.8. CHAPTER-SPECIFIC ACKNOWLEDGEMENTS

This work in this chapter is supported by the TATA-MIT GridEdge Solar Research program. This material is based upon work supported by the National Science Foundation Graduate Research Fellowship under Grant No. (1122374). We would also like to acknowledge support from NSF/CBET-BSF under Grant No. 1605406 (EP/L000202). We thank Dak Benjia Dou for his guidance in the preparation of the triple-cation perovskite thin films; Nina Hong, from J.A. Woollam Co., Inc., for her technical support analyzing the ellipsometry data; and Luis Pazos-Outón and Thomas Mahony for valuable discussions.

PART II.
WEAK LIGHT-MATTER INTERACTIONS AND FIELD-MODULATED PHOTOPHYSICS IN QUANTUM DOTS

CHAPTER 2

2. CD-FREE QUANTUM DOTS: TOWARDS ENVIRONMENTALLY BENIGN HIGH-EFFICIENCY LIGHT-EMITTING DEVICES

2.1. OVERVIEW

Quantum dots (QDs) have emerged as a leading light-emitting material, with extremely high quantum efficiencies, narrow emission linewidths, synthetic flexibility, and high operating stability. The demand for energy efficient displays utilizing environmentally benign materials has expanded efforts beyond high-performing yet heavy metal-containing QDs towards less toxic materials with comparable optical properties. In this work, we use time-resolved optical microscopy to probe the spectrally resolved decay dynamics of InP/ZnSe/ZnS QD thin films and light-emitting diodes (QD-LEDs) to reveal the interplay between carrier diffusion, charge transfer, and exciton dissociation in the absence and presence of external fields. In the thin film, we report wavelength-dependent energy transfer rates up to 0.02 ns^{-1}, and quantify two energy relaxation rates corresponding to spectrally-distinct populations of mobile and immobile field-screened photogenerated or field-ionized carriers of 0.04 ns^{-1} and $1.8x10^{-3}$ ns^{-1}, respectively. Additionally, we study the photoluminescence (PL) quenching of QD-LEDs in reverse bias, demonstrating 87% PL quenching towards efficient voltage-controlled optical downconverters, informing the rational design of Cd-free, high-efficiency emitters and devices for next-gen displays.

Portions of this chapter are reprinted with permission from:

Laitz, M., Xie, S., Zhu, H., Proppe, A., Jang, E., Kim, T., Bawendi, M., and Bulović, V., *in prep* (2022).

2.2. INTRODUCTION

Semiconducting quantum dots (QDs) have garnered interest in both light emitting and absorbing applications due to highly desirable and synthetically-modifiable optical properties,[123] such has high quantum efficiencies,[124–127] narrow emission linewidths,[128–130] flexible deposition schemes,[131,132] bandgap tunability,[133,134] and surface functionalization capacity.[135–137] High-efficiency light-emitting diodes (LEDs)[138–140] and photovoltaics (PVs)[141–143] utilizing QD active layers present opportunities for light-weight, solution-processed electronics. To date, heavy metal-containing QDs (Pb, Cd-based) are the colloidal archetype and most well-studied, though there is an emerging effort to identify and optimize environmentally benign materials with comparable optical properties. Recent studies have shown color-tunable InP[30,144–146] and blue-emitting ZnSe[33,147] QDs with competitive optical properties for lighting and display technologies, yet a rigorous understanding of the photophysics, carrier dynamics, non-radiative processes, and behavior under applied fields is required for material and device optimization towards high-efficiency lighting and displays.[124,145,148,149]

An understanding of the underlying photophysics, exciton recombination dynamics, and transport processes within the inhomogeneous QD distribution is essential for the rational engineering of QD nanostructures and device architectures with effective transport layers and optimal electric field profiles.[150–152] Depending on the degree of quantum confinement and exciton binding energy, some QD systems display photogenerated excitons that dissociate on short time scales into free carriers even in the absence of an electric field,[153] demonstrating band-like electron transport.[154–156] In contrast, high exciton binding energy material systems with slight variations in QD size polydispersity, like InP-based QD thin films,[34] have been shown to result in energy transfer from smaller (higher energy, donor) to larger (lower energy, acceptor) QDs via Förster resonance energy transfer (FRET) utilizing inter-dot dipole-dipole interactions due to low material Stokes shift, as quantified by the absorption/emission spectral overlap integral.[150,157,158]

Here, we investigate exciton transport, spectral diffusion, and field-induced luminescence quenching in state-of-the-art InP/ZnSe/ZnS QD thin films and QD-LEDs, probing energy transfer mechanisms in QD systems that have recently been shown to demonstrate 100% solution quantum yield, 21.4% maximum theoretical external quantum efficiency, and long operating lifetimes of one million hours at 100 candelas per square meter.[30] InP-based QDs are poised to compete with Cd-based QDs, and a nuanced understanding of exciton dynamics in thin films and devices is essential to close the gap, enabling heavy metal-free light emitting and display technologies. In this work, we quantify the impact of increasing electric field on exciton diffusion processes and determine the impact of field-induced photoluminescence quenching by reverse-biasing an optically excited QD-LED.[159] We report 87% PL quenching in reverse bias, which is, to the best of our knowledge, the highest quenching efficiency for InP-based QDs. We identify two spectrally distinct populations of QDs characterized by (1) mobile excitons with energy-dependent transfer rates to low energy sites and (2) immobile excitons demonstrating an order of magnitude slower energy relaxation rate. We propose an optical characterization metric by which to evaluate QD thin film mobile exciton populations effecting photoluminescence quenching efficiency and bias-recovery time, with implications for device performance based on efficient charge extraction and injection.

2.3. FIELD-DEPENDENT LUMINESCENCE LIFETIME IN INP QD FILMS & LEDS

To characterize the energetic disorder in an ensemble of InP/ZnSe/ZnS QDs, we spectrally resolve the PL decay dynamics of photogenerated carriers. Additionally, we investigate these energy transfer processes in a LED architecture utilizing poly(3,4-ethylenedioxythiophene) polystyrene sulfonate (PEDOT:PSS) as the hole transport layer (HTL), poly(9,9-dioctylfluorene-alt-N-(4-sec-butylphenyl)-diphenylamine) (TFB) as the hole injection layer (HIL), ~15 nm of InP/ZnSe/ZnS QDs (~2 monolayers), ZnMgO as the electron transport layer (ETL), and Al as

the top contact (Figure 2.1a, Figure 2.10b). In these devices, we achieve excellent charge injection and the reverse process, charge extraction, should likewise result in the efficient quenching of photoexcited carriers.[30,159]

For the QD thin film, the maximum of the Gaussian PL distribution is tracked over time, revealing a monotonic redshift from the initial, nonequilibrium energy distribution to the thermalized energy distribution (Figure 2.1b) and bulk, energy-integrated lifetime of τ_{film} = 35.4 ns (Figure 2.2a). The QD lifetime in the QD-LED is effectively quenched by the transport layers (Figure 2.1c), and, in reverse bias, the energy-integrated lifetime further decreases (Figure 2.1d), consistent with field-induced exciton dissociation ($\tau_{LED,0V}$ = 17.8 ns and $\tau_{LED,-5V}$ = 11.6 ns, respectively; Figure 2.2a).[147,160]

The spectrally resolved apparent lifetime of the bare QD film reveals a near monotonic increase in the lifetime with increasing wavelength, ranging from ~20 ns for higher energy photons to ~48 ns for lower energy photons (Figure 2.2b, black trace). The observed spectral dynamics can be attributed to the spectral diffusion of higher energy carriers to lower energy sites due to the QD size polydispersity and bandgap variation. Such dynamics have been reported in various QD systems, with the rate of energy relaxation and exciton population thermalization dependent on QD chemistry and ligand composition, ranging from 10s of ps in CdSe,[161] PbSe,[162] and PbS[163] QDs to 100s of ps in ligand-exchanged PbS QDs.[164,165]

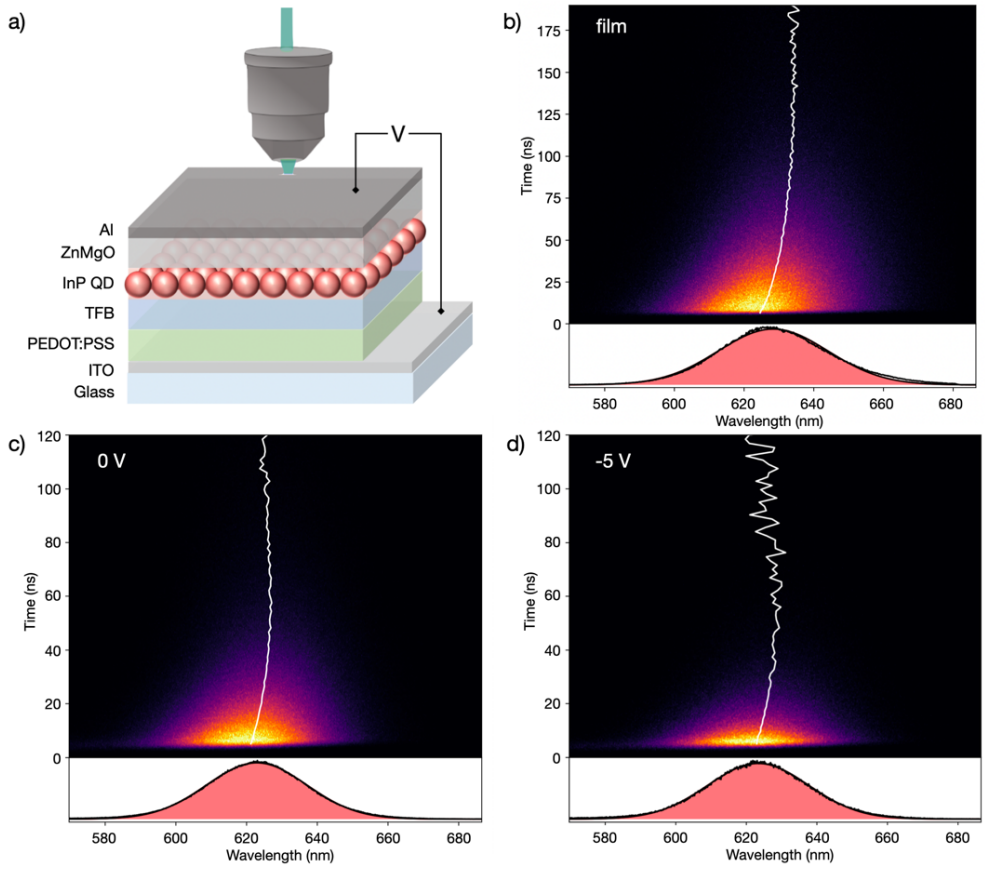

Figure 2.1: a) LED architecture Al/ZnMgO/QDs/TFB/PEDOT:PSS/ITO/glass with optical excitation. b-d) Spectrally-resolved lifetime of the QD thin film, the QD-LED with no bias applied, and the QD-LED with 5V applied in reverse bias (-5V). The center wavelength of the Gaussian emission profile is tracked over time (white trace), and the temporally-integrated PL spectra with Gaussian fit shown (lower panel).

When placed in an LED structure, the spectrally-resolved lifetime decreases for all emission wavelengths, though a more dramatic reduction in the lifetime of red photons is observed, with a factor of 2.8 reduction in the lifetime of the highest energy photons and a factor of 4 reduction in the lifetime of the lowest energy photons (Figure 2.2b). This reduction in lifetime and its spectral asymmetry with the introduction of transport layers and built-in electric field is a strong indication of efficient charge extraction and field-enhanced exciton dissociation limiting diffusive processes.[159,166] With an increasing applied reverse bias to enhance exciton dissociation, we measure a concomitant reduction in the energy-integrated radiative lifetime from 17.9 ns to

11.6 ns at -1V and -5V, respectively (Figure 2.2a, Figure 2.11-Figure 2.12). The spectrally-resolved dynamics in reverse bias show a similar reduction in lifetime across emission energies (Figure 2.2c), with the effect more pronounced for lower energy photons (Figure 2.2d), consistent with a reduction of exciton diffusion and subsequent decrease in radiative recombination events from the low-energy tail of the bare QD film thermalized distribution. The multi-component spectrally-integrated lifetimes as a function of increasing reverse bias in an LED structure are reported in Table 2.1, with spectrally-resolved decay traces shown in Figure 2.3a-d (green and red traces corresponding to the LED with no bias applied and the LED with -5V applied in reverse bias, respectively).

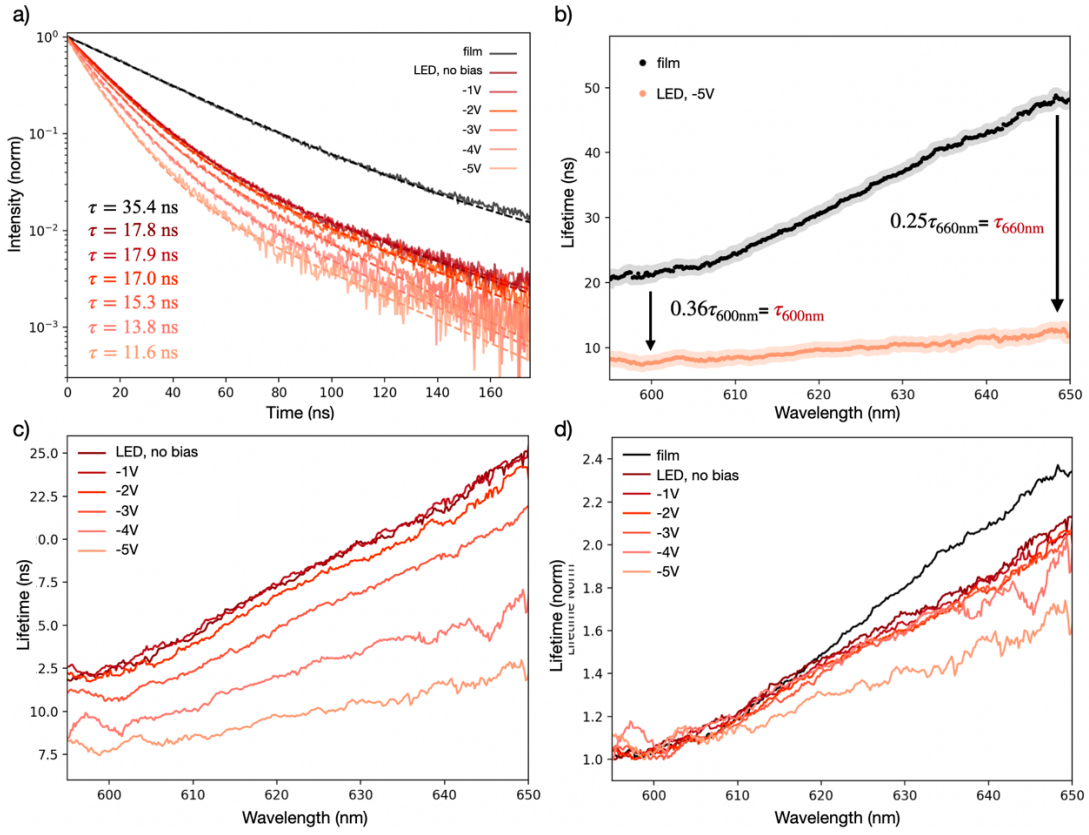

Figure 2.2: (a) Lifetimes extracted from streak camera data (integrated over wavelength) of the QD thin film (black trace) and QD-LED with increasing reverse bias (red traces), showing a decreasing radiative lifetime with increasing bias. (b) The spectrally resolved apparent

lifetime of the QD thin film shows increasing lifetimes with decreasing energy while the QD-LED radiative lifetime as a function of wavelength flattens, revealing a greater reduction in lifetime for redder photons. (c) The QD-LED emissive lifetime as a function of wavelength continues to flatten with increasing reverse bias, with a consistently greater impact on redder photons, as can be seen by the (d) lifetime data normalized to the shortest wavelength.

Bias (E-field)	τ_1 (ns)	τ_2 (ns)	A1	A2	τ_{wt} (ns)
0V, no bias	14.6	46.0	0.90	0.10	17.8
-1V (0.175 MV/cm)	14.9	49.0	0.91	0.09	17.9
-2V (0.35 MV/cm)	14.0	41.3	0.89	0.11	17.0
-3V (0.525 MV/cm)	12.2	32.7	0.85	0.15	15.3
-4V (0.7 MV/cm)	11.9	37.0	0.92	0.08	13.8
-5V (0.875 MV/cm)	10.0	36.2	0.94	0.06	11.6

Table 2.1: Spectrally integrated decay lifetimes in a QD-LED as a function of applied reverse bias. The short and long lifetime components are reported as τ_1 and τ_2, along with the weighted average, τ_{wt}.

2.4. ENERGY TRANSFER RATES: INP QDS

In the QD thin film, we observe increasing delayed emission with decreasing energy in the spectrally resolved TRPL traces (Figure 2.3a-d, blue trace), a signature of spectral diffusion. The delayed emission feature is absent from the low energy TRPL traces in the LED structure without bias and with -5V applied in reverse bias (Figure 2.3a-d, green and red traces, respectively), where field-enhanced dissociation competes with the diffusive processes and serves as an additional non-radiative pathway reducing the number of carriers hopping to lower energy sites.[37,167,168] In the 2D film, only the excitons on the highest energy sites with the fastest radiative rates radiatively recombine before diffusing, a “hopping” process in which the exciton energy

progressively decreases due to the inelastic nature of the dipole-dipole coupling diffusive process.[169–171] The excitons lose energy as they diffuse, and, when they ultimately radiatively recombine, emit a lower energy photon from the thermalized population distribution.

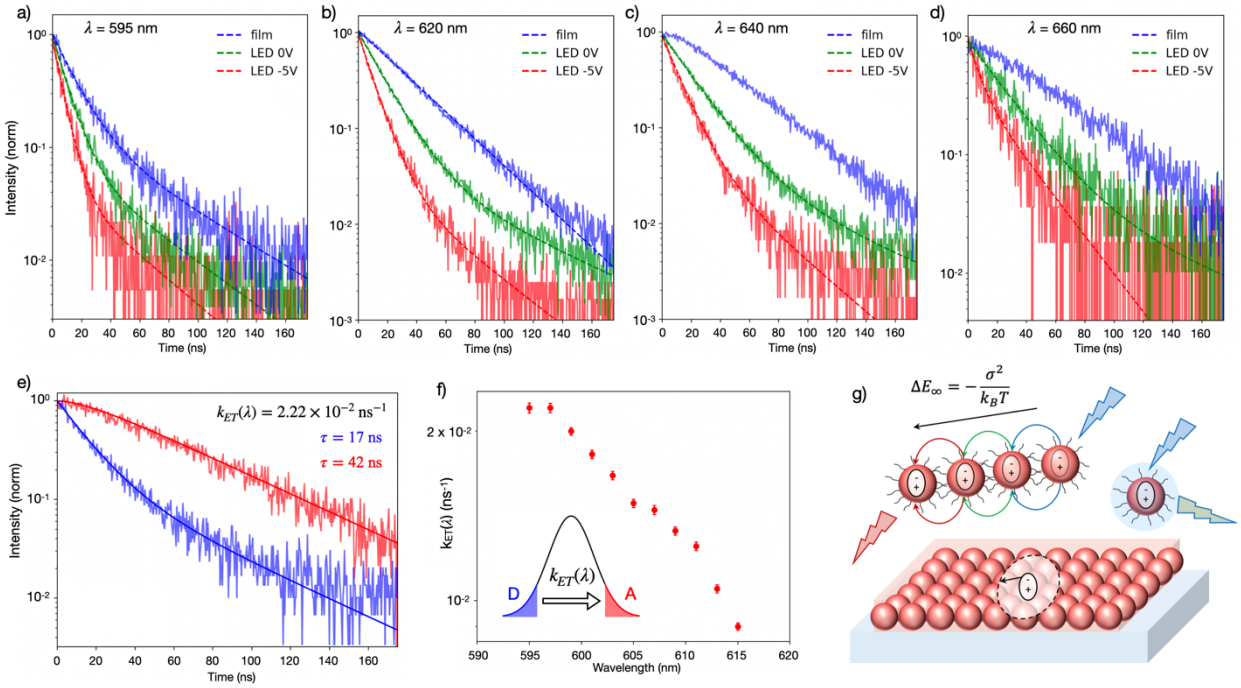

Figure 2.3: (a-d) Time-resolved photoluminescence (PL) decay traces extracted from spectrally-resolved lifetimes at 595 nm, 620 nm, 640 nm, and 660 nm for the QD thin film, the QD-LED with no bias applied, and the QD-LED with 5V applied in reverse bias (-5V). (e) QD thin film lifetimes at 595 nm and 660 nm fit with Eq. 1-3 demonstrating delayed red emission due to exciton diffusion. (f) The energy transfer rate ($k_{ET}(\lambda)$) is fastest for the highest energy excitons with the greatest density of states, and decreases with decreasing energy. Inset: schematic of Gaussian PL distribution with high energy (donor, blue) sites and low energy (acceptor, red) sites. (g) Schematic revealing high energy photon absorption, exciton diffusion, and emission from two species of dots – one population that can feel the applied electric field and emits at low energies after diffusion, and the other population that cannot feel the field, does not diffuse, and ultimately emits at higher energies.

The rate at which excitons at high energy sites hop, or energy transfer, to lower energy sites is dependent on the initial energy and the availability of lower energy states in the disordered

landscape, following the density of states.[161] This rate, $k_{ET}(\lambda)$, is thus dependent on the starting site (donor) energy and the probability of transferring to a lower energy (acceptor) site, which is dependent on the density of acceptor states. In the thin film case, $k_{ET}(\lambda)$ was determined by extracting the time-resolved photoluminescence (TRPL) traces at variable high and fixed low photon energies and fitting the energy transfer rate using Eqs. 2.1-2.3 to include photon recycling due to the small material Stokes shift (Figure 2.13).[11,170,172,173]

$$\frac{dn_D}{dt} = -k_{rD}n_D - k_{ET}(\lambda)n_D + \frac{c}{n_r}\sum_\lambda \alpha_\lambda \gamma_\lambda \quad 2.1$$

$$\frac{dn_A}{dt} = -k_{rA}n_A + k_{ET}(\lambda)n_A \quad 2.2$$

$$\frac{d\gamma_\lambda}{dt} = -\frac{c}{n_r}\sum_\lambda \alpha_\lambda \gamma_\lambda + k_D n_D(1 - P_{esc}) + k_{rA}n_A(1 - P_{esc}) \quad 2.3$$

where k_D and k_A are the radiative recombination rates of the donor and acceptor exciton, respectively, $k_{ET}(\lambda)$ is the wavelength-dependent energy transfer rate, n_D and n_A are the donor and acceptor site carrier densities, respectively, c is the speed of light, α_λ is the absorption coefficient averaged over emission wavelengths, γ_λ is the photon concentration within the film for a given wavelength due to radiative recombination and photon recycling, n_r is the index of refraction, and P_{esc} the probability of a radiatively recombined photon leaving the film within the escape cone.

For a donor wavelength of λ = 595 nm and an acceptor wavelength of 660 nm, k_{ET}(595 nm) = 2.22x10^{-2} ns^{-1} (Figure 2.3e), which is in excellent agreement with previous reports of InP QDs quantifying resonance transfer rates of 4-7x10^{-2} ns^{-1},[169,174] and is consistent with other reports of CdSe QDs with ns resonance transfer timescales.[151,157,175] Other systems, such as PbSe and PbS QDs, demonstrated spectral diffusion due to energy and charge transfer on the ps timescale.[162,163] By varying the donor wavelength from 595 nm to 615 nm and fixing the acceptor wavelength to 660 nm, the wavelength-dependent energy transfer rate can be quantified (Figure 2.3f, Figure 2.14), consistent with the density of states due to spectral overlap in the absorption and emission and magnitude of dipole-dipole coupling.[176] The Förster radius can be calculated from the energy

transfer rates, $k_{ET}(\lambda, d) = \frac{1}{\tau}\left(\frac{R_0}{d}\right)^6$, yielding an average radius of R_0 = 5.6 nm (Figure 2.15), which is comparable to similar InP QD systems.[174,177,178]

2.5. THERMALIZATION RATES: MOBILE AND IMMOBILE EXCITONS IN INP QDS

In addition to the wavelength-dependent energy transfer rate, the bulk rate of population thermalization or ensemble energy relaxation, $k_{\Delta E}$, can be determined for carrier systems exhibiting hopping diffusion and dynamically red-shifting Gaussian energy distributions.[161] The center emission wavelength is tracked over time from its initial energy, E_0, to the saturated energy at long timescales, E_∞, with energy difference $\Delta E_\infty = E_0 - E_\infty$ (Eqs. 2.4-2.5).[161,179]

$$\Delta E = \Delta E_\infty[1 - \exp(-k_{\Delta E}t)] \quad 2.4$$

$$\Delta E_\infty = -\frac{\sigma_{ih}^2}{k_B T} \quad 2.5$$

where ΔE is the difference in energy as a function of time from the initial peak of the Gaussian PL distribution, ΔE_∞ is the difference between the initial and long timescale saturated peak of the Gaussian PL distributions, $k_{\Delta E}$ is the ensemble energy relaxation rate, σ_{ih} is the inhomogeneous energy distribution width, k_B is the Boltzmann constant, and T is the system temperature taken here as room temperature. In Eq. 2.5, we approximate the energy distribution due to hopping processes by a Boltzman distribution, consistent with other reports in similar systems.[161,176]

In the QD thin film, the PL center wavelength exhibits a 9.5 nm (33 meV) monotonic redshift (Figure 2.4a-b, black trace; Figure 2.16), which can be fitted with Eqs. 2.4-2.5. The inhomogeneous broadening is determined by fwhm = $2[2 \cdot \ln(2)]^{1/2}\sigma_{ih}$ as a function of time (Figure 2.4c), corresponding to a decrease in energy from 45 meV to 33 meV in the thin film.

Similarly, the QD center emission wavelength can be tracked in the QD-LED architecture with no bias applied and as a function of increasing reverse bias, in which, for all biases, we observe an initial redshift followed by an anomalous blue-shift of the center emission wavelength (Figure 2.4a-b, Figure 2.17). As compared to the bare QD film, the center wavelength in the QD-LED architecture is blue-shifted, and the FWHM of the emission narrower, indicating a reduction in the low energy spectral contribution (Figure 2.4a,c, Figure 2.19).

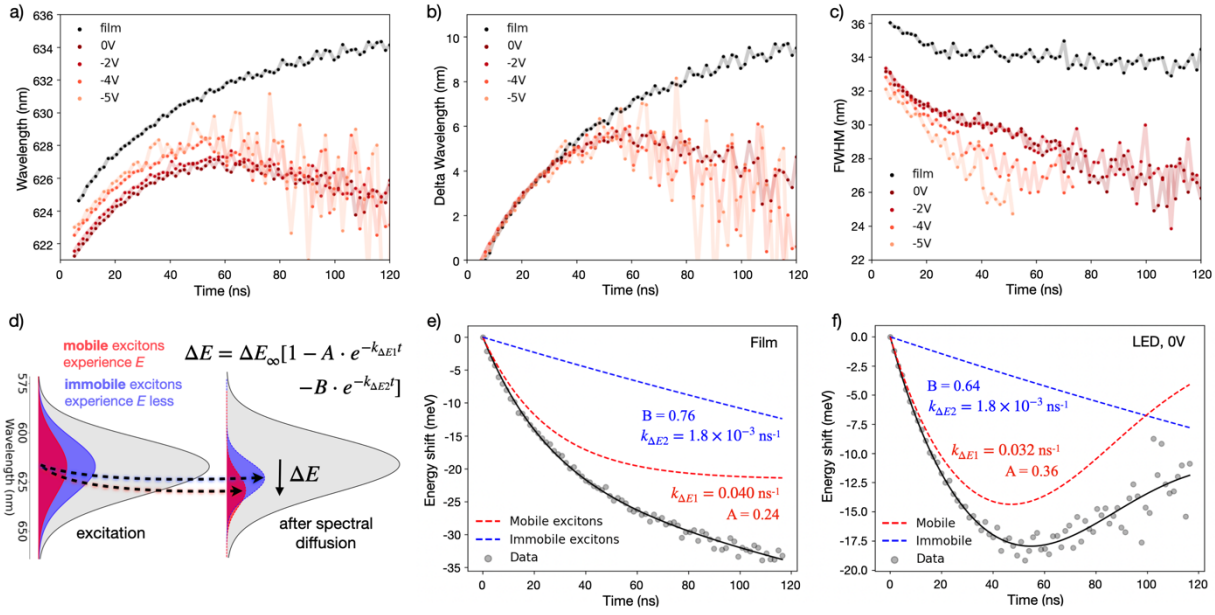

Figure 2.4: (a) Spectral evolution of the photoluminescence (PL) peak maximum for the QD thin film and QD-LED as a function of increasing reverse bias. The thin film demonstrates a monotonic red-shift of the center peak, while the QD-LED center wavelength first red-shifts and then blue-shifts after 55 ns. (c) The full-width at half-maximum (FWHM) of the Gaussian PL peak narrows over time for the thin film, and narrows to a greater extent for QD-LEDs with increasingly negative applied biases. (d) Depiction of two QD populations within the thin film and QD-LED, showing greater spectral diffusion for the mobile QDs. (e,f) These two populations can be modeled to fit the experimental bulk energy relaxation dynamics in both a thin film and QLED where the mobile excitons are extracted over time. For the thin film (e), the experimental data (gray scatter) can be well-reproduced by the summation (black trace) of two fitted populations representing the fast mobile exciton population contribution to the overall spectral shift (red dashed trace) and slow immobile exciton contribution to the overall spectral shift (blue dashed trace). For the QD-LED with no bias, the experimental data (gray scatter) is well-reproduced by the summation (black trace) of both the mobile exciton

contribution to the spectral shift (red dashed trace, modulated by a Fermi-Dirac distribution as mobile excitons are depleted) and the slow immobile exciton contribution to the spectral shift (blue dashed trace).

The spectral feature of an initially red-shifting center emission wavelength followed by a blue-shift can be well-explained by the presence of two populations of QDs, one subset that responds to an applied electric field and is depleted over time (mobile), and the other subset that is less perturbed by the field (immobile). The two populations of QDs can arise from inhomogeneous dielectric environments in both the thin film and LED case, in which the bottom and top QDs are in contact with glass, air, or organic/metal oxide transport layers, resulting in varying degrees of polarizability (Figure 2.3g).[180,181] Additionally, solution-processed QD films can form islands, in which QDs are electrically insulated from neighboring QDs, or embedded in electron/hole transporting layer materials, resulting in immobile sites.[182–184] The electric field can also be locally screened by photo-generated charges or field-ionized carriers, contributing additionally to the immobile population of QDs.[185,186] In the QD-LED architecture, we observe the center emission wavelength returning to shorter wavelengths at longer timescales due to the emission of immobile QDs, the luminescence efficiency of which has likely not been significantly impacted by the field. When the mobile excitons have been depleted by the field, the immobile population remains as the brightest emitters.

By expanding Eq. 2.4 to include the disparate bulk energy relaxation rates for these two populations of QDs – those that respond to applied fields and rapidly thermalize to the lowest available energy states, and those that feel applied fields less and saturate to lower energies at a slower rate – we can quantify the contributions of the two populations to the ensemble energy relaxation.

$$\Delta E = \Delta E_{\infty}[1 - A \cdot \exp(-k_{\Delta E1}t) - B \cdot \exp(-k_{\Delta E2}t)] = \Delta E_1 + \Delta E_2 \qquad 2.6$$

where A, $k_{\Delta E1}$ and B, $k_{\Delta E2}$ are the population coefficients and energy relaxation rates for the mobile and immobile QD subsets, respectively.

In the QD-LED case, we have the additional bias-dependent non-radiative pathway of field-induced exciton dissociation and carrier extraction, which can be accounted for by the introduction of a time-evolving loss rate following a Fermi-Dirac distribution as the prefactor to the mobile exciton population (Eq. 2.7).[162] The summation of the rapidly thermalizing yet simultaneously depleting mobile exciton spectral contribution and slowly thermalizing immobile exciton spectral contribution yields the early timescale red-shift and long timescale blue-shift (Figure 2.4d).

$$\Delta E = \frac{1}{\left[\exp\left(\frac{C(t)}{k_B T}\right)+1\right]} \cdot \Delta E_1 + \Delta E_2 \qquad 2.7$$

where $C(t)$ is a fit parameter associated with the rate of field-induced dissociation and quenching.

Xie *et al.* similarly demonstrated two exciton populations in CdSe QDs, in which they report one subset demonstrating field-induced dissociation and carrier extraction with a concomitant decrease in emissive lifetimes quantified by reductions in the short lifetime component, while the other subset of the QD population appears impervious to even strong applied fields, with a nearly unchanging long PL lifetime component at various biases.[159] Similarly, in the spectrally-integrated TRPL traces, we observe a short lifetime component, τ_1, that decreases with increasing reverse bias, while the long lifetime component, τ_2, is less sensitive to the increasing reverse bias (Table 2.1).

Differently, we infer that the immobile population can contribute to the PL signal at both early and late timescales due to the distribution of radiative lifetimes in the inhomogeneous QD film[187] and the mechanism of immobility, such as immobile bound charge-transfer states generated immediately following excitation[180,181] and the confinement of initially mobile charges by trap states at longer timescales.[188] In the thin film case – in which mobile carriers are not dissociated by built-in/applied fields and extracted via transport layers – the PL decay is monoexponential. In the QD-LED case, the decay becomes biexponential, due to the introduction of additional non-radiative extraction pathways for mobile carriers (Figure 2.2a).

The PL signal at long timescales in the QD-LED structure can be attributed predominantly to the fraction of immobile excitons with long radiative lifetimes, with the PL signal at early timescales comprised of both mobile and immobile exciton emission.

By fitting the PL spectral shift over time with Eqs. 2.6-2.7, we determine that the thin film mobile exciton population demonstrates an energy relaxation rate of $k_{\Delta E1} = 0.040\ \mathrm{ns}^{-1}$, consistent with previous reports in similar QD systems,[161] and the immobile population relaxes at a much slower rate of $k_{\Delta E2} = 1.8 \times 10^{-3}\mathrm{ns}^{-1}$ (Figure 2.4e). Mobile excitons contribute 24% to the bulk spectral thermalization, with 76% of the spectral shift due to the slowly relaxing immobile population.

For the LED with no bias applied, we obtain $k_{\Delta E1} = 0.032\ \mathrm{ns}^{-1}$ and $k_{\Delta E2} = 1.8 \times 10^{-3}\mathrm{ns}^{-1}$ for the mobile (36%) and immobile (64%) populations, respectively (Figure 2.4f). In the QD-LED structure, the rate of energy relaxation of mobile carriers is slightly reduced as compared to the thin film due to the depletion of mobile carriers resulting in a diminishing bulk rate of mobile exciton energy thermalization. The immobile population, conversely, possesses the same rate of energy relaxation, though represents a smaller fraction of all charged species as the built-in field liberates ~10% of the thin QD film immobile carriers. With 5V applied in reverse bias (corresponding to 0.875 MV/cm, assuming the voltage drop across the ZnMgO layer is minimal due to its high electron mobility[159]), the population of mobile QDs increases to 57% and the rate of energy relaxation for mobile carriers continues to slow as non-radiative processes increase with increasing field strength, resulting in $k_{\Delta E1} = 0.025\ \mathrm{ns}^{-1}$ (Figure 2.20).

We observe and quantify the reduction in radiative lifetime due to increasing electrical bias and the augmentation of the mobile QD exciton population with increasing field strength due to the liberation of a fraction of the previously immobile QD subset. We next investigate the PL quenching efficiency to begin to understand the extent to which the population of immobile QD excitons adversely impacts the electrical modulation of PL intensity.

2.6. VOLTAGE-CONTROLLED PHOTOLUMINESCENCE MODULATION OF INP QDS

Voltage-controlled active modulation of QD PL has been demonstrated in several QD material systems, with efforts to achieve high contrast ratios and rapid response rates yielding recent progress in Cd-based QDs, where Xie *et al.* report a record contrast ratio of 200:1,[159] more than an order of magnitude higher than previous demonstrations of Cd-based QD contrast ratios ~0.28-0.9:1.[37,38,189–195] For InP/ZnS QDs, there exist fewer demonstrations of PL quenching, with the highest report, to the best of our knowledge, achieving a 6.7:1 ratio.[196] The ability to achieve high contrast ratios approaching commercial displays (1000:1) and reversible quenching with a fast temporal response is essential for the development of biomedical and optoelectronic devices based on the electrical modulation of active layer PL, including cellular probes and selectively-addressable voltage-dimmable pixels.[38,195]

To characterize the PL quenching efficiency in this system of InP/ZnSe/ZnS QD-LEDs, we apply an increasing reverse bias from 0V to 15V (0 - 2.3 MV/cm) under constant 520 nm photoexcitation (Figure 2.5a). We observe a decrease in the integrated PL spectrum with increasing reverse bias, though no spectral shift is observed, contrary to Cd-based QDs demonstrating the signature red-shift indicative of the quantum-confined Stark effect (QCSE)[159] (Figure 2.5b, -10V corresponding to 1.6 MV/cm; Figure 2.21, -15V corresponding to 2.3 MV/cm). The lack of notable QCSE is likely due to the greater degree of confinement of the electron and hole wavefunctions in the core of the QD as compared to Type II CdSe/CdS QDs, in which the electron and holes are confined less strongly due to the small conduction band offset (0.3 eV).[34] At the excitation wavelength of 520 nm, we achieve 87% PL quenching efficiency at 15V applied in reverse bias, resulting in a 7.7:1 contrast ratio, which is, to the best of our knowledge, the highest PL quenching efficiency for InP-based QDs.

Additionally, the PL quenching response is explored as a function of excitation wavelength, in which higher energy excitations can generate hot-carriers with energy greater than the InP

core bandgap energy, reducing the difficulty of tunnelling through the wider bandgap ZnSe/ZnS QD shell to the adjacent transport layers in this Type-I QD.[34] Such excitation wavelength-dependent relaxation to the band edge and charge extraction has been shown in PbSe and CdSe QDs.[197,198] Here, the PL quenching efficiency was measured for decreasing excitation wavelength (535 nm, 525 nm, 505 nm, 485 nm, and 405 nm). As the excitation wavelength decreases from 535 nm to 405 nm, we observe a trend of increasing PL quenching efficiency as a function of reverse bias (Figure 2.5c,d). The efficiency increases sharply as a function of bias for 405 nm excitation, which can be understood in the context of the InP/ZnSe/ZnS band alignment.[199,200] The ZnSe inner shell possesses a bandgap of 2.7 eV,[201] corresponding to 460 nm, and thus the hot-carriers generated with 405 nm light possess sufficient energy to tunnel through the wider bandgap inner shell layer to neighboring transport materials more effectively (Figure 2.22).[159,198,202]

The ability for the PL to recovery after the bias is lifted diminishes with increasing field strength (Figure 2.5c, light traces). Such effects were not observed in the Cd-based QDs reaching a 200:1 contrast ratio, in which the PL counts before bias were recovered post-bias.[159] Möbius *et al.* cite the higher valence band as compared to CdSe QDs resulting in a greater barrier through which to tunnel for the hole as the key factor in long PL recovery times for InP QD systems.[196] The recovery time is additionally a function of the excitation wavelength. While the higher energy 405 nm excitation does indeed result in more efficient PL quenching, this scheme also demonstrates slower PL recovery when the reverse bias is lifted. This behavior is consistent with photo-charging effects due to hot-carrier transfer to trap sites on the exterior of the QD, as seen in PbSe nanocrystals.[203] Such transfer of hot-carriers to external traps has been shown to decrease the PL quantum efficiency and increase Auger trion recombination due to the build-up of trapped charges as a function of increasing excitation energy.[204,205]

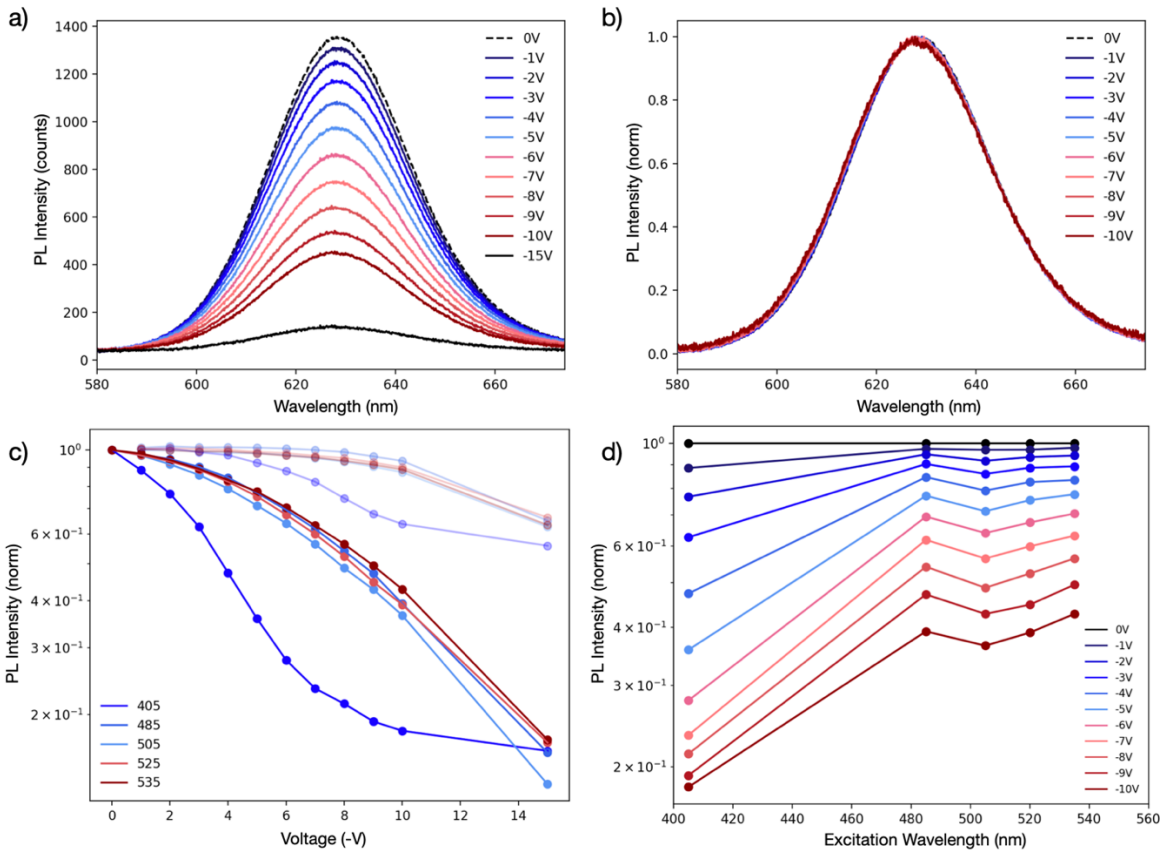

Figure 2.5: (a-b) QD-LED photoluminescence (PL) intensity with increasing applied reverse bias at 520 nm excitation, showing effective PL quenching and (b) no quantum-confined Stark effect. (c) A PL quenching efficiency of 87% (contrast ratio of 7.7:1) was achieved at 520 nm excitation (dark traces), with a decreasing ability to recover initial PL counts as the increasingly large reverse bias is lifted (light traces). (d) The trend in PL quenching efficiency as a function of bias increases with increasing excitation energy, with most effective quenching seen for 405 nm excitation.

Additionally, the two populations of QDs – mobile and immobile – will also impact the PL quenching efficiency and PL recovery after bias. The mobile population, subject to the electric field, should respond fairly rapidly (ns) to changing field strengths, while the immobile population remains unperturbed when faced with changing fields. The immobile subset could be due, in part, to electric field screening from field-ionized, photogenerated, or injected charges, greatly slowing the PL response and recovery when the bias is lifted. It is anticipated that a

uniform population of mobile QDs would respond more rapidly to applied fields, both in the magnitude of PL quenching beyond a 7.7:1 contrast ratio and the restoration of pre-bias PL levels. In this way, it is possible to relate the center emission wavelength spectral shift over time as a function of increasing reverse bias, and corresponding fraction of mobile/immobile subsets, with PL quenching efficiency and recovery.

2.7. STRONG 3D OPTICAL CONFINEMENT TOWARDS INP QD ASE

Quantum dots (QDs) have demonstrated high functionality as an active layer material in light emitting diodes (LEDs) and devices.[30,33,206–208] Beyond utility in LEDs, the emission wavelength tunability, high photoluminescence efficiency, charge localization, spectral overlap between absorption and emission, charge transport properties, and stability render these materials excellent candidates for amplified spontaneous emission (ASE) and, ultimately, provide a pathway to electrically injected lasers.[209–213] To achieve lasing in QD systems, architectures such as high-Q distributed Bragg reflector (DBR) microcavities,[214] photonic crystals,[215] micropillars,[216] and micro disks[217] have been employed to localize the electric field and photon modes to achieve resonance with the active layer spectral gain region, thus lowering the lasing threshold. These devices, however, are difficult to incorporate into structures for electrically injected lasing due to growth complexity, thermal management, mechanical fragility, and limited electrical conductivity.[207]

Here, we explore the possibility of achieving ASE from the fundamental mode of a three-dimensional metallic cavity with vertical and lateral optical confinement utilizing an InP/ZnSe/ZnS QD active layer. We demonstrate spectral discretization in reciprocal (k) space, consistent with lateral confinement of the active layer. We utilize the enhanced photon and carrier density from the cavity multi-dimensional photon confinement and the material spectral region of absorption and emission overlap. In this way, we achieve highly directional, narrow

line-width emission and quantify the Purcell enhancement from the fundamental mode. By utilizing low quality factor (Q) metallic mirrors, we demonstrate a discretized emitter microcavity system sustaining ASE than can be readily incorporated into traditional LED structures already employing highly reflective metallic top electrodes towards electrically injected lasing.

InP/ZnSe/ZnS QDs present a heavy metal-free alternative to traditional Cd-based QDs and display a small Stokes shift in the absorption and emission spectrum (Figure 2.10a), high oscillator strengths, and compatibility with solution processing techniques.[34] The flat photoluminescence (PL) dispersion of a QD thin film (~15 nm, two monolayers) is shown in Figure 2.6a as a function of wavelength and angle (*k*-space, resolving in-plane $k_{||}$), revealing a PL full-width half-maximum (FWHM) of ~36 nm.

We fabricate metallic microcavity structures on fused silica with the following architecture: Ag mirror (110 nm) / SiO_2 (108 nm) / QD active layer / poly(methyl methacrylate) (PMMA) (150 nm) / Ag mirror (35 nm). By engineering the spin-coating speed of our solution-processed optically-inert cavity layer (PMMA), we achieve a radial wedged cavity, with increasing cavity length from center to substrate edge. The resulting monotonic thickness variation allows for changes to the cavity mode by scanning the photoexcitation on the cavity surface. When the QD thin film is embedded in the microcavity, the QD emission is modulated by the cavity mode, and we see the PL escaping from the cavity mode when energetically resonant (Figure 2.6b). The FWHM of the QD emission in the cavity is decreased from the bare thin film case as determined by the cavity Q. We achieve a Q of ~110, and subsequently resolve a 10 nm FWHM peak from the cavity mode QD PL.

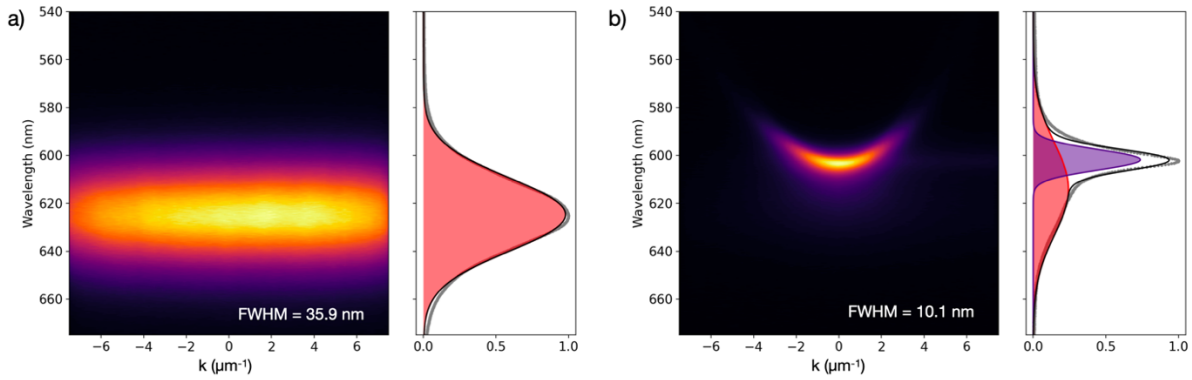

Figure 2.6: (a) Bare QD thin film exciton emission with FWHM of 36 nm resolved in *k*-space. Right panel: *k*-space-integrated photoluminescence (PL). b) QD PL leaking through a vertical cavity mode detuned to 608 nm at $k_{//} = 0$ with FWHM of 10 nm. Right panel: *k*-space-integrated photoluminescence (PL) showing the narrow cavity emission and broad QD exciton PL leaking through the semi-transparent Ag top mirror.

When the cavity energy is scanned across the exciton emission energy band, we observe certain regions on the cavity in which discrete energy levels emerge, superimposed on the bare cavity mode through which the QD film emits (Figure 2.7a,b). The dispersionless discrete energetic levels are consistent with fabrication process-induced stochastic intracavity mesa formation, in which agglomerates of QDs deposited during the solution-processing of the active layer create local, μm-scale lateral regions of confinement (Figure 2.7d).[218–223] These confined photon modes resulting from mesa-induced vertical and lateral confinement have been observed in many systems, effectively modulating the PL in *k*-space through dispersionless, spectrally discretized modes with smaller angular spread than planar cavity modes in organic materials (e.g., Alq_3),[219,224] inorganic materials (e.g., InAs, GaAs),[209,218,222,223,225–229] and strongly coupled exciton-polaritons (e.g., GaAs, GaN, CdTe, organic polymers).[220,221,230–237]

In our system, mesa formation is consistent with the conformal coating of the top Ag mirror around a QD agglomerate. The resulting cavity mode in this region, confined vertically by the top and bottom Ag mirrors, is additionally confined laterally, which limits the mode propagation resulting in the local optical confinement of the electric field.[221,224] The change in cavity length

and cavity resonance surrounding the mesa further contributes to the confinement of the optical mode.[209,225] Muller *et al.* describe the propagation constants within ($\vec{k} = (\vec{k}_\perp, \vec{k}_z)$) and beyond ($\vec{K} = \vec{K}_\perp, \vec{K}_z$) the mesa, in which $\vec{k} < \vec{K}$.[218] Under these conditions, for real $\vec{k}_\perp$, there are solutions resulting in imaginary $\vec{K}_\perp$ for $\frac{\omega}{c} = \sqrt{\vec{k}_z^2 + \vec{k}_\perp^2} = \sqrt{\vec{K}_z^2 + \vec{K}_\perp^2}$, as also found by considering an effective index step further confining the mode in the lateral dimension.[218,225]

The number of modes confined by the mesa has been shown to be a function of lateral confinement length, with smaller mesas exhibiting a greater degree of confinement resulting in a smaller number of modes displaying increased energetic spacing.[218] Larger mesas sustain higher modes with decreased energetic spacing. The limitation of the number of modes by small mesas can reduce the ASE threshold in certain systems due to the reduction of higher order mode emission competition.[224]

Figure 2.7a shows a single laterally confined mode with strong emission and the faint, superimposed emission from the higher energy planar cavity mode. The emission from this fundamental laterally confined mode displays a further reduction in spectral broadening as compared to the planar cavity mode, resulting in a FWHM of ~6 nm. The corresponding real space PL mode image appears similar to cylindrical waveguide LP_{nm} modes, where *n* and *m* are the number of nodes in the radial and azimuthal directions, respectively (LP_{01}, characterized by a single PL spot) (Figure 2.7c).[218,221,226,234] Figure 2.7b depicts multi-mode optical confinement, indicating a larger lateral mesa dimension. The emission distribution is consistent with higher order modes observed in similar systems, and the real space PL mode image again resembles the spectrally integrated LP_{01} and LP_{11} modes, with the LP_{11} mode characterized by two real space elliptical PL spots (Figure 2.7e).[218,226,234] The emission is broader spectrally than the single mode region shown in Figure 2.7a due to the lesser degree of confinement. It is noted that the mesa size is several factors smaller than the real space mode emission,[218] indicating mesa sizes ranging from ~0.75 μm to ~2.5 μm, consistent with other reports.[209,218,226] Such bright PL modes are not

observed in the real space images of non-mesa regions in which QD PL leaks through a single planar cavity mode (Figure 2.23).

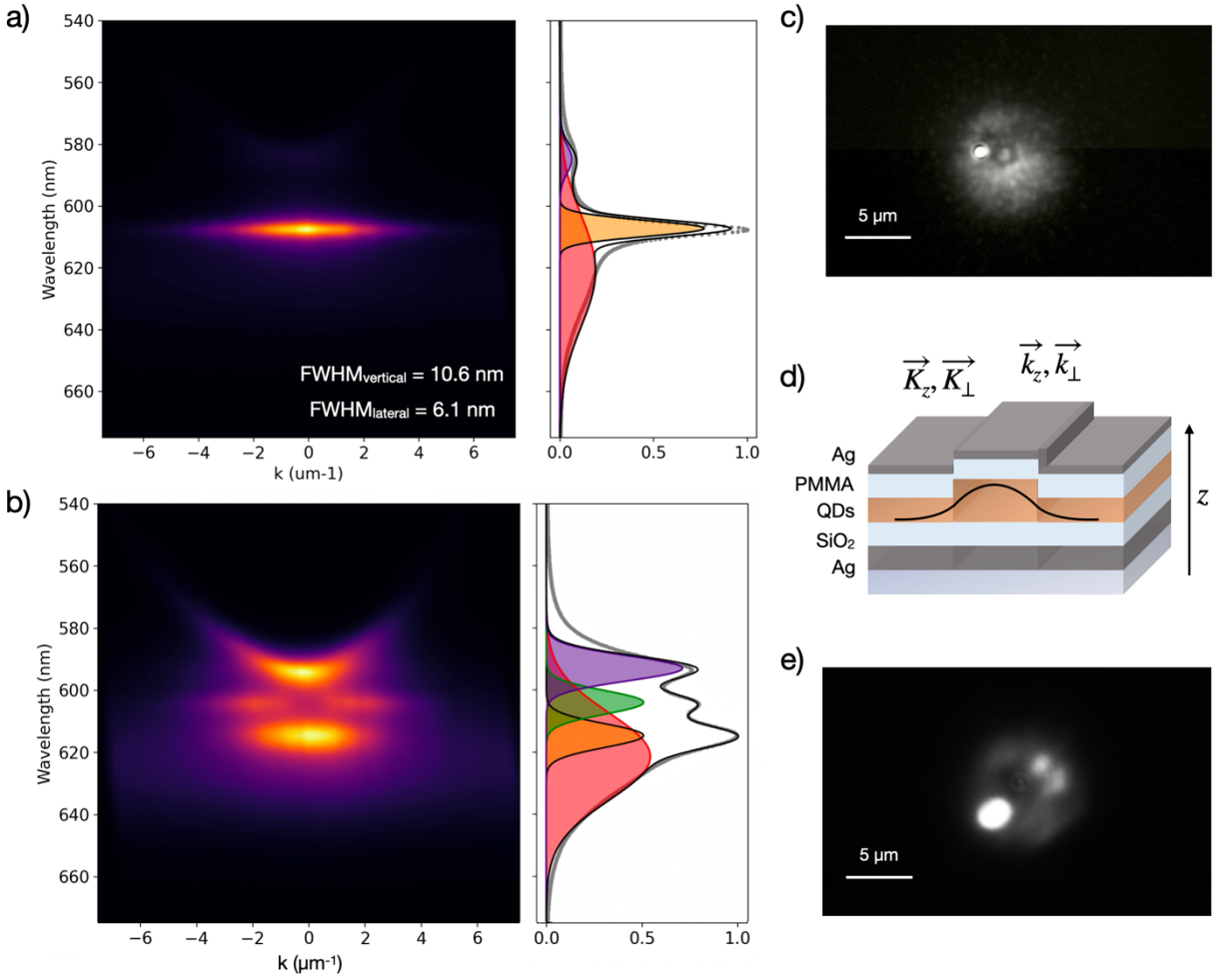

Figure 2.7: (a) *K*-space photoluminescence (PL) dispersion of the smaller, strongly confined mesa region with single mode emission and (b) larger mesa with multi-mode emission. (c) Real-space PL consistent with the LP_{01} mode. (d) Mesa depiction with varying vertical cavity resonance within and beyond the mesa bounds. (c) Real-space PL consistent with both LP_{01} and LP_{11} modes.

We observe the strongest emission from the fundamental mode in both the single laterally confined photon mode region (small mesa) and multi-mode region (larger mesa), with weaker emission from higher order modes, consistent with literature reports.[221,224,231,232] Such dominant emission from the lowest order mode has been demonstrated to additionally contribute to reductions in ASE thresholds, though multi-mode lasing has also been shown.[209,225,228,229]

By resonantly positioning the fundamental laterally confined photon mode with the active layer spectral gain region (corresponding dispersion, Figure 2.7a), we investigated the PL intensity as a function of pump power, with an ASE threshold of 150 $\mu J/cm^2$/pulse (Figure 2.8a-c). The superlinear exponential prefactor of the power dependence indicates the contributions from the background lower energy QD exciton PL leaking through the semi-transparent Ag mirror and higher energy planar cavity mode PL.

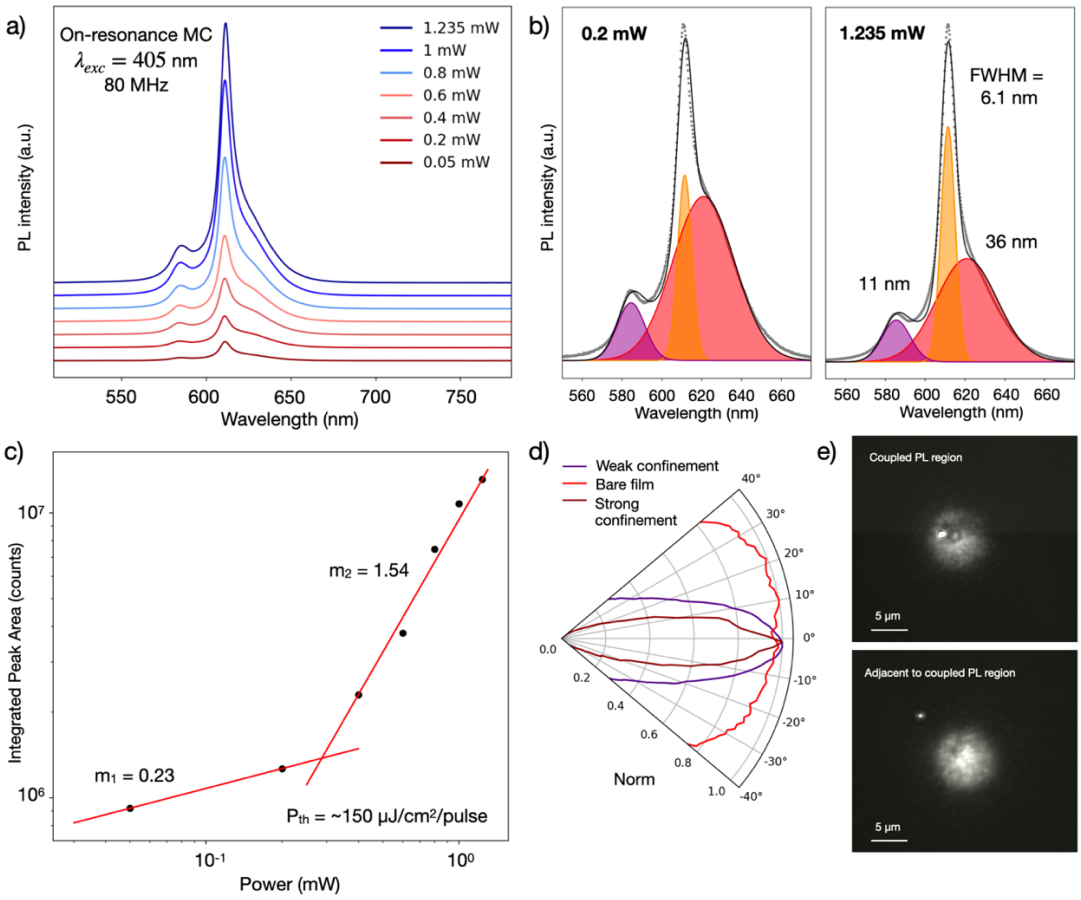

Figure 2.8: (a-b) Emission spectrum as a function of pump power. (c) Integrated area under the primary curve demonstrates a threshold of ~150 μJ/cm^2/pulse. (d) Angular dispersion of the bare QD thin film (red trace), weakly-confined mesa (Figure 2.24, purple), and strongly confined mesa exhibiting ASE (brown) showing increasingly narrow emission angles for highly directional emission. (e) Real-space image of photoluminescence for the ASE region (upper image) and region adjacent to the ASE region showing strong waveguiding effect to the mesa (lower image).

In addition to the enhanced electric field from lateral confinement contributing to ASE processes, there is likely further benefit from photon recycling in this specific spectral regime (575 nm to 625 nm, Figure 2.10a) due to the overlap in the absorption and emission which serves to increase the gain: photon recycling-induced gain.[238] This allows for the wavelength regime in which the overlap exists to sustain ASE at lower thresholds. The stochastic locality of the ASE

regions benefit from the fundamental mesa mode coinciding with a planar cavity mode trapping high energy photons with strong spectral absorption overlap to promote photon recycling-enhanced gain.

The real space PL mode from the region of ASE (single mode laterally confined mesa) demonstrates persistent emission even as the laser excitation is scanned away from the mesa, indicating that light is waveguided within the microcavity and selectively emitted in this region of confinement (Figure 2.8e).

We quantify the reduction in the angular dispersion for the strongly confined single-mode mesa region as compared to the bare QD thin film (Figure 2.6a) and weakly confined single-mode mesa (Figure 2.24). Emission is detected out to ~40 degrees (limited by the 100X Nikon L Plan 0.85 NA dry objective) for the bare QD film (Figure 2.8d). For the strongly confined single-mode mesa region, the ASE dispersion shrinks to <10 degrees.

We next quantify the spectrally resolved Purcell enhancement for the strongly confined single-mode mesa region (Figure 2.9b) and for a low energy planar cavity mode emission in a non-mesa region (Figure 2.9c,f).[218] We measure a reduction in the lifetime of the single lateral mode mesa as compared to the bare QD thin film, with a greater decrease in lifetime in the spectral region of ASE (Figure 2.9a,b,d,e). This is compared to a low energy detuned vertical cavity mode, which possesses a longer lifetime at shorter wavelengths (605 nm to 635 nm) corresponding to off-normal ($k_{||} > 0$) emission due to cavity inhibition extending the measured exciton lifetime (Figure 2.9c,d,e).[239] The vertical cavity mode $k_{||} = 0$ emission (wavelengths > 635 nm) benefits from cavity Purcell enhancement, with a markedly shorter lifetime than the bare QD film. The spectrally resolved Purcell factor is shown in Figure 2.9e, with a local maxima at 608 nm corresponding to the ASE emission (red trace) and dramatic reduction at 623 nm corresponding to the peak emission wavelength of the bare QD film possessing enhanced radiative lifetimes due to the electric field enhancement of the laterally confined mesa (Purcell factor ~1.7).

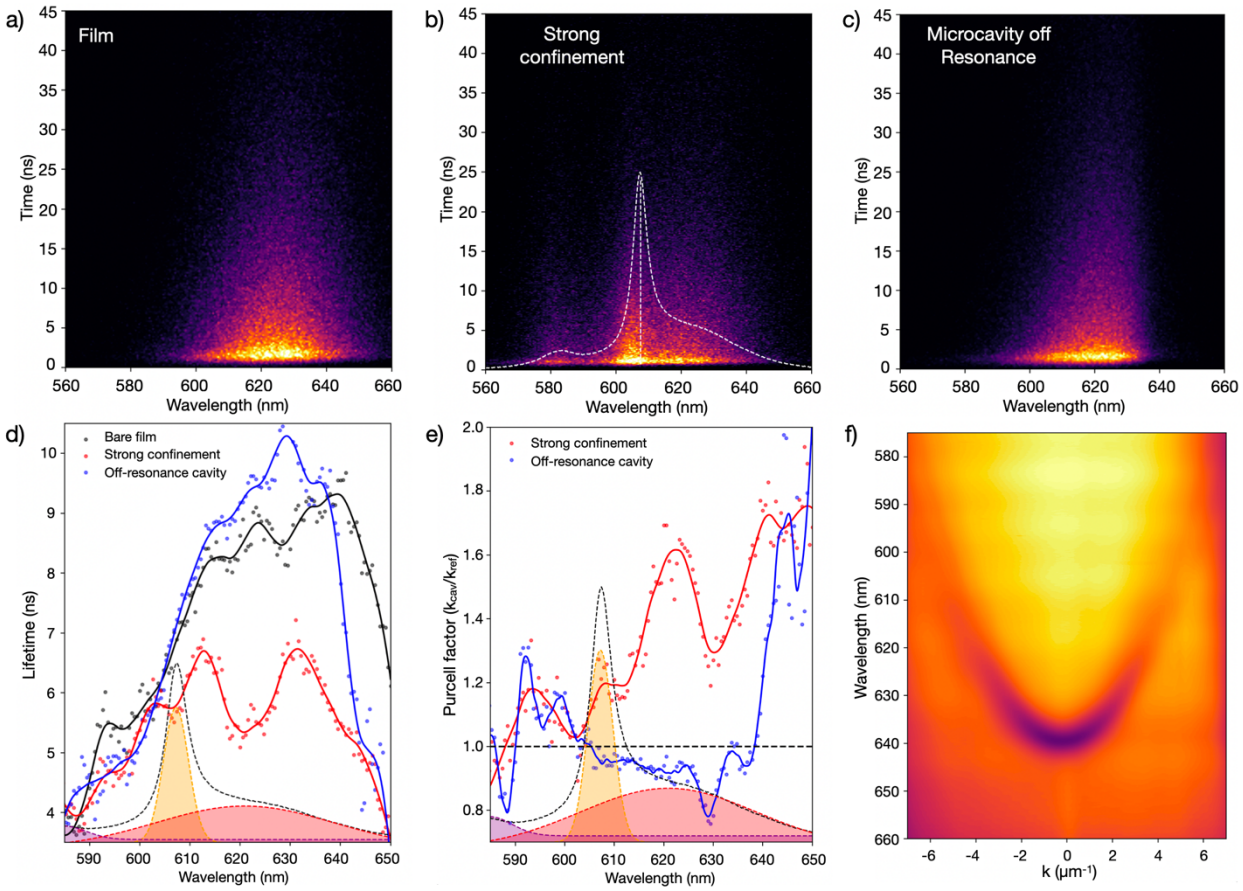

Figure 2.9: Emission from the (a) bare QD thin film, (b) strongly confined mesa demonstrating ASE, and (c) non-mesa vertical cavity mode spectrally and temporally resolved. (d) Fitted lifetimes of the bare QD thin film (black trace), lateral strongly confined mesa (red trace), and vertical cavity (blue trace). The photoluminescence (PL) spectrum from the strongly confined mesa region is shown (gray dashed trace), with fitted vertical cavity leaking contribution (purple), ASE region (orange), and bare QD leaking emission (red). (e) Purcell factor relating the bare QD thin film lifetime to the vertical cavity emission (blue) and strongly confined mesa emission (red) with PL spectrum similarly overlayed.

In this work, we study environmentally benign III-V semiconducting QDs (InP/ZnSe/ZnS) as a Cd-free alternative for high-efficiency light-emitting devices. We quantify the impact of increasing electric field on radiative PL lifetime showing quenching due to field-induced exciton dissociation and charge extraction. Through spectrally resolved streak camera measurements of the decay dynamics, we can quantify the wavelength-dependent energy transfer rate ($k_{ET}(\lambda)$). By tracking the peak of the PL Gaussian emission over time, we can extract bulk thermalization or energy relaxation rates ($k_{\Delta E}$) for two distinct populations of QDs – a mobile subset that feels the field and an immobile subset that is less perturbed by applied fields. As field strength increases, the fraction of mobile dots increases from 24% to 57%, and the rate of energy relaxation slows as non-radiative processes compete increasingly with hopping diffusion processes and subsequent radiative recombination.

The population of immobile carriers negatively impacts the PL quenching efficiency and bias recovery in these QDs, resulting in a 7.7:1 contrast ratio (87% efficient PL quenching) at 15V in reverse bias, with only 63% of the initial PL intensity is recovered post-bias. While this contrast ratio is, to the best of our knowledge, the highest yet reported for InP-based QDs, there is much room for improvement by mitigating deleterious effects from the immobile QD population, with field-induced screening and varying polarizability due to different dielectric environments resulting in limited PL quenching and slow recovery times post-bias. By evaluating the center wavelength spectral shift over time, it is possible to quantify the various QD populations contributing to the PL signal, and to determine whether increasing the fraction of mobile QDs correlates to improved PL quenching efficiencies and bias recovery time as a predictive performance metric for future device iterations, enabling efficient active electrical modulation of QD PL in optoelectronic devices.

We also show vertically and laterally confined photon modes from stochastic mesas resulting in discrete energetic levels dependent on the degree of lateral confinement in InP/ZnSe/ZnS

QD metallic microcavities. ASE is observed from the fundamental mode of a highly confined, single-mode mesa with a threshold of ~150 μJ/cm^2/pulse. Unlike similar systems employing complex architectures, these metallic cavities are readily incorporated into standard LED architectures by the addition of a conductive bottom semi-transparent metallic electrode to the conventional stack with top metallic electrode. In this way, it is anticipated that electrically injected lasing is achievable through careful three-dimensional optical confinement via microstructured metallic microcavities embedded in an LED architecture. The threshold can be lowered by tuning the vertical distance between metallic mirrors such that the planar cavity mode is resonant with the region of high QD gain - the spectral overlap region between absorption and emission - and increasing the lateral confinement to promote single-mode lasing from the fundamental lateral mode.[209,238]

2.9. SUPPLEMENTARY RESULTS AND DISCUSSION

2.9.1. Experimental Methods

Sample Preparation: All quantum dot (QD) samples used in this work were provided by Samsung Advanced Institute of Technology (SAIT). To prevent oxidation of the thin films and devices over the course of measurements in air, samples were encapsulated under inert atmosphere using a clean glass slide and epoxy. The QDs used in the QD-LED and spectral diffusion study are 5R InP/ZnSe/ZnS (4.3 nm InP core, 3.5 nm ZnSe shell, and 0.15 nm ZnS shell, solution QY: 97%) with oleic acid (OA) ligands exchanged for hexanoic acid (HA) ligands (post ligand exchange composition: 63% of OA replaced by HA) following the procedure described by Won *et al.*[30] The QD-LED architecture used was ITO/PEDOT:PSS (35 nm)/TFB (25 nm)/QD (20 nm)/ZnMgO (40 nm)/ Al (100 nm).[30] The QDs used in the ASE study were 15 mg/mL 3R InP/ZnSe/ZnS similarly fabricated. The 3R QDs were spin-coated under nitrogen with a poly(methyl methacrylate) encapsulant.

Steady-State Photoluminescence and Quenching: All steady-state PL measurements were performed in air with films and devices that were encapsulated in a nitrogen glovebox post fabrication and before measurements. A test fixture connected to a Keithley 2636A source meter was installed using a Nikon Eclipse-Ti inverted microscope fitted with an infinity corrected 50 × dry objective (Nikon L Plan, NA = 0.7). A 405 nm pulsed diode laser (PDL-800 LDH-P-C-405B, 300 ps pulse width) was used for excitation with repetition rate of 80 MHz. The sample photoluminescence (PL) was filtered through a 405 nm dichroic beamsplitter (Nikon DiO1-R405) and the output coupled in free space into a Princeton Instruments Acton 2300i spectrometer (300 g/mm) and Pixis 100b cooled CCD (100 (k-space) x 1340 (wavelength) pixels).

Streak Camera Spectroscopy: Optical spectroscopy was performed using a Nikon Eclipse-Ti inverted microscope fitted with an infinity corrected 50 × dry objective (Nikon L Plan, NA = 0.7). A 405 nm pulsed diode laser (PDL-800 LDH-P-C-405B, 300 ps pulse width) was used for

excitation with repetition rate of 62.5 kHz. The sample emission was filtered through a 405 nm laser dichroic beamsplitter (Nikon DiO1-R405) as well as an additional 450 nm long pass filter and then coupled in free space into a streak camera (Hamamatsu C5680) equipped with a slow speed sweep unit (M5677). The time delay between the laser source and sweep unit was controlled using a digital delay generator (Stanford Research Systems, Inc. Model DG645). Data was collected using the time-correlated single photon counting mode in the HPD-TA 8.4.0 software (Hamamatsu).

Excitation Wavelength-Dependent Photoluminescence: Excitation wavelength-dependent PL measurements were obtained using a variable wavelength NKT Photonics SuperK laser with an AOTF (40 MHz) and 405 nm (40 MHz) diode laser (PDL-800 LDH-P-C-405B). The fluence was adjusted to maintain the same carrier density across excitation energies.

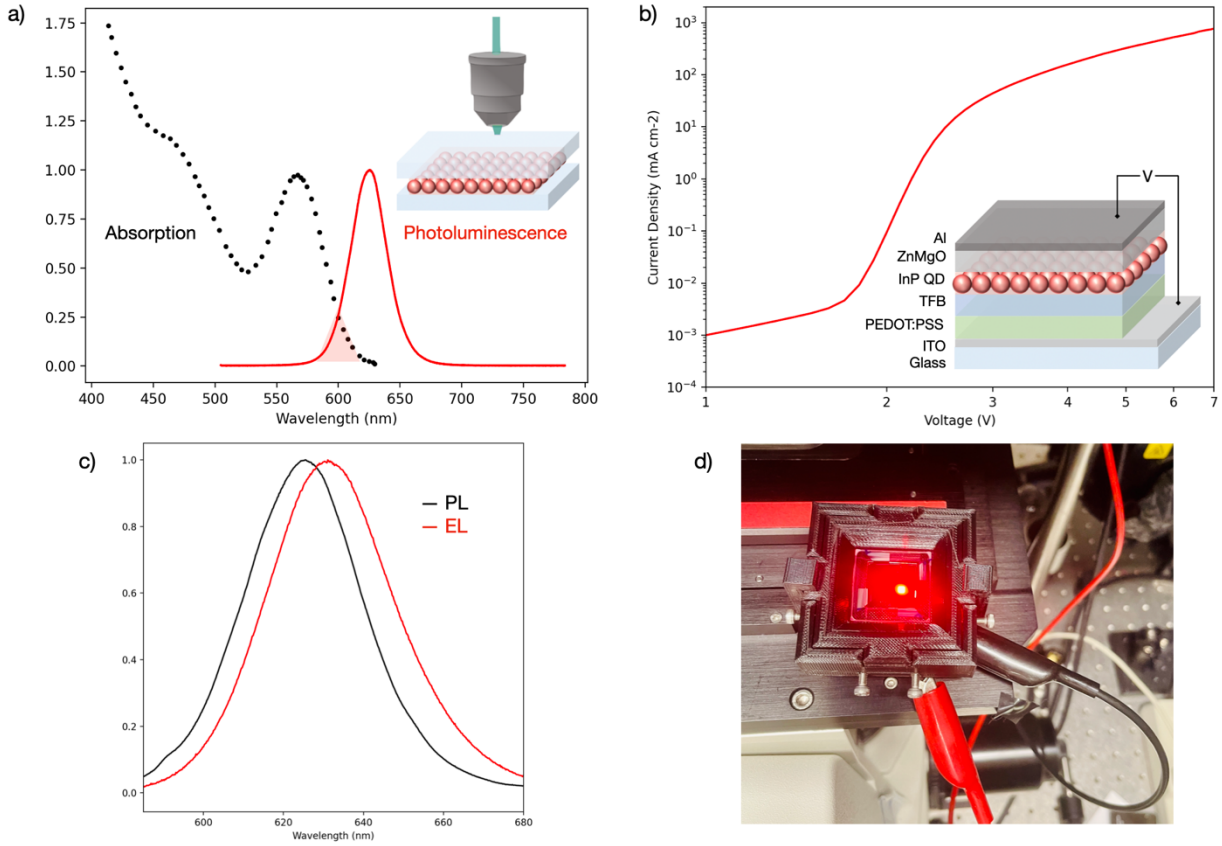

Figure 2.10: (a) Absorption (black trace, InP/ZnSe/ZnS 3R QDs from Won *et al.*[30]) and photoluminescence (red trace) of encapsulated InP QDs. Inset: excitation scheme for glass-encapsulated QD thin film. (b) J-V characteristics of corresponding LED architecture utilizing poly(3,4-ethylenedioxythiophene) polystyrene sulfonate (PEDOT:PSS) as the hole transport layer (HTL), poly(9,9-dioctylfluorene-alt-N-(4-sec-butylphenyl)-diphenylamine) (TFB) as the hole injection layer (HIL), ~15 nm of InP/ZnSe/ZnS QDs (~2 monolayers), ZnMgO as the electron transport layer (ETL), and Al as the top contact. (c) Photoluminescence spectrum (black) and red-shifted electroluminescence spectrum (red). (d) Image of the QD-LED with electroluminescent pad.

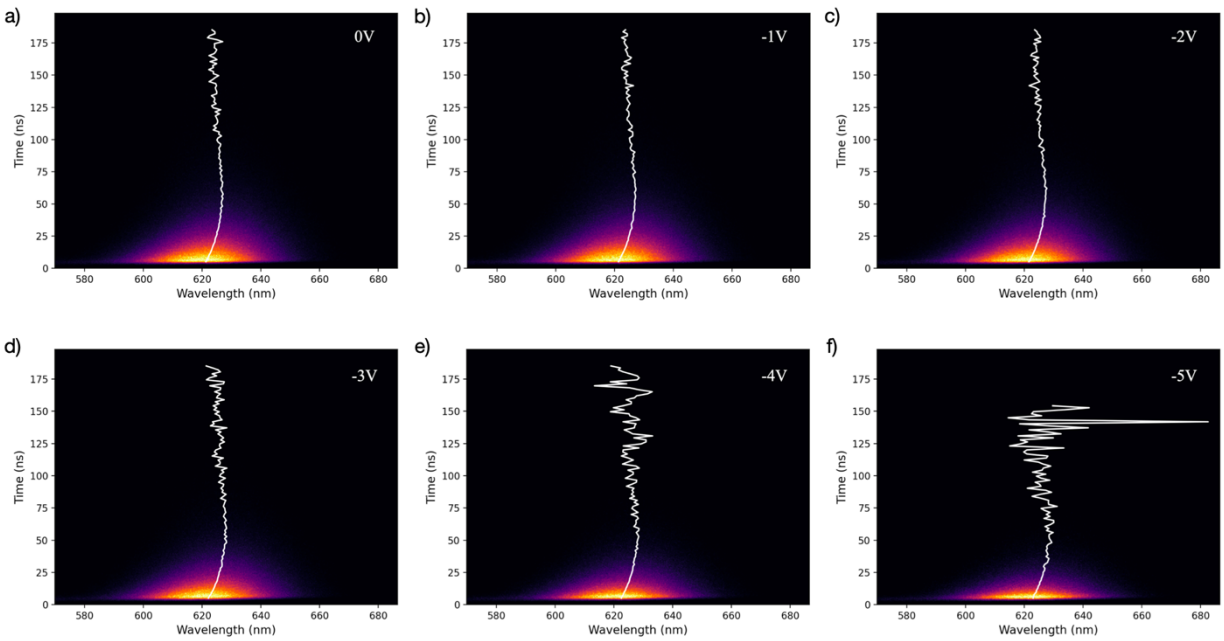

Figure 2.11: (a-f) Spectrally resolved lifetime of QD-LED with applied bias ranging from 0V to -5V, showing decreasing lifetime with increasing reverse bias.

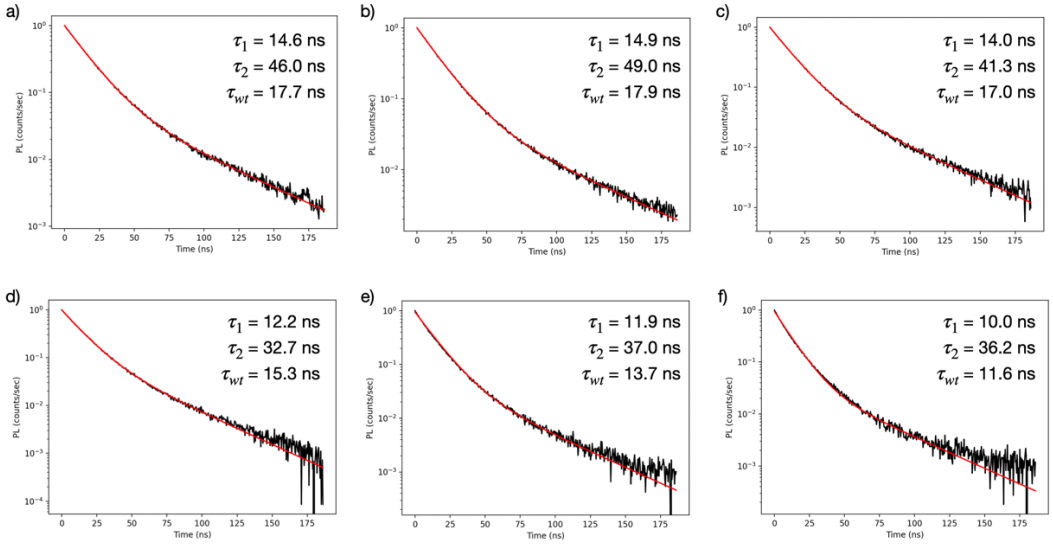

Figure 2.12: (a-f) Spectrally integrated lifetime of QD-LED with applied bias ranging from 0V to -5V, showing decreasing weighted lifetime (τ_{wt}) with increasing reverse bias. The increasing electric field demonstrates a greater effect on the short lifetime (τ_1) component as compared to the long lifetime component (τ_2).

Energy Transfer Dynamics with Photon Recycling: To determine the energy transfer rate from the high energy (donor) spectral region to the low energy (acceptor) spectral region, a set of coupled ODEs was solved to include photon recycling (Eqs. 2.8-2.10). Photon recycling is the ability for a photon emitted following radiative recombination to be waveguided within the film and re-absorbed. The probability of photon escape (P_{esc}) is calculated via Eqs. 2.11-2.12, in which the indices of refraction for the thin film, substrate, and air interface are taken into account, as well as the optical density (OD) at the wavelengths of emission.[11,20,70]

$$\frac{dn_D}{dt} = -k_{rD}n_D - k_{ET}(\lambda)n_D + \frac{c}{n_r}\sum_\lambda \alpha_\lambda \gamma_\lambda \quad 2.8$$

$$\frac{dn_A}{dt} = -k_{rA}n_A + k_{ET}(\lambda)n_A \quad 2.9$$

$$\frac{d\gamma_\lambda}{dt} = -\frac{c}{n_r}\sum_\lambda \alpha_\lambda \gamma_\lambda + k_D n_D(1 - P_{esc}) + k_{rA}n_A(1 - P_{esc}) \quad 2.10$$

where k_D and k_A are the radiative recombination rates of the donor and acceptor exciton, respectively, $k_{ET}(\lambda)$ is the wavelength-dependent energy transfer rate, n_D and n_A are the donor and acceptor site carrier densities, respectively, c is the speed of light, α_λ is the absorption coefficient averaged across emission wavelengths, γ_λ is the photon concentration within the film for a given wavelength due to radiative recombination and photon recycling, n_r is the index of refraction, and P_{esc} the probability of a radiatively recombined photon leaving the film within the escape cone.

$$\eta_t = \frac{\Omega_{esc}}{4\pi}T \approx \frac{n_{r2}^3}{n_{r1}(n_{r1}+n_{r2})^2} \quad 2.11$$

$$P_{esc} = 10^{-\frac{OD_{PL}}{2}} \cdot \left(n_{t,QD-glass} + n_{t,QD-glass} + 10^{-OD_{PL}} \cdot \left(n_{t,QD-glass} - n_{t,QD-glass}\right)\right) \quad 2.12$$

where η_t is the transmission efficiency, Ω_{esc} is the solid angle of photon escape, and n_{rx} is the index of refraction of the given material (QD thin film/glass interface). We estimate the probability of photon escape for QD thin films to be P_{esc} = ~75%.

Energy Transfer Dynamics without Photon Recycling:

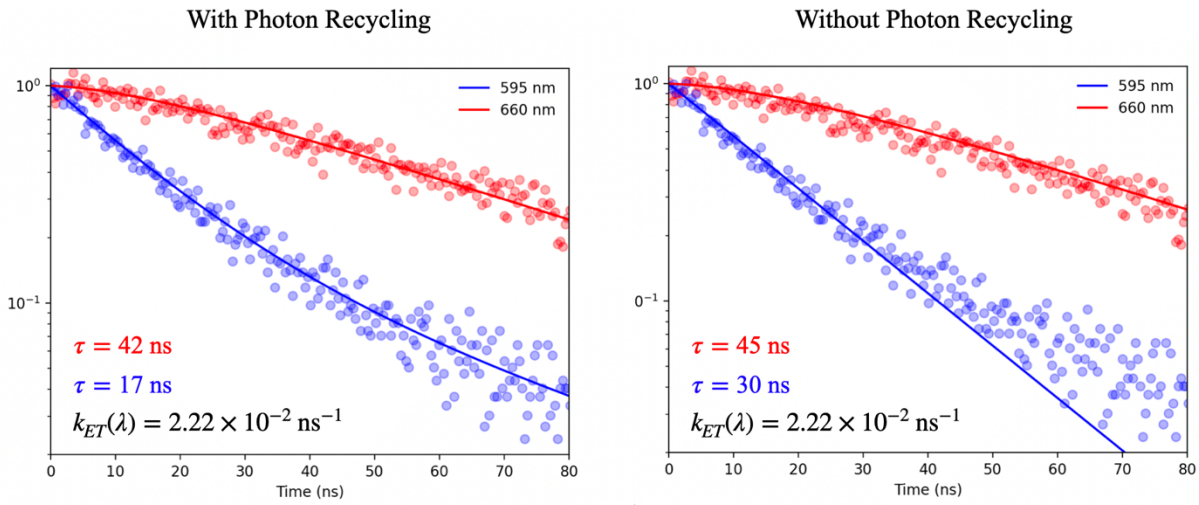

Figure 2.13: (a) QD thin film lifetimes at 595 nm and 660 nm fit with Eq. 2.8-2.10 including photon recycling, demonstrating delayed red emission due to exciton diffusion. (b) QD thin film lifetimes at 595 nm and 660 nm fit with Eq. 2.13-2.14 excluding photon recycling. A long radiative lifetime for 595 nm emission is required when photon recycling is not included.

$$\frac{dn_D}{dt} = -k_{rD}n_D - k_{ET}(\lambda)n_D \qquad 2.13$$

$$\frac{dn_A}{dt} = -k_{rA}n_A + k_{ET}(\lambda)n_A \qquad 2.14$$

where k_D and k_A are the radiative recombination rates of the donor and acceptor exciton, respectively, $k_{ET}(\lambda)$ is the wavelength-dependent energy transfer rate, n_D and n_A are the donor and acceptor site carrier densities, respectively.

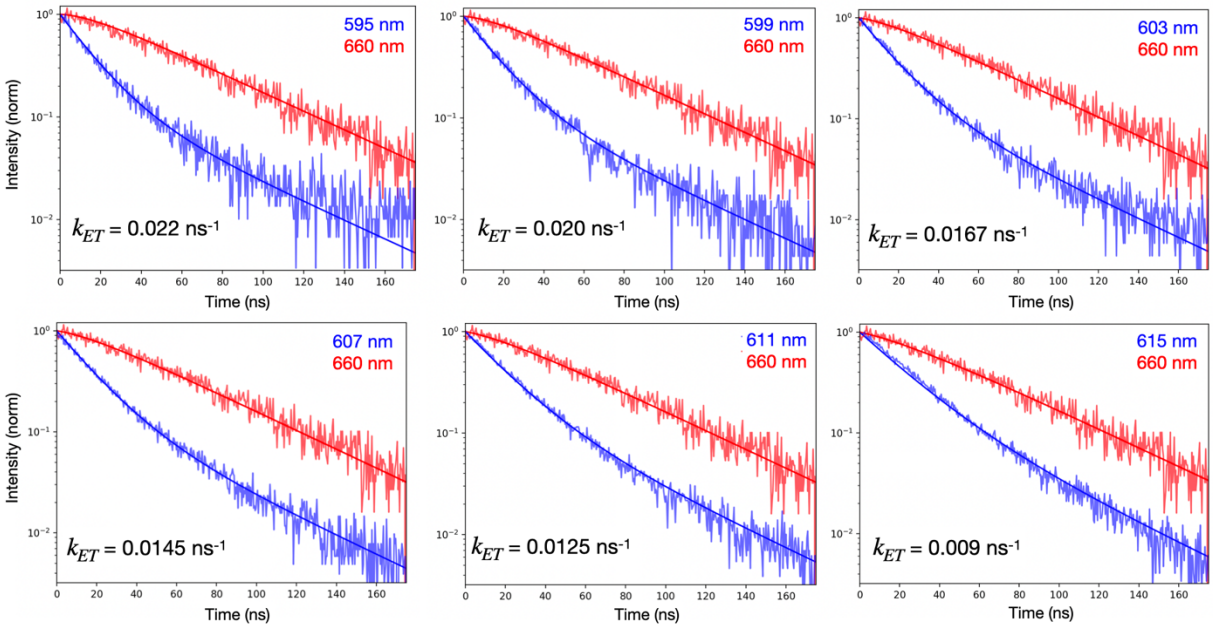

Figure 2.14: (a-k) By varying the donor wavelength from 595 nm to 615 nm and fixing the acceptor wavelength to 660 nm, the wavelength-dependent energy transfer rate ($k_{ET}(\lambda)$) can be fit and quantified, consistent with the density of states due to spectral overlap in the absorption and emission and magnitude of dipole-dipole coupling.[176]

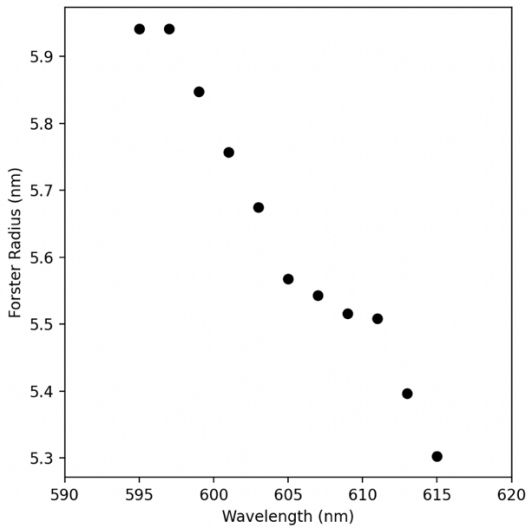

Figure 2.15: The Förster radius calculated from the wavelength-dependent energy transfer rates, ($k_{ET}(\lambda,d)$) = $\tau^{-1}(R_0/d)^6$, yielding an average radius of R_0 = 5.6 nm, which is comparable to similar InP QD systems.[174,177,178]

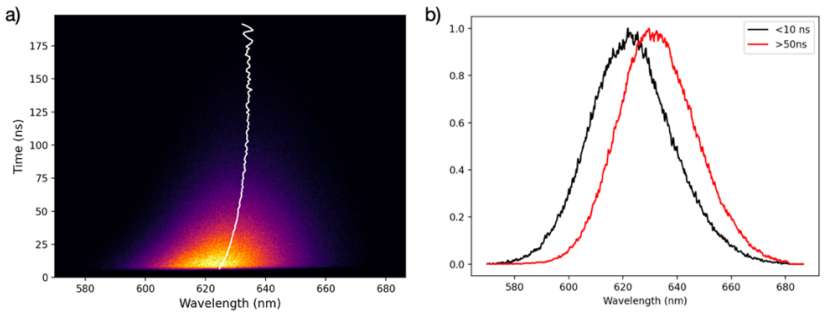

Figure 2.16: (a) Spectrally resolved streak camera lifetime data for the bare QD demonstrating (b) a red-shifting peak as a function of time.

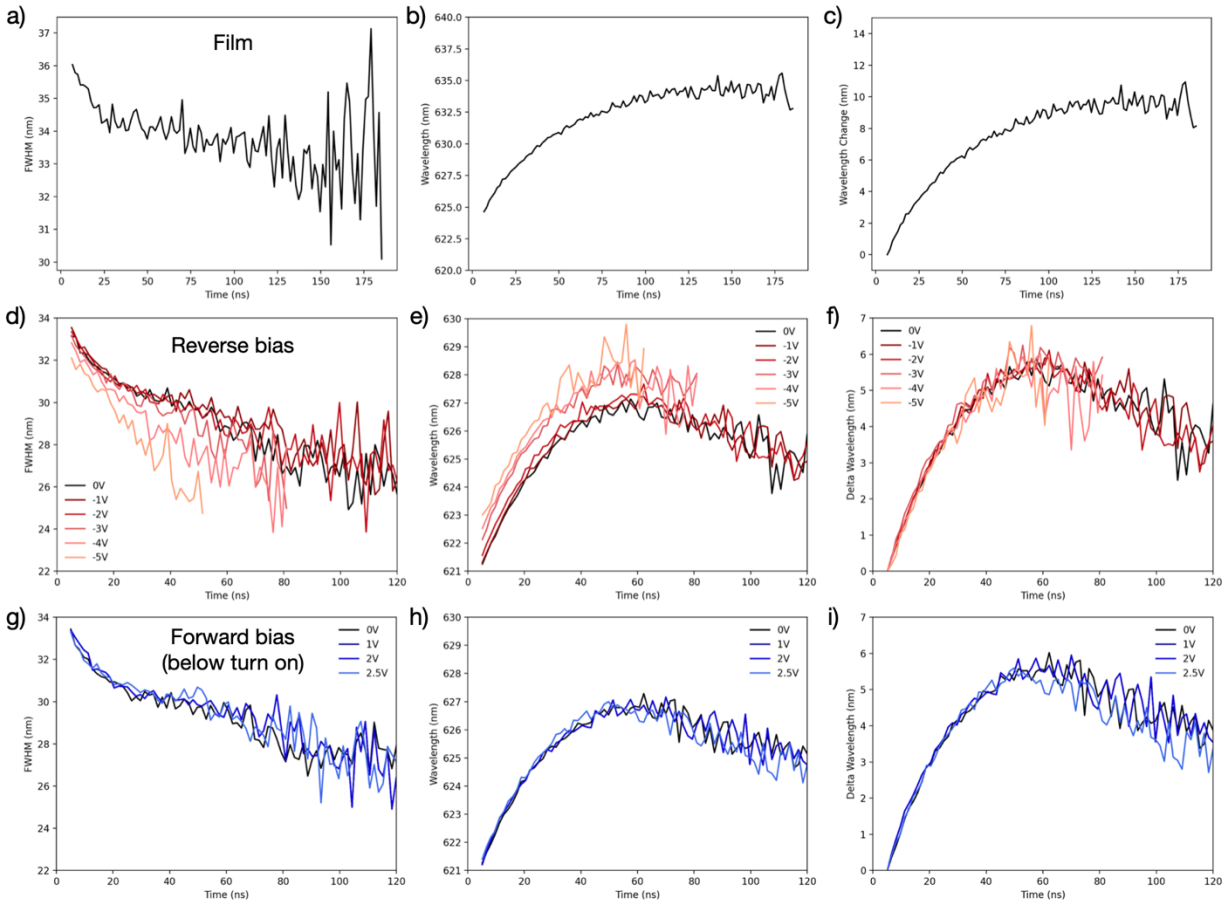

Figure 2.17: FWHM, change in peak wavelength, and absolute peak wavelength over time for (a-c) bare QD thin film, (d-f) QD-LED with increasing reverse bias, and (g-i) QD-LED with increasing low forward bias (below turn-on, 2.5V).

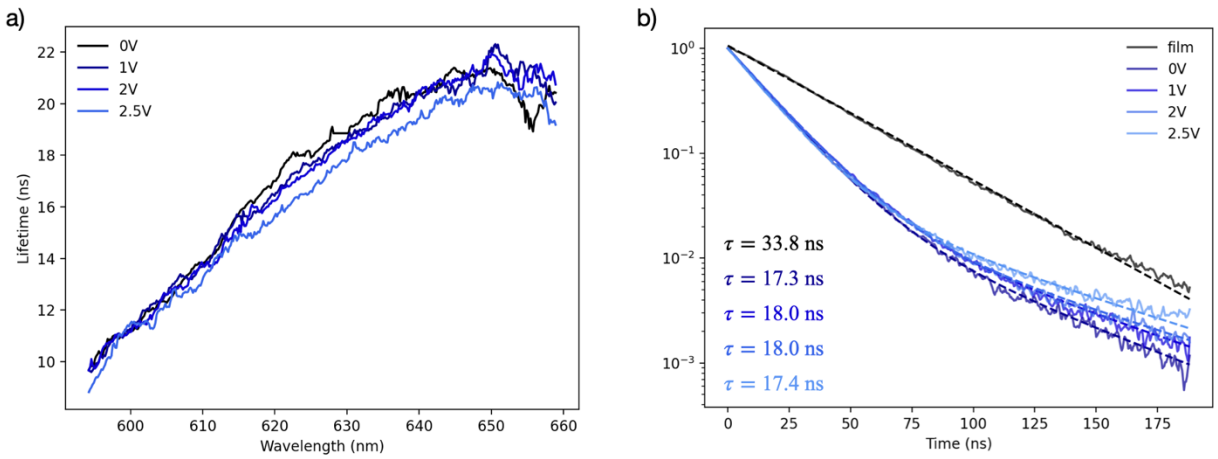

Figure 2.18: (a) Wavelength-resolved lifetimes for QD-LED with increasing low forward bias, and (b) spectrally integrated lifetimes with increasing low forward bias below turn on. By applying a gentle forward bias below turn-on, we resolved an increase in the long lifetime component. In forward bias, excitons still dissociate, but the field injects charges back on themselves, which can be seen as an increase in the long lifetime tail of the TRPL traces. This implies that the second lifetime is due to re-injection of charges that would otherwise dissociate without the electric field pushing them back.

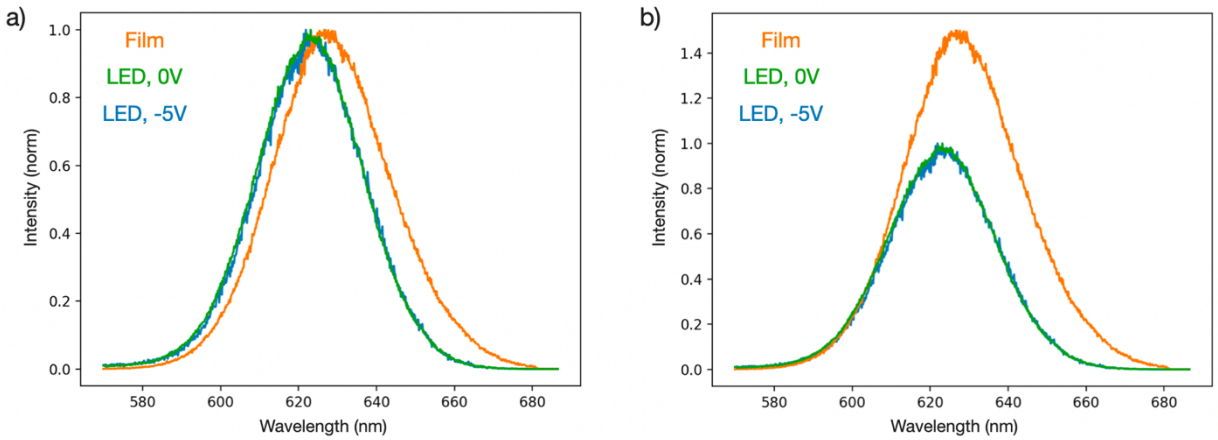

Figure 2.19: PL spectrum of the bare QD thin film (orange trace), QD-LED with no bias applied (green trace), and QD-LED with 5V applied in reverse bias (blue trace) normalized to (a) the peak emission and (b) the high energy slope, showing that the QD-LED emission is a reduced fraction of the thin film emission weighted to the high energy blue spectrum.

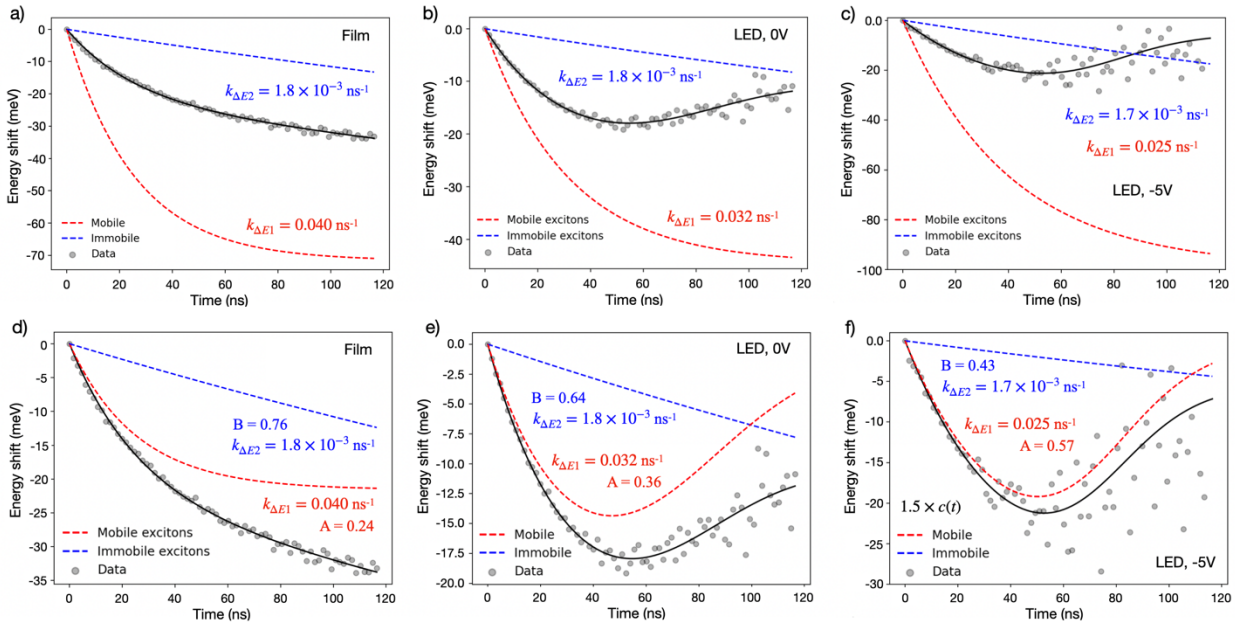

Figure 2.20: For the thin film (a,d; unweighted and weighted subset contributions to the spectral shift, respectively), the experimental data (gray scatter) can be well-reproduced by the summation (black trace) of two fitted populations representing the fast mobile exciton population contribution to the overall spectral shift (red dashed trace) and slow immobile exciton contribution to the overall spectral shift (blue dashed trace). For the QD-LED with no bias (b,c; unweighted and weighted + Fermi-Dirac subset contributions to the spectral shift, respectively), the experimental data (gray scatter) is well-reproduced by the summation (black trace) of both the mobile exciton contribution to the spectral shift (red dashed trace, modulated by a Fermi-Dirac distribution ($c(t)$) as mobile excitons are depleted) and the slow immobile exciton contribution to the spectral shift (blue dashed trace). For the QD-LED with 5V applied in reverse bias (c,d; unweighted and weighted + Fermi-Dirac subset contributions to the spectral shift, respectively), the experimental data (gray scatter) is again well-reproduced by the summation (black trace) of both the mobile exciton contribution to the spectral shift (red dashed trace, modulated by a Fermi-Dirac distribution (1.5 x $c(t)$) as mobile excitons are depleted) and the slow immobile exciton contribution to the spectral shift (blue dashed trace).

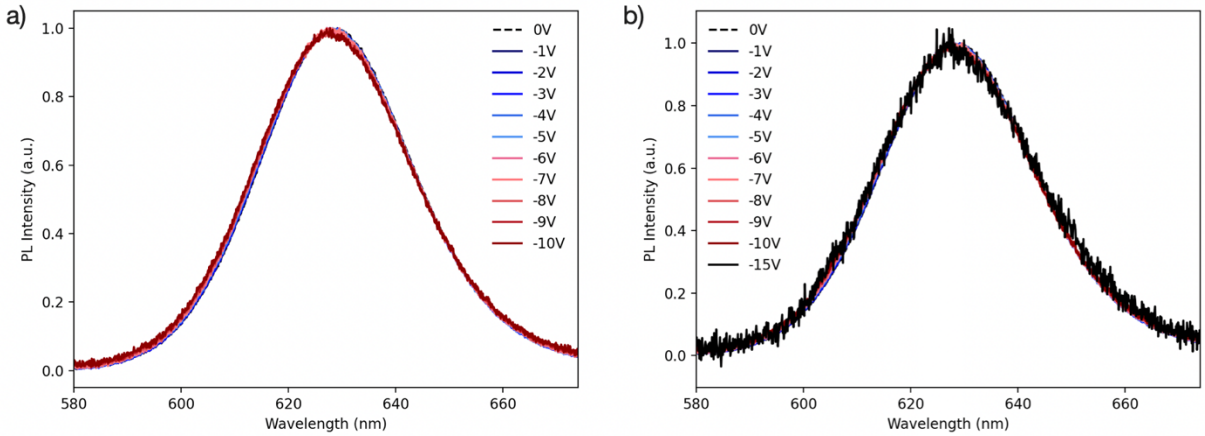

Figure 2.21: QD-LED photoluminescence (PL) intensity with increasing applied reverse bias at 520 nm excitation, showing (a) no quantum-confined Stark effect down to -10V and (b) -15V.

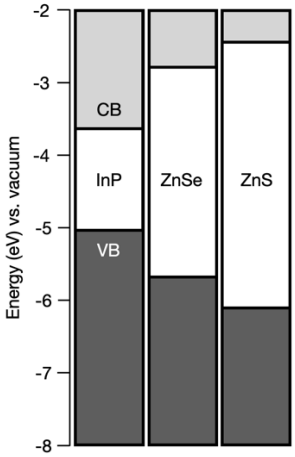

Figure 2.22: Band alignment for InP core, ZnSe inner shell, and ZnS outer shell Type I QD structure.[199–201]

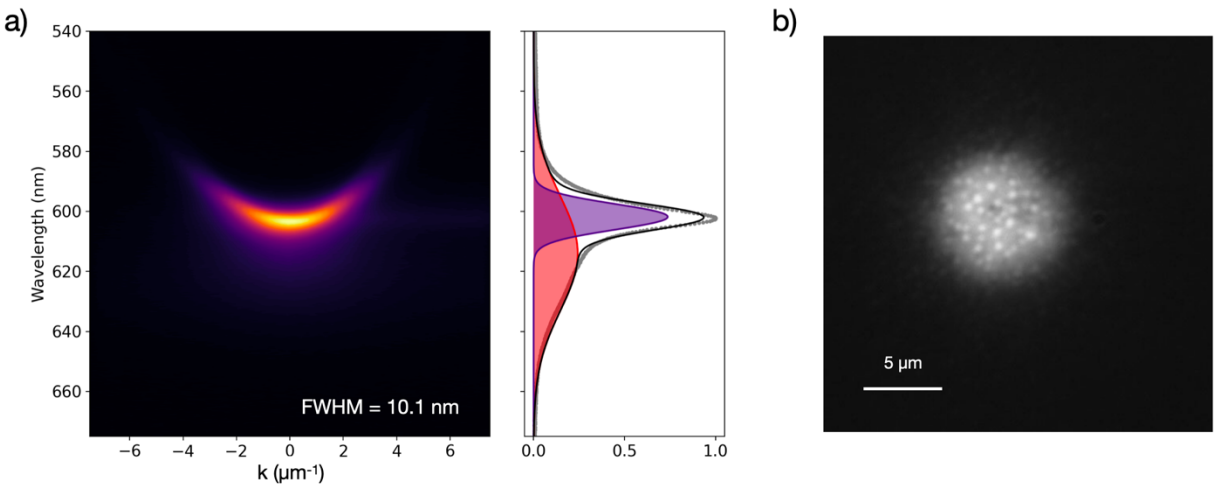

Figure 2.23: (a) Vertical cavity mode in non-mesa region with QD photoluminescence (PL) leaking through the mode at $k_{||} = 0$, $\lambda = 608$ nm. Side panel: k-space-integrated PL. (b) Corresponding real space PL image showing the absence of the localized mode due to lateral confinement in mesa regions.

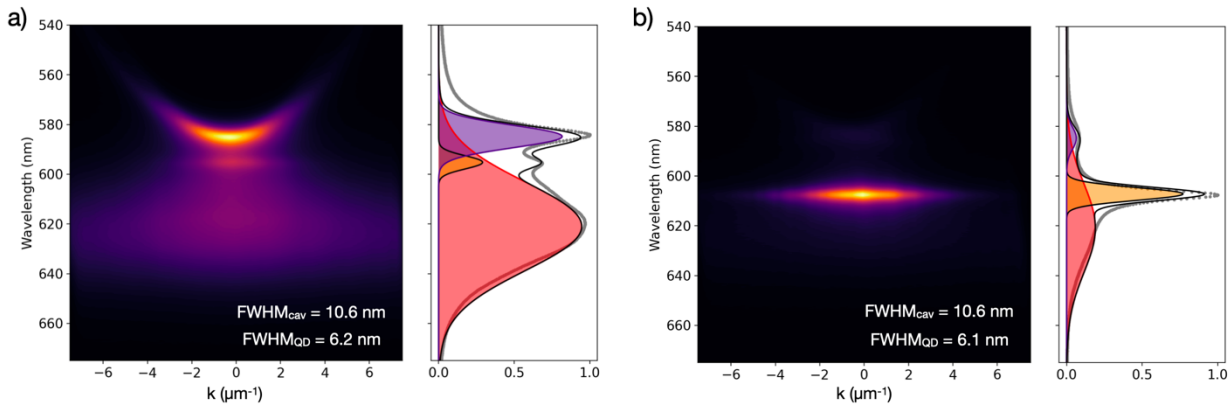

Figure 2.24: (a) Single-mode laterally confined mesa demonstrating weak confinement likely due to defects in the mesa structures such as incomplete coverage of Ag by the thermally evaporated top mirror. Side panel: k-space-integrated PL. (b) Single-mode laterally confined mesa showing strong confinement. Side panel: k-space-integrated PL.

2.10. CHAPTER-SPECIFIC ACKNOWLEDGEMENTS

This material is based upon work supported by the National Science Foundation Graduate Research Fellowship under Grant No. (1122374). We thank Mayuran Saravanapavanantham for valuable discussions and insights, Rich Swartwout for LED test fixture design, and Alex E.K. Kaplan for valuable discussion regarding QD microcavity dynamics.

PART III.
STRONG LIGHT-MATTER INTERACTIONS IN 2D PEROVSKITE MICROCAVITIES

CHAPTER 3

3. MICROCAVITY EXCITON-POLARITONS: TOWARDS EFFICIENT POLARITON RELAXATION AND STRONG COUPLING-MEDIATED TUNABLE KINETICS

3.1. OVERVIEW

State-of-the-art hybrid perovskites have demonstrated excellent functionality in photovoltaics and light-emitting applications and have emerged as a promising material candidate for exciton-polariton (polariton) optoelectronics. In the strong light-matter coupling regime, polariton formation and Bose-Einstein condensation (BEC) have been demonstrated at room-temperature in several perovskite formulations. Thermodynamically, low-threshold BEC requires efficient scattering to the polariton energy dispersion minimum at $k_{//} = 0$, and many applications demand precise control of polariton interactions. Thus far, the primary mechanisms by which polaritons relax in perovskites remains unclear.

In this work, we perform temperature-dependent measurements of polaritons in low-dimensional hybrid perovskite $\lambda/2$ microcavities and demonstrate high light-matter coupling strengths with a Rabi splitting of $\hbar\Omega_{Rabi}$ = 260 ±5 meV. By embedding the perovskite active layer near the optical field antinode of a wedged microcavity, we are able to change the Hopfield coefficients by moving the optical excitation along the wedge length and thus tune the strength of the primary polariton relaxation mechanisms in this material for the first time. We observe the polariton bottleneck regime and show that it can be overcome by harnessing the interplay between the different excitonic species whose corresponding dynamics are modified by strong coupling. We demonstrate the dependence of the bottleneck suppression on cavity detuning and achieve efficient relaxation to $k_{//} = 0$ at cryogenic temperatures. This new understanding contributes to the design of polariton microcavities that could be used in future demonstrations

of BEC benefiting from efficient, material-specific relaxation pathways and intracavity pumping schemes from thermally brightened excitonic species.

Portions of this chapter are reprinted with permission from:

Laitz, M., Kaplan, A.E.K., Deschamps, J., Barotov, U., Proppe, A., García-Benito, I., Osherov, A., Grancini G., deQuilettes, D.W.*, Nelson, K.A., Bawendi, M., and Bulović, V.*, arXiv:2203.13816 (2022). *Co-corresponding.

Exciton-polaritons (polaritons) are formed in optical microcavities in the strong coupling regime between material excitons and cavity photons. This quantum superposition results in a hybrid state of light and matter, and the formation of a bosonic quasi-particle.[39–41] Polaritons can be modified to adjust the photonic/excitonic character, so that, even when tuned to have a large photonic fraction, polaritons can interact due to the non-zero excitonic component. Such interactions provide several advantages over purely photonic systems in designing logic elements in integrated circuits, such as facile cascadability[240] and large nonlinearities due to the polariton matter component,[241] creating the potential for engineering fast, low-power optical transistors.[45,242] These properties also establish opportunities for studying Bose-Einstein condensation,[48] quantum vortices,[46] and low-threshold polariton lasing[47] for quantum photonic technologies[243] and next-generation qubits.[244–248] Additionally, recent reports utilizing strong coupling to modify electronic structure and energy transfer rates show great promise for the polariton-mediated tuning of chemical reactivity and photophysics.[249] The possibility of improving energy conversion processes without synthetic changes to the chemical system allows for external modification of kinetics, energy, and electronic and vibrational transitions[250,251] by the precise engineering and control of strongly coupled device structures.[252]

To date, room-temperature polaritons have been sustained in inorganic materials (e.g., GaN, ZnO), organics (e.g., J-aggregates), transition metal dichalcogenides (e.g., WS_2, WSe_2), and perovskites (e.g., $CsPbBr_3$, $CsPbCl_3$, $(C_6H_5(CH_2)_2NH_3)_2PbI_4$).[253] In perovskites, room-temperature polariton formation,[254–260] manipulation,[261,262] lasing,[263,264] and condensation[62,241,265–273] have been shown, in which perovskite single crystals, exfoliated flakes, platelets, or thin films are embedded in microcavities typically comprised of either a single distributed Bragg reflector (DBR) and metallic mirror or two high quality DBRs. Although these demonstrations have shown the exceptional potential of perovskite materials for polaritonics, most optoelectronic applications rely on careful control of polariton momentum. Currently, for perovskites, the scattering and relaxation mechanisms that lead to changes in polariton energy and momentum

are not well understood. Additionally, there have been very few demonstrations of polariton lasing and condensation in quasi-two-dimensional (herein referred to as 2D) perovskites, which is believed to result from the low room-temperature photoluminescence quantum efficiency (PLQE), low quality factor (Q) cavities leading to short polariton lifetimes, and high exciton-exciton annihilation rates.[253,273–276] Therefore, a deeper understanding of polariton scattering and relaxation mechanisms is needed in order to fully harness polariton utility for a wide range of applications.

Despite these challenges, 2D perovskites remain one of the most promising materials for room-temperature polaritonic devices due to optimal optical properties, chemical versatility, and facile deposition and fabrication schemes. 2D perovskites function as self-assembled quantum well structures, and can be formed as single crystals or polycrystalline thin films. The smaller band gap inorganic monolayers (e.g. PbI_4), where the excitons are confined, act as the quantum well and the larger energy gap organic spacers serve as potential barriers.[277–280] The low Stokes shift, high absorption coefficient, narrow emission, controllable dipole orientation,[260,281,282] and high exciton binding energy (100-500 meV)[68,283] render these materials excellent candidates for facilely-fabricated room-temperature polaritonic devices.[253]

Here we explore strong coupling in a test-bed 2D system based on phenethylammonium lead iodide perovskite ($(C_6H_5(CH_2)_2NH_3)_2PbI_4$ (PEA_2PbI_4) thin films embedded in a wedged microcavity and demonstrate, to the best of our knowledge, a record room-temperature Rabi splitting for PEA_2PbI_4 of $\hbar\Omega_{Rabi}$ = 260 ± 5 meV. This figure of merit denotes the magnitude of the photon-exciton coupling,[284] and larger Rabi splittings lead to reduced BEC thresholds as demonstrated by nonequilibrium models[285] and experimental work in organic polaritons.[286] We probe polariton formation by Fourier spectroscopy to image momentum (in-plane $k_{||}$) space via reflectivity and photoluminescence (PL) measurements. We show the emergence of a polariton bottleneck for negative cavity detunings ($E_{cav} - E_{exc} < 0$), where E_{cav} is the energy of the microcavity photon and E_{exc} is the energy of the perovskite thin film exciton, and explore temperature-dependent polariton photophysics, revealing, for the first time, the role of and

interplay between reservoir excitons, phonons, and cavity polaritons for efficient polariton relaxation in these materials. We measure the significant brightening of the dark excitons in PEA_2PbI_4 perovskite polariton structures at cryogenic temperatures, and suggest their role together with the role of biexcitons and resonant longitudinal optical (LO) phonon interactions as they jointly mediate exciton-polariton relaxation to $k_{//} = 0$. Additionally, we show that perovskite excited states can be tuned via strong coupling to achieve new dynamics (i.e. kinetic rates). These insights inform microcavity and polariton dispersion design to harness material-specific, efficient polariton relaxation pathways to $k_{//} = 0$ enabling future measurements of low-threshold Bose-Einstein condensation in 2D perovskites.[242,287]

3.3. ROOM-TEMPERATURE STRONG COUPLING IN 2D PEROVSKITE MICROCAVITIES

We realize room-temperature polaritons by fabricating $\lambda/2$ metallic microcavities with a spin-cast PEA_2PbI_4 active layer possessing a high degree of crystallinity resembling single crystals (Figure 3.6).[288] The strongly-coupled system achieves a Rabi splitting of Ω_{Rabi} = 260 meV, which is, to the best of our knowledge, the highest reported coupling strength in a PEA_2PbI_4 planar microcavity.[253] High-quality epitaxially-grown GaAs quantum well microcavities have previously been fabricated in a wedged geometry, which yields a spatially-varying cavity length that allows for the probing of multiple cavity detunings to investigate polaritons with varying photonic/excitonic character.[289,290] By engineering the spin-coating speeds in our solution-processed cavity layers, we achieve a radial wedged cavity, with monotonically increasing cavity length from center to substrate edge which allows for facile changes to the polariton detuning (~30 meV/mm cavity mode gradient, as compared to 13 meV/mm in previously demonstrated epitaxially-grown GaAs quantum well wedged cavities[291]). The reflectivity and photoluminescence dispersions are probed by Fourier spectroscopy, in which the emission of the lower polariton branch (LPB) is observed in photoluminescence and both the upper (UPB) and

lower polariton branches can be resolved in reflectivity (Figure 3.1a-c). To verify minimal change in the polariton coupling strength as a function of position on the cavity, the upper and lower polariton branches are extracted from reflectivity measurements and fit at each detuning with Eq. 3.1,[292] showing that, for each position, the coupling strength remains virtually constant as the cavity mode shifts to lower energies (Figure 3.1e, $\hbar\Omega_{Rabi}$ = 260 meV $\pm$ 5 meV).

$$E_{LP,UP}(k_{||}) = \frac{1}{2}\left[E_{exc} + E_{cav}(k_{||}) \pm \sqrt{4g_0^2 + \left(E_{exc} - E_{cav}(k_{||})\right)^2}\right] \quad 3.1$$

where $E_{LP,UP}(k_{||})$ corresponds to the upper and lower polariton branch energies as a function of $k_{//}$, E_{exc} is the exciton energy (considered dispersionless over $k_{//}$ values measured), $E_{cav}(k_{||})$ is the uncoupled cavity energy as a function of $k_{//}$, and $2g_0 = \hbar\Omega_{\text{Rabi}}$ is the normal mode splitting, or Rabi splitting as in a single-atom microcavity system.[41]

The Hopfield coefficients for each dispersion quantify the excitonic and photonic fraction as a function of $k_{//}$ (Eq. 3.2), with the most excitonic detuning possessing >50% excitonic character at $k_{//}$ = 0 and the most photonic detuning possessing >50% photonic character at $k_{//}$ = 0 (Figure 3.1a-c and Figure 3.7, lower panels).

$$|X_k|^2, |C_k|^2 = \frac{1}{2}\left(1 \pm \frac{\Delta E(k_{||})}{\sqrt{\Delta E(k_{||})^2 + 4g_0^2}}\right) \quad 3.2$$

where $|X_k|^2$ and $|C_k|^2$ are the excitonic and photonic Hopfield coefficients, respectively.

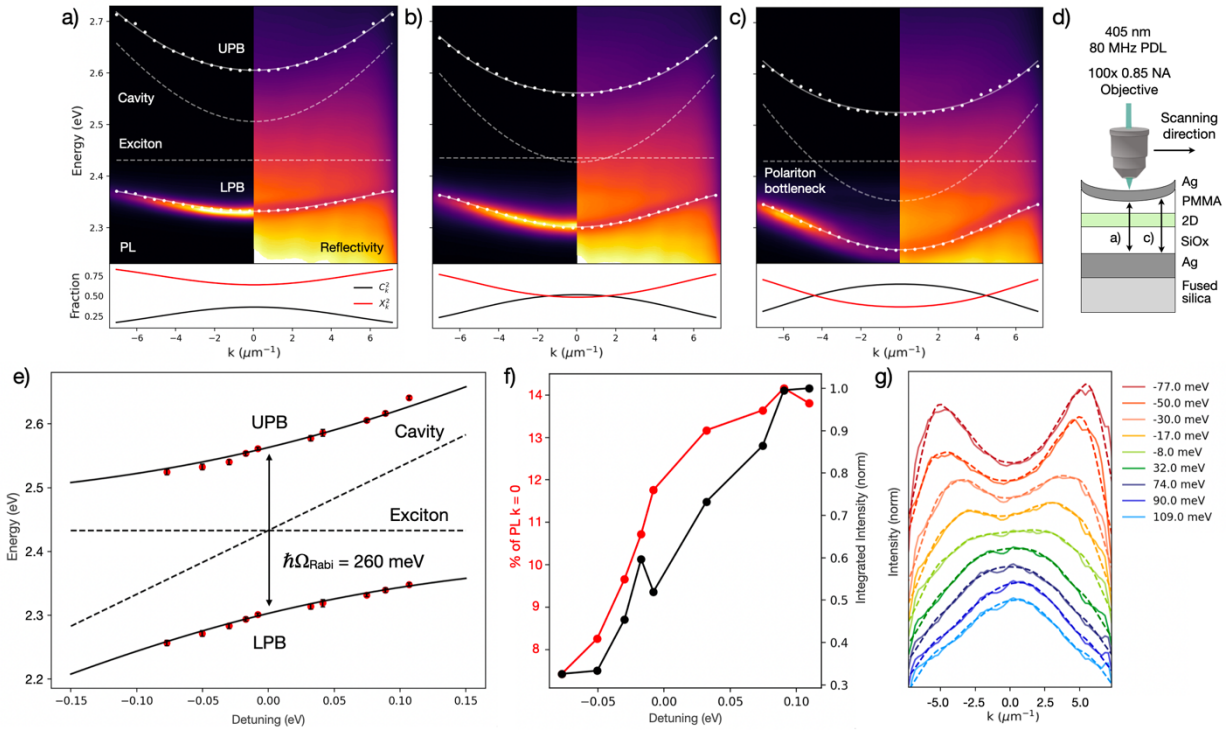

Figure 3.1: Exciton-polariton photoluminescence (PL) (left) and reflectivity (right) dispersions with increasing cavity length from (a) higher cavity mode energy to (c) lower cavity mode energy as shown schematically in (d). As the cavity shifts to lower energies and the polariton dispersion becomes increasingly photonic (c), the bottleneck effect emerges with the greatest emission intensity at high $k_{||}$ values. The upper and lower polariton branches are extracted from reflectivity minima (white dotted line) and fitted (white solid line) using Eq. 3.1 (fitted cavity and exciton energies shown, white dashed line) with a Rabi splitting of $\hbar\Omega_{\text{Rabi}}$ = 260 meV. (a-c, lower figures) Hopfield coefficients for cavity detunings (photonic fraction C_k^2, black trace; excitonic fraction X_k^2, red trace) ranging from (a) excitonic to (c) photonic depicting the light-matter characteristics of the generated polaritons as a function of $k_{||}$ (Eq. 3.2). (e) Experimental (red dots) and theoretical (black traces) upper and lower polariton branch energies at $k_{||}$ = 0 with Ω_{Rabi} = 260 meV. Dashed black traces correspond to the exciton energy and cavity energy changing with cavity length. (f) As the cavity energy decreases and the dispersion becomes more negatively detuned, the photoluminescence (PL) distribution shifts to higher $k_{||}$, resulting in a decrease in the fraction of PL within $k_{||}$ = 0 ± 0.2 um^{-1} (red trace). Integrated PL intensity as a function of increasingly negative detuning exhibits inhibited emission (black trace). (g) The energy-integrated PL spectra reveal the re-distribution of the maximum PL intensity to higher $k_{||}$ with increasingly photonic detunings (raw data, solid trace; smoothed data, dashed trace).

As the cavity mode shifts to lower energy and the polariton dispersion becomes more photonically detuned, the emission distribution shifts from the maximum PL intensity at $k_{||} = 0$ to higher $k_{||}$ (Figure 3.1f,g), known as the polariton bottleneck regime, a well-studied effect in inorganic and organic polariton systems.[293–300]

The bottleneck effect is a manifestation of the reduced scattering rate of high $k_{||}$ polaritons as they relax down the LPB. This effect is a combined consequence of the decreased excitonic character as polaritons move down their dispersion curve, which makes exciton-phonon scattering less efficient, and of the reduced density of states as the polariton effective mass decreases, that is, as the LPB curvature increases. Additionally, an increase in photonic character is accompanied by an increase in radiative rates, which leads to the depletion of the polariton population near $k_{||} = 0$ if the scattering rates into nearby states is too low.[293–295] As the overall excitonic character of polaritons diminishes, and as the LPB curvature increases, the bottleneck effect becomes more pronounced for negative (photonic) detunings. The polariton lifetime at negative detunings is longer than at positive detunings due to the increase in excitonic character of polaritons above the bottleneck region, consistent with our measurements in this system (Figure 3.8).

The polariton bottleneck effect has been shown to be thermally activated – by decreasing the system temperature, exciton-phonon scattering is similarly reduced, resulting in the emergence of the bottleneck even for polaritons with mostly excitonic character.[296,297] This phenomenon is difficult to study in systems that require cyrogenic temperatures to achieve strong coupling (e.g., GaAs heterostructures), but room-temperature strong coupling systems present an opportunity to investigate the role of phonon scattering in polariton relaxation by lowering the temperature. Thus, we are able to explore the impact of LO-phonon-exciton Fröhlich interactions and acoustic phonon-induced deformation potential mechanisms that can accelerate or hamper key polariton scattering pathways.[297]

By reducing the microcavity temperature and carefully controlling the cavity length along the cavity wedge to modulate the detuning, we probe the emergence of the bottleneck regime for polaritons with varying excitonic/photonic character and thus changing energy differences between the exciton reservoir and the bottom of the lower polariton branch. Additionally, the impact of the magnitude of photon-exciton coupling on temperature-dependent scattering mechanisms is investigated by modifying the Rabi splitting to determine the contribution of enhanced coupling strength on polariton relaxation toward $k_{||} = 0$.

To begin deconvoluting these various relaxation mechanisms, we explore the temperature-dependent k-space PL distribution for two coupling strengths: $\hbar\Omega_{Rabi}$ = 175 meV (Figure 3.2) and $\hbar\Omega_{Rabi}$ = 260 meV (Figure 3.9) by changing the perovskite active layer thickness (i.e. number of oscillators N, $\hbar\Omega_{Rabi} \propto \sqrt{N}$).[301–303] Additionally, temperature cycles are performed on two detunings (Δ = +28 meV and +45 meV). For both positive cavity detunings with emission from $k_{||} = 0$ at 295 K, we probe the emergence of the bottleneck region with decreasing temperature due to the reduction of phonon scattering pathways.

We begin to observe the redistribution of PL to high $k_{||}$ at ~200 K, with the most pronounced bottleneck at ~140 K (Figure 3.2). Unexpectedly, the PL distribution in k-space for Δ = +28 meV re-centers at $k_{||} = 0$ for temperatures below 15 K, and, for Δ = +45 meV, re-centers to $k_{||} = 0$ for temperatures below 60 K (Figure 3.2d,e). For both detunings, we see the appearance and suppression of the bottleneck effect, with PL moving away from $k_{||} = 0$ when cooling down to 140 K and shifting back to $k_{||} = 0$ when cooling down to 4 K (Figure 3.2f, Figure 3.9f). To understand this behavior, we note several key factors at play with decreasing temperature, both for the perovskite film system in isolation and for the strongly coupled microcavity system.

If there are temperature-dependent changes in the bare excitonic thin film outside of the microcavity (e.g., structural changes, bandgap and concomitant emission energy shifts, PLQE changes), these effects could manifest as temperature-dependent alterations in the polariton

density and therefore polariton-polariton scattering rates. For the bare 2D film, we confirm that there are no significant changes in the perovskite structure (i.e. phase change) as a function of temperature (Figure 3.10), and, as previously shown in PEA_2PbI_4 2D perovskites, we observe a redshift in the PL with decreasing temperature which is consistent with the Varshni effect.[304–306] Additionally, we quantify a ~100-fold increase in PLQE, from ~0.7% at 295 K (consistent with other reports)[307] to between 30% and 40% as the temperature drops from 180 K to 40 K to 77% at 4 K (Figure 3.11). While the increase in film PLQE as the temperature decreases serves to increase the polariton population and thus should enhance polariton-polariton scattering, this effect is likely not the dominant relaxation mechanism for $k_{||} = 0$ emission at 4 K, as we see very little change to the *k*-space PL distribution as a function of excitation power spanning five orders of magnitude (Figure 3.12-Figure 3.13). If enhanced polariton-polariton scattering due to the increase in material PLQE were the dominant mechanism for relaxation to $k_{||} = 0$ at low temperature, we would expect the re-emergence of the bottleneck effect at sufficiently low excitation powers, or low polariton densities, which we do not observe. Even at low fluences (~30 nJ/cm^2/pulse), efficient relaxation to $k_{||} = 0$ at 4 K is achieved.

For the microcavity system, the exciton PL redshift (~5 nm), combined with the thermal contraction of the microcavity due to cavity cooling (primarily due to the shrinking of the optically inert organic spacer layer) results in an overall blue-shift of the cavity energy (~3 nm, Figure 3.14), which leads to progressive increases in the detuning with decreasing temperature, from Δ = +28 meV at 295 K to Δ = +68 meV at 4 K, or from 70% excitonic character to 80% excitonic character (Figure 3.2g). This change in detuning alone is not responsible for the re-centering of the PL distribution around $k_{||} = 0$, as the bottleneck effect and its suppression are observed even when fixing the detuning by moving to lower energy cavity mode regions at lower temperatures on the radial wedged cavity (Figure 3.15).

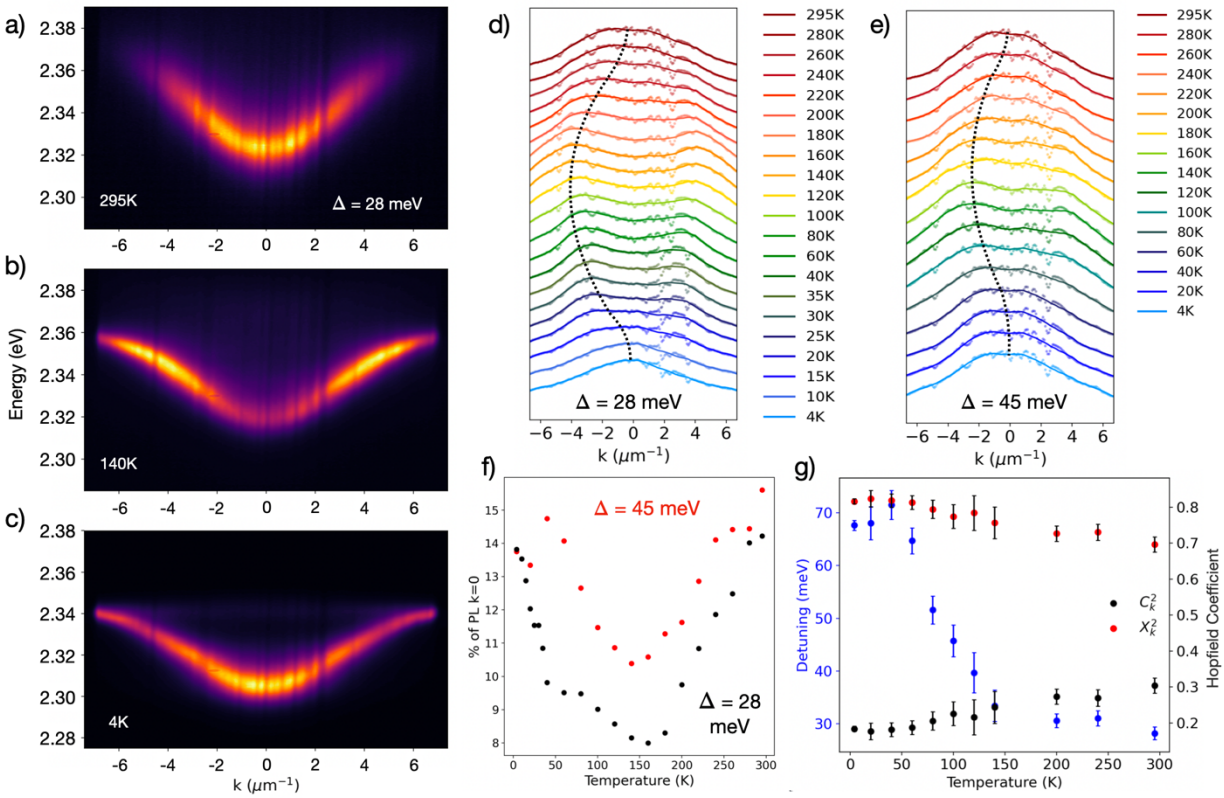

Figure 3.2: (a-c) Lower polariton branch (LPB) photoluminescence (PL) for Δ = +28 meV cavity detuning as a function of temperature revealing (e) the shifting of the maximum PL intensity to higher $k_{||}$ at intermediate temperatures before returning to $k_{||}$ = 0 at 4 K. (d-f) The temperature-dependence of the energy-integrated PL was monitored for two detunings established at room temperature ($\hbar\Omega_{\text{Rabi}}$ = 175 meV, Δ = +28 meV and +45 meV), with both detunings showing bottlenecked PL at intermediate temperatures and emission from $k_{||}$ = 0 at sufficiently low temperatures (raw data, dashed trace; smoothed data, solid trace; peak PL trend to guide the eye, symmetric about $k_{||}$ = 0, dotted trace). (g) Cavity detuning and Hopfield coefficients as a function of temperature for Δ = +28 meV, revealing that the detuning becomes more positive as temperature decreases with polaritons shifting from 70% excitonic at 295K to 80% excitonic at 4 K.

The luminescence spectrum of the uncoupled, bare 2D perovskite film at room temperature (295 K) shows a dominant bright exciton (X) peak at 2.370 eV (Figure 3.3a). As the film is cooled, the PL monotonically red-shifts, reaching a center energy of 2.348 eV at 4 K (Figure 3.16).

A second, low-energy peak emerges below ~140 K, which is consistent with reports of a dark exciton (DX) with center energy 2.323 eV at 4 K (Figure 3.3a and Figure 3.16), and has been shown to increase in PL intensity in the presence of an external magnetic field.[308–310] Emission of the DX state in the absence of the magnetic field has also been observed due to spin-orbit coupling and dipole mixing with the bright exciton (X).[309,310] Though the films possess a high degree of crystallinity (Figure 3.10), we are unable to resolve the four states previously reported within the fine structure for the bright and dark excitons due to PL broadening resulting from disorder of the polycrystalline thin film.[308–313]

Below 80 K, we observe a third, low energy peak below the DX (center energy 2.305 eV at 4 K, Figure 3.16), which can be attributed to either electron-phonon coupling, self-trapped excitons, and/or to biexcitons (XX) (Figure 3.3a).[305,308–310,312,313] Given earlier reports, we attribute this third, low energy peak in the PL to the biexciton, for which we calculate a biexciton binding energy of $\Delta E_{XX} = 43$ meV, utilizing PL as a proxy for state energies and relative energies, in agreement with Thouin *et al.*[314] Here, the biexciton binding energy is defined as the energy difference between two free X excitons and the bound biexciton state (XX), namely $\Delta E_{XX} = 2 \cdot E_X - E_{XX}$. The first step of biexciton radiative recombination results in an emitted photon with energy $E_X - \Delta E_{XX}$, which is then followed by the emission of the remaining free exciton (X) with energy E_X. The assignment of this peak to the biexciton species is also consistent with other reports indicating a power-dependent slope of two and reporting a short lifetime for the lowest energy PL peak.[309,314–316] The increase in biexciton emission with decreasing temperature is expected with the observed increase in the radiative luminescence efficiency, and hence the increase in the radiative exciton density.

Though multiple excitonic species are visible in the low-temperature 2D film PL, single-mode polariton dispersions are observed down to 4 K, direct evidence that the cavity mode strongly couples to only one exciton species.[254,285] To better understand the polariton photophysics and excitonic state to which the cavity couples at low-temperature, we investigate the bare 2D film bright, X, and dark, DX, state dynamics by selecting high and low energy regions of the film PL spectrum with spectral filters, capturing separately the decay of X and DX, respectively (Figure 3.3). Furthermore, to separate the DX and XX response, as they are in the same low energy region, these measurements are performed at 80 K and 60 K, temperatures at which DX emission is present and the XX emission is not yet significant.

We observe delayed emission from DX (low energy spectral region, Figure 3.3e,f), which is strong evidence for a spin-flip process[317–319] facilitated by the dark exciton gaining oscillator strength from the bright exciton by mixing due to spin-orbit coupling,[310,320] and by limiting the non-radiative phonon-assisted relaxation at low temperatures. This transfer process can be modeled by a set of coupled differential equations. These equations capture the three-state model, in which radiative recombination from the bright exciton (denoted as *X* in Eq. 3.3-3.5) competes with transfer to the dark exciton population (denoted as *DX* in Eq. 3.3-3.5) and vice versa through microscopic reversibility.[187,321,322] The temperature-dependent spin-flip rate ($k_s(T)$) and the reverse process ($k_{s-}(T)$) maintain thermodynamic equilibrium, weighted by the Arrhenius factor: $k_{s-} = e^{(E_X - E_{DX})/kT} \cdot k_s$ (Figure 3.17b).[187,323–328]

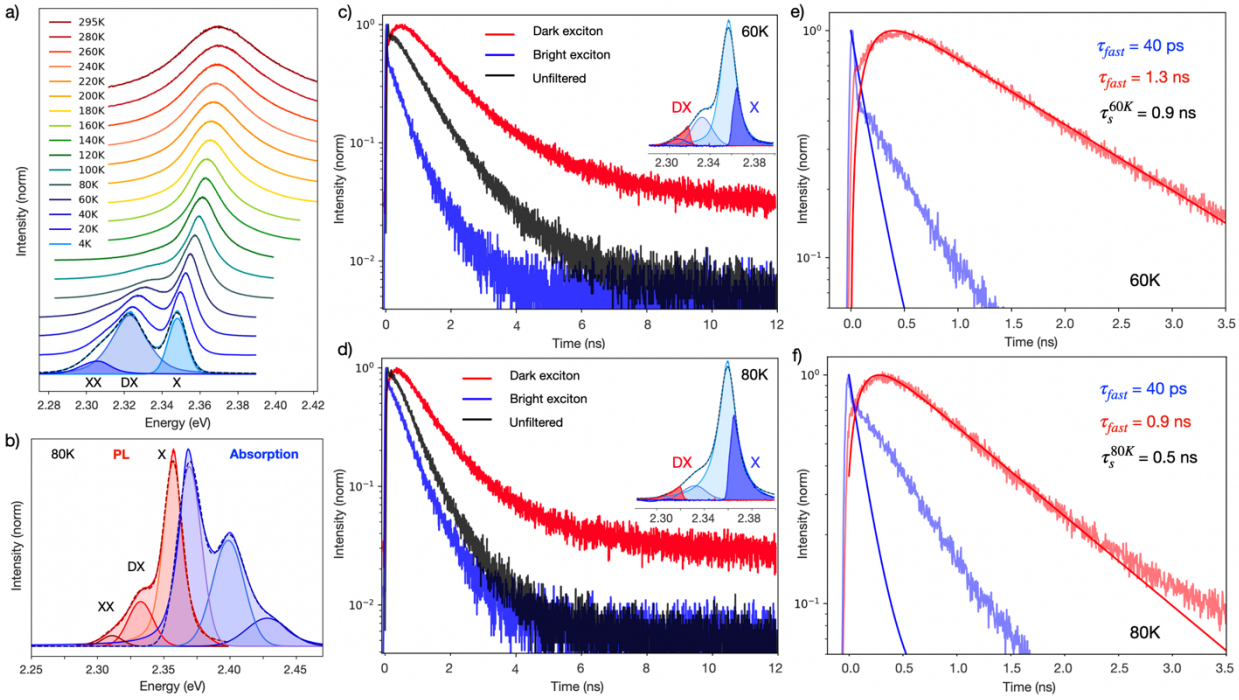

Figure 3.3: (a) 2D perovskite thin film photoluminescence (PL) spectra as a function of temperature revealing, beyond the primary PL peak, the emergence of secondary and tertiary PL peaks assigned to (b) the bright exciton (X), the dark exciton (DX), and the biexciton (XX) with PL shown in red and absorption in blue. (c,d) Time-resolved PL for the unfiltered bare 2D film spectrum (black), X filtered spectrum (blue), and DX filtered spectrum (red). Insets: 2D perovskite thin film PL at (c) 60K and (d) 80K with fitted Gaussian constituent peaks. High (dark blue) and low (dark red) energy regions highlighted, showing the experimentally measured PL spectra with tunable edge-pass filters for X and DX decay measurements, respectively. (e,f) Lifetimes of the X emission (blue) and DX emission (red) simulated with Eqs. 3.3-3.5.

To fully capture the exciton/photon dynamics in the photoexcited 2D perovskite film, we take into account photon recycling due to the low material Stokes shift and high absorption (Figure 3.3b), creating additional terms that contribute to the excited state dynamics through radiative recombination of either a bright or dark exciton (Eq. 3.3, 3.5). Photon recycling occurs when a photon generated via radiative recombination is re-absorbed by the active layer.[70] These multiple absorption/emission events serve to increase the carrier density in the thin film for a given excitation power as compared to a material that does not exhibit photon recycling. The impact

of photon recycling is dependent on the material absorption coefficient, index of refraction, radiative lifetime, and PLQE (Figure 3.18).[70,329] At low temperature, the perovskite material PLQE eventually reaches 100-fold the room temperature PLQE, indicating that photon recycling plays an ever-greater role with decreasing temperature.[329]

$$\frac{dn_X}{dt} = -k_{rX}n_X - k_s(T)n_X + k_{s-}(T)n_{DX} + \frac{c}{n_r}\sum_\lambda \alpha_\lambda \gamma_\lambda \quad 3.3$$

$$\frac{dn_{DX}}{dt} = -k_{rDX}n_{DX} + k_s(T)n_{DX} - k_{s-}(T)n_{DX} \quad 3.4$$

$$\frac{d\gamma_\lambda}{dt} = -\frac{c}{n_r}\sum_\lambda \alpha_\lambda \gamma_\lambda + (1 - P_{esc}) \cdot [k_{rX}n_X + k_{rDX}n_{DX}] \quad 3.5$$

where k_{rX} and k_{rDX} are the radiative recombination of X and DX, respectively, $k_s(T)$, and $k_{s-}(T)$ are the temperature-dependent (T) spin-flip rates from X to DX and DX to X allowing for interconversion between both species, respectively, n_X and n_{DX} are the X and DX energy carrier concentrations, respectively, c is the speed of light, α_λ is the absorption coefficient averaged over the emission band, γ_λ is the photon concentration within the film for a given wavelength due to radiative recombination and photon recycling, n_r is the index of refraction, and P_{esc} the probability of a radiatively recombined photon leaving the film within the escape cone.

In this way, $k_s(T)$ can be quantified as a function of temperature in this material system. At 60 K (Figure 3.3c,e), the system of coupled differential equations yields a fast bright exciton lifetime $\tau^X_{60K,fast}$ < 40 ps, limited by the instrument response function (IRF) of the detection scheme (Figure 3.20). The long tail of the time-resolved photoluminescence (TRPL) trace is not included in the model given system IRF limitations and the non-zero spectral overlap of the dark exciton contributing to the counts at longer timescales. The dark exciton has a fast component, $\tau^{DX}_{60K,fast}$ = 1.3 ns, and long component, fit with an exponential decay, of $\tau^{DX}_{60K,slow}$ = 15 ns (Figure 3.21), which is consistent with reports of the long DX lifetime in these materials.[310]

The transfer process at 60 K, τ_{60K}^{S} = 0.9 ns, is relatively slow,[330] but several studies show similarly long time-scales for spin dynamics in perovskites and other materials at low temperature.[331–339]

When the temperature is increased from 60 K to 80 K, the lifetime of the bright exciton remains IRF-limited ($\tau_{80K,fast}^{X}$ < 40 ps), the dark exciton fast-component lifetime decreases ($\tau_{80K,fast}^{DX}$ = 0.9 ns), and the transfer rate increases (τ_{80K}^{S} = 0.5 ns), which is anticipated considering the Arrhenius relation and large bright-dark state splitting in this material, and is consistent with a thermally activated spin-flip (Figure 3.3d,f).[187,321,323–327,340,341]

Both X and DX states can be populated following photoexcitation, with additional DX population contributions due to transfer from the higher energy X to DX at rate $k_S(T)$, and additional X population due to the thermally dependent back-transfer from DX to X at rate $k_{S-}(T)$.[342–344] As temperature decreases and non-radiative phonon scattering events are reduced, luminescence of the long-lived DX population can outcompete the phonon-assisted non-radiative emission resulting in the observable DX emission peak. Additionally, the bi-directional interconversion between X and DX ($k_S(T)$, $k_{S-}(T)$), as previously demonstrated in many material systems,[187,345] favors the population of the lower-lying DX as temperature decreases. We calculate $\tau^{S-} = 1/k_{S-}(T)$ to be τ_{80K}^{S-} = 63 ns and τ_{60K}^{S-} = 110 ns, which is much slower than the measured radiative emission time of the DX state. Thus, we observe a steady increase in the DX emission with decreasing temperature due to both a reduction in non-radiative phonon scattering and the Arrhenius decrease of thermal excitation from DX to X, as seen in similar systems.[322] Additionally, the impact of photon recycling on these dynamics is non-trivial, as for a PLQE of 77% at 4 K, the average number of recycling events per emitted photon in the 2D perovskite thin film is 3.5, with recycling events increasing to 13 in the radiative limit (Figure 3.18). Photon recycling effectively functions as a mechanism for repopulating the bright state exciton reservoir, allowing another opportunity for the regenerated bright excitons to spin-flip into the dark state.

Figure 3.4 shows the temperature-dependent emission lifetimes for the bare 2D film and strongly coupled cavity (additional temperature-dependent TRPL traces are shown in Figure 3.23). At room-temperature, the bare 2D film luminescence lifetime is $\tau_{295K} = 350$ ps, and the LPB lifetime is $\tau_{295K,cav} = 260$ ps, representative of the transient response near the cavity polaritons (Figure 3.4a). This decay is longer than the expected polariton lifetime (<100 fs for Q ~ 110) due to the widely observed confounding influence of reservoir states that are not strongly coupled and only weakly perturbed by cavity polaritons[252] as well as by photoinduced effects unique to the cavity system.[346] For example, in organic thin films, it has been shown that the polariton lifetime of low-Q cavities, intrinsically on the order of 10's of fs, in practice follows the time-evolution of the fundamental carrier and spin dynamics of material excitons on much longer timescales (ns to μs in duration), resulting in strongly coupled PL decay dynamics that are similar to the bare film exciton dynamics.[252]

In the bare 2D film, as the temperature decreases from 295 K to 100 K, the X emission lifetime decreases and the DX emission emerges with an increasingly long lifetime and increasingly strong intensity, as has previously been observed by Fang *et al.* (Figure 3.4b, dark teal trace, 100 K).[313] Further reductions in temperature show that, as the back transfer $k_{s-}(T)$ slows, the X emissive lifetime shortens and its early timescale emission increases, while DX demonstrates an increasingly long emissive lifetime (Figure 3.4c,d, dark purple and blue traces). Indeed, by 4 K, the DX state constitutes most of the emission of the bare perovskite film, with a 100-fold increase in the overall luminescence efficiency, as compared to the PLQE at 295 K.

The improvements in the perovskite film PLQE and the emergence of significant emission from the DX state (Figure 3.3) occur over the same temperature range in which the cavity LPB dispersion undergoes its own spectral emission changes (Figure 3.2). In the strongly coupled cavity at 100 K, the extent of delayed emission is similar to but slightly reduced from the bare 2D film, and the fast component contribution increases as the strong coupling between the bright

exciton and cavity mode forms the short-lifetime LPB emissive state (Figure 3.4b, light teal trace, 100 K). As the temperature decreases from 60 K to 4 K in the cavity, the fast emission from the LPB shifts in energy (Figure 3.2) and the emission rate increases (Figure 3.4c, light purple trace). At 4 K in the cavity, we measure nearly IRF-limited emission largely from the strongly coupled state emitting near $k_{//} = 0$ and do not observe significant delayed emission or the long tail from the DX emission (Figure 3.4d, light blue trace).

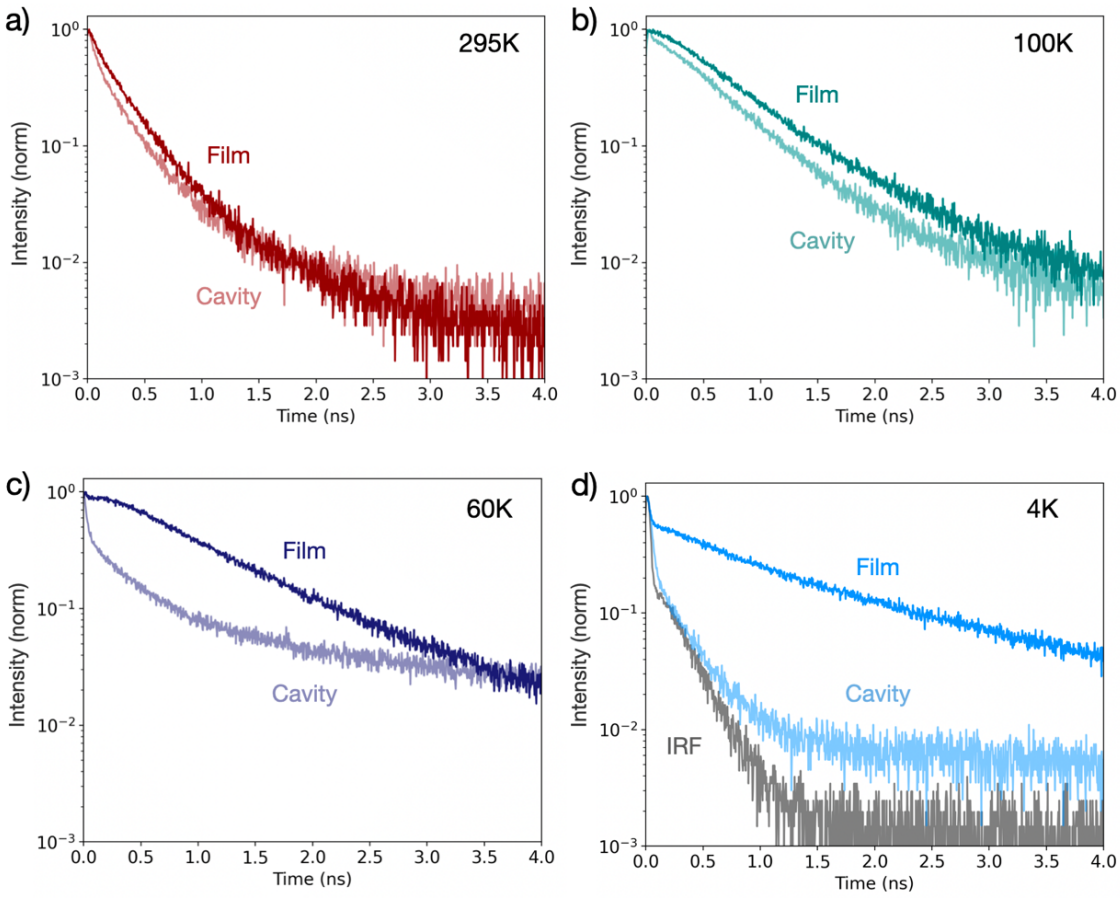

Figure 3.4: (a-d) The bare 2D perovskite film time-resolved photoluminescence (TRPL) decay (dark traces, Film) compared to the strongly coupled microcavity ($\hbar\Omega_{Rabi} = 175$ meV, Δ = +28 meV) lower polariton branch (LPB) emission (light traces, Cavity) as a function of temperature (295 K, 100 K, 60 K, 4 K). In the bare film, as temperature decreases, the bright exciton (X) emission lifetime decreases and the dark exciton (DX) emission emerges with an increasingly long lifetime, visible as a short-timescale fast component with delayed emission

into a longer tail ((b-c), dark traces). In the cavity ((b-d), light traces), the extent of delayed emission is reduced. At 60 K in the cavity ((c), light trace), the fast LPB emission begins to dominate the TRPL decay dynamics at early timescales, with weaker emission contribution from the DX state resulting in a long lifetime tail. ((d), light trace) At 4 K in the cavity, a nearly IRF-limited decay is observed with no long lifetime contribution.

3.7. INTRACAVITY PUMPING, LO-PHONON SCATTERING, BIEXCITON-ASSISTED RELAXATION

While the strong coupling between the bright exciton, X, and cavity mode results in a short polariton emissive lifetime, there can still exist the DX population inside the cavity, generated after photoexcitation but not strongly coupled to the cavity, consistent with the weak oscillator strength and dipole misorientation of the DX state.[342–344] The brightening of the DX state at lower temperatures allows its luminescence to then be observed via the LPB mode, which is resonant in energy with the DX state. Decay of a lower energy DX state through the resonant LPB mode has been observed in strongly coupled organic microcavities,[347,348] and increased polariton density has been demonstrated by cavity-enhanced, $k_{||}$-dependent transfer of the DX population to the LPB[349] as well as the radiative pumping of polariton modes by a secondary, uncoupled or weakly coupled isoenergetic emitter within the cavity.[350–354]

In our system, as the temperature of the cavity drops from 100 K to 4 K, the higher energy $k_{||} > 0$ LPB population can resonantly transfer to the luminescent DX state due to weak coupling facilitated by the DX acquiring oscillator strength at high-$k_{||}$.[349] The energy in the DX state can be rapidly transferred back to the isoenergetic LPB state (Figure 3.5), creating a new pathway of emission as compared to the long-lived DX state in the bare 2D film case. The DX state can then also be described as an intermediary that shuttles the $k_{||} > 0$ LPB energy to the $k_{||}$ state of the same energy as the DX. When the bottom of the LPB, or $k_{||} = 0$ mode, is resonant with the DX state, the result is the suppression of the bottleneck effect with primary emission from $k_{||} = 0$ (Figure 3.5d,f). A similar isoenergetic release of, or radiative pumping by, the XX luminescence

through the LPB mode can also be sustained at sufficiently low temperatures when the XX state emits (Figure 3.5e).

Additionally, while the cavity does not strongly couple to the DX or XX states, transitions between these species and bright excitons appear resonant with LO-phonon modes in PEA_2PbI_4 as computed by Straus *et al.* for energies below 50 meV (400 cm^{-1}) using DFT calculations.[305] Straus *et al.* quantify mode contributions from the high-energy organic cation vibrations (25 meV and 41 meV) that are resonant with the DX and XX energy differences from the bright exciton (X-DX = 25 meV, X-XX = 42 meV).[305,355] In this work, we excite above band gap, and generate hot carriers that can cool via nonradiative relaxation with vibronic replicas – states that resonantly emit phonons into the XX state and DX state during spin-flip transfer processes.[356–358] These phonon modes are always present, but it is only when the red-shifting exciton reservoir and corresponding LPB minimum is resonant with a transition involving one of these phonon modes at low temperature that LO-phonon assisted relaxation can enhance scattering processes (Figure 3.5). When the detuning is such that the energy difference between the bottom of the LPB and the exciton reservoir matches the energy of one LO-phonon, efficient LO-phonon-mediated relaxation pathways can be utilized.

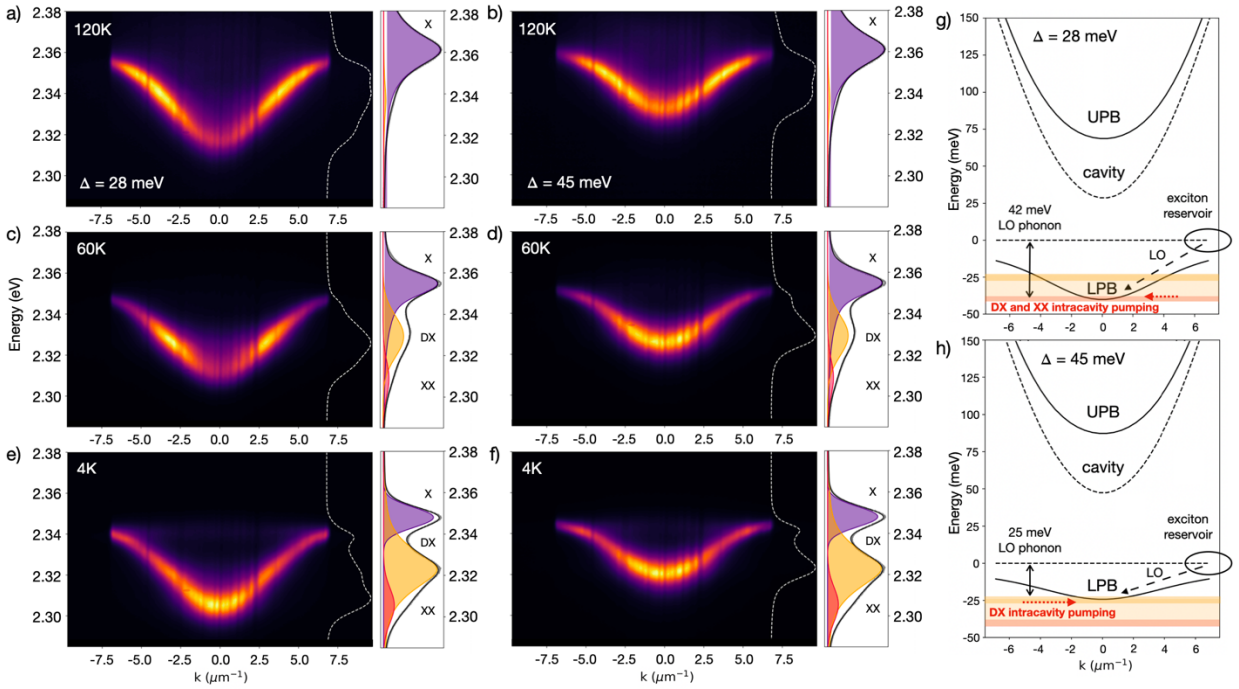

Figure 3.5: (a-f) Lower polariton branch (LPB) photoluminescence (PL) as a function of temperature for two detunings established at room temperature ($\hbar\Omega_{\text{Rabi}}$ 175 meV, Δ = +28 meV and +45 meV) with (right panel) bare 2D perovskite film PL at the corresponding temperature (bright exciton = X; dark exciton = DX; biexciton = XX). (a,c,e) For the more photonic detuning (Δ = +28 meV), the re-centering of the PL distribution to $k_{//}$ = 0 occurs when the bottom of the LPB is resonant with XX due to the (g) 42 meV LO-phonon-mediated relaxation and DX reservoir intracavity pumping. (b,d,f) For the more excitonic detuning (Δ = +45 meV), the re-centering of the PL distribution to $k_{//}$ = 0 occurs when the bottom of the LPB is resonant with DX due to the (h) 25 meV LO-phonon-mediated relaxation and DX reservoir intracavity pumping.

Emission from $k_{//}$ = 0 at low temperature can be described as a combined consequence of intracavity pumping from the DX and XX populations, resonant LO-phonon scattering, and biexciton-assisted relaxation. For Δ = +28 meV at 120 K (Figure 3.5a), the brightest emission is observed at high $k_{//}$ (bottleneck), whereas, at 60 K, the brightest emission has shifted to lower $k_{//}$, peaked at the resonant DX energy and benefitting from isoenergetic intracavity pumping with further opportunity for bottleneck suppression via X-DX LO-phonon scattering (Figure 3.5c). At 4 K, the LPB minimum red-shifts, becoming resonant with the XX state, and the LPB emission

profile redistributes due to the isoenergy of the XX state and $k_{||} = 0$ mode, with available scattering pathways from relaxation via X-XX LO-phonons (Figure 3.5e,g).

For $\Delta = +45$ meV at 120 K (Figure 3.5b), the bottleneck effect is again observed, though to a lesser extent as the increased excitonic character reduces the curvature of the LPB and increases the DOS, allowing for greater scattering towards $k_{||} = 0$. Because of the flatter dispersion, the bottom of the LPB never reaches the XX energy resonance, but instead is resonant with the DX state and again matches the smaller LO-phonon energy difference from X (X-DX). This occurs at higher temperatures than its less excitonic counterpart, $\Delta = +28$ meV, resulting in $k_{||} = 0$ emission at an elevated temperature of 60 K (Figure 3.5d), maintaining $k_{||} = 0$ primary emission down to 4 K (Figure 3.5f,h). These proposed scattering pathways are consistent with reports on inorganic polaritons, identifying LO-phonon-assisted transfer – including the first LO-phonon replica of the biexciton – as efficient mechanisms for directly populating $k_{||} = 0$.[287,298,359–362] We can observe additional signatures of biexciton-assisted relaxation given that the biexciton has two viable pathways for dissociation, as described by Corfdir *et al.*:[287]

$$\text{Biexciton} \rightarrow \text{LPB Polariton at } k_{||} = 0 + \text{LO-Phonon} + \text{Bright Exciton}$$

$$\text{Biexciton} \rightarrow \text{LPB Polariton at } k_{||} = 0 + \text{LO-Phonon} + \text{LPB Polariton at High } k_{||}$$

In both 4 K dispersions (Figure 3.5e,f), there exists uncoupled exciton PL in a flat, dispersionless line at the low energy tail of the bare exciton energy band. This uncoupled PL is only visible for temperatures in which the biexciton emission is prominent (<20 K, Figure 3.26). We also observe brightening of the high-$k_{||}$ wings of the LPB for $T < 15$ K (Figure 3.26), consistent with contributions to the LPB PL distribution from both mechanisms above.

Isoenergetic DX and XX intracavity pumping can be assisted by LO-phonon-mediated scattering and biexciton-assisted polariton relaxation for $k_{||} = 0$ emission in this 2D perovskite exciton-polariton system, presenting opportunities for engineering the microcavity detuning such that the bottom of the lower polariton branch can be directly populated. These insights are critical for the rational engineering of microcavity systems requiring careful control of polariton

momentum and benefiting from the non-synthetic, strong coupling-mediated tuning of the kinetic rates of 2D perovskite excitonic species. By targeted synthetic, passivation, or applied external field approaches, the brightening of these excitonic states can be harnessed to increase the polariton population at elevated temperatures towards low-threshold polariton lasing and condensation.[298,363–366]

3.8. CONCLUSION

We have identified, for the first time, the interplay between PEA_2PbI_4 perovskite excitonic states and exciton-polariton formation as a function of temperature in wedged microcavity systems. By careful control of the Hopfield coefficients, the impact of changing cavity detuning and thus changing polariton photonic/excitonic character on the lower polariton branch (LPB) emission profile in *k*-space was determined. We have shown that, for excitonic detunings, the bottleneck effect emerges at intermediate temperatures and can then be suppressed at low temperatures with the emergence of dark exciton (DX) and biexciton (XX) luminescence. We quantify the spin-flip transfer process from the bright exciton (X) to the DX state at low temperature in the bare 2D perovskite film, and investigate the competition between strong coupling in the microcavity and transfer from the X to DX state. In this way, we demonstrate, without synthetic modifications, tuning of the perovskite electronic structure via strong coupling to enable new kinetic rates. These insights provide cavity and material design principles for next generation polaritonic devices and condensates requiring careful control of polariton momentum and relaxation, and demonstrate the utility of polariton formation to modify recombination dynamics and energy conversion processes towards optoelectronic devices with tunable emissive properties.

3.9.1. Experimental Methods

Perovskite Preparation: Perovskite precursors were obtained from Sigma Aldrich (phenethylammonium iodide, SKU 805904) and TCI (lead(II) iodide, TCI-L0279), and prepared in dimethyl sulfoxide (Sigma Adlrich, SKU 34869) stoichiometrically for n = 1. Films were spincast in a two-step procedure: 1) 1000 rpm, 10 s, 500 accel; 2) 5000 rpm, 30 s, 2000 accel with a chlorobenzene quench 15 s before the end of the second step (Sigma Aldrich, SKU 284513). The films were annealed at 100°C for 10 min. All synthesis and process steps under nitrogen. The resulting thin films ranged from approximately 25-50 nm (+/- approximately 3 nm) as a function of solution concentration, as measured on silicon substrates by ellipsometry.

Solution-Processed Spacer Layer Preparation: Poly(methyl methacrylate) was purchased from Sigma Aldrich (SKU) and dissolved in chlorobenzene (Sigma Aldrich, SKU 284513) at 50°C. Films were spincast using a single-step procedure: 1500 rpms, 60 s, 1000 accel. Films were gently annealed at 60°C for 1 min to assist in driving off excess solvent. All process steps under nitrogen. The resulting thin films were approximately 110 nm thick, as measured on fused silica substrates by profilometry.

Microcavity Preparation: Fused silica substrates were cleaned by sonication in water, diluted detergent, acetone, and isopropyl alcohol followed by boiling isopropyl alcohol. The bottom Ag mirror was thermally evaporated at 110 nm followed by sputter deposition of a 108 nm SiOx layer in argon. The perovskite active layer was spin-cast and annealed under nitrogen (~25 nm), followed by the Poly(methyl methacrylate) layer. The microcavity was capped with a semi-transparent thermally evaporated Ag layer (35 nm).

Room-Temperature Fourier Spectroscopy: K-space emission was imaged using a Nikon Eclipse-Ti inverted microscope fitted with an infinity corrected 100 × dry objective (Nikon L Plan, NA = 0.85). A 405 nm pulsed diode laser (PDL-800 LDH-P-C-405B, 300 ps pulse width)

was used for excitation with repetition rate of 80 MHz. The sample photoluminescence (PL) was filtered through a 405 nm dichroic beamsplitter (Nikon DiO1-R405) and the reflectivity collected via a halogen lamp white light source (Nikon Eclipse-Ti) and 50/50 beamsplitter (Chroma 21014-UF3 C188781). The output for both PL and reflectivity was then coupled in free space via a 4F imaging system into a Princeton Instruments Acton spectrometer and Pixis camera (100 (k-space) x 1340 (wavelength) pixels).

Low-Temperature (4-295 K) Fourier Spectroscopy: K-space emission was imaged using a Montana Instruments closed-cycle liquid He crysotat with piezo-controlled 3D-moveable sample stage, cryo-optic low-working distance 100x 0.9NA objective, vacuum housing, radiation shield, and local objective heater. A wavelength-tunable ultrafast laser (Toptica Photonics FemtoFiber Pro) was used for 488 nm excitation with 80MHz repetition rate, guided into the cryo-optic with electrically-controlled Thorlabs Galvo mirrors. The sample emission was filtered through a Semrock tunable edge pass (set to 490 nm long pass) filter and directed via a 4F imaging system into a Princeton Instruments Acton spectrometer and either a 512 (k-space) x 512 (wavelength) pixel or 1024 (k-space) x 1024 (wavelength) pixel Pixis camera.

Time-Resolved Photoluminescence: A wavelength-tunable ultrafast laser (Toptica Photonics FemtoFiber Pro) was used for 488 nm excitation with 80MHz repetition rate. The emission was filtered through a Semrock tunable edge pass (set to 490 nm long pass) filter and directed to a Micro Photon Devices (MPD) PicoQuant PDM Series single photon avalanche photodiode with a 50 μm active area and 40 ps IRF. Photon arrival times were time-tagged using a time-correlated single photon counter (TimeHarp 260).

Variable Angle Spectroscopic Ellipsometry: Spectroscopic ellipsometry was performed using a variable angle spectroscopic ellipsometer (Woollam) at 65°, 70°, and 75° angles of incidence. Ellipsometry data was fitted to obtain perovskite thin film thicknesses.

Photoluminescence Quantum Efficiency (PLQE) Measurements: PLQE measurements were acquired using a center-mount integrating sphere setup (Labsphere CSTM-QEIS-060-SF)

and Ocean Optics USB-4000 spectrometer. The integrating sphere setup was intensity calibrated with a quartz tungsten halogen lamp (Newport 63355) with known spectral irradiance set at a distance 0.5 m away from the integrating sphere illumination port. A fiber-coupled 405 nm diode laser in CW mode (PDL-800 LDH-P-C-405B) was collimated with a triplet collimator (Thorlabs TC18FC-405) to produce a beam with an approximate $1/e^2$ diameter of 2.8mm. The beam was used to excite the sample and a variable neutral density filter was used to attenuate the laser. Data acquisition followed the protocol described by de Mello et al.,[367] with a scattering correction.

Cryo XRD: Temperature-dependent XRD was performed using a Panalytical Multipurpose Diffractometer with a liquid He cryostat for in-situ low temperature measurements. 30 minute scans were taken for 5-67 degrees at each temperature in increments of 20 K from 295 K to 11 K, with 15 minutes between scans for temperature equilibration. The temperature was scanned from high to low and cycled back from low to high to determine whether the temperature cycle damaged the 2D perovskite. No structural changes (peak intensity or position) were noted in the up cycle.

Cryo Absorption: Reflection spectrophotometry was performed with light incident from the film side using an Agilent Cary 5000 dual-beam UV–vis–NIR spectrophotometer with home-built, liquid N_2 cryostat quartz window attachment. The 2D perovskite was coated onto a 15 mm diameter fused silica optical window (see substrate cleaning procedure above) for compatibility with cryo sample holder. Specular reflectance was collected at an incident angle of 8°. A 3 mm round aperture was used for all measurements.

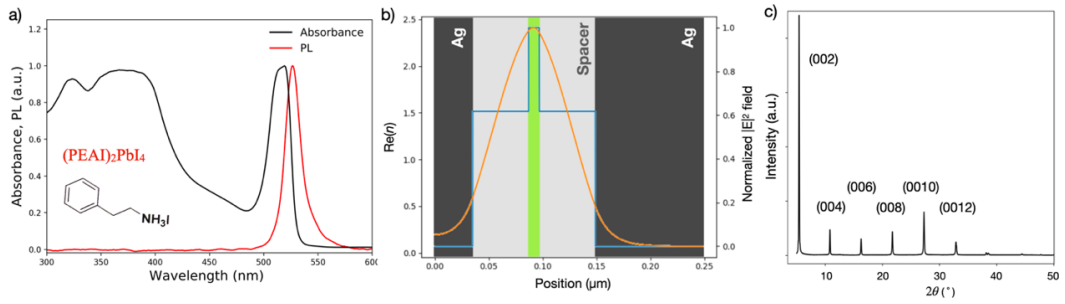

Figure 3.6: (a) Absorption (black trace) and photoluminescence (red trace) spectra for the PEA_2PbI_4 thin film. (b) Metallic microcavity structure with normalized electric field profile (orange trace) and index of refraction (blue trace) simulated with a transfer matrix model of the cavity architecture: Ag (110nm)/SiOx (108nm)/spin-cast PEA_2PbI_4 active layer (~20nm)/PMMA (~110nm). (c) Room-temperature XRD demonstrating a high degree of crystallinity equivalent to single crystals.[288]

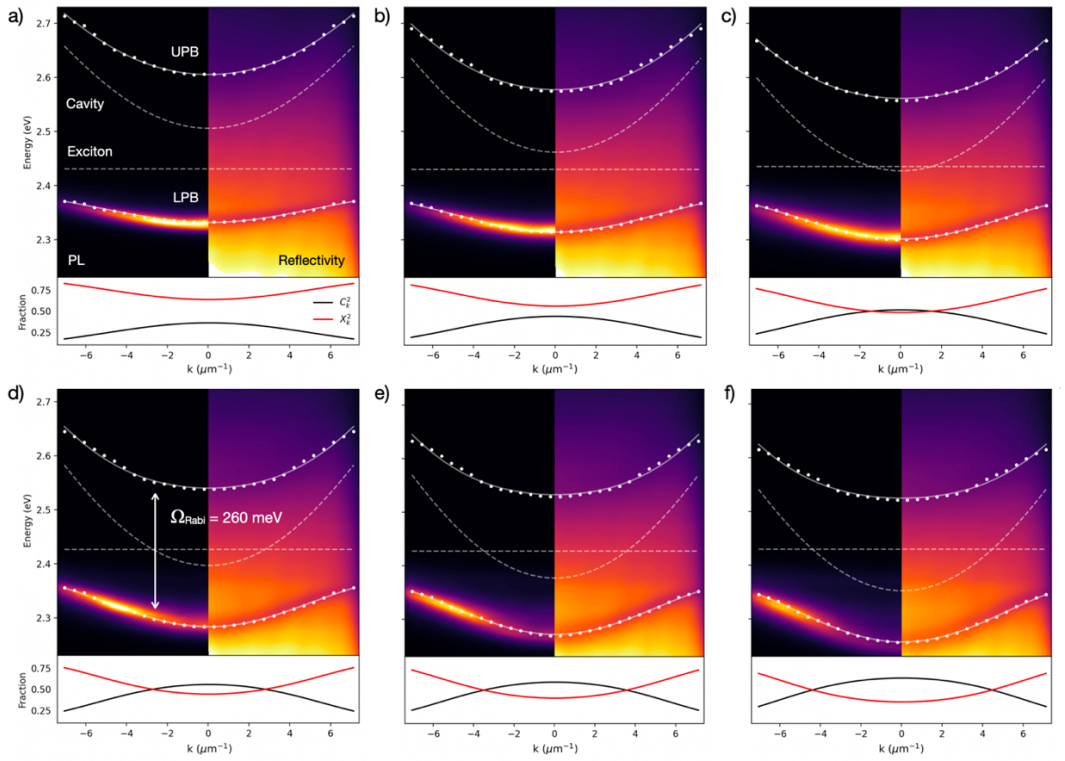

Figure 3.7: Exciton-polariton photoluminescence (left) and reflectivity (right) dispersions with increasing cavity length from (a) higher cavity mode energy to (f) lower cavity mode energy

(f). As the cavity shifts to lower energies and the polariton dispersion becomes increasingly photonic (d-f), the bottleneck effect emerges with the greatest emission intensity at high k values. The upper and lower polariton branches are extracted from reflectivity (white dotted line) and fit (white solid line) with a Rabi splitting of $\hbar\Omega_{Rabi}$ = 260 meV. (a-f, lower figures) Hopfield coefficients for cavity detunings (photonic fraction C_k^2, black trace; excitonic fraction X_k^2, red trace) ranging from (a) excitonic to (f) photonic depicting the light-matter characteristics of the generated polaritons as a function of $k_{//}$.

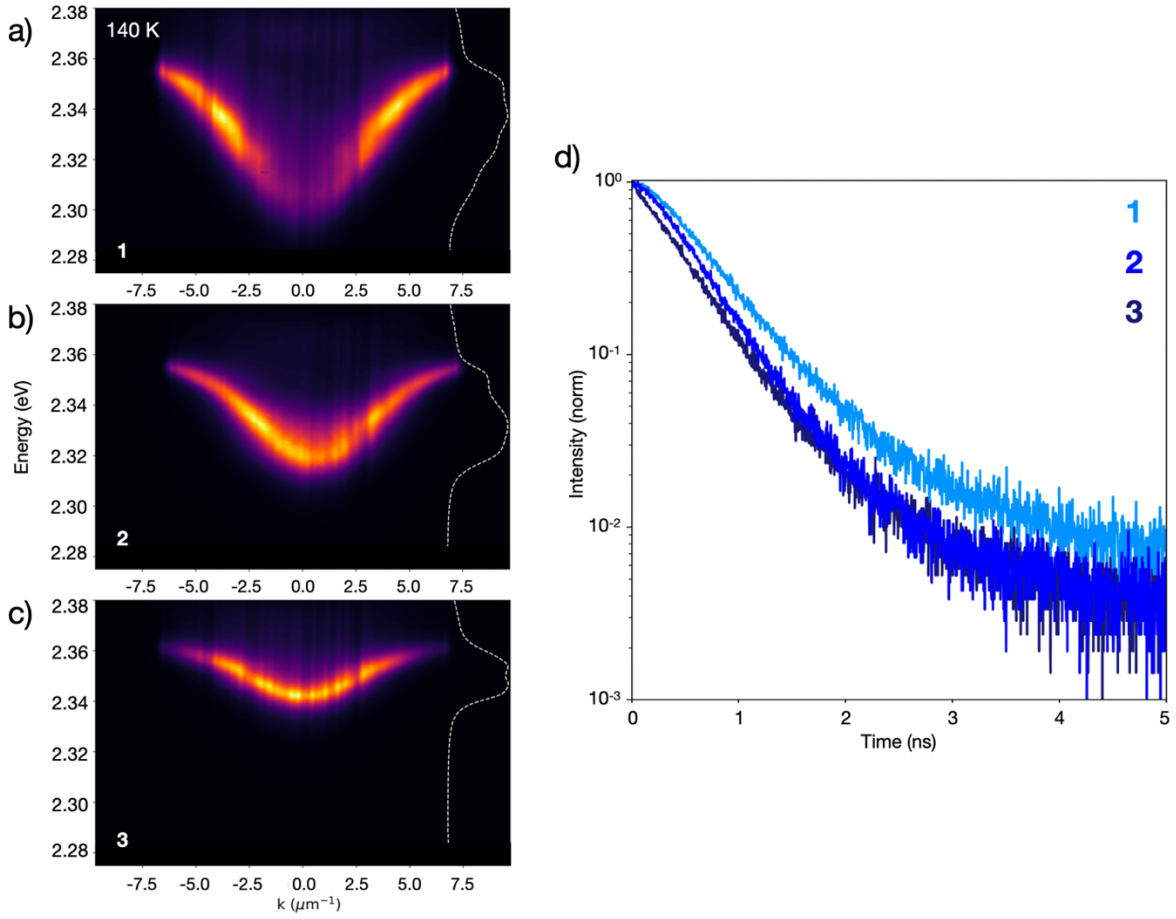

Figure 3.8: Photoluminesence (PL) in k-space for $\hbar\Omega_{Rabi}$ = 175 meV at 140 K for (a) highly photonic (negative) detuning with severe bottleneck, (b) photonic detuning with the beginnings of a bottleneck, and (c) excitonic (positive) detuning with no bottleneck. (d) Increasingly positive detunings result in polaritons with shorter radiative lifetimes due to the suppression of the bottleneck effect (blue traces 1-3 corresponding to (a)-(c), respectively). PL from higher $k_{//}$ in the bottleneck region corresponds to more excitonic polaritons, which possess greater scattering rates and longer radiative lifetimes, accounting for the slower emission at early timescales and longer lifetime tails.

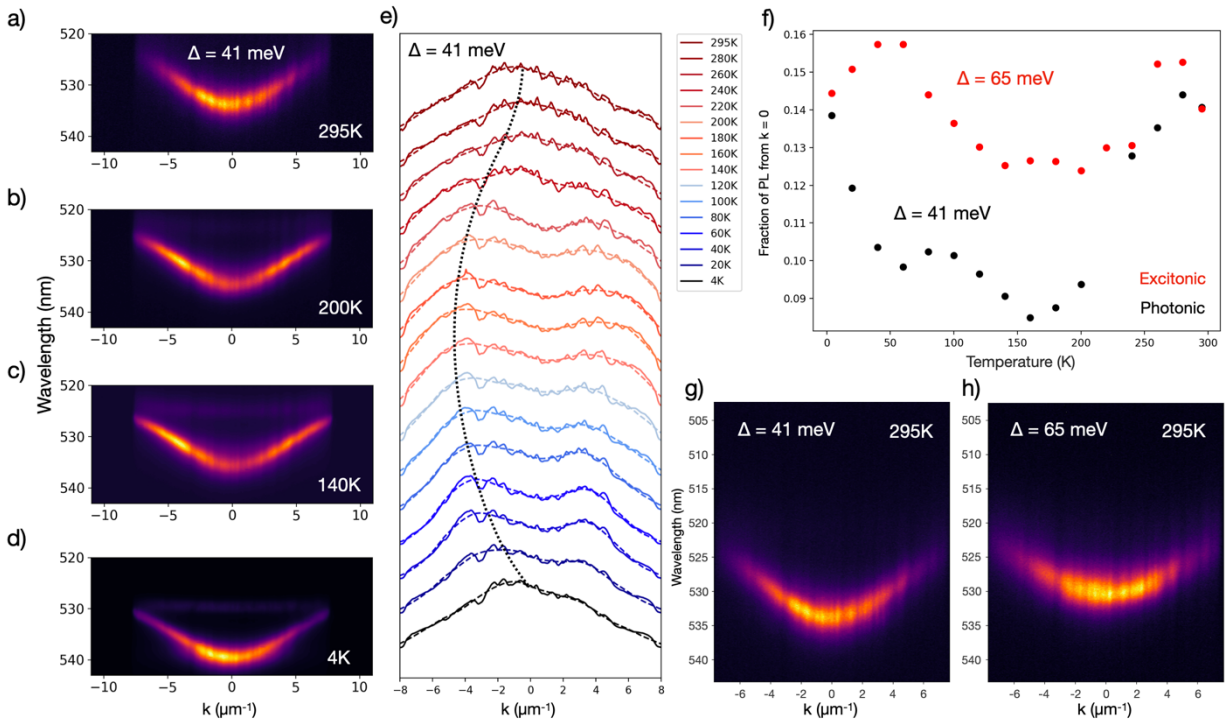

Figure 3.9: (a-d) Lower polariton branch (LPB) photoluminescence (PL) as a function of temperature for $\hbar\Omega_{Rabi}$ = 260 meV revealing e) the migration of the maximum PL intensity to higher $k_{||}$ at intermediate temperatures before returning to $k_{||}$ = 0 at 4K. (e,f) The temperature-dependence of the energy-integrated PL for Δ = +41 meV showing bottlenecked PL at intermediate temperatures and emission from $k_{||}$ = 0 at sufficiently low temperatures. (g,h) PL spectra for two detunings (Δ = +41 meV and +65 meV) at 295K, corresponding to the temperature series in (f). Note: asymmetries in PL distribution arise from imperfectly flat substrate seating due to Ag cryo paste used for thermal contact. Additionally, the thicker perovskite active layer results in increased uncoupled exciton PL at elevated temperatures as compared to the thinner active layer yielding $\hbar\Omega_{Rabi}$ = 175 meV.

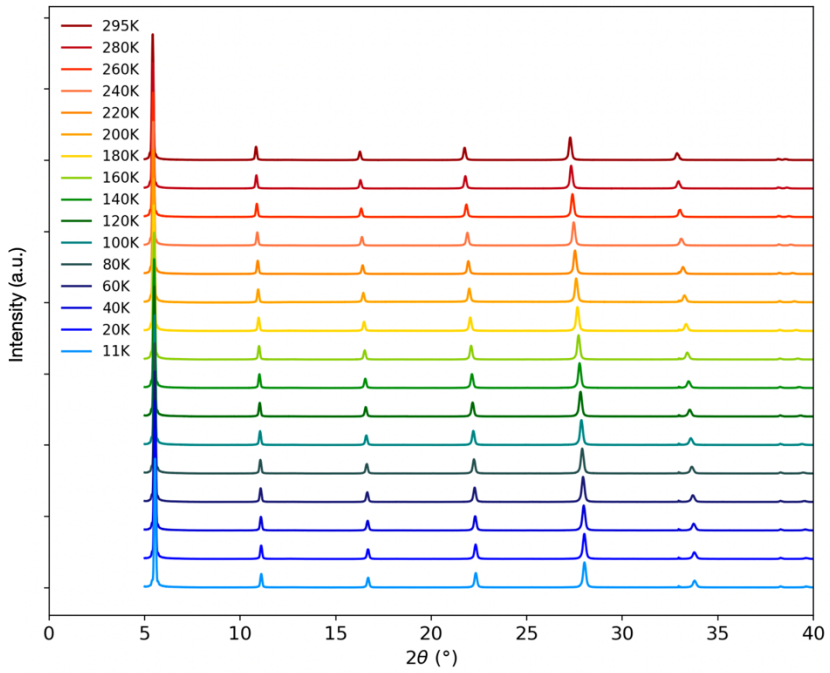

Figure 3.10: Temperature-dependent XRD from 295 K to 11 K showing no phase change as a function of temperature.

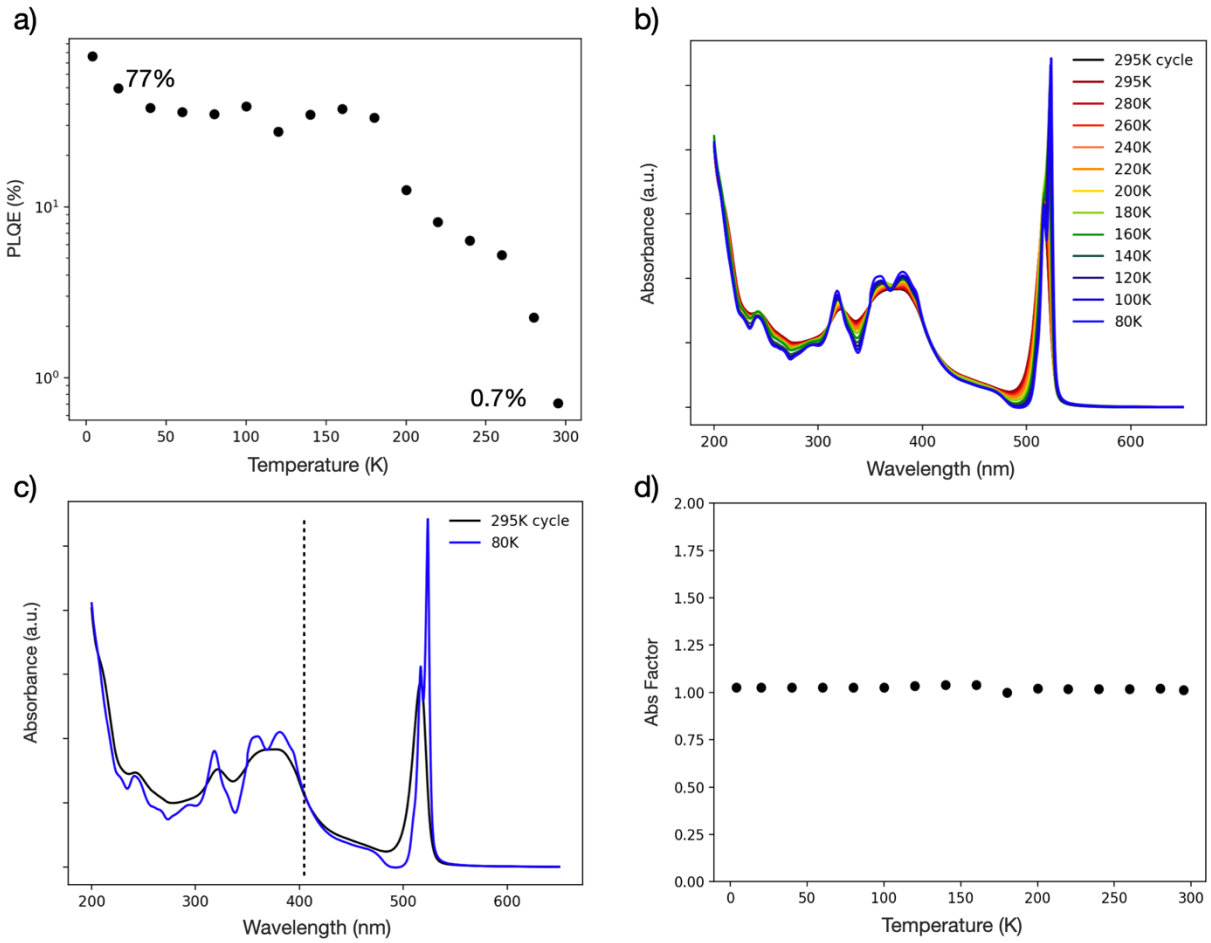

Figure 3.11: (a) PLQE measured at 295 K with integrating sphere and 405 nm laser excitation in cw-mode (~0.7%), and used to calculate a 100-fold PLQE increase as a function of temperature. To ensure the PL increase was not from changes in the absorption of the excitation as a function of temperature, (b) temperature-dependent absorption measurements were performed from 295 K to 80 K. The excitation wavelength was tuned to a region with very little change in absorption (c, dashed black trace indicating laser excitation wavelength), with small fluctuations in absorbance quantified in the (d) Abs Factor extrapolated to 4K.

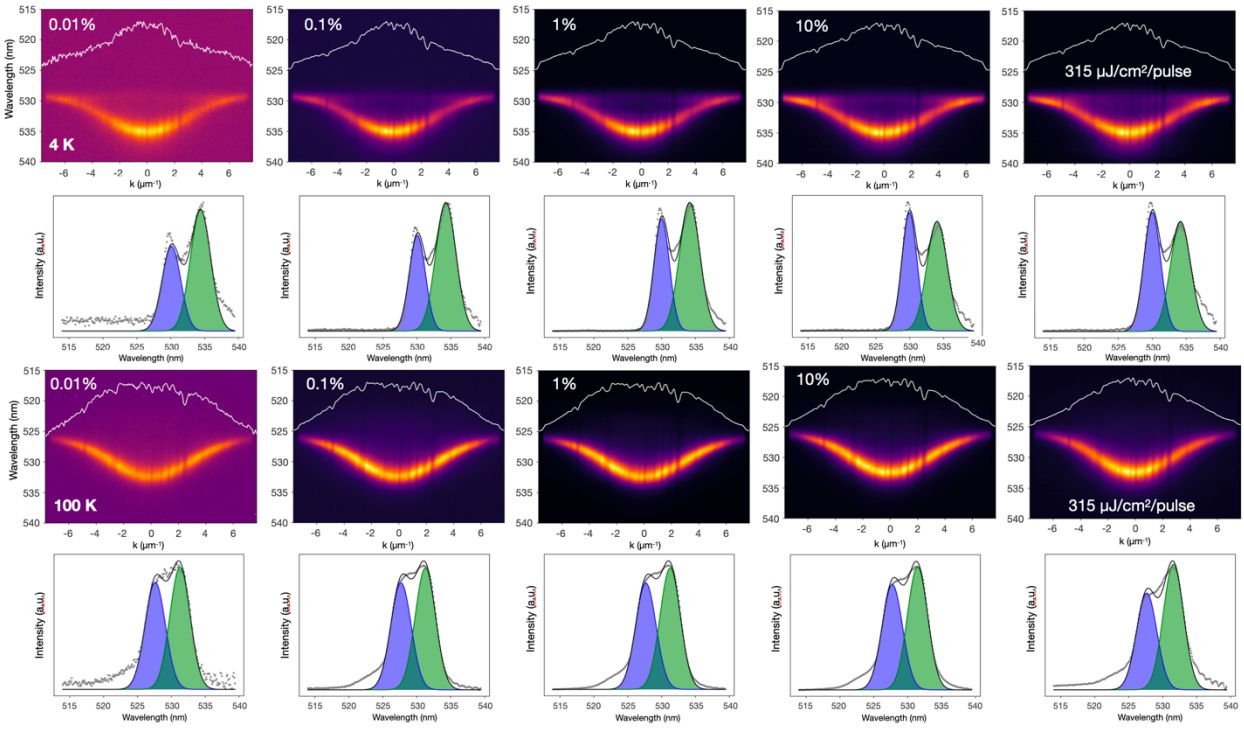

Figure 3.12: Lower polariton branch (LPB) photoluminescence (PL) ($\hbar\Omega_{Rabi}$ = 175 meV, Δ = +40 meV) as a function of excitation power spanning five orders of magnitude. The top row shows the k-space dispersion, and the bottom row shows the k-space-integrated PL with high-$k_{||}$ (high energy) and low-$k_{||}$ (low energy) spectral regions fit to determine whether the increase in power results in an increase in emission from the bottom of the LPB due to increased polariton-polariton scattering. No such trends are observed at 4 K, and only a weak increase in the low-$k_{||}$ region is seen at 100 K, indicating that polariton-polariton scattering is likely not the primary factor for the dramatic redistribution of PL to $k_{||}$ = 0 at low temperature. *Row 1,2*: 4 K power series (demonstrates a more rapid increase in high $k_{||}$ PL (blue Gaussian) than low $k_{||}$ (green Gaussian) indicating greater biexciton emission enhancement with increasing power); *Row 3,4:* 100 K power series (ratio between high $k_{||}$ (blue Gaussian) and low $k_{||}$ (green Gaussian) emission preserved).

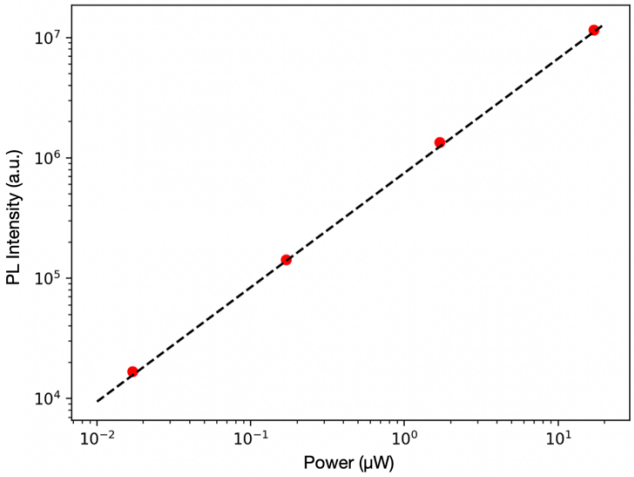

Figure 3.13: Integrated lower polariton branch PL at 4 K for $\hbar\Omega_{Rabi}$ = 260 meV spanning four orders of magnitude, revealing a slope of m = 0.95, consistent with bright exciton power dependence.[309,314,315,368]

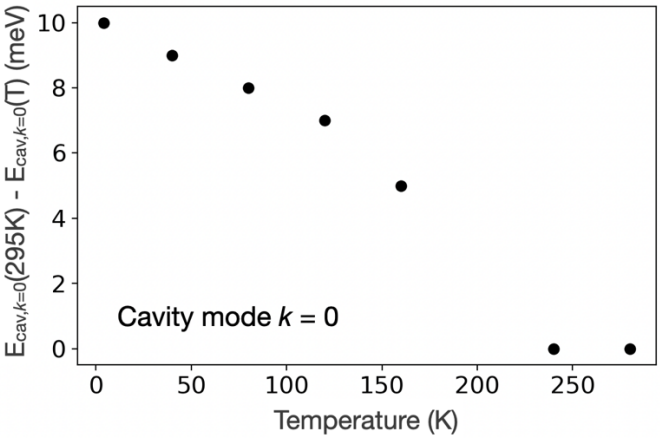

Figure 3.14: Cavity mode shift from 295 K (meV) at $k_{//}$ = 0 due to the thermal contraction of the microcavity as a function of temperature resulting in ~3 nm blue-shift with decreasing temperature.

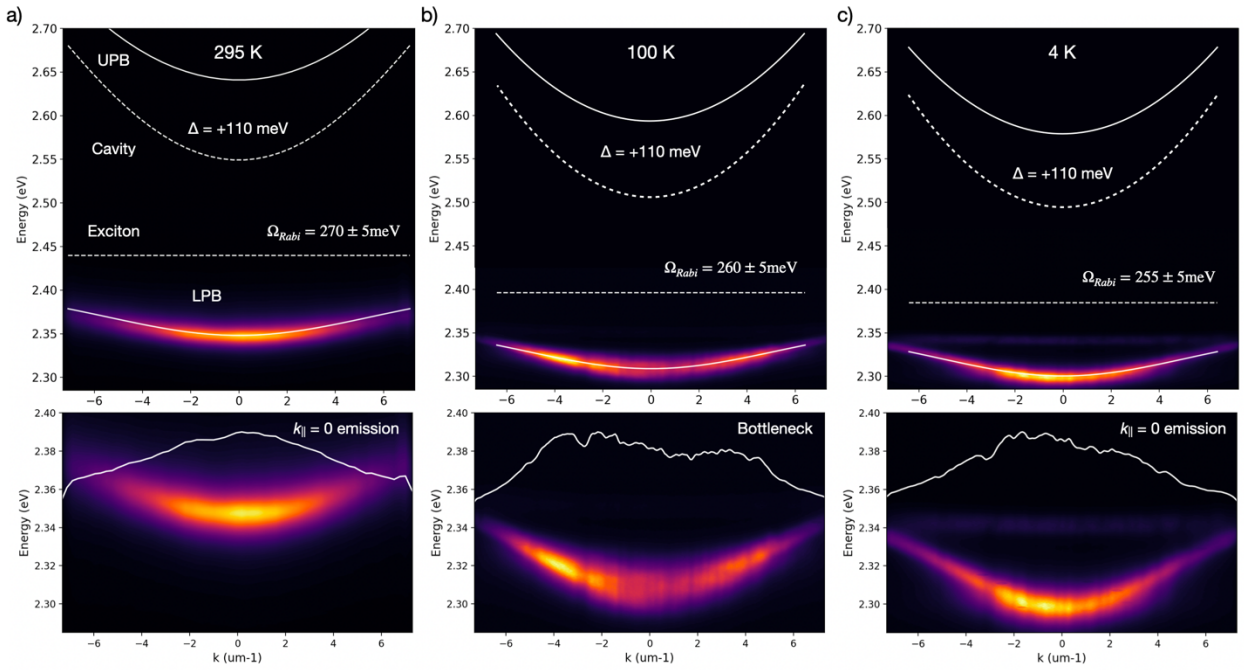

Figure 3.15: Lower polariton branch (LPB) emission for $\hbar\Omega_{\text{Rabi}}$ = 260 meV fixing the detuning at Δ = +110 meV by selecting a longer cavity length to keep E_{cav} - E_{exc} constant as the exciton energy redshifts with decreasing temperature. Dispersions (upper panels) shown for (a) 295 K, (b) 100 K, and (c) 4 K, revealing the bottleneck effect at intermediate temperatures and emission from $k_{//}$ = 0 at low temperatures (upper and lower polariton branches (solid white traces), exciton energy corresponding to the exciton absorption and bare cavity mode (dashed white traces).[287] Lower panels: LPB photoluminescence (PL) with the energy-integrated PL *k*-space distribution (white trace). We note that the bottleneck effect is more pronounced with increasing coupling strength (e.g., greater for $\hbar\Omega_{\text{Rabi}}$ = 260 meV than $\hbar\Omega_{\text{Rabi}}$ = 175 meV).

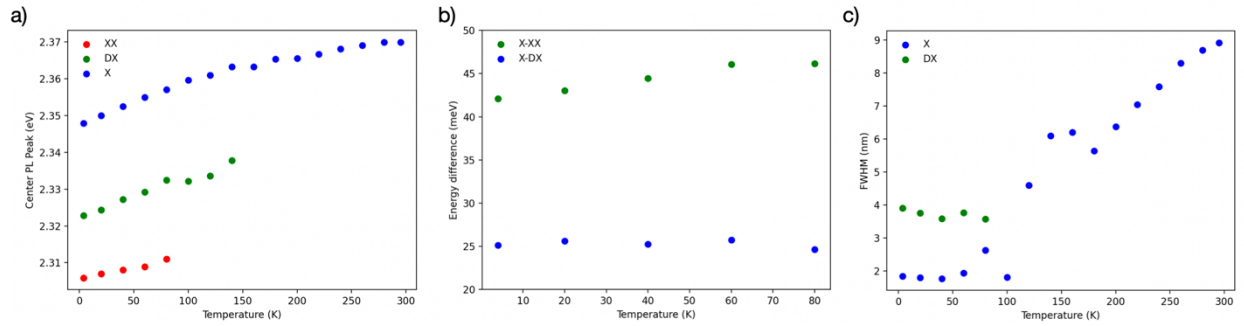

Figure 3.16: Bare 2D perovskite thin film energetics as a function of film temperature. (a) The center PL peak (in eV) for the bright exciton (blue), dark exciton (green), and biexciton

(red). (b) The difference in PL emission energy between the bright exciton and dark exciton (X-DX, blue) and bright exciton and biexciton (X-XX, green). The full-width half-maximum (FWHM, in nm) for the bright exciton (blue) and dark exciton (green, below 100 K) as a function of temperature, showing a reduction of >4x in the bright exciton FWHM.

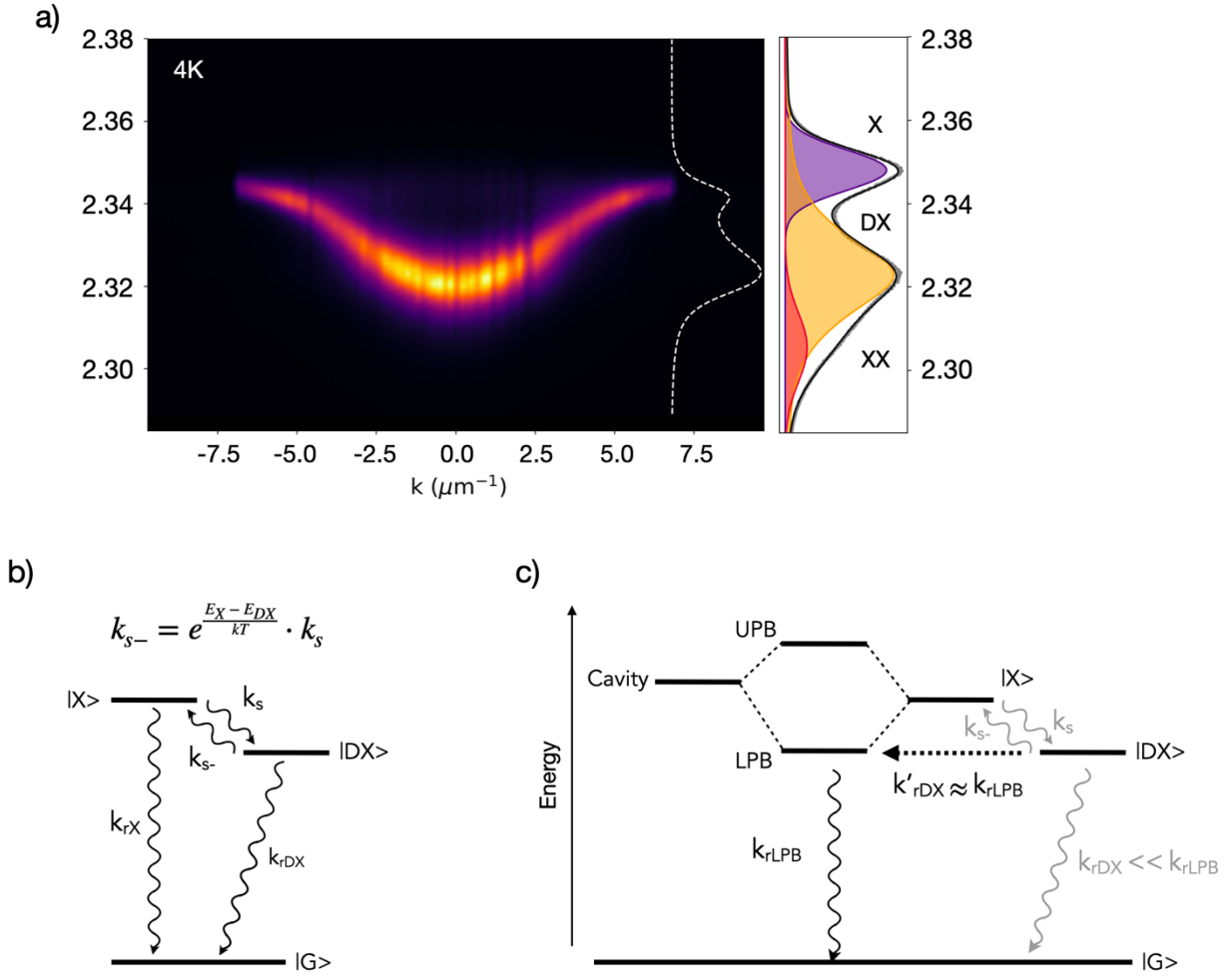

Figure 3.17: (a) 4 K lower polariton branch photoluminescence (PL) ($\hbar\Omega_{Rabi}$ = 175 meV, Δ = +45 meV) with primary emission from $k_{||}$ = 0. (b) Spin-flip process from X to DX with spin-flip rate k_s. The spin-flip back to the bright state, k_{s-}, calculated via the Arrhenius relationship as a function of temperature (modified from Kim *et al.*).[187] (c) At low-temperature in the microcavity system when k_{s-} is very slow, the strong coupling of the bright exciton to the cavity mode and resulting LPB to G polariton emission outcompetes the spin-flip process. The DX population generated immediately following photoexcitation is influenced by from the isoenergetic lower polariton branch mode (dashed arrow from DX to LPB), and can directly and rapidly emit through this resonant mode, taking on the kinetics of the strongly-coupled LPB state (k'_{rDX}) which outcompetes emission from DX directly to G (k_{rDX}).

Bright/Dark Exciton Dynamics with Photon Recycling in 2D Perovskite Films: To determine the spin flip rate from the bright to dark state, a set of coupled ODEs was solved to include microscopic reversibility in Eqs. 3.6-3.8 and photon recycling. Photon recycling is the ability for a photon emitted following radiative recombination to be waveguided within the film and re-absorbed. The probability of photon escape (P_{esc}) is calculated via Eqs. 3.9-3.10, in which the indices of refraction for the thin film, substrate, and air interface are taken into account, as well as the optical density (OD) at the wavelengths of emission.[11,20,70] For this system of a ~25 nm tick perovskite film, at 4 K, the PLQE increases 100-fold to ~77%, and the OD increases by nearly a factor of two (Figure 3.11, extrapolated).

$$\frac{dn_X}{dt} = -k_{rX}n_X - k_s n_X + e^{(E_X - E_{DX})/k_B T} \cdot k_s n_{DX} + \frac{c}{n_r}\sum_\lambda \alpha_\lambda \gamma_\lambda \quad 3.6$$

$$\frac{dn_{DX}}{dt} = -k_{rDX}n_{DX} + k_s n_{DX} - e^{(E_X - E_{DX})/k_B T} \cdot k_s n_{DX} \quad 3.7$$

$$\frac{d\gamma_\lambda}{dt} = -\frac{c}{n_r}\sum_\lambda \alpha_\lambda \gamma_\lambda + k_{rX}n_X(1 - P_{esc}) + k_{rDX}n_{DX}(1 - P_{esc}) \quad 3.8$$

where k_{rX}, k_{rDX}, and k_s are the radiative recombination constant for the high energy species, low energy species, and spin-flip rate allowing for interconversion between both species, respectively, n_X and n_{DX} are the high energy and low energy carrier concentrations, respectively, E_x and E_{DX} are the energies of the bright and dark excitons, respectively, k_B is Boltzmann's constant, c is the speed of light, α_λ is the absorption coefficient at a given wavelength, γ_λ is the photon concentration within the film for a given wavelength due to radiative recombination and photon recycling, n_r is the index of refraction, and P_{esc} the probability of a radiatively recombined photon leaving the film within the escape cone.

$$\eta_t = \frac{\Omega_{esc}}{4\pi}T \approx \frac{n_{r2}^3}{n_{r1}(n_{r1}+n_{r2})^2} \quad 3.9$$

$$P_{esc} = 10^{-\frac{OD_{PL}}{2}} \cdot \left(n_{t,2D-fs} + n_{t,2D-pmma} + 10^{-OD_{PL}} \cdot \left(n_{t,2D-fs} - n_{t,2D-pmma}\right)\right) \quad 3.10$$

where η_t is the transmission efficiency, Ω_{esc} is the solid angle of photon escape, and n_{rx} is the index of refraction of the given material (2D perovskite/fused silica interface and 2D

perovskite/PMMA interface). The transmission efficiency for both the 2D perovskite/fused silica interface and the 2D perovskite/PMMA interface is ~17%. The OD of the sister film to the microcavity active layer possessed an OD of ~0.45 at the PL emission wavelength at 4 K. Eq. 3.10 takes into account the various transmission efficiencies depending on the interface through which a photon escapes the film (in this instance, the interfaces have nearly the same index of refraction contrast). We estimate the probability of photon escape for these highly absorbing 2D thin films to be P_{esc} = 20%.

The impact of photon recycling serves to increase the steady-state carrier density, effectively increasing the average radiative lifetime within the film as compared to a film with no photon recycling.[329] In this system at low temperature, photon recycling effectively feeds the bright state reserve, increasing the pool and allowing a portion of bright excitons to spin-flip into the dark state despite fairly slow spin-flip rates. Based on the spectral overlap between absorption and emission, it is also primarily the radiatively recombined bright excitons whose emission will be re-absorbed and recycled, creating more opportunities to engage in transfer to the energetically lowest-lying dark state at low temperature. We can quantify the number of photon recycling events in the film following the method defined by Pazos-Outón et al. to determine the impact of increasing PLQE with decreasing temperature on photon recycling events in the 2D perovskite film.[11]

$$\text{Recycling events} = \frac{1}{1-f_c \cdot PLQE} \tag{3.11}$$

$$f_c = 1 - \frac{1}{4{n_r}^2} \tag{3.12}$$

where f_c is the confinement factor dictated by the index of refraction, where n_r = 1.8. The dependence of the number of recycling events on PLQE is shown in Figure 3.18, where, for a PLQE of ~77% (corresponding to 4 K thin film properties), the average number of recycling events is 3.5. In the radiative limit, for PLQE = 100%, the film can sustain 13 recycling events per photon.

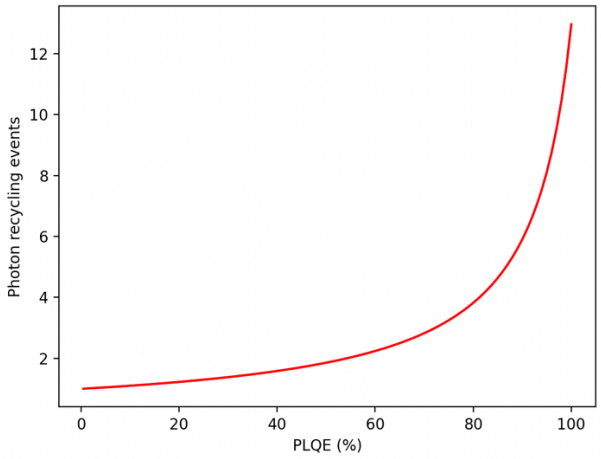

Figure 3.18: Number of photon recycling events in 2D perovskite thin film as a function of film PLQE, indicating that, for PLQE > ~50%, photon recycling events exceed 2 per photon and can contribute significantly to carrier dynamics.[329]

Bright/Dark Exciton Dynamics without Photon Recycling in 2D Perovskite Films: The dynamics can alternatively be simulated excluding the effects of photon recycling (Eq. 3.13-3.14). In this way, the bright exciton lifetime is required to exceed 200 ps for agreement with the raw data (Figure 3.19).

$$\frac{dn_X}{dt} = -k_{rX}n_X - k_s n_X + e^{(E_X - E_{DX})/k_B T} \cdot k_s n_{DX} \quad 3.13$$

$$\frac{dn_{DX}}{dt} = -k_{rDX}n_{DX} + k_s n_{DX} - e^{(E_X - E_{DX})/k_B T} \cdot k_s n_{DX} \quad 3.14$$

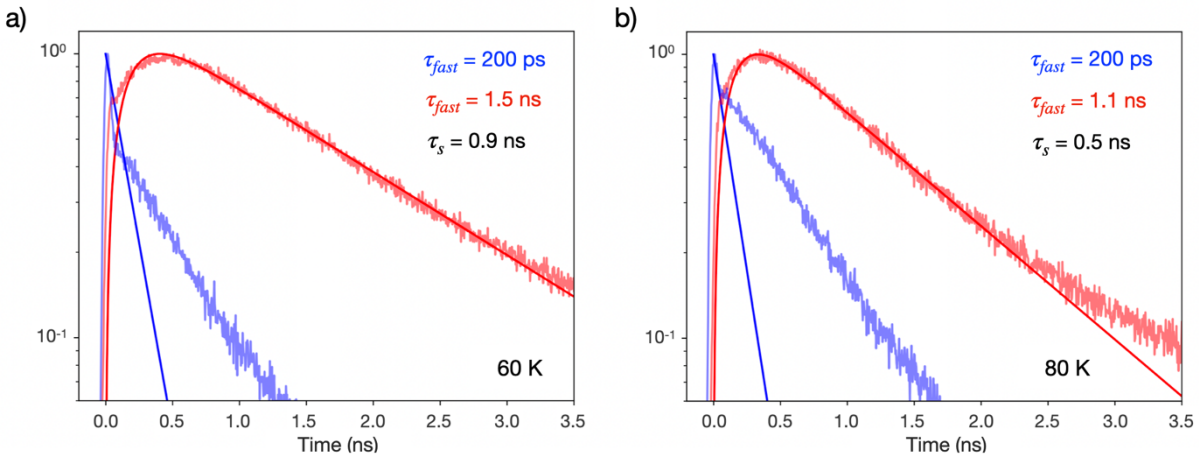

Figure 3.19: Lifetimes of the bright exciton (X) emission (blue) and dark exciton (DX) emission (red) in 2D perovskite films simulated with Eqs. 3.13-3.14, excluding photon recycling, at (a) 60 K and (b) 80 K.

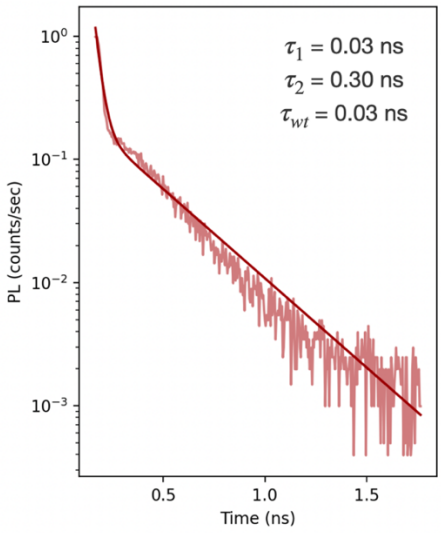

Figure 3.20: Instrument response function of the Toptica wavelength-tunable 80 MHz sub-ps laser and MPD detector. Fits for each trace above (τ_1 = short decay component, τ_2 = long decay component, τ_{wt} = weighted pulse duration [ns]).

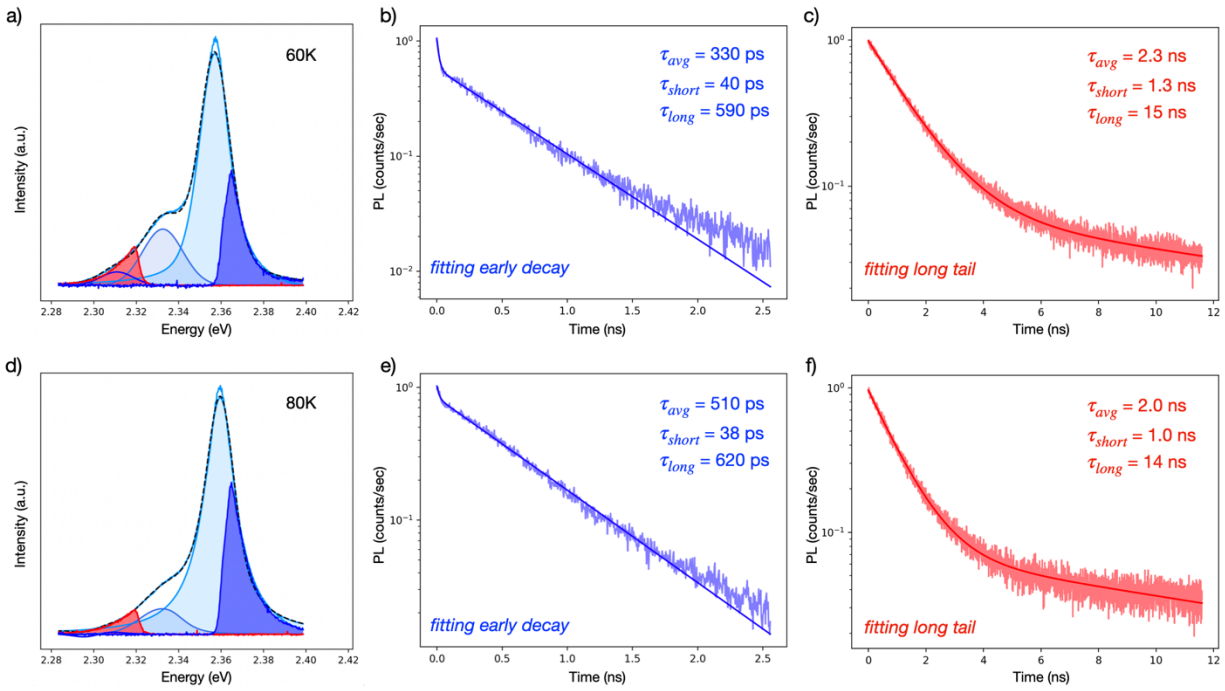

Figure 3.21: (a) 60 K photoluminescence (PL) spectrum of the 2D film with multi-peak fitting and spectrally filtered regions highlighted in dark blue/dark red. (b) Time-resolved photoluminescence (TRPL) trace with spectral filter (short-pass) showing the short lifetime, fit with an exponential, attributed to the bright exciton (40 ps) and (c) (long-pass) showing only the long tail of the dark exciton (truncating the energy transfer delayed emission portion) to quantify the long component lifetime (15 ns). (d-f) PL spectrum at 80 K and extracted high energy short lifetime, fit with an exponential, of 38 ps. The long tail of the dark exciton decreases in lifetime at elevated temperature, with an exponential fit of 14 ns.

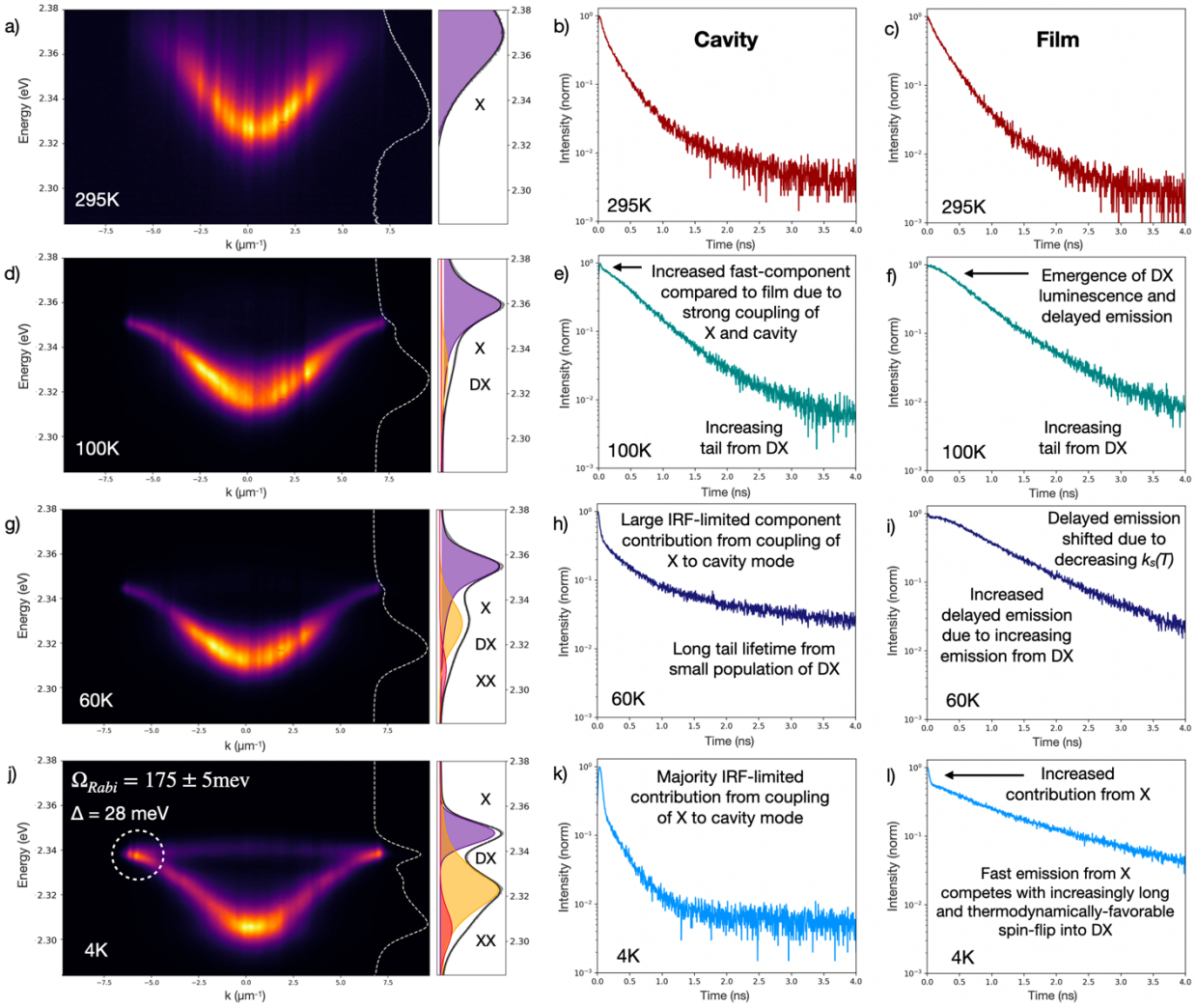

Figure 3.22: The lower polariton branch (LPB) emission from the microcavity ($\hbar\Omega_{\mathrm{Rabi}}$ = 175 meV, Δ = 28 meV, right panel bare 2D film PL spectrum showing bright exciton (X), dark exciton (DX), and biexciton (XX) emission) with time-resolved photoluminescence (TRPL) decay traces for the corresponding LPB cavity emission and bare 2D film at (a,b,c) 295 K, (d,e,f) 100 K, (g,h,i) 60 K, and (j,k,l) 4 K (white dashed circle indicating biexciton-assisted relaxation signature of high $k_{//}$ PL257). As temperature decreases, the X emission lifetime decreases and the DX emission emerges with an increasingly long lifetime, visible as a short-timescale fast component with delayed emission into a longer tail ((e,f) green trace, 100 K). In the cavity (e), the extent of delayed emission is reduced as compared to the bare 2D film (f), and the fast component contribution increased due to the additional pathway of coupling the X and cavity mode to form the strongly coupled short-lifetime polariton emissive state competing with the spin-flip from X to DX. For the bare 2D film, further reductions in temperature show (i,l) the X emission contribution increasing at early timescales as its emissive lifetime decreases and the spin-flip rate ($k_s(T)$) slows, with the DX demonstrating an increasingly long emissive lifetime and $k_s(T)$ additionally slowed via the Arrhenius factor

(Figure 3.18b). Conversely, in the cavity, the IRF-limited strong coupling emission of X and the cavity mode competes with the spin-flip and begins to dominate the TRPL decay dynamics at 60 K (h), with weak emission contribution to the decay from the DX state resulting in a long lifetime tail. (k) At 4 K in the cavity, the delayed emission due to the slow k_s(4K) and long tail from the DX is not observed, showing nearly exclusively IRF-limited strongly-coupled emission between the X and cavity mode.

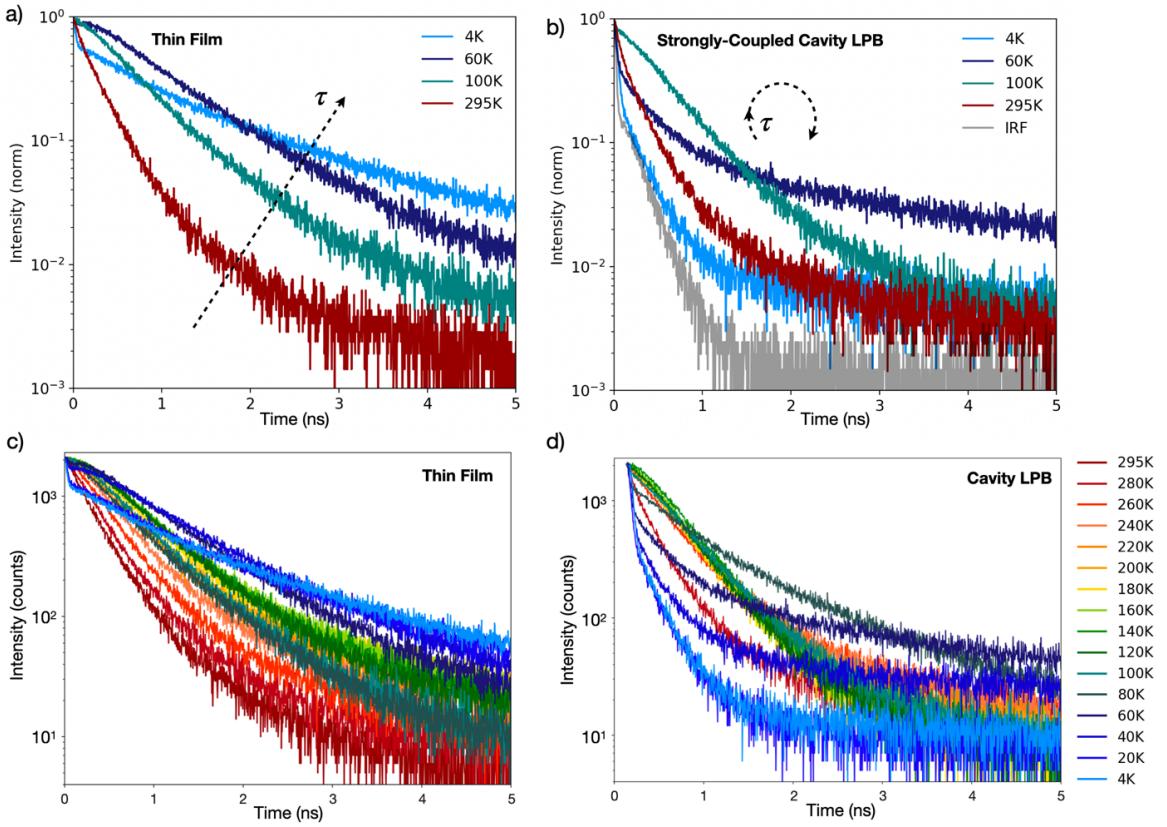

Figure 3.23: (a) The bare 2D perovskite film time-resolved photoluminescence decay (TRPL) traces as a function of temperature show a 295 K lifetime of τ_{295K} = 350 ps, increasing with decreasing temperature. With the emergence of the dark exciton (DX) emission in the PL spectrum, the film lifetime trace develops an initial fast decay component attributed to the bright exciton (X) with a longer lifetime component attributed to the DX. (b) The strongly-coupled microcavity ($\hbar\Omega_{Rabi}$ = 175 meV, Δ = +28 meV) lower polariton branch (LPB) emission demonstrates similar trends to the thin film at high temperatures, but deviates sharply at low temperatures, exhibiting only the fast, IRF-limited (40 ps) lifetime of the bare 2D film initial fast decay component. (c) Temperature-dependent 2D thin film TRPL traces with finer temperature steps, showing that, with decreasing temperature, the film lifetime increases to τ_{295K} = 740 ps, consistent with a reduction in non-radiative pathways which quench the lifetime. For temperatures between 180 K and 100 K, we observe reduced emission at early timescales.

Below 100 K, with the prominent emergence of the DX, and subsequently XX, emission in the PL spectrum, the film lifetime trace develops an early fast decay component before the flat, delayed emission leading into a long tail. This multi-component lifetime behavior becomes quite pronounced as the system approaches 4 K (light blue trace), and has been observed by Fang *et al.*[313] (d) The cavity LPB emission with finer temperature steps demonstrates similar trends to the thin film at high temperatures, but deviates sharply at low temperatures, exhibiting only the fast, IRF-limited (40 ps) lifetime of the bare film initial fast decay component attributed to X.

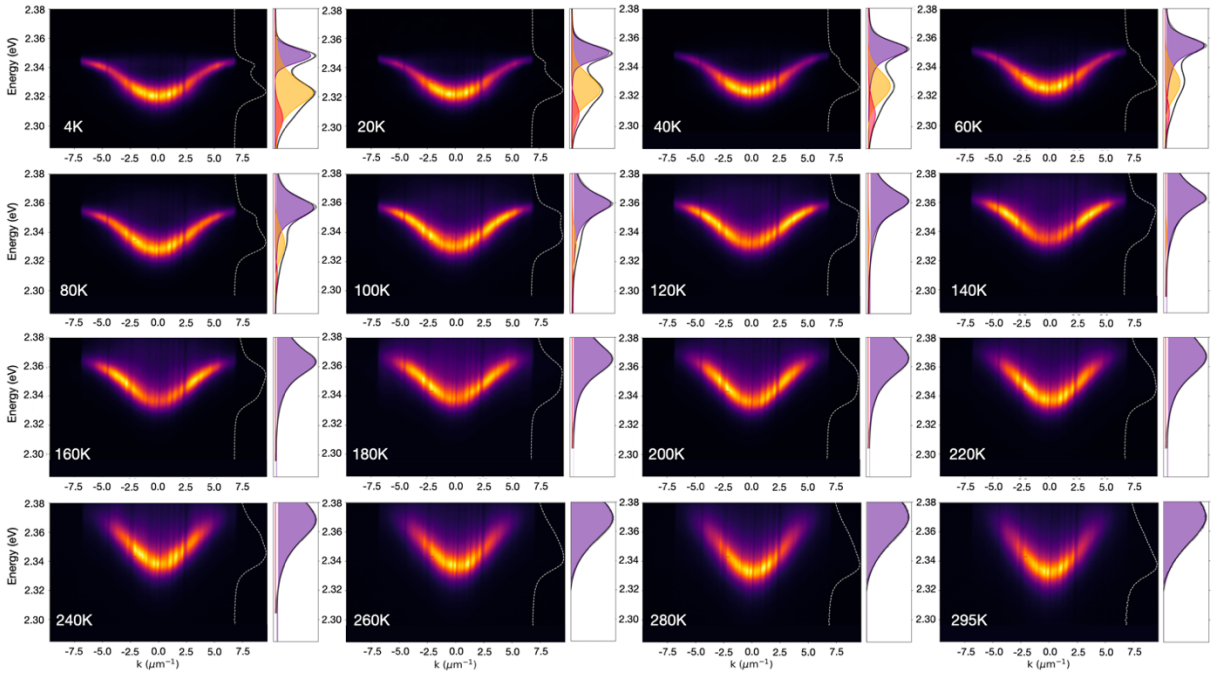

Figure 3.24: Photoluminescence (normalized) k-space temperature series ($\hbar\Omega_{\mathrm{Rabi}}$ = 175 meV) from 4 K (upper left) to 295 K (lower right) for Δ = +45 meV.

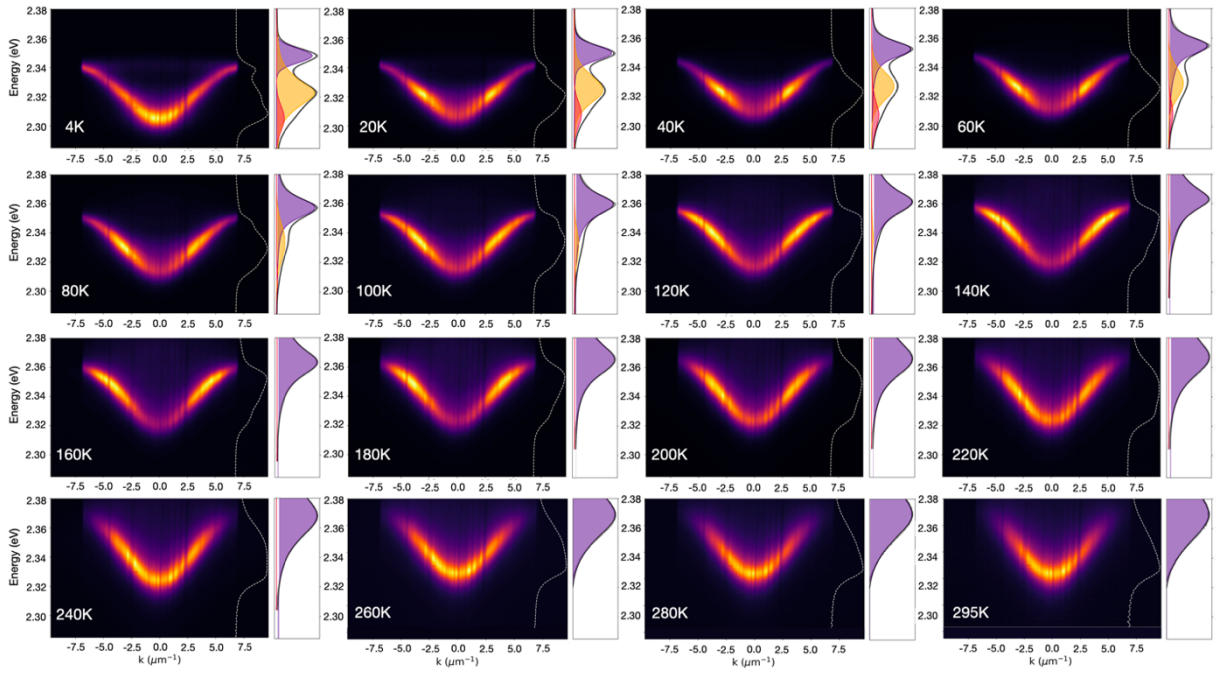

Figure 3.25: Photoluminescence (normalized) k-space temperature series ($\hbar\Omega_{\mathrm{Rabi}}$ = 175 meV) from 4 K (upper left) to 295 K (lower right) for Δ = +28 meV.

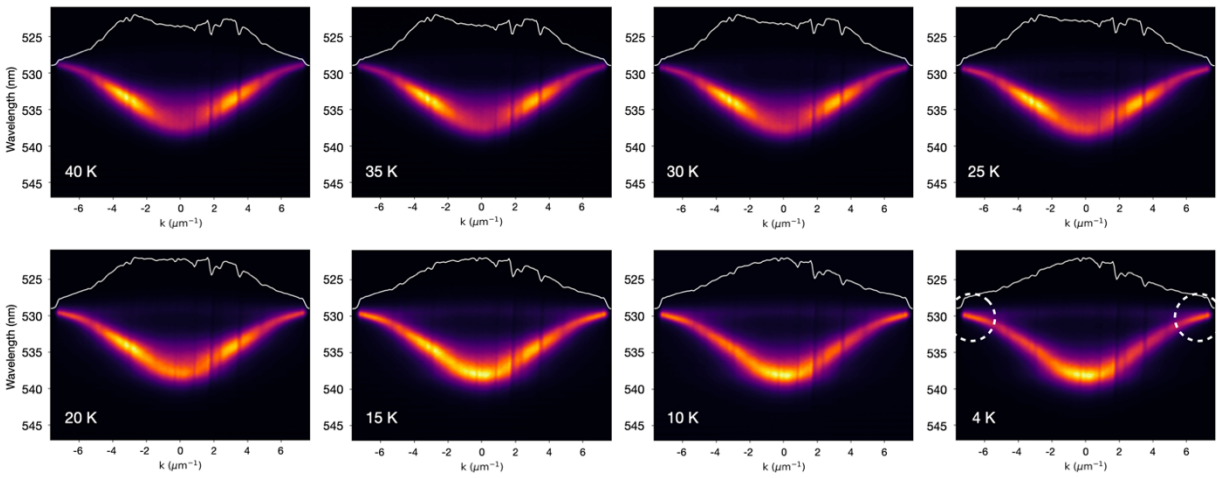

Figure 3.26: Photoluminescence (normalized) k-space temperature series ($\hbar\Omega_{\mathrm{Rabi}}$ = 175 meV) from 40 K (upper left) to 4 K (lower right) for Δ = +28 meV with temperature increments of 5 K to resolve the suppression of the bottleneck and emergence of uncoupled exciton PL and high $k_{||}$ polariton PL from biexciton-assisted relaxation mechanisms.

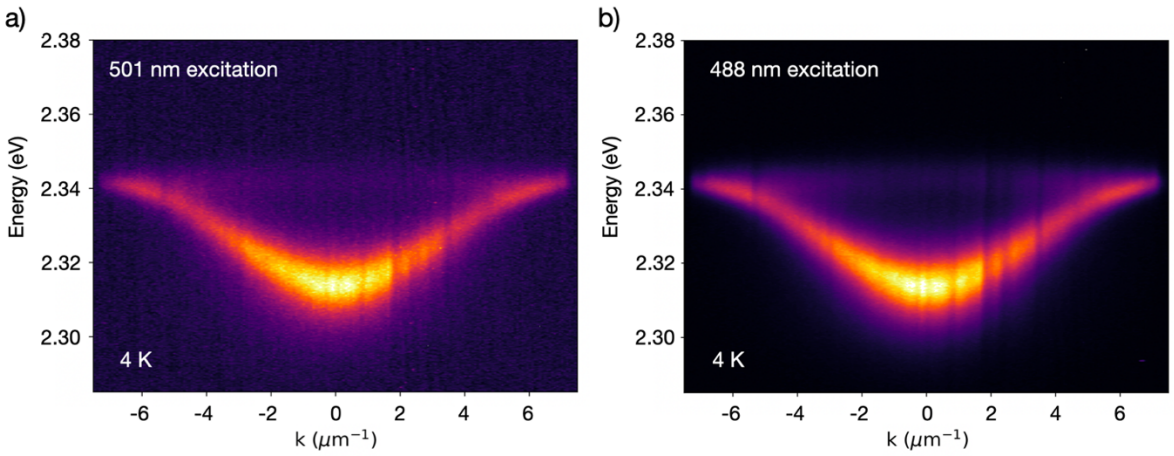

Figure 3.27: 4 K lower polariton branch photoluminescence (PL, normalized) ($\hbar\Omega_{\mathrm{Rabi}}$ = 175 meV, Δ = +35 meV) with 501 nm excitation and 488 nm excitation showing no change to the distribution of PL in k-space as a function of excitation wavelength (e.g., via mechanisms such as resonant upper polariton branch excitation). Differences in k-space contrast stem from the decreased absorption cross section at 501 nm as compared to 488 nm.

3.10. CHAPTER-SPECIFIC ACKNOWLEDGEMENTS

This work is supported by the TATA-MIT GridEdge Solar Research program. This material is based upon work supported by the National Science Foundation Graduate Research Fellowship under Grant No. (1122374). This project has received funding from the European Research Council (ERC) under the European Union's Horizon 2020 research and innovation programme ERC HYNANO (grant agreement n° 802862). M.L. acknowledges support from MIT's Hugh Hampton Young fellowship and Samsung Advanced Institute of Technology. A.E.K.K acknowledges support from the US Department of Energy, Office of Basic Energy Sciences, Division of Materials Sciences and Engineering under award no. DE-SC0021650. J.D. acknowledges support from the NSERC Postgraduate Scholarship program and U.S. Department of Energy. J.D. and K.A.N. acknowledge support from the Army Research Laboratory, through the Institute for Soldier Nanotechnologies, under Cooperative Agreement Number W911NF-18-2-0048. U.B. acknowledges support from the National Science Foundation, Award Number CHE-2108357. A.H.P. acknowledges support from the U.S. Department of Energy, Office of Science, Basic Energy Sciences under Award DE-SC0021650, and the Natural Sciences and Engineering Research Council of Canada (NSERC PDF). We thank Thomas Mahony for valuable discussions and insights; Roberto Brenes for spectrometer software integration and integrating sphere calibration; and Charles Settens for assistance with XRD.

4.1.1. High-Efficiency Photovoltaics

In this work, we quantify the impact of photon recycling on perovskite solar cell performance, demonstrating power conversion efficiency enhancements of 2% in the radiative limit due to harnessing photon recycling and maximizing corresponding open-circuit voltage gains. For practical target non-radiative recombination rates in perovskite thin films of $k_1 < 1x10^4\ s^{-1}$, power conversion efficiency (PCE) gains due to photon recycling of up to 1.79% are possible. To achieve these non-radiative rates from an active layer material quality perspective, further passivation strategies to effectively reduce surface defects are needed. From a device perspective, optimizing charge transport layers to minimize interfacial recombination and parasitic absorption, enhance carrier extraction, and optimize band alignment will be important in realizing photon recycling performance improvements. Additional device optimization via the incorporation of highly reflective back-contacts, as was done for high-efficiency GaAs photovoltaics, will further capitalize on photon recycling-based open-circuit voltage and PCE increases.

Additionally, large-scale studies with statistical significance correlating active layer material optical properties to ultimate device performance would allow for the rapid screening of novel perovskite formulations and evaluation of their potential in a device setting. By comparing the theoretical performance of a bare film to the experimental device performance, it is possible to deconvolute the various non-radiative processes introduced by device stack layers and processing conditions to push perovskite solar cell performance closer to the theoretical limit.

4.1.2. Cd-Free Light-Emitting Devices

In the search for Cd-free, environmentally benign light-emitting technologies, InP-based quantum dots (QDs) have risen to the fore as a promising alternative to heavy metal-containing QD formulations. Here, we explore the energy and charge transport properties of InP/ZnSe/ZnS QD thin films and light-emitting diodes (QD-LEDs) to better understand the impact of increasing electric field on Förster resonance energy transfer processes and spectral diffusion. We quantify two populations of QDs within the inhomogeneous thin film distribution characterized by mobile and immobile carriers – two subsets in which one responds to an electric field and the other is less perturbed by the field. The differing subsets of QDs and effect of field screening from field-ionized, photogenerated or injected charges results in lower photoluminescence (PL) quenching efficiencies in reverse-biased QD-LEDs than has been demonstrated for Cd-based QDs. Even so, we report, to the best of our knowledge, the highest PL quenching efficiency for InP-based QDs of 87% at 15 V in reverse bias (2.3 MV/cm). To achieve a greater extent of PL quenching and PL recovery post-bias, we propose the optimization of the QD thin film to shift the population distribution to form mobile/immobile QDs to largely mobile QDs that respond quickly to applied fields. Reducing field-enhanced charge build-up and Auger trion recombination by bandgap engineering and passivation strategies will further enhance the PL quenching efficiency of InP-based QDs.

Towards low-threshold QD ASE and electrically injected lasers, further work is required to create deterministic arrays of identical QD mesas incorporated into an LED structure to ensure lateral cavity dimensions promoting primary emission from the fundamental mode are resonant with the QD gain region. Such devices require a high degree of control of spectral and spatial alignment. Higher Q cavities can further reduce ASE thresholds and result in greater Purcell enhancement, but such architectures face challenges with LED integration. By utilizing semi-transparent metallic mirrors, the mechanism for mode modification and control towards ASE can be used in microcavity light emitting devices with limited parasitic absorption benefiting from high color purity and directional emission.

4.1.3. Microcavity Exciton-Polaritons

Combining and expanding upon the principles from the perovskite photon recycling and microcavity quantum dot (QD) studies, we investigate two-dimensional perovskites in metallic microcavities in the strong coupling regime to generate room-temperature exciton-polaritons (polaritons). We show, to the best of our knowledge, record exciton-photon coupling strengths in planar $(C_6H_5(CH_2)_2NH_3)_2PbI_4$ (PEA_2PbI_4) perovskite microcavities with a Rabi splitting of $\hbar\Omega_{Rabi} = 260 \pm 5$ meV. We demonstrate novel solution-processed perovskite wedged microcavities in which the cavity detuning and resulting polariton exciton/photon fraction can be dynamically changed. For the first time, we reveal temperature-dependent 2D perovskite polariton photophysics, highlighting material-specific LO-phonon-mediated polariton scattering pathways, biexciton-assisted relaxation pathways, and dark state intracavity pumping schemes. These insights can be used to inform materials and microcavity design targeting efficient polariton scattering and relaxation for low-threshold Bose-Einstein condensation.

Towards condensation, we propose the use of high-quality factor microcavities to extend the polariton lifetime and enable low-threshold condensation by capitalizing on these intrinsic material relaxation pathways. Additionally, improving 2D perovskite multi-excitonic PL quantum efficiencies and reducing higher order non-radiative processes like exciton-exciton annihilation at high fluence would further enable the generation of sufficient polariton densities for condensation at room temperature. Additionally, towards electrically-injected polaritons, the metallic microcavity architecture presented in this work affords ready incorporation into microcavity LED structures employing 2D perovskites as the emissive layer, optically-inert organic transport layers, and reflective metallic top and semi-transparent bottom electrodes.

References

1. Park, N. G. Perovskite solar cells: An emerging photovoltaic technology. *Materials Today* vol. 18 (2015).

2. Jung, H. S. & Park, N. G. Perovskite solar cells: From materials to devices. *Small* vol. 11 (2015).

3. Min, H. *et al.* Perovskite solar cells with atomically coherent interlayers on SnO2 electrodes. *Nature* **598**, (2021).

4. Wang, R. *et al.* A Review of Perovskites Solar Cell Stability. *Advanced Functional Materials* vol. 29 (2019).

5. Pazos-Outón, L. M., Xiao, T. P. & Yablonovitch, E. Fundamental Efficiency Limit of Lead Iodide Perovskite Solar Cells. *Journal of Physical Chemistry Letters* **9**, 1703–1711 (2018).

6. Yablonovitch, E. Lead halides join the top optoelectronic league. *Science (1979)* **351**, 1401 (2016).

7. Miller, O. D. & Yablonovitch, E. Photon extraction: the key physics for approaching solar cell efficiency limits. **880807**, 880807 (2013).

8. Miller, O. D., Yablonovitch, E. & Kurtz, S. R. Strong internal and external luminescence as solar cells approach the Shockley-Queisser limit. *IEEE Journal of Photovoltaics* **2**, 303–311 (2012).

9. Steiner, M. A. *et al.* Optical enhancement of the open-circuit voltage in high quality GaAs solar cells. *Journal of Applied Physics* **113**, (2013).

10. Walker, A. W. *et al.* Impact of Photon Recycling on GaAs Solar Cell Designs. *IEEE Journal of Photovoltaics* **5**, 1636–1645 (2015).

11. Pazos-Outon, L. M. *et al.* Photon recycling in lead iodide perovskite solar cells. *Science (1979)* **351**, 1430–1433 (2016).

12. Fang, Y., Wei, H., Dong, Q. & Huang, J. Quantification of re-Absorption and re-emission processes to determine photon recycling efficiency in perovskite single crystals. *Nature Communications* **8**, 14417 (2017).

13. Tress, W. Perovskite Solar Cells on the Way to Their Radiative Efficiency Limit – Insights Into a Success Story of High Open-Circuit Voltage and Low Recombination. *Advanced Energy Materials* **7**, (2017).

14. Yang, W. S. *et al.* High-performance photovoltaic perovskite layers fabricated through intramolecular exchange. *Science (1979)* **348**, (2015).

15. Kim, H. S. *et al.* Lead iodide perovskite sensitized all-solid-state submicron thin film mesoscopic solar cell with efficiency exceeding 9%. *Scientific Reports* **2**, (2012).

16. Lee, M. M., Teuscher, J., Miyasaka, T., Murakami, T. N. & Snaith, H. J. Efficient hybrid solar cells based on meso-superstructured organometal halide perovskites. *Science (1979)* **338**, (2012).

17. Kojima, A., Teshima, K., Shirai, Y. & Miyasaka, T. Organometal halide perovskites as visible-light sensitizers for photovoltaic cells. *J Am Chem Soc* **131**, (2009).

18. Dequilettes, D. W. *et al.* Photoluminescence Lifetimes Exceeding 8 μs and Quantum Yields Exceeding 30% in Hybrid Perovskite Thin Films by Ligand Passivation. *ACS Energy Letters* **1**, 438–444 (2016).

19. Christians, J. A. *et al.* Tailored interfaces of unencapsulated perovskite solar cells for >1,000 hour operational stability. *Nature Energy* **3**, 68–74 (2018).

20. Richter, J. M. *et al.* Enhancing photoluminescence yields in lead halide perovskites by photon recycling and light out-coupling. *Nature Communications* **7**, (2016).

21. Johnston, M. B. & Herz, L. M. Hybrid Perovskites for Photovoltaics: Charge-Carrier Recombination, Diffusion, and Radiative Efficiencies. *Accounts of Chemical Research* **49**, 146–154 (2016).

22. Abdi-Jalebi, M. *et al.* Maximizing and stabilizing luminescence from halide perovskites with potassium passivation. *Nature* **555**, 497–501 (2018).

23. deQuilettes, D. W. *et al.* Maximizing the external radiative efficiency of hybrid perovskite solar cells. *Pure and Applied Chemistry* **92**, 697–706 (2020).

24. Saliba, M. *et al.* Cesium-containing triple cation perovskite solar cells: Improved stability, reproducibility and high efficiency. *Energy and Environmental Science* **9**, 1989–1997 (2016).

25. Panfil, Y. E., Oded, M. & Banin, U. Colloidal Quantum Nanostructures: Emerging Materials for Display Applications. *Angewandte Chemie - International Edition* vol. 57 (2018).

26. Dai, X., Deng, Y., Peng, X. & Jin, Y. Quantum-Dot Light-Emitting Diodes for Large-Area Displays: Towards the Dawn of Commercialization. *Advanced Materials* vol. 29 (2017).

27. Shirasaki, Y., Supran, G. J., Bawendi, M. G. & Bulović, V. Emergence of colloidal quantum-dot light-emitting technologies. *Nature Photonics* vol. 7 (2013).

28. Kim, T. H., Jun, S., Cho, K. S., Choi, B. L. & Jang, E. Bright and stable quantum dots and their applications in full-color displays. *MRS Bulletin* **38**, (2013).

29. Klimov, V. I. *Nanocrystal Quantum dots -2nd edition. CRC Press* (2010).

30. Won, Y. H. *et al.* Highly efficient and stable InP/ZnSe/ZnS quantum dot light-emitting diodes. *Nature* **575**, (2019).

31. Shirasaki, Y., Supran, G. J., Bawendi, M. G. & Bulović, V. Emergence of colloidal quantum-dot light-emitting technologies. *Nature Photonics* vol. 7 (2013).

32. Hahm, D. *et al.* Environmentally benign nanocrystals: challenges and future directions. *Journal of Information Display* **20**, (2019).

33. Kim, T. *et al.* Efficient and stable blue quantum dot light-emitting diode. *Nature* **586**, (2020).

34. Kim, T., Won, Y. H., Jang, E. & Kim, D. Negative Trion Auger Recombination in Highly Luminescent InP/ZnSe/ZnS Quantum Dots. *Nano Letters* **21**, (2021).

35. Chen, J., Hardev, V., Hartlove, J., Hofler, J. & Lee, E. A high-efficiency wide-color-gamut solid-state backlight system for lcds using quantum dot enhancement film. in *Digest of Technical Papers - SID International Symposium* vol. 43 (2012).

36. Jang, E. *et al.* White-light-emitting diodes with quantum dot color converters for display backlights. *Advanced Materials* **22**, (2010).

37. Bozyigit, D., Yarema, O. & Wood, V. Origins of low quantum efficiencies in quantum dot LEDs. *Advanced Functional Materials* **23**, (2013).

38. Rowland, C. E. *et al.* Electric Field Modulation of Semiconductor Quantum Dot Photoluminescence: Insights into the Design of Robust Voltage-Sensitive Cellular Imaging Probes. *Nano Letters* **15**, (2015).

39. Lagoudakis, K. *The physics of exciton-polariton condensates. The Physics of Exciton-Polariton Condensates* (2013). doi:10.1201/b15531.

40. Ballarini, D. *et al.* All-optical polariton transistor. *Nature Communications* **4**, 1778 (2013).

41. Deng, H., Haug, H. & Yamamoto, Y. Exciton-polariton Bose-Einstein condensation. *Reviews of Modern Physics* (2010) doi:10.1103/RevModPhys.82.1489.

42. Hopfield, J. J. Theory of the contribution of excitons to the complex dielectric constant of crystals. *Physical Review* **112**, (1958).

43. Weisbuch, C., Nishioka, M., Ishikawa, A. & Arakawa, Y. Observation of the coupled exciton-photon mode splitting in a semiconductor quantum microcavity. *Physical Review Letters* **69**, (1992).

44. Sun, Y. *et al.* Direct measurement of polariton-polariton interaction strength. *Nature Physics* **13**, (2017).

45. Liew, T. C. H. *et al.* Exciton-polariton integrated circuits. *Physical Review B - Condensed Matter and Materials Physics* (2010) doi:10.1103/PhysRevB.82.033302.

46. Sanvitto, D. *et al.* Persistent currents and quantized vortices in a polariton superfluid. *Nature Physics* (2010) doi:10.1038/nphys1668.

47. Kéna-Cohen, S. & Forrest, S. R. Room-temperature polariton lasing in an organic single-crystal microcavity. *Nature Photonics* (2010) doi:10.1038/nphoton.2010.86.

48. Amo, A. *et al.* Collective fluid dynamics of a polariton condensate in a semiconductor microcavity. *Nature* (2009) doi:10.1038/nature07640.

49. Anderson, M. H., Ensher, J. R., Matthews, M. R., Wieman, C. E. & Cornell, E. A. Observation of Bose-Einstein condensation in a dilute atomic vapor. *Science (1979)* **269**, (1995).

50. Davis, K. B. *et al.* Bose-Einstein condensation in a gas of sodium atoms. *Physical Review Letters* **75**, (1995).

51. Kasprzak, J. *et al.* Bose-Einstein condensation of exciton polaritons. *Nature* **443**, 409–414 (2006).

52. Bouteyre, P. *et al.* Room temperature cavity polaritons with 3D hybrid perovskite - Towards low cost polaritonic devices. 1–7.

53. Song, J. H., He, Y., Nurmikko, A. V., Tischler, J. & Bulovic, V. Exciton-polariton dynamics in a transparent organic semiconductor microcavity. *Physical Review B - Condensed Matter and Materials Physics* (2004) doi:10.1103/PhysRevB.69.235330.

54. Tischler, J. R., Bradley, M. S., Bulović, V., Song, J. H. & Nurmikko, A. Strong coupling in a microcavity LED. *Physical Review Letters* (2005) doi:10.1103/PhysRevLett.95.036401.

55. Tischler, J. R., Bradley, M. S. & Bulović, V. Critically coupled resonators in vertical geometry using a planar mirror and a 5 nm thick absorbing film. *Optics Letters* (2006) doi:10.1364/OL.31.002045.

56. Zhang, Q. *et al.* Highly efficient resonant coupling of optical excitations in hybrid organic/inorganic semiconductor nanostructures. *Nature Nanotechnology* (2007) doi:10.1038/nnano.2007.253.

57. Tischler, J. R. *et al.* Solid state cavity QED: Strong coupling in organic thin films. *Organic Electronics: physics, materials, applications* (2007) doi:10.1016/j.orgel.2007.01.008.

58. Akselrod, G. M., Tischler, Y. R., Young, E. R., Nocera, D. G. & Bulovic, V. Exciton-exciton annihilation in organic polariton microcavities. *Physical Review B - Condensed Matter and Materials Physics* (2010) doi:10.1103/PhysRevB.82.113106.

59. Fieramosca, A. *et al.* Two-Dimensional hybrid perovskites sustaining strong polariton interactions at room temperature. 1–16 (2018) doi:arXiv:1811.04041v1.

60. Tang, J. *et al.* Room temperature exciton–polariton Bose–Einstein condensation in organic single-crystal microribbon cavities. *Nature Communications* **12**, (2021).

61. Plumhof, J. D., Stöferle, T., Mai, L., Scherf, U. & Mahrt, R. F. Room-temperature Bose-Einstein condensation of cavity exciton-polaritons in a polymer. *Nature Materials* **13**, (2014).

62. Spencer, M. S. *et al.* Spin-orbit–coupled exciton-polariton condensates in lead halide perovskites. *Science Advances* **7**, (2021).

63. Brenes, R. *et al.* Metal Halide Perovskite Polycrystalline Films Exhibiting Properties of Single Crystals. *Joule* **1**, 155–167 (2017).

64. Du, W., Zhang, S., Zhang, Q. & Liu, X. Recent Progress of Strong Exciton–Photon Coupling in Lead Halide Perovskites. *Advanced Materials* (2018) doi:10.1002/adma.201804894.

65. Lanty, G., Bréhier, A., Parashkov, R., Lauret, J. S. & Deleporte, E. Strong exciton-photon coupling at room temperature in microcavities containing two-dimensional layered perovskite compounds. *New Journal of Physics* (2008) doi:10.1088/1367-2630/10/6/065007.

66. Su, R. *et al.* Room-Temperature Polariton Lasing in All-Inorganic Perovskite Nanoplatelets. *Nano Letters* (2017) doi:10.1021/acs.nanolett.7b01956.

67. Wang, J. *et al.* Room Temperature Coherently Coupled Exciton Polaritons in Two-Dimensional Organic-Inorganic Perovskite. *ACS Nano* (2018) doi:10.1021/acsnano.8b03737.

68. García-Benito, I. *et al.* Fashioning Fluorous Organic Spacers for Tunable and Stable Layered Hybrid Perovskites. *Chemistry of Materials* (2018) doi:10.1021/acs.chemmater.8b03377.

69. Chakraborty, R. & Nag, A. Correlation of Dielectric Confinement and Excitonic Binding Energy in 2D Layered Hybrid Perovskites Using Temperature Dependent Photoluminescence. *Journal of Physical Chemistry C* **124**, (2020).

70. Brenes, R., Laitz, M., Jean, J., Dequilettes, D. W. & Bulović, V. Benefit from Photon Recycling at the Maximum-Power Point of State-of-the-Art Perovskite Solar Cells. *Physical Review Applied* (2019) doi:10.1103/PhysRevApplied.12.014017.

71. Ahrenkiel, R. K. *et al.* Ultralong minority-carrier lifetime epitaxial GaAs by photon recycling. *Applied Physics Letters* **55**, 1088–1090 (1989).

72. Braun, A., Katz, E. A., Feuermann, D., Kayes, B. M. & Gordon, J. M. Photovoltaic performance enhancement by external recycling of photon emission. *Energy and Environmental Science* **6**, 1499–1503 (2013).

73. Staub, F. *et al.* Beyond Bulk Lifetimes: Insights into Lead Halide Perovskite Films from Time-Resolved Photoluminescence. *Physical Review Applied* **6**, 044017 (2016).

74. Staub, F., Kirchartz, T., Bittkau, K. & Rau, U. Manipulating the Net Radiative Recombination Rate in Lead Halide Perovskite Films by Modification of Light Outcoupling. *Journal of Physical Chemistry Letters* (2017) doi:10.1021/acs.jpclett.7b02224.

75. Ahrenkiel, R. K. *et al.* Minority-carrier lifetime and photon recycling in *n* -GaAs. *Journal of Vacuum Science & Technology A: Vacuum, Surfaces, and Films* **10**, 990–995 (1992).

76. Balenzategui, J. L. & Martí, A. Detailed modelling of photon recycling: Application to GaAs solar cells. *Solar Energy Materials and Solar Cells* **90**, 1068–1088 (2006).

77. Renaud, P., Raymond, F., Bensaïd, B. & Vèrié, C. Influence of photon recycling on lifetime and diffusion coefficient in GaAs. *Journal of Applied Physics* **71**, 1907–1913 (1992).

78. Dong, Q. *et al.* Electron-hole diffusion lengths > 175 μm in solution-grown $CH_3NH_3PbI_3$ single crystals. *Science (1979)* **347**, 967–970 (2015).

79. Fang, Y., Dong, Q., Shao, Y., Yuan, Y. & Huang, J. Highly narrowband perovskite single-crystal photodetectors enabled by surface-charge recombination. *Nature Photonics* **9**, 679–686 (2015).

80. Yamada, Y., Yamada, T. & Kanemitsu, Y. Free Carrier Radiative Recombination and Photon Recycling in Lead Halide Perovskite Solar Cell Materials. *Bull Chem Soc Jpn* **90**, 1129–1140 (2017).

81. Yamada, T., Yamada, Y., Nakaike, Y., Wakamiya, A. & Kanemitsu, Y. Photon Emission and Reabsorption Processes in CH3NH3PbBr3 Single Crystals Revealed by Time-

Resolved Two-Photon-Excitation Photoluminescence Microscopy. *Physical Review Applied* **7**, 1–8 (2017).

82. Kanemitsu, Y. Luminescence spectroscopy of lead-halide perovskites: materials properties and application as photovoltaic devices. *Journal of Materials Chemistry C* **5**, 3427–3437 (2017).

83. Schnitzer, I., Yablonovitch, E., Caneau, C. & Gmitter, T. J. Ultrahigh spontaneous emission quantum efficiency, 99.7% internally and 72% externally, from AlGaAs/GaAs/AlGaAs double heterostructures. *Applied Physics Letters* **62**, 131–133 (1993).

84. Durbin, S. M. & Gray, J. L. Numerical modeling of photon recycling in solar cells. *IEEE Transactions on Electron Devices* **41**, 239–245 (1994).

85. Gholipour, S. & Saliba, M. From Exceptional Properties to Stability Challenges of Perovskite Solar Cells. *Small* **1802385**, 1–10 (2018).

86. Saliba, M. *et al.* Incorporation of rubidium cations into perovskite solar cells improves photovoltaic performance. *Science (1979)* **354**, 206–209 (2016).

87. Saliba, M. *et al.* How to Make over 20% Efficient Perovskite Solar Cells in Regular (n-i-p) and Inverted (p-i-n) Architectures. *Chemistry of Materials* **30**, 4193–4201 (2018).

88. Tress, W. *et al.* Interpretation and evolution of open-circuit voltage, recombination, ideality factor and subgap defect states during reversible light-soaking and irreversible degradation of perovskite solar cells. *Energy & Environmental Science* **11**, 151–165 (2018).

89. Liu, Z. *et al.* Open-Circuit Voltages Exceeding 1.26 V in Planar Methylammonium Lead Iodide Perovskite Solar Cells. *ACS Energy Letters* **4**, 110–117 (2019).

90. Kirchartz, T., Staub, F. & Rau, U. Impact of Photon Recycling on the Open-Circuit Voltage of Metal Halide Perovskite Solar Cells. *ACS Energy Letters* **1**, 731–739 (2016).

91. Rau, U., Paetzold, U. W. & Kirchartz, T. Thermodynamics of light management in photovoltaic devices. *Physical Review B - Condensed Matter and Materials Physics* **90**, 1–16 (2014).

92. Martí, A., Balenzategui, J. L. & Reyna, R. F. Photon recycling and Shockley's diode equation. *Journal of Applied Physics* **82**, 4067–4075 (1997).

93. Katahara, J. K. & Hillhouse, H. W. Quasi-Fermi level splitting and sub-bandgap absorptivity from semiconductor photoluminescence. *Journal of Applied Physics* **116**, 173504 (2014).

94. Miller, O. D., Yablonovitch, E. & Kurtz, S. R. Strong Internal and External Luminescence as Solar Cells Approach the Shockley–Queisser Limit. *IEEE Journal of Photovoltaics* **2**, 303–311 (2012).

95. Bisquert, J. *The Physics of Solar Cells*. (CRC Press, 2017). doi:10.1201/b22380.

96. van Roosbroeck, W. & Shockley, W. Photon-Radiative Recombination of Electrons and Holes in Germanium. *Physical Review* **94**, 1558–1560 (1954).

97. Kumar, A. *et al.* Ultrafast THz photophysics of solvent engineered triple-cation halide perovskites. *Journal of Applied Physics* **124**, 215106 (2018).

98. Mahboubi Soufiani, A. *et al.* Impact of microstructure on the electron–hole interaction in lead halide perovskites. *Energy & Environmental Science* **10**, 1358–1366 (2017).

99. Crothers, T. W. *et al.* Photon Reabsorption Masks Intrinsic Bimolecular Charge-Carrier Recombination in CH 3 NH 3 PbI 3 Perovskite. *Nano Letters* **17**, 5782–5789 (2017).

100. Wright, A. D. *et al.* Band-Tail Recombination in Hybrid Lead Iodide Perovskite. *Advanced Functional Materials* **27**, 1700860 (2017).

101. Mattheis, J., Rau, U. & Werner, J. H. Light absorption and emission in semiconductors with band gap fluctuations—A study on Cu(In,Ga)Se2 thin films. *Journal of Applied Physics* **101**, 113519 (2007).

102. Green, M. A. *et al.* Solar cell efficiency tables (Version 53). *Progress in Photovoltaics: Research and Applications* **27**, 3–12 (2019).

103. National Renewable Enery Laboratory. Perovskite efficiency chart. *NREL* (2018).

104. Yang, S. *et al.* Tailoring Passivation Molecular Structures for Extremely Small Open-Circuit Voltage Loss in Perovskite Solar Cells. *J Am Chem Soc* **141**, 5781–5787 (2019).

105. Rau, U. Reciprocity relation between photovoltaic quantum efficiency and electroluminescent emission of solar cells. *Physical Review B* **76**, 085303 (2007).

106. Tress, W. *et al.* Predicting the Open-Circuit Voltage of CH 3 NH 3 PbI 3 Perovskite Solar Cells Using Electroluminescence and Photovoltaic Quantum Efficiency Spectra: the Role of Radiative and Non-Radiative Recombination. *Advanced Energy Materials* **5**, 1400812 (2015).

107. Green, M. A. & Bremner, S. P. Energy conversion approaches and materials for high-efficiency photovoltaics. *Nature Materials* **16**, 23–34 (2017).

108. Green, M. A. Radiative efficiency of state-of-the-art photovoltaic cells. *Progress in Photovoltaics: Research and Applications* **20**, 472–476 (2012).

109. Iveland, J., Martinelli, L., Peretti, J., Speck, J. S. & Weisbuch, C. Direct Measurement of Auger Electrons Emitted from a Semiconductor Light-Emitting Diode under Electrical Injection: Identification of the Dominant Mechanism for Efficiency Droop. *Physical Review Letters* **110**, 177406 (2013).

110. Kioupakis, E., Rinke, P., Delaney, K. T. & Van de Walle, C. G. Indirect Auger recombination as a cause of efficiency droop in nitride light-emitting diodes. *Applied Physics Letters* **98**, 161107 (2011).

111. Ross, R. T. Some Thermodynamics of Photochemical Systems. *The Journal of Chemical Physics* **46**, 4590–4593 (1967).

112. Abebe, M. G. *et al.* Rigorous Treatment of Photon Recycling in Thermodynamics of Photovoltaics: The Case of Perovskite Thin-Film Solar Cells. **075141**, 1–12 (2018).

113. Jean, J. *et al.* Radiative Efficiency Limit with Band Tailing Exceeds 30% for Quantum Dot Solar Cells. *ACS Energy Letters* (2017) doi:10.1021/acsenergylett.7b00923.

114. Ritter, D. & Weiser, K. Suppression of interference fringes in absorption measurements on thin films. *Optics Communications* (1986) doi:10.1016/0030-4018(86)90270-1.

115. De Wolf, S. *et al.* Organometallic Halide Perovskites: Sharp Optical Absorption Edge and Its Relation to Photovoltaic Performance. *J Phys Chem Lett* **5**, 1035–9 (2014).

116. Sadhanala, A. *et al.* Preparation of single-phase films of CH3NH3Pb(I1- xBrx)3with sharp optical band edges. *Journal of Physical Chemistry Letters* (2014) doi:10.1021/jz501332v.

117. Mattheis, J., Werner, J. H. & Rau, U. Finite mobility effects on the radiative efficiency limit of pn -junction solar cells. *Physical Review B* **77**, 085203 (2008).

118. Guerrero, A., Juarez-Perez, E. J., Bisquert, J., Mora-Sero, I. & Garcia-Belmonte, G. Electrical field profile and doping in planar lead halide perovskite solar cells. *Applied Physics Letters* **105**, (2014).

119. Herz, L. M. Charge-Carrier Mobilities in Metal Halide Perovskites: Fundamental Mechanisms and Limits. *ACS Energy Letters* **2**, 1539–1548 (2017).

120. Mahboubi Soufiani, A. *et al.* Impact of microstructure on the electron–hole interaction in lead halide perovskites. *Energy & Environmental Science* **10**, 1358–1366 (2017).

121. Yablonovitch, E. Statistical ray optics. *J Opt Soc Am* **72**, 899 (1982).

122. Khan, M. R., Wang, X. & Alam, M. A. Fundamentals of PV Efficiency: Limits for Light Absorption. *arXiv:1212.2897* (2012).

123. Alivisatos, A. P. Semiconductor clusters, nanocrystals, and quantum dots. *Science (1979)* **271**, (1996).

124. Lee, T. *et al.* Highly Efficient and Bright Inverted Top-Emitting InP Quantum Dot Light-Emitting Diodes Introducing a Hole-Suppressing Interlayer. *Small* **15**, (2019).

125. Fuke, N. *et al.* CdSe quantum-dot-sensitized solar cell with ~100% internal quantum efficiency. *ACS Nano* **4**, (2010).

126. Song, J. *et al.* Over 30% External Quantum Efficiency Light-Emitting Diodes by Engineering Quantum Dot-Assisted Energy Level Match for Hole Transport Layer. *Advanced Functional Materials* **29**, (2019).

127. Zhang, H., Chen, S. & Sun, X. W. Efficient Red/Green/Blue Tandem Quantum-Dot Light-Emitting Diodes with External Quantum Efficiency Exceeding 21%. *ACS Nano* **12**, (2018).

128. Wood, V. & Bulović, V. Colloidal quantum dot light-emitting devices. *Nano Reviews* **1**, (2010).

129. Zhang, F. *et al.* Super color purity green quantum dot light-emitting diodes fabricated by using CdSe/CdS nanoplatelets. *Nanoscale* **8**, (2016).

130. Lee, J., Sundar, V. C., Heine, J. R., Bawendi, M. G. & Jensen, K. F. Full color emission from II-VI semiconductor quantum dot-polymer composites. *Advanced Materials* **12**, (2000).

131. Debnath, R., Bakr, O. & Sargent, E. H. Solution-processed colloidal quantum dot photovoltaics: A perspective. *Energy and Environmental Science* vol. 4 (2011).

132. Qian, L., Zheng, Y., Xue, J. & Holloway, P. H. Stable and efficient quantum-dot light-emitting diodes based on solution-processed multilayer structures. *Nature Photonics* **5**, (2011).

133. Cui, J. *et al.* Direct probe of spectral inhomogeneity reveals synthetic tunability of single-nanocrystal spectral linewidths. *Nature Chemistry* **5**, (2013).

134. Anikeeva, P. O., Halpert, J. E., Bawendi, M. G. & Bulović, V. Quantum dot light-emitting devices with electroluminescence tunable over the entire visible spectrum. *Nano Letters* **9**, (2009).

135. Bilan, R., Fleury, F., Nabiev, I. & Sukhanova, A. Quantum dot surface chemistry and functionalization for cell targeting and imaging. *Bioconjugate Chemistry* vol. 26 (2015).

136. Medintz, I. L., Uyeda, H. T., Goldman, E. R. & Mattoussi, H. Quantum dot bioconjugates for imaging, labelling and sensing. *Nature Materials* vol. 4 (2005).

137. Karakoti, A. S., Shukla, R., Shanker, R. & Singh, S. Surface functionalization of quantum dots for biological applications. *Advances in Colloid and Interface Science* vol. 215 (2015).

138. Sun, Y. *et al.* Investigation on Thermally Induced Efficiency Roll-Off: Toward Efficient and Ultrabright Quantum-Dot Light-Emitting Diodes. *ACS Nano* **13**, (2019).

139. Shen, H. *et al.* Visible quantum dot light-emitting diodes with simultaneous high brightness and efficiency. *Nature Photonics* **13**, (2019).

140. Shirasaki, Y., Supran, G. J., Bawendi, M. G. & Bulović, V. Emergence of colloidal quantum-dot light-emitting technologies. *Nature Photonics* vol. 7 (2013).

141. Kim, T., Jin, X., Song, J. H., Jeong, S. & Park, T. Efficiency Limit of Colloidal Quantum Dot Solar Cells: Effect of Optical Interference on Active Layer Absorption. *ACS Energy Letters* vol. 5 (2020).

142. Kramer, I. J. & Sargent, E. H. Colloidal quantum dot photovoltaics: A path forward. *ACS Nano* vol. 5 (2011).

143. Kirmani, A. R. *et al.* Molecular Doping of the Hole-Transporting Layer for Efficient, Single-Step-Deposited Colloidal Quantum Dot Photovoltaics. *ACS Energy Letters* **2**, (2017).

144. Hahm, D. *et al.* Design Principle for Bright, Robust, and Color-Pure InP/ZnSe x S 1- x /ZnS Heterostructures. *Chemistry of Materials* **31**, (2019).

145. Wu, Z., Liu, P., Zhang, W., Wang, K. & Sun, X. W. Development of InP Quantum Dot-Based Light-Emitting Diodes. *ACS Energy Letters* vol. 5 (2020).

146. Jang, E., Kim, Y., Won, Y. H., Jang, H. & Choi, S. M. Environmentally Friendly InP-Based Quantum Dots for Efficient Wide Color Gamut Displays. *ACS Energy Letters* **5**, (2020).

147. Han, C.-Y. *et al.* More Than 9% Efficient ZnSeTe Quantum Dot-Based Blue Electroluminescent Devices. *ACS Energy Letters* **5**, (2020).

148. Yang, Z. *et al.* Recent advances in quantum dot-based light-emitting devices: Challenges and possible solutions. *Materials Today* vol. 24 (2019).

149. Moon, H., Lee, C., Lee, W., Kim, J. & Chae, H. Stability of Quantum Dots, Quantum Dot Films, and Quantum Dot Light-Emitting Diodes for Display Applications. *Advanced Materials* **31**, (2019).

150. Miyazaki, J. & Kinoshita, S. Site-selective spectroscopic study on the dynamics of exciton hopping in an array of inhomogeneously broadened quantum dots. *Physical Review B - Condensed Matter and Materials Physics* **86**, (2012).

151. Kagan, C., Murray, C. & Bawendi, M. Long-range resonance transfer of electronic excitations in close-packed CdSe quantum-dot solids. *Physical Review B - Condensed Matter and Materials Physics* **54**, (1996).

152. Pietryga, J. M. *et al.* Spectroscopic and device aspects of nanocrystal quantum dots. *Chemical Reviews* vol. 116 (2016).

153. Choi, J. J. *et al.* Photogenerated exciton dissociation in highly coupled lead salt nanocrystal assemblies. *Nano Letters* **10**, (2010).

154. Talgorn, E. *et al.* Unity quantum yield of photogenerated charges and band-like transport in quantum-dot solids. *Nature Nanotechnology* **6**, (2011).

155. Lan, X. *et al.* Quantum dot solids showing state-resolved band-like transport. *Nature Materials* (2020) doi:10.1038/s41563-019-0582-2.

156. Lee, J. S., Kovalenko, M. v., Huang, J., Chung, D. S. & Talapin, D. v. Band-like transport, high electron mobility and high photoconductivity in all-inorganic nanocrystal arrays. *Nature Nanotechnology* **6**, (2011).

157. Crooker, S. A., Hollingsworth, J. A., Tretiak, S. & Klimov, V. I. Spectrally Resolved Dynamics of Energy Transfer in Quantum-Dot Assemblies: Towards Engineered Energy Flows in Artificial Materials. *Physical Review Letters* **89**, (2002).

158. Mićić, O. I., Jones, K. M., Cahill, A. & Nozik, A. J. Optical, electronic, and structural properties of uncoupled and close-packed arrays of inP quantum dots. *Journal of Physical Chemistry B* **102**, (1998).

159. Xie, S., Zhu, H., Li, M. & Bulović, V. Voltage-Controlled Reversible Modulation of Colloidal Quantum Dot Thin Film Photoluminescence. *arXiv* (2020).

160. Sun, Y. *et al.* High-Performance Quantum Dot Light-Emitting Diodes Based on Al-Doped ZnO Nanoparticles Electron Transport Layer. *ACS Applied Materials and Interfaces* **10**, (2018).

161. Akselrod, G. M. *et al.* Subdiffusive exciton transport in quantum dot solids. *Nano Letters* **14**, (2014).

162. Gao, Y. *et al.* Enhanced hot-carrier cooling and ultrafast spectral diffusion in strongly coupled PbSe quantum-dot solids. *Nano Letters* **11**, (2011).

163. Proppe, A. H. *et al.* Picosecond Charge Transfer and Long Carrier Diffusion Lengths in Colloidal Quantum Dot Solids. *Nano Letters* **18**, (2018).

164. Yang, Z. *et al.* Mixed-quantum-dot solar cells. *Nature Communications* **8**, (2017).

165. Gilmore, R. H., Lee, E. M. Y., Weidman, M. C., Willard, A. P. & Tisdale, W. A. Charge Carrier Hopping Dynamics in Homogeneously Broadened PbS Quantum Dot Solids. *Nano Letters* **17**, (2017).

166. Lee, E. M. Y. & Tisdale, W. A. Determination of exciton diffusion length by transient photoluminescence quenching and its application to quantum dot films. *Journal of Physical Chemistry C* **119**, (2015).

167. Sun, L. *et al.* Bright infrared quantum-dot light-emitting diodes through inter-dot spacing control. *Nature Nanotechnology* **7**, (2012).

168. Park, S. *et al.* Improved exciton dissociation efficiency by a carbon-quantum-dot doped workfunction modifying layer in polymer solar cells. *Current Applied Physics* **21**, (2021).

169. Devatha, G., Rao, A., Roy, S. & Pillai, P. P. Förster Resonance Energy Transfer Regulated Multicolor Photopatterning from Single Quantum Dot Nanohybrid Films. *ACS Energy Letters* **4**, (2019).

170. Georgitzikis, E., Genoe, J., Heremans, P. & Cheyns, D. Carrier Mobility, Lifetime, and Diffusion Length in Optically Thin Quantum Dot Semiconductor Films. *ACS Applied Materials and Interfaces* **12**, (2020).

171. Zhang, H., Su, Q. & Chen, S. Suppressing Förster Resonance Energy Transfer in Close-Packed Quantum-Dot Thin Film: Toward Efficient Quantum-Dot Light-Emitting Diodes with External Quantum Efficiency over 21.6%. *Advanced Optical Materials* **8**, (2020).

172. Das, S. *et al.* Bacteriorhodopsin Enhances Efficiency of Perovskite Solar Cells. *ACS Applied Materials and Interfaces* **11**, (2019).

173. Dursun, I. & Guzelturk, B. Exciton diffusion exceeding 1 μm: run, exciton, run! *Light: Science and Applications* vol. 10 (2021).

174. Thomas, A., Nair, P. v. & Thomas, K. G. InP quantum dots: An environmentally friendly material with resonance energy transfer requisites. *Journal of Physical Chemistry C* **118**, (2014).

175. Achermann, M., Petruska, M. A., Crooker, S. A. & Klimov, V. I. Picosecond Energy Transfer in Quantum Dot Langmuir - Blodgett Nanoassemblies. *Journal of Physical Chemistry B* **107**, (2003).

176. Madigan, C. & Bulović, V. Modeling of exciton diffusion in amorphous organic thin films. *Physical Review Letters* **96**, (2006).

177. Clapp, A. R., Medintz, I. L. & Mattoussi, H. Förster resonance energy transfer investigations using quantum-dot fluorophores. *ChemPhysChem* vol. 7 (2006).

178. Poulikakos, L. v., Prins, F. & Tisdale, W. A. Transition from thermodynamic to kinetic-limited excitonic energy migration in colloidal quantum dot solids. *Journal of Physical Chemistry C* **118**, (2014).

179. Bässler, H. Charge Transport in Disordered Organic Photoconductors a Monte Carlo Simulation Study. *physica status solidi (b)* vol. 175 (1993).

180. Bnyai, L., Gilliot, P., Hu, Y. Z. & Koch, S. W. Surface-polarization instabilities of electron-hole pairs in semiconductor quantum dots. *Physical Review B* **45**, (1992).

181. Rajadell, F., Movilla, J. L., Royo, M. & Planelles, J. Theory of dielectrically induced surface excitonic states in spherical quantum dots. *Physical Review B - Condensed Matter and Materials Physics* **76**, (2007).

182. Neuhauser, R. G., Shimizu, K. T., Woo, W. K., Empedocles, S. A. & Bawendi, M. G. Correlation between fluorescence intermittency and spectral diffusion in single semiconductor quantum dots. *Physical Review Letters* **85**, (2000).

183. Issac, A., von Borczyskowski, C. & Cichos, F. Correlation between photoluminescence intermittency of CdSe quantum dots and self-trapped states in dielectric media. *Physical Review B - Condensed Matter and Materials Physics* **71**, (2005).

184. Zhu, M., Zhou, J., Hu, Z., Qin, H. & Peng, X. Effects of Local Dielectric Environment on Single-Molecule Spectroscopy of a CdSe/CdS Core/Shell Quantum Dot. *ACS Photonics* **5**, (2018).

185. Faraon, A., Majumdar, A., Kim, H., Petroff, P. & Vučković, J. Fast electrical control of a quantum dot strongly coupled to a photonic-crystal cavity. *Physical Review Letters* **104**, (2010).

186. Heller, W. & Bockelmann, U. Electric-field effects on excitons in quantum dots. *Physical Review B - Condensed Matter and Materials Physics* **57**, (1998).

187. Bawendi, M. G., Carroll, P. J., Wilson, W. L. & Brus, L. E. Luminescence properties of CdSe quantum crystallites: Resonance between interior and surface localized states. *The Journal of Chemical Physics* **96**, (1992).

188. Bakulin, A. A. *et al.* Charge trapping dynamics in pbs colloidal quantum dot photovoltaic devices. *ACS Nano* **7**, (2013).

189. Korlacki, R., Saraf, R. F. & Ducharme, S. Electrical control of photoluminescence wavelength from semiconductor quantum dots in a ferroelectric polymer matrix. *Applied Physics Letters* **99**, (2011).

190. Bozyigit, D., Wood, V., Shirasaki, Y. & Bulovic, V. Study of field driven electroluminescence in colloidal quantum dot solids. in *Journal of Applied Physics* vol. 111 (2012).

191. Prasai, D. *et al.* Electrical Control of near-Field Energy Transfer between Quantum Dots and Two-Dimensional Semiconductors. *Nano Letters* **15**, (2015).

192. Moebius, M. *et al.* Using quantum dot photoluminescence for load detection. *Applied Physics Reviews* **6**, (2016).

193. Scott, R. *et al.* Time-Resolved Stark Spectroscopy in CdSe Nanoplatelets: Exciton Binding Energy, Polarizability, and Field-Dependent Radiative Rates. *Nano Letters* **16**, (2016).

194. Rowland, C. E. *et al.* Effects of shell thickness on the electric field dependence of exciton recombination in CdSe/CdS core/shell quantum dots. *Optical Materials Express* **7**, (2017).

195. Salihoglu, O., Kakenov, N., Balci, O., Balci, S. & Kocabas, C. Graphene-Quantum Dot Hybrid Optoelectronics at Visible Wavelengths. *ACS Photonics* **5**, (2018).

196. Möbius, M. *et al.* Photoluminescence quenching of InP/ZnS quantum dots by charge injection. in *Quantum Sensing and Nanophotonic Devices XII* vol. 9370 (2015).

197. Tisdale, W. A. *et al.* Hot-electron transfer from semiconductor nanocrystals. *Science (1979)* **328**, (2010).

198. Tvrdy, K., Frantsuzov, P. A. & Kamat, P. v. Photoinduced electron transfer from semiconductor quantum dots to metal oxide nanoparticles. *Proc Natl Acad Sci U S A* **108**, (2011).

199. Wei, S. H. & Zunger, A. Calculated natural band offsets of all II-VI and III-V semiconductors: Chemical trends and the role of cation d orbitals. *Applied Physics Letters* **72**, (1998).

200. Reiss, P., Protière, M. & Li, L. Core/shell semiconductor nanocrystals. *Small* vol. 5 (2009).

201. Hinuma, Y., Grüneis, A., Kresse, G. & Oba, F. Band alignment of semiconductors from density-functional theory and many-body perturbation theory. *Physical Review B - Condensed Matter and Materials Physics* **90**, (2014).

202. Mashford, B. S. *et al.* High-efficiency quantum-dot light-emitting devices with enhanced charge injection. *Nature Photonics* **7**, (2013).

203. McGuire, J. A. *et al.* Spectroscopic signatures of photocharging due to hot-carrier transfer in solutions of semiconductor nanocrystals under low-intensity ultraviolet excitation. *ACS Nano* **4**, (2010).

204. Roy, D. *et al.* Why Does the Photoluminescence Efficiency Depend on Excitation Energy in Case of a Quantum Dot? A Case Study of CdSe-Based Core/Alloy Shell/Shell Quantum Dots Employing Ultrafast Pump-Probe Spectroscopy and Single Particle Spectroscopy. *Journal of Physical Chemistry C* **123**, (2019).

205. Righetto, M., Minotto, A. & Bozio, R. Bridging energetics and dynamics of exciton trapping in core-shell quantum dots. *Journal of Physical Chemistry C* **121**, (2017).

206. Zhang, H., Su, Q. & Chen, S. Quantum-dot and organic hybrid tandem light-emitting diodes with multi-functionality of full-color-tunability and white-light-emission. *Nature Communications* **11**, (2020).

207. Jung, H., Ahn, N. & Klimov, V. I. Prospects and challenges of colloidal quantum dot laser diodes. *Nature Photonics* vol. 15 (2021).

208. Yuan, S. *et al.* Self-Assembled High Quality CsPbBr3 Quantum Dot Films toward Highly Efficient Light-Emitting Diodes. *ACS Nano* **12**, (2018).

209. Muller, A. *et al.* High Q (33 000) all-epitaxial microcavity for quantum dot vertical-cavity surface-emitting lasers and quantum light sources. *Applied Physics Letters* **88**, (2006).

210. Dang, C. *et al.* Red, green and blue lasing enabled by single-exciton gain in colloidal quantum dot films. *Nature Nanotechnology* **7**, (2012).

211. Yan, D. *et al.* Ultrastable CsPbBr3 Perovskite Quantum Dot and Their Enhanced Amplified Spontaneous Emission by Surface Ligand Modification. *Small* **15**, (2019).

212. Malko, A. v. *et al.* From amplified spontaneous emission to microring lasing using nanocrystal quantum dot solids. *Applied Physics Letters* **81**, (2002).

213. Moreels, I. *et al.* Nearly temperature-independent threshold for amplified spontaneous emission in colloidal CdSe/CdS quantum dot-in-rods. *Advanced Materials* **24**, (2012).

214. Huang, C. Y. *et al.* CsPbBr3 Perovskite Quantum Dot Vertical Cavity Lasers with Low Threshold and High Stability. *ACS Photonics* **4**, (2017).

215. Vila-Liarte, D. *et al.* Templated-Assembly of CsPbBr3 Perovskite Nanocrystals into 2D Photonic Supercrystals with Amplified Spontaneous Emission. *Angewandte Chemie - International Edition* **59**, (2020).

216. Peinke, E. *et al.* Tailoring the properties of quantum dot-micropillars by ultrafast optical injection of free charge carriers. *Light: Science and Applications* vol. 10 (2021).

217. Lin, C. H. *et al.* Large-Scale Robust Quantum Dot Microdisk Lasers with Controlled High Quality Cavity Modes. *Advanced Optical Materials* **5**, (2017).

218. Muller, A. *et al.* Self-aligned all-epitaxial microcavity for cavity QED with quantum dots. *Nano Letters* **6**, (2006).

219. Brückner, R. *et al.* Phase-locked coherent modes in a patterned metal-organic microcavity. *Nature Photonics* **6**, (2012).

220. Kaitouni, R. I. *et al.* Engineering the spatial confinement of exciton polaritons in semiconductors. *Physical Review B - Condensed Matter and Materials Physics* **74**, (2006).

221. Scafirimuto, F., Urbonas, D., Scherf, U., Mahrt, R. F. & Stöferle, T. Room-Temperature Exciton-Polariton Condensation in a Tunable Zero-Dimensional Microcavity. *ACS Photonics* **5**, (2018).

222. Constantin, C. *et al.* Quantum wires in multidimensional microcavities: Effects of photon dimensionality on emission properties. *Physical Review B - Condensed Matter and Materials Physics* **66**, (2002).

223. Anguiano, S. *et al.* Three-dimensional trapping of light with light in semiconductor planar microcavities. *Physical Review B* **99**, (2019).

224. Langner, M. *et al.* Strong optical confinement and multimode emission of organic photonic dots. *Applied Physics Letters* **91**, (2007).

225. Lu, D., Ahn, J., Huang, H. & Deppe, D. G. All-epitaxial mode-confined vertical-cavity surface-emitting laser. *Applied Physics Letters* **85**, (2004).

226. Sanvitto, D. *et al.* Observation of ultrahigh quality factor in a semiconductor microcavity. *Applied Physics Letters* **86**, (2005).

227. Lohmeyer, H. *et al.* Confined optical modes in monolithic II-VI pillar microcavities. *Applied Physics Letters* **88**, (2006).

228. Balakrishnan, S. *et al.* Confined optical modes and amplified spontaneous emission from a microtube cavity formed by vacuum assisted filtration. *Applied Physics Letters* **89**, (2006).

229. Zhao, G., Zhang, Y., Deppe, D. G., Konthasinghe, K. & Muller, A. Buried heterostructure vertical-cavity surface-emitting laser with semiconductor mirrors. *Applied Physics Letters* **101**, (2012).

230. Grosso, G. *et al.* Nonlinear relaxation and selective polychromatic lasing of confined polaritons. *Physical Review B - Condensed Matter and Materials Physics* **90**, (2014).

231. Urbonas, D., Stöferle, T., Scafirimuto, F., Scherf, U. & Mahrt, R. F. Zero-Dimensional Organic Exciton-Polaritons in Tunable Coupled Gaussian Defect Microcavities at Room Temperature. *ACS Photonics* **3**, (2016).

232. Tao, R., Kamide, K., Arita, M., Kako, S. & Arakawa, Y. Room-Temperature Observation of Trapped Exciton-Polariton Emission in GaN/AlGaN Microcavities with Air-Gap/III-Nitride Distributed Bragg Reflectors. *ACS Photonics* **3**, (2016).

233. Winkler, K. *et al.* Collective state transitions of exciton-polaritons loaded into a periodic potential. *Physical Review B* **93**, (2016).

234. Ouellet-Plamondon, C. *et al.* Spatial multistability induced by cross interactions of confined polariton modes. *Physical Review B* **93**, (2016).

235. Jayaprakash, R. *et al.* Ultra-low threshold polariton lasing at room temperature in a GaN membrane microcavity with a zero-dimensional trap. *Scientific Reports* **7**, (2017).

236. Kuznetsov, A. S., Helgers, P. L. J., Biermann, K. & Santos, P. v. Quantum confinement of exciton-polaritons in a structured (Al,Ga)As microcavity. *Physical Review B* **97**, (2018).

237. Navadeh-Toupchi, M., Jabeen, F., Oberli, D. Y. & Portella-Oberli, M. T. Localized photon lasing in a polaritonic lattice landscape. *Physical Review Applied* **14**, (2020).

238. Stern, F. & Woodall, J. M. Photon recycling in semiconductor lasers. *Journal of Applied Physics* **45**, (1974).

239. Lodahl, P. *et al.* Controlling the dynamics of spontaneous emission from quantum dots by photonic crystals. *Nature* **430**, (2004).

240. Giacobino, E. *et al.* All-optical polariton transistor. (2013) doi:10.1038/ncomms2734.

241. Feng, J. *et al.* All-optical switching based on interacting exciton polaritons in self-assembled perovskite microwires. *Science Advances* **7**, (2021).

242. Zasedatelev, A. v. *et al.* A room-temperature organic polariton transistor. *Nature Photonics* vol. 13 (2019).

243. Gu, J. *et al.* Enhanced nonlinear interaction of polaritons via excitonic Rydberg states in monolayer WSe2. *Nature Communications* **12**, (2021).

244. Ghosh, S. & Liew, T. C. H. Quantum computing with exciton-polariton condensates. *npj Quantum Information* **6**, (2020).

245. Puri, S., Kim, N. Y. & Yamamoto, Y. Exciton-polariton mediated universal quantum computing. in *2013 Conference on Lasers and Electro-Optics, CLEO 2013* (2013). doi:10.1364/cleo_qels.2013.qm3c.5.

246. Demirchyan, S. S., Chestnov, I. Y., Alodjants, A. P., Glazov, M. M. & Kavokin, A. v. Qubits based on polariton rabi oscillators. *Physical Review Letters* **112**, (2014).

247. Cuevas, Á. *et al.* First observation of the quantized exciton-polariton field and effect of interactions on a single polariton. *Science Advances* **4**, (2018).

248. Xue, Y. *et al.* Split-ring polariton condensates as macroscopic two-level quantum systems. *Physical Review Research* **3**, (2021).

249. Wasielewski, M. R. *et al.* Exploiting chemistry and molecular systems for quantum information science. *Nature Reviews Chemistry* **4**, (2020).

250. Kolaric, B., Maes, B., Clays, K., Durt, T. & Caudano, Y. Strong Light–Matter Coupling as a New Tool for Molecular and Material Engineering: Quantum Approach. *Advanced Quantum Technologies* vol. 1 (2018).

251. Galego, J., Garcia-Vidal, F. J. & Feist, J. Cavity-induced modifications of molecular structure in the strong-coupling regime. *Physical Review X* **5**, (2015).

252. Liu, B., Menon, V. M. & Sfeir, M. Y. The Role of Long-Lived Excitons in the Dynamics of Strongly Coupled Molecular Polaritons. *ACS Photonics* **7**, (2020).

253. Su, R. *et al.* Perovskite semiconductors for room-temperature exciton-polaritonics. *Nature Materials* vol. 20 (2021).

254. Fieramosca, A. *et al.* Two-dimensional hybrid perovskites sustaining strong polariton interactions at room temperature. *Science Advances* (2019) doi:10.1126/sciadv.aav9967.

255. Wang, J. *et al.* Room Temperature Coherently Coupled Exciton Polaritons in Two-Dimensional Organic-Inorganic Perovskite. *ACS Nano* (2018) doi:10.1021/acsnano.8b03737.

256. Anantharaman, S. B. *et al.* Self-Hybridized Polaritonic Emission from Layered Perovskites. *Nano Letters* **21**, (2021).

257. Brehier, A., Parashkov, R., Lauret, J. S. & Deleporte, E. Strong exciton-photon coupling in a microcavity containing layered perovskite semiconductors. *Applied Physics Letters* (2006) doi:10.1063/1.2369533.

258. Wenus, J. *et al.* Hybrid organic-inorganic exciton-polaritons in a strongly coupled microcavity. *Physical Review B - Condensed Matter and Materials Physics* (2006) doi:10.1103/PhysRevB.74.235212.

259. Lanty, G. *et al.* Hybrid cavity polaritons in a ZnO-perovskite microcavity. *Physical Review B - Condensed Matter and Materials Physics* (2011) doi:10.1103/PhysRevB.84.195449.

260. Fieramosca, A. *et al.* Tunable Out-of-Plane Excitons in 2D Single-Crystal Perovskites. *ACS Photonics* (2018) doi:10.1021/acsphotonics.8b00984.

261. Polimeno, L. *et al.* Tuning of the Berry curvature in 2D perovskite polaritons. *Nature Nanotechnology* **16**, (2021).

262. Kim, S. *et al.* Topological Control of 2D Perovskite Emission in the Strong Coupling Regime. *Nano Letters* **21**, (2021).

263. Zhang, Q., Shang, Q., Su, R., Do, T. T. H. & Xiong, Q. Halide Perovskite Semiconductor Lasers: Materials, Cavity Design, and Low Threshold. *Nano Letters* vol. 21 (2021).

264. Su, R. *et al.* Room-Temperature Polariton Lasing in All-Inorganic Perovskite Nanoplatelets. *Nano Letters* **17**, 3982–3988 (2017).

265. Li, H. *et al.* Localization of anisotropic exciton polariton condensates in perovskite microcavities. *Applied Physics Letters* **120**, 11104 (2022).

266. Su, R., Ghosh, S., Liew, T. C. H. & Xiong, Q. Optical switching of topological phase in a perovskite polariton lattice. *Science Advances* **7**, (2021).

267. Wang, J. *et al.* Spontaneously coherent orbital coupling of counterrotating exciton polaritons in annular perovskite microcavities. *Light: Science and Applications* **10**, (2021).

268. Wu, J. *et al.* Nonlinear Parametric Scattering of Exciton Polaritons in Perovskite Microcavities. *Nano Letters* **21**, (2021).

269. Han, Q. *et al.* Transition between Exciton-Polariton and Coherent Photonic Lasing in All-Inorganic Perovskite Microcuboid. *ACS Photonics* **7**, (2020).

270. Zhang, S. *et al.* Trapped Exciton-Polariton Condensate by Spatial Confinement in a Perovskite Microcavity. *ACS Photonics* **7**, (2020).

271. Shang, Q. *et al.* Role of the Exciton-Polariton in a Continuous-Wave Optically Pumped CsPbBr3Perovskite Laser. *Nano Letters* **20**, (2020).

272. Su, R. *et al.* Observation of exciton polariton condensation in a perovskite lattice at room temperature. *Nature Physics* vol. 16 (2020).

273. Polimeno, L. *et al.* Observation of Two Thresholds Leading to Polariton Condensation in 2D Hybrid Perovskites. *Advanced Optical Materials* **8**, (2020).

274. Delport, G. *et al.* Exciton-exciton annihilation in two-dimensional halide perovskites at room temperature. *Journal of Physical Chemistry Letters* **10**, (2019).

275. Qin, C. *et al.* Stable room-temperature continuous-wave lasing in quasi-2D perovskite films. *Nature* **585**, (2020).

276. Ardizzone, V. *et al.* Emerging 2D materials for room-temperature polaritonics. *Nanophotonics* (2019) doi:10.1515/nanoph-2019-0114.

277. Ishihara, T., Takahashi, J. & Goto, T. Optical properties due to electronic transitions in two-dimensional semiconductors (CnH2n+1NH3)2PbI4. *Physical Review B* **42**, (1990).

278. Tanaka, K. *et al.* Comparative study on the excitons in lead-halide-based perovskite-type crystals CH3NH3PbBr3 CH3NH 3PbI3. *Solid State Communications* **127**, (2003).

279. Lin, Y. *et al.* Unveiling the operation mechanism of layered perovskite solar cells. *Nature Communications* **10**, (2019).

280. Wu, X., Trinh, M. T. & Zhu, X. Y. Excitonic Many-Body Interactions in Two-Dimensional Lead Iodide Perovskite Quantum Wells. *Journal of Physical Chemistry C* **119**, (2015).

281. Zhang, T. *et al.* Controlling Quantum-Well Width Distribution and Crystal Orientation in Two-Dimensional Tin Halide Perovskites via a Strong Interlayer Electrostatic Interaction. *ACS Applied Materials and Interfaces* **13**, (2021).

282. Cinquino, M. *et al.* Managing Growth and Dimensionality of Quasi 2D Perovskite Single-Crystalline Flakes for Tunable Excitons Orientation. *Advanced Materials* **33**, (2021).

283. Blancon, J. C. *et al.* Scaling law for excitons in 2D perovskite quantum wells. *Nature Communications* **9**, (2018).

284. Yu, G. *et al.* Two-round quasi-whispering gallery mode exciton polaritons with large Rabi splitting in a GaN microrod. *Optics Express* **29**, (2021).

285. Arnardottir, K. B., Moilanen, A. J., Strashko, A., Törmä, P. & Keeling, J. Multimode Organic Polariton Lasing. *Physical Review Letters* **125**, (2020).

286. Ishii, T. *et al.* Enhanced Light–Matter Interaction and Polariton Relaxation by the Control of Molecular Orientation. *Advanced Optical Materials* **9**, (2021).

287. Corfdir, P. *et al.* Impact of biexcitons on the relaxation mechanisms of polaritons in III-nitride based multiple quantum well microcavities. *Physical Review B - Condensed Matter and Materials Physics* **85**, (2012).

288. Li, H. *et al.* Sensitive and Stable 2D Perovskite Single-Crystal X-ray Detectors Enabled by a Supramolecular Anchor. *Advanced Materials* **32**, (2020).

289. Steger, M. *et al.* Long-range ballistic motion and coherent flow of long-lifetime polaritons. *Physical Review B - Condensed Matter and Materials Physics* **88**, (2013).

290. Nelsen, B. *et al.* Dissipationless flow and sharp threshold of a polariton condensate with long lifetime. *Physical Review X* **3**, (2014).

291. Steger, M., Gautham, C., Snoke, D. W., Pfeiffer, L. & West, K. Slow reflection and two-photon generation of microcavity exciton–polaritons. *Optica* **2**, (2015).

292. Deng, H., Haug, H. & Yamamoto, Y. Exciton-polariton Bose-Einstein condensation. *Reviews of Modern Physics* (2010) doi:10.1103/RevModPhys.82.1489.

293. Coles, D. M., Grant, R. T., Lidzey, D. G., Clark, C. & Lagoudakis, P. G. Imaging the polariton relaxation bottleneck in strongly coupled organic semiconductor microcavities. *Physical Review B - Condensed Matter and Materials Physics* **88**, (2013).

294. Rappel, W. J., Feiner, L. F. & Schuurmans, M. F. H. Exciton-polariton picture of the free-exciton lifetime in GaAs. *Physical Review B* **38**, (1988).

295. Tassone, F., Piermarocchi, C., Savona, V. & Quattropani, A. Bottleneck effects in the relaxation and photoluminescence of microcavity polaritons. *Physical Review B - Condensed Matter and Materials Physics* (1997) doi:10.1103/PhysRevB.56.7554.

296. Tartakovskii, A. *et al.* Relaxation bottleneck and its suppression in semiconductor microcavities. *Physical Review B - Condensed Matter and Materials Physics* **62**, (2000).

297. Stokker-Cheregi, F. *et al.* Polariton relaxation bottleneck and its thermal suppression in bulk GaN microcavities. *Applied Physics Letters* **92**, (2008).

298. Maragkou, M., Grundy, A. J. D., Ostatnick, T. & Lagoudakis, P. G. Longitudinal optical phonon assisted polariton laser. *Applied Physics Letters* **97**, (2010).

299. Müller, M., Bleuse, J., André, R. & Ulmer-Tuffigo, H. Observation of bottleneck effects on the photoluminescence from polaritons in II-VI microcavities. *Physica B: Condensed Matter* **272**, (1999).

300. Heim, U. & Wiesner, P. Direct evidence for a bottleneck of exciton-polariton relaxation in CdS. *Physical Review Letters* **30**, (1973).

301. Graf, A., Tropf, L., Zakharko, Y., Zaumseil, J. & Gather, M. C. Near-infrared exciton-polaritons in strongly coupled single-walled carbon nanotube microcavities. *Nature Communications* **7**, (2016).

302. Snoke, D. The Connection of Polaritons and Vacuum Rabi Splitting. *arXiv* (2015).

303. Ebbesen, T. W. Hybrid Light-Matter States in a Molecular and Material Science Perspective. *Accounts of Chemical Research* vol. 49 (2016).

304. Feldstein, D. *et al.* Microscopic Picture of Electron-Phonon Interaction in Two-Dimensional Halide Perovskites. *Journal of Physical Chemistry Letters* **11**, (2020).

305. Straus, D. B. *et al.* Direct Observation of Electron-Phonon Coupling and Slow Vibrational Relaxation in Organic-Inorganic Hybrid Perovskites. *J Am Chem Soc* **138**, (2016).

306. Long, H. *et al.* Exciton-phonon interaction in quasi-two dimensional layered (PEA)2(CsPbBr3): N -1PbBr4 perovskite. *Nanoscale* **11**, (2019).

307. Li, R. *et al.* Room-temperature electroluminescence from two-dimensional lead halide perovskites. *Applied Physics Letters* **109**, (2016).

308. Do, T. T. H. *et al.* Bright Exciton Fine-Structure in Two-Dimensional Lead Halide Perovskites. *Nano Letters* **20**, (2020).

309. Tang, W. *et al.* Thickness dependent dark exciton emission in (PEA)2PbI4 nanoflake and its brightening by in-plane magnetic field. *arXiv* (2021).

310. Neumann, T. *et al.* Manganese doping for enhanced magnetic brightening and circular polarization control of dark excitons in paramagnetic layered hybrid metal-halide perovskites. *Nature Communications* **12**, (2021).

311. Hong, X., Ishihara, T. & Nurmikko, A. v. Dielectric confinement effect on excitons in PbI4-based layered semiconductors. *Physical Review B* **45**, (1992).

312. DeCrescent, R. A. *et al.* Bright magnetic dipole radiation from two-dimensional lead-halide perovskites. *Science Advances* **6**, (2020).

313. Fang, H. H. *et al.* Band-Edge Exciton Fine Structure and Exciton Recombination Dynamics in Single Crystals of Layered Hybrid Perovskites. *Advanced Functional Materials* **30**, (2020).

314. Thouin, F. *et al.* Stable biexcitons in two-dimensional metal-halide perovskites with strong dynamic lattice disorder. *Physical Review Materials* **2**, (2018).

315. Kondo, T., Azuma, T., Yuasa, T. & Ito, R. Biexciton lasing in the layered perovskite-type material (C6H13NH3)2PbI4. *Solid State Communications* **105**, (1998).

316. Burgos-Caminal, A., Socie, E., Bouduban, M. E. F. & Moser, J. E. Exciton and Carrier Dynamics in Two-Dimensional Perovskites. *Journal of Physical Chemistry Letters* **11**, (2020).

317. Baker, H., Strandell, D. & Kambhampati, P. Emitting State of Bulk CsPbBr3Perovskite Nanocrystals Reveals a Quantum-Confined Excitonic Structure. *Journal of Physical Chemistry C* **124**, (2020).

318. Wang, Z. *et al.* Intravalley Spin-Flip Relaxation Dynamics in Single-Layer WS2. *Nano Letters* **18**, (2018).

319. Biadala, L. *et al.* Band-Edge Exciton Fine Structure and Recombination Dynamics in InP/ZnS Colloidal Nanocrystals. *ACS Nano* **10**, (2016).

320. Qiao, T. *et al.* Magnetic Effect of Dopants on Bright and Dark Excitons in Strongly Confined Mn-Doped CsPbI3Quantum Dots. *Nano Letters* **21**, (2021).

321. Vinattieri, A. *et al.* Exciton dynamics in GaAs quantum wells under resonant excitation. *Physical Review B* **50**, (1994).

322. Zhang, X. X., You, Y., Zhao, S. Y. F. & Heinz, T. F. Experimental Evidence for Dark Excitons in Monolayer WSe2. *Physical Review Letters* **115**, (2015).

323. Snoke, D. & Rühle, W. Spin flip of excitons in GaAs quantum wells. *Physical Review B - Condensed Matter and Materials Physics* **55**, (1997).

324. Muñoz, L., Pérez, E., Viña, L. & Ploog, K. Spin relaxation in intrinsic GaAs quantum wells: Influence of excitonic localization. *Physical Review B* **51**, (1995).

325. Viña, L. Spin relaxation in low-dimensional systems. *Journal of Physics Condensed Matter* **11**, (1999).

326. Zerrouati, K. *et al.* Spin-lattice relaxation in p-type gallium arsenide single crystals. *Physical Review B* **37**, (1988).

327. Fishman, G. & Lampel, G. Spin relaxation of photoelectrons in p-type gallium arsenide. *Physical Review B* **16**, (1977).

328. Sallen, G. *et al.* Exciton dynamics of a single quantum dot embedded in a nanowire. *Physical Review B - Condensed Matter and Materials Physics* **80**, (2009).

329. deQuilettes, D. W. *et al.* Impact of Photon Recycling, Grain Boundaries, and Nonlinear Recombination on Energy Transport in Semiconductors. *ACS Photonics* **0**, null (2022).

330. Snoke, D. W., Hübner, J., Rühle, W. W. & Zundel, M. Spin flip from dark to bright states in InP quantum dots. *Physical Review B - Condensed Matter and Materials Physics* **70**, (2004).

331. Kirstein, E. *et al.* Lead-Dominated Hyperfine Interaction Impacting the Carrier Spin Dynamics in Halide Perovskites. *Advanced Materials* **34**, (2022).

332. Yu, Z. G. & Li, Y. S. Unraveling the Spin Relaxation Mechanism in Hybrid Organic-Inorganic Perovskites. *Journal of Physical Chemistry C* **123**, (2019).

333. Odenthal, P. *et al.* Spin-polarized exciton quantum beating in hybrid organic-inorganic perovskites. *Nature Physics* **13**, (2017).

334. Long, G. *et al.* Chiral-perovskite optoelectronics. *Nature Reviews Materials* vol. 5 (2020).

335. Belykh, V. v. *et al.* Coherent spin dynamics of electrons and holes in CsPbBr3 perovskite crystals. *Nature Communications* **10**, (2019).

336. Yang, L. *et al.* Long-lived nanosecond spin relaxation and spin coherence of electrons in monolayer MoS 2 and WS 2. *Nature Physics* **11**, (2015).

337. Denev, S. & Snoke, D. W. Stress dependence of exciton relaxation processes in Cu2O. *Physical Review B - Condensed Matter and Materials Physics* **65**, (2002).

338. Jang, J. I., O'Hara, K. E. & Wolfe, J. P. Spin-exchange kinetics of excitons in Cu2O: Transverse acoustic phonon mechanism. *Physical Review B - Condensed Matter and Materials Physics* **70**, (2004).

339. Colton, J. S., Kennedy, T. A., Bracker, A. S. & Gammon, D. Microsecond spin-flip times in n − GaAs measured by time-resolved polarization of photoluminescence. *Physical Review B - Condensed Matter and Materials Physics* **69**, (2004).

340. Prada, M., Blick, R. H. & Joynt, R. Singlet-triplet relaxation in two-electron silicon quantum dots. *Physical Review B - Condensed Matter and Materials Physics* **77**, (2008).

341. Meunier, T. *et al.* Experimental signature of phonon-mediated spin relaxation in a two-electron quantum dot. *Physical Review Letters* **98**, (2007).

342. Swift, M. *et al.* Dark and Bright Excitons in Halide Perovskite Nanoplatelets. in (2021). doi:10.29363/nanoge.incnc.2021.013.

343. Shornikova, E. v. *et al.* Addressing the exciton fine structure in colloidal nanocrystals: The case of CdSe nanoplatelets. *Nanoscale* **10**, (2018).

344. Schmidt, D. *et al.* Tracking Dark Excitons with Exciton Polaritons in Semiconductor Microcavities. *Physical Review Letters* **122**, (2019).

345. Xu, K., Vliem, J. F. & Meijerink, A. Long-Lived Dark Exciton Emission in Mn-Doped CsPbCl 3 Perovskite Nanocrystals. *Journal of Physical Chemistry C* **123**, (2019).

346. Renken, S. *et al.* Untargeted effects in organic exciton-polariton transient spectroscopy: A cautionary tale. *Journal of Chemical Physics* **155**, (2021).

347. Lüttgens, J. M., Berger, F. J. & Zaumseil, J. Population of Exciton-Polaritons via Luminescent sp3Defects in Single-Walled Carbon Nanotubes. *ACS Photonics* **8**, (2021).

348. Dhavamani, A., Haeberlé, L., Wang, J., Kéna-Cohen, S. & Arnold, M. S. Cavity-Mediated Hybridization of Bright and Dark Excitons in an Ultrastrongly Coupled Carbon Nanotube Microcavity. *ACS Photonics* **8**, (2021).

349. Lundt, N. *et al.* Observation of macroscopic valley-polarized monolayer exciton-polaritons at room temperature. *Physical Review B* **96**, (2017).

350. Akselrod, G. M., Young, E. R., Bradley, M. S. & Bulović, V. Lasing through a strongly-coupled mode by intra-cavity pumping. *Optics Express* **21**, (2013).

351. Bradley, M. S. & Bulović, V. Intracavity optical pumping of J-aggregate microcavity exciton polaritons. *Physical Review B - Condensed Matter and Materials Physics* **82**, (2010).

352. Putintsev, A. *et al.* Nano-second exciton-polariton lasing in organic microcavities. *Applied Physics Letters* **117**, (2020).

353. Grant, R. T. *et al.* Efficient Radiative Pumping of Polaritons in a Strongly Coupled Microcavity by a Fluorescent Molecular Dye. *Advanced Optical Materials* **4**, (2016).

354. Lodden, G. H. & Holmes, R. J. Electrical excitation of microcavity polaritons by radiative pumping from a weakly coupled organic semiconductor. *Physical Review B - Condensed Matter and Materials Physics* **82**, (2010).

355. Zhang, Y. *et al.* Optical Properties of Two-Dimensional Perovskite Films of (C 6 H 5 C 2 H 4 NH 3) 2 [PbI 4] and (C 6 H 5 C 2 H 4 NH 3) 2 (CH 3 NH 3) 2 [Pb 3 I 10]. *Journal of Physical Chemistry Letters* **10**, (2019).

356. Wang, Z. W., Liu, L. & Li, S. S. Spin-flip relaxation via optical phonon scattering in quantum dots. *Journal of Applied Physics* **114**, (2013).

357. Wang, Z. W., Li, Z. Q. & Li, S. S. The optical phonon resonance scattering with spin-conserving and spin-flip processes between Landau levels in graphene. *Journal of Physics Condensed Matter* **26**, (2014).

358. Scott, J. F. Spin-flip plus phonon scattering. *Physical Review B* vol. 19 (1979).

359. Pau, S. *et al.* LO-phonon-enhanced microcavity polariton emission. *Physical Review B - Condensed Matter and Materials Physics* **55**, (1997).

360. Imamog¯lu, A., Ram, R. J., Pau, S. & Yamamoto, Y. Nonequilibrium condensates and lasers without inversion: Exciton-polariton lasers. *Physical Review A - Atomic, Molecular, and Optical Physics* **53**, (1996).

361. Bœuf, F. *et al.* Evidence of polariton stimulation in semiconductor microcavities. *Physica Status Solidi (A) Applied Research* **183**, (2001).

362. Trichet, A. *et al.* Long-range correlations in a 97% excitonic one-dimensional polariton condensate. *Physical Review B - Condensed Matter and Materials Physics* **88**, (2013).

363. Coles, D. M. *et al.* Vibrationally assisted polariton-relaxation processes in strongly coupled organic-semiconductor microcavities. *Advanced Functional Materials* **21**, (2011).

364. Ishii, T. *et al.* Low-Threshold Exciton-Polariton Condensation via Fast Polariton Relaxation in Organic Microcavities. *Advanced Optical Materials* (2021) doi:10.1002/adom.202102034.

365. Mazza, L., Kéna-Cohen, S., Michetti, P. & la Rocca, G. C. Microscopic theory of polariton lasing via vibronically assisted scattering. *Physical Review B - Condensed Matter and Materials Physics* **88**, (2013).

366. Michetti, P. & la Rocca, G. C. Exciton-phonon scattering and photoexcitation dynamics in J-aggregate microcavities. *Physical Review B - Condensed Matter and Materials Physics* **79**, (2009).

367. de Mello, J. C., Wittmann, H. F. & Friend, R. H. An improved experimental determination of external photoluminescence quantum efficiency. *Advanced Materials* **9**, (1997).

368. Kim, J. C., Wake, D. R. & Wolfe, J. P. Thermodynamics of biexcitons in a GaAs quantum well. *Physical Review B* **50**, (1994).